SLAC-R-621
April 2003

Beam Techniques – Beam Control and Manipulation

Michiko G. Minty
Stanford Linear Accelerator Center, Stanford, CA 94309, USA

Frank Zimmermann
CERN, SL Division, 1211 Geneva 23, Switzerland

We describe commonly used strategies for the control of charged particle beams and the manipulation of their properties. Emphasis is placed on relativistic beams in linear accelerators and storage rings. After a brief review of linear optics, we discuss basic and advanced beam control techniques, such as transverse and longitudinal lattice diagnostics, matching, orbit correction and steering, beam-based alignment, and linac emittance preservation. A variety of methods for the manipulation of particle beam properties are also presented, for instance, bunch length and energy compression, bunch rotation, changes to the damping partition number, and beam collimation. The different procedures are illustrated by examples from various accelerators. Special topics include injection and extraction methods, beam cooling, spin transport and polarization.

Proceedings of
Lectures given at the US Particle Accelerator School,
University of Chicago and Argonne National Laboratory,
June 14–25, 1999

Work supported in part by the Department of Energy contract DE-AC03-76SF00515.

Contents for Ph513/IU-USPAS P671B 6/99

M. Minty (SLAC), F. Zimmermann (CERN)

Chapter 1

Introduction

This report describes commonly used strategies for the control of charged particle beams and the manipulation of their properties. Emphasis is placed on relativistic beams in linear accelerators and storage rings. After briefly reviewing the fundamentals of accelerator optics, we discuss basic and advanced beam control techniques, such as transverse and longitudinal lattice diagnostics and matching procedures, orbit correction and steering, beam-based alignment, and linac emittance preservation. Techniques for the manipulation of particle beam properties are presented next, including bunch length and energy compression, bunch rotation, changes to the damping partition number, and beam collimation issues. Finally, we discuss a few special topics, such as injection and extraction methods, beam cooling, spin transport and polarization.

The different techniques are illustrated by examples from various existing or past accelerators: the large electron-positron collider LEP [1] at CERN, the SLAC PEP-II B factory [2], the linac of the KEK B factory [3], the Stanford Linear Collider (SLC) [4,5], TRISTAN at KEK [6], the synchrotron light source SPEAR at SLAC [7], the CERN Low Energy Antiproton Ring (LEAR) [8], the Accelerator Test Facility (ATF) at KEK [9], the electron-proton collider HERA at DESY [10], the final-focus test beam at SLAC [11], the CERN $p\bar{p}$ collider SPS [12], the ASSET experiment at SLAC [13], and the ISR at CERN [14]. At various places, we will also extrapolate to planned or proposed future accelerators, such as the Large Hadron Collider [15], the Next Linear Collider [16], the TESLA Linear Collider [17], and the Muon Collider [18].

1.1 Review of Transverse Linear Optics

In linear approximation, the transverse motion of a single particle in an accelerator can be described as the sum of three components[19,20]

$$u(s) = u_{c.o.}(s) + u_\beta(s) + \eta(s)\delta \tag{1.1}$$

where $u_\beta(s) = x$ or y is the horizontal or vertical coordinate at the (azimuthal) location s, and $u_{c.o.}$ denotes the closed equilibrium orbit (or, in a transport line, some reference trajectory), u_β the orbit variation due to betatron motion (transverse oscillations), and $\eta\delta$ the orbit change resulting from an energy offset; η is the dispersion function, and $\delta = \Delta p/p$ the relative deviation from the design momentum.

The betatron motion can be parametrized by a pseudo-harmonic oscillation of the form[19]

$$u_\beta(s) = \sqrt{2I_{x,y}\beta_{x,y}(s)}\ \cos(\phi_{x,y}(s) + \phi_0) \tag{1.2}$$

where $\beta_{x,y}(s)$ is called the beta function, $\phi_{x,y}(s)$ the betatron phase, and $I_{x,y}$ is an action variable. The functions $\phi_{x,y}(s)$ and $\beta_{x,y}(s)$ depend on the azimuthal location s, while the action $I_{x,y}$ and initial phase ϕ_0 are constants of motion. The value of $I_{x,y}$ averaged over all particles of a beam is equal to the rms beam emittance, $\epsilon_{x,y}^{rms} =< I_{x,y} >$. The `betatron oscillation' described by Eq. (1.2) refers to a particle at a fixed design energy. Later, we will discuss how the motion is modified if the energy is not constant, presenting the two concepts of dispersion and chromaticity. Furthermore, when the beam is accelerated, as in a linac, Eq. (1.2) must be multiplied by a factor $\sqrt{\gamma(0)/\gamma(s)}$, since the increase in longitudinal momentum p_s reduces the transverse beam size (it effectively introduces a damping force $d^2u/ds^2 \approx -p_u/p_s^2\ dp_s/ds$).

In addition to the beta function β, two closely related functions are often introduced to characterize the betatron motion. These are

$$\alpha(s) = -\frac{1}{2}\beta'(s) \qquad \text{and} \qquad \gamma(s) = \frac{1+\alpha^2(s)}{\beta(s)} \tag{1.3}$$

where the prime indicates a derivative with respect to the longitudinal position s, and we have dropped the subindex `x, y'. Henceforth, we will use x instead of u, but, here and in the following, the same equations apply in the horizontal and in the vertical plane. The main difference is that quadrupoles which are focusing in one plane are defocusing in the other. Finally note that if the location is inside a linac accelerating structure the formula for α reads $\alpha(s) = (-\beta'(s)/2 + \beta E'(s)/(2E(s)))$, where $E(s)$ is the beam energy at location s.

The three optical functions $\beta(s)$, $\alpha(s)$ and $\gamma(s)$ are proportional to the three second moments of the beam distribution, with the beam emittance as constant of

proportionality:

$$< x^2 >_s \;=\; \beta(s)\,\epsilon \tag{1.4}$$

$$< xx' >_s \;=\; -\alpha(s)\,\epsilon \tag{1.5}$$

$$< x'^2 >_s \;=\; \gamma(s)\,\epsilon \tag{1.6}$$

where $< \ldots >_s$ denotes an average over the beam distribution at the location s. Thus, the actual values of β, α and γ can be deduced from the measured beam distribution. It is a challenge to the accelerator physicist to make them coincide with their design values.

In a storage ring, the optical functions α, β and γ are periodic: $\beta(s) = \beta(s+L)$, $\alpha(s) = \alpha(s+L)$, and $\gamma(s) = \gamma(s+L)$, where L is the ring circumference. For a transport line, or linac, no such periodic boundary condition exists; so the values of the optical functions depend on the incoming beam distribution.

An alternative description represents the motion of a single particle in terms of a transport matrix[21,22]. Here, a trajectory is given by a point in phase space (x, x') which is transformed from the initial location i to a new (final) location f through a linear transformation

$$\begin{pmatrix} x \\ x' \end{pmatrix}_f = \begin{pmatrix} R_{11} & R_{12} \\ R_{21} & R_{22} \end{pmatrix}_{fi} \begin{pmatrix} x \\ x' \end{pmatrix}_i . \tag{1.7}$$

This can also be generalized to a 6×6 transport matrix for motion with coupling between the horizontal, vertical and longitudinal planes. In the 6-dimensional case, the vector (x, x') is replaced by $(x, x', y, y', z, \delta)$, where δ, the relative energy error, and z, the longitudinal distance to a reference particle, are the coordinates in the longitudinal phase space.

Let us look at a few examples. For a drift space of length L, the 2-dimensional transport matrix is

$$\mathbf{R}_{drift} = \begin{pmatrix} 1 & L \\ 0 & 1 \end{pmatrix}. \tag{1.8}$$

The matrix for a focusing quadrupole of gradient $K = (\partial B/\partial x)/(B\rho)$ and of length l_q is

$$\mathbf{R}_{quad} = \begin{pmatrix} \cos\phi & \sin\phi/\sqrt{|K|} \\ -\sqrt{|K|}\sin\phi & \cos\phi \end{pmatrix} \tag{1.9}$$

where $\phi = l_q\sqrt{|K|}$. If we take the limit of vanishing quadrupole length $l_{quad} \to 0$, while holding the integrated gradient $k = |K|l_q$ constant, we arrive at the matrix for an idealized `thin-lens' quadrupole

$$\mathbf{R}_{thin-lens} = \begin{pmatrix} 1 & 0 \\ -k & 1 \end{pmatrix}. \tag{1.10}$$

Thus, the focal length of the thin quadrupole is given by $1/k$. The R matrix for a sequence of quadrupoles and drift spaces is simply the product of the R matrices for the individual elements.

It is important to note that the description in terms of optical functions and the R matrix formalism are equivalent and complementary: we can transform the optical functions from one location to another using the elements of the R matrix:

$$\begin{pmatrix} \beta \\ \alpha \\ \gamma \end{pmatrix}_f = \begin{pmatrix} R_{11}^2 & -2R_{11}R_{12} & R_{12}^2 \\ -R_{11}R_{21} & 1+2R_{12}R_{21} & -R_{12}R_{22} \\ R_{21}^2 & -2R_{21}R_{22} & R_{22}^2 \end{pmatrix}_{fi} \begin{pmatrix} \beta \\ \alpha \\ \gamma \end{pmatrix}_i \tag{1.11}$$

Alternatively, we can express the elements of the R matrix from i to f in terms of the optical functions at the initial and final locations,

$$\mathbf{R}_{fi} = \begin{pmatrix} \sqrt{\frac{\beta_f}{\beta_i}}(\cos\phi_{fi} + \alpha_i \sin\phi_{fi}) & \sqrt{\beta_f\beta_i}\,\sin\phi_{fi} \\ -\frac{1+\alpha_f\alpha_i}{\sqrt{\beta_f\beta_i}}\,\sin\phi_{fi} + \frac{\alpha_i-\alpha_f}{\sqrt{\beta_f\beta_i}}\,\cos\phi_{fi} & \sqrt{\frac{\beta_i}{\beta_f}}\,(\cos\phi_{fi} - \alpha_f \sin\phi_{fi}) \end{pmatrix}, \tag{1.12}$$

where $\phi_{fi} = (\phi_f - \phi_i)$ is the betatron phase advance between the two locations.

1.2 Review of Longitudinal Dynamics

If the energy of the beam, or of a particle in the beam, differs from the design energy its trajectory may deviate from the trajectory of a particle at the right energy. In first order, this deviation is linear in the momentum deviation $\delta = \Delta p/p$. For a transport line we can write

$$\Delta x(s) = R_{16}\delta \tag{1.13}$$

where R_{16} is the (1,6) transport matrix element from the location where the energy error δ was induced to the location s. In a storage ring, the orbit deviation due to an energy offset is given by the periodic dispersion function $\eta(s)$ as

$$\Delta x(s) = \eta(s)\delta \tag{1.14}$$

Also the R_{16} matrix element of Eq. (1.13) is often called dispersion, but it should be kept in mind that this term is not uniquely defined and can be very different for different energy-error sources. As a result, the correction of dispersion in a transport line or a linac can become conceptually quite complicated.

If the beam (or particle) energy is varied, the radius of curvature and, thus, path length in the bending magnet changes. The first order path length change is characterized by the momentum compaction factor α:

$$\alpha = \frac{\Delta L/L}{\delta} = \frac{1}{L}\oint \frac{\eta(s)}{\rho(s)}\,ds. \tag{1.15}$$

If $\gamma > 1/\sqrt{\alpha}$, a ring is said to operate `above transition'; this is the case for most electron and high-energy proton rings. For a transport line, α and $\eta(s)$ in Eq. (1.15) must be replaced by

$$R_{56}(s) = \int_{s_0}^{s} \frac{R_{16}(s')}{\rho(s')}\, ds', \tag{1.16}$$

where $\mathbf{R}(s)$ is the transport matrix from the location at which the energy is changed (*e.g.*, a cavity) to the location s.

Just as the beam, or an individual particle in the beam, executes betatron oscillations, it also performs oscillations in the longitudinal phase space, in a storage ring with nonzero rf voltage. The frequency of the synchrotron motion is much lower than the two betatron-oscillation frequencies (one synchrotron period typically corresponds to 100s of turns). It can be expressed in terms of a synchrotron tune Q_s (which is the synchrotron frequency f_s in units of the revolution frequency f_{rev}):

$$Q_s = \frac{f_s}{f_{rev}} = \sqrt{\frac{(\gamma^{-2} - \alpha) h e \hat{V} \cos\psi_s}{2\pi c p_0}} \tag{1.17}$$

where α is the momentum compaction factor, $\hat{V}$ the amplitude of the rf voltage (assumed as simply sinusoidal), h the rf harmonic number ($f_{rf} = h f_{rev}$), e the particle charge, p_0 the equilibrium momentum, c the speed of light, and ψ_s the synchronous phase angle. The latter is determined by the equality $e\hat{V}\sin\psi_s = U_0$, where U_0 is the average energy loss per turn, and by the condition for phase stability, $\pi/2 < \psi_s < \pi$ above transition.

1.3 Beam Matrix

The beam matrix σ is defined, in this case in the horizontal (x) plane, as:

$$\begin{aligned} \sigma &= \epsilon \begin{pmatrix} \beta & -\alpha \\ -\alpha & \gamma \end{pmatrix} \\ &= \begin{pmatrix} \langle x^2 \rangle - \langle x \rangle^2 & \langle x x' \rangle - \langle x \rangle \langle x' \rangle \\ \langle x' x \rangle - \langle x' \rangle \langle x \rangle & \langle x'^2 \rangle - \langle x' \rangle^2 \end{pmatrix}. \end{aligned} \tag{1.18}$$

Here α, β, and γ are the ellipse parameters (see Fig. 1.1, from Ref.[21,22]), ϵ is the beam emittance, and the bracketed terms are various moments of the beam distribution; i.e. $\langle x \rangle$ is the first moment, or mean, of the distribution in position, $\langle x' \rangle$ is the first moment, or mean, of the distribution in angle, and $\langle x^2 \rangle$, $\langle x'^2 \rangle$ are the second moments

of the beam distribution. Specifically, for a beam intensity distribution $f(x)$,

$$\langle x \rangle = \frac{\int_0^\infty x f(x) dx}{\int_0^\infty f(x) dx}, \tag{1.19}$$

and

$$\langle x^2 \rangle = \frac{\int_0^\infty x^2 f(x) dx}{\int_0^\infty f(x) dx}. \tag{1.20}$$

The root-mean-square (rms) of the distribution σ_x is (usually) the physical quantity of interest:

$$\sigma_x = \sqrt{\langle x^2 \rangle - \langle x \rangle^2}. \tag{1.21}$$

If the mean of the distribution is neglected (i.e. disregard the static position offset of the core of the beam, or define the coordinates with respect to this offset), then Eq. (1.18) reduces to

$$\sigma = \begin{pmatrix} \langle x^2 \rangle & \langle x x' \rangle \\ \langle x x' \rangle & \langle x'^2 \rangle \end{pmatrix} \tag{1.22}$$

and the rms of the distribution is simply $\sigma_x = \langle x^2 \rangle^{\frac{1}{2}}$.

The transformation between an initial beam matrix σ_0 to the beam matrix σ at a desired observation point is

$$\sigma = R \sigma_0 R^T, \tag{1.23}$$

where R is the transfer matrix and R^T is the transpose of R. For an uncoupled system,

$$\sigma = \begin{pmatrix} \sigma_{11} & \sigma_{12} & 0 & 0 \\ \sigma_{21} & \sigma_{22} & 0 & 0 \\ 0 & 0 & \sigma_{33} & \sigma_{34} \\ 0 & 0 & \sigma_{43} & \sigma_{44} \end{pmatrix}, \tag{1.24}$$

and

$$R = \begin{pmatrix} R_{11} & R_{12} & 0 & 0 \\ R_{21} & R_{22} & 0 & 0 \\ 0 & 0 & R_{33} & R_{34} \\ 0 & 0 & R_{43} & R_{44} \end{pmatrix}. \tag{1.25}$$

Note that the σ-matrix is symmetric with $\sigma_{12} = \sigma_{21}$ (cf. Eq. (1.18)), however in general, $R_{34} \neq R_{43}$.

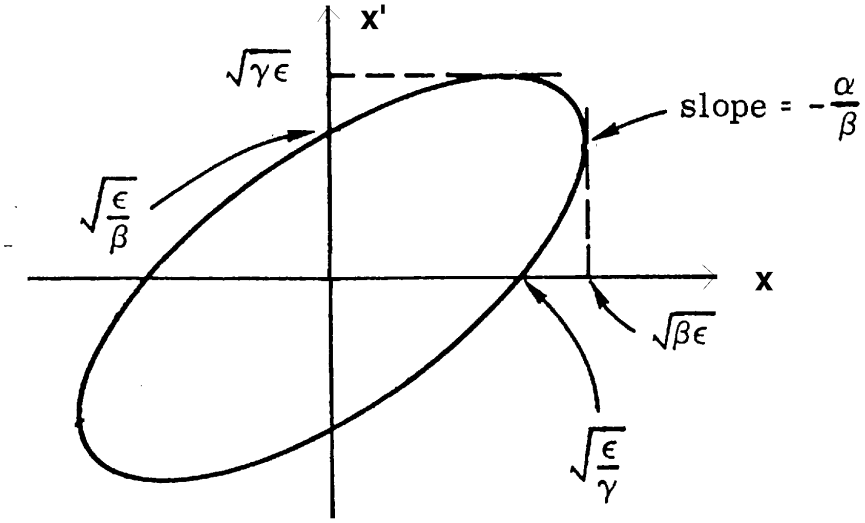

Figure 1.1: Ellipse parameters for the beam matrix.

Ex.1.1. Projected beam emittances
a) Consider a beam whose distribution function depends only on the action variable; i.e. $\rho(I_x, \phi_x) = \rho(I_x)$. *Define the horizontal emittance as* $\epsilon_x =< x^2 > /\beta_x$. *Show that* $\epsilon_x =< I_x >$, *where the square brackets denote an average over the beam distribution.*
b) Consider now a 2-d distribution which is Gaussian and uncorrelated in the 4 variables x_0, x_0', y_0 *and* y_0' *with emittances* ϵ_x *and* ϵ_y. *Suppose the beam passes a skew quadrupole of strength* k *with beta functions at the quadrupole equal to* β_x *and* β_y. *Afterwards the coordinates of the new distribution are* x, x', y *and* y'. *They are correlated as*

$$x' = x_0' + k_s y_0 \tag{1.26}$$
$$y' = y_0' + k_s x_0 \tag{1.27}$$
$$x = x_0 \tag{1.28}$$
$$y = y_0 \tag{1.29}$$

Calculate the beam matrix.
c) The projected horizontal and vertical emittances are given by the square root of the determinant of the 2×2 *submatrices. Calculate the projected emittances and express them in terms of the initial uncoupled emittances, and the skew quadrupole strength* k_s.

1.4 References

1. S. Myers, "The LEP Collider, from Design to Approval and Commissioning", CERN Accelerator School, 6th John Adams Memorial Lecture, CERN-91-08 (1991).
2. "PEP-II An Asymmetric B Factory", SLAC-418 (1993).
3. "KEKB B-Factory Design Report", KEK Report 95-7 (1995).
4. J.T. Seeman, "The Stanford Linear Collider", Ann. Rev. Nucl. Part. Sci. 40, p. 389 (1990).
5. P. Emma, "The Stanford Linear Collider", Proc. of 1995 IEEE PAC, Dallas, p. 606 (1995).
6. Y. Kimura, "Status of Tristan", Proc. of the XVth International Conference on High Energy Accelerators, Hamburg, p. 72 (1992).
7. SPEAR Storage Ring Group, "SPEAR: Status and Improvement Program", Proc. of IXth Conference International Conference on High Energy Accelerators, Stanford, p. 37 (1974).
8. P. Lefevre, "LEAR, Present Status: Future Developments", presented at 3rd LEAR Workshop, Tignes, France, Jan 19-26, 1985, CERN-PS/85-37 (1985).
9. F. Hinode *et al.*, "Accelerator Test Facility–Design and Study Report", KEK Internal Report 95-4 (1995).
10. P. Schmüser, "The Electron-Proton Colliding Beam Facility HERA", Nucl. Instr. Methods A 235, p. 201 (1985).
11. M. Berndt, *et al.*, "Final Focus Test Beam: Project Design Report", SLAC-0376 (1991).
12. J. Gareyte, "The SPS P Anti-P Collider", Proc. of Antiprotons for Colliding Beam Facilities, CERN, Geneva, 1983, CERN report 84-15 (1984).
13. C. Adolphsen, *et al.*, "Measurement of Wake Field Suppression in an Detuned X Band Accelerator Structure", Phys. Rev. Letters 74, p. 2475 (1995).
14. K. Johnsen, "Present Status and Future Plans for the ISR", Proc. of IXth Conference International Conference on High Energy Accelerators, Stanford, p. 32 (1974).
15. The LHC Study Group, "The Large Hadron Collider – Conceptual Design", CERN/AC/95-05 (1995).
16. "Zeroth Order Design Report for the Next Linear Collider," *SLAC-Report* 474 (1996).
17. R. Brinkmann, *et al.*, "Conceptual Design of a 500 GeV e^+e^- Linear Collider with Integrated X-ray Laser Facility", DESY 1997-048, ECFA 1997-182 (1997).
18. "$\mu^=\mu^-$ Collider. A Feasibility Study." Submitted to the APS Summer Study, Snowmass 1996, on "New Directions for High-Energy Physics", BNL-52503

(1996).
19. E.D. Courant and H.S. Snyder, “Theory of the Alternating-Gradient Synchrotron”, Annals of Physics 3, 1-48 (1958).
20. M. Sands, “The Physics of Electron Storage Rings”, SLAC-121 (1970)
21. K.L. Brown, “A First and Second-Order Matrix Theory for the Design of Beam Transport Systems and Charged Particle Spectrometers”, SLAC-75 (1982).
22. K.L. Brown, F. Rothacker, D. Carey, C. Iselin, “Transport. A Computer Program for Designing Charged Particle Beam Transport Systems”, SLAC-91 (1977).

Chapter 2

Transverse Optics Measurement and Correction - Part I

2.1 Betatron Tune

2.1.1 Introduction

In a storage ring, the Q value, or betatron tune, is defined as the number of betatron oscillations per revolution (often it is also called ν):

$$Q = \frac{\phi(L)}{2\pi} = \frac{1}{2\pi} \oint_L \frac{ds}{\beta(s)} \tag{2.1}$$

where the integral is taken around the ring of circumference L. The integer part of the tune Q is easily inferred from the orbit distortion induced by exciting a single steering corrector. This orbit distortion is essentially a betatron oscillation; thus, counting the number of oscillation periods around the ring determines the integer value of the tune. A more intricate method, discussed in Section 2.2, is to perform a harmonic analysis of betatron oscillations recorded by multi-turn beam-position monitors. Thereby the betatron phase advance between adjacent BPMs can be determined, and the total phase advance around the ring gives the tune. If the integer part of the tune agrees with model predictions, large optics errors can be ruled out. More important than the integer value of the tune is its fractional part, since the latter can have a strong effect on beam lifetime or emittance.

Tune measurements are useful for quite a variety of applications: the tune shift with quadrupole strength gives the local beta function, the tune shift with rf frequency the chromaticity, the tune shift with current the effective transverse impedance, and the tune shift with betatron amplitude the strength of the nonlinear fields. Further, optimizing and controlling the tunes improves the beam lifetime and the dynamic aperture, and it can reduce beam loss or emittance growth during acceleration. For example, Fig. 2.1 shows the variation of the extracted vertical beam size as a function of the vertical betatron tune which was measured at the SLC electron damping ring.

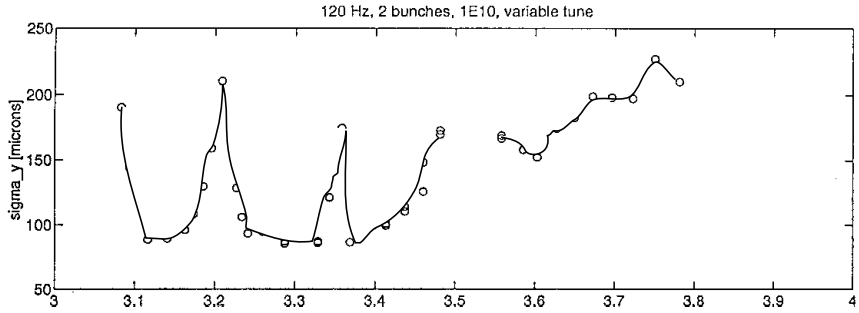

Figure 2.1: Rms vertical size of the electron beam extracted from the SLC damping ring as a function of the vertical betatron tune. This measurement was performed under unusually poor vacuum conditions[1].

Also space charge, ionized gas molecules, beam-beam interaction and radiation damping can affect the tune signal, for example, the shape of the beam response to a swept-frequency excitation. An example for the dramatic effect of the nonlinear beam-beam force is shown in Fig. 2.2. In addition, fast decoherence and filamentation, head-tail damping or instabilities may make it difficult to extract a clean and reproducible tune signal. On the other hand, this also implies that all these processes can be studied by means of tune measurements.

In the following we will describe three approaches to measure the fractional part of the tune. These approaches fall into two different categories: (1) precision tune measurements and (2) tune tracking (to monitor and control fast changes, *e.g.*, during acceleration). For simplicity, the fractional part of the tune will also be denoted by Q.

2.1.2 Fast Fourier Transform (FFT)

A common method to measure the fractional part of the betatron tune is to excite transverse beam motion and to detect the transverse beam position over a number of successive turns N. The excitation may consist of white noise or a single kick. Beam oscillations caused by injection are also often used, in order not to interfere

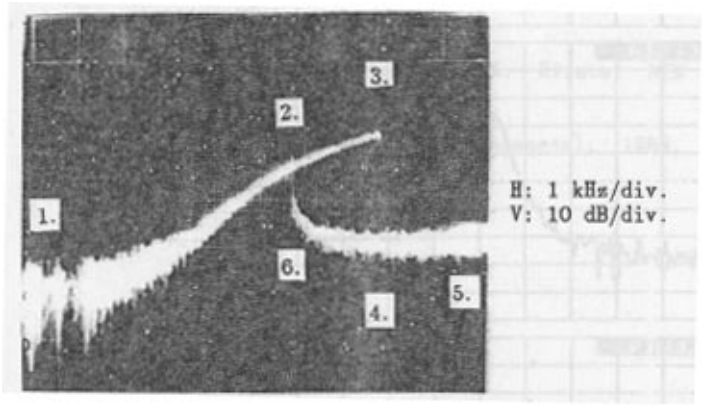

Figure 2.2: Transverse tune measurement (swept-frequency excitation) with 2 colliding bunches at Tristan [2]. (Courtesy K. Hirata, 1998.)

with the machine operation. The power density of the detected signal is computed via a Fourier transformation, and the betatron tunes are identified as the frequencies with the highest amplitude peak (this is not always the case, as sometimes the beam is strongly excited at other frequencies). Figure 2.3 shows typical multi-turn BPM measurements. Alternatively, a spectrum analyzer could be used to frequency analyze the detected signal.

A Fourier analysis uses a time series $x(1),\ x(2), ..., x(N)$ of N orbit measurements for consecutive turns as input. This time series is expanded as a linear combination of N orthonormal functions,

$$x(n) = \sum_{j=1}^{N} \psi(Q_j)\ \exp(2\pi i n Q_j). \tag{2.2}$$

The expansion can be done efficiently with a Fast Fourier Transform algorithm. The frequency corresponding to the largest value of ψ is taken as the approximate tune (see Fig. 2.4). The error due to the discreteness of the frequency steps is equal to

$$|\delta Q| \leq \frac{1}{2N} \tag{2.3}$$

Thus, to obtain a tune value with a resolution of 0.001 or better using Eq. (2.2) requires orbit data for about 1000 turns. As an illustration, Fig. 2.4 displays FFT spectra of the orbit motion measured at the two BPMs of Fig. 2.3. The FFT demonstrates that a large part of the orbit motion in the dispersive region is due to synchrotron oscillations.

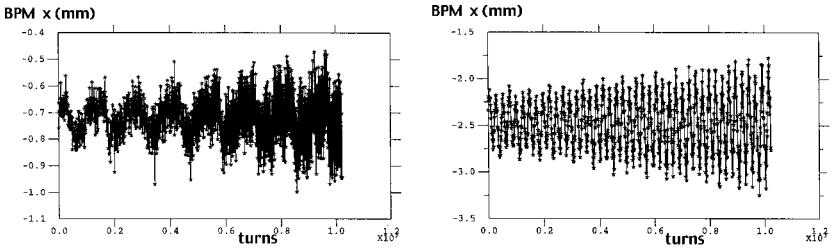

Figure 2.3: Multi-turn orbit measurement for the motion of the 500th bunch in a train of 1760 bunches at PEP-II. Shown are horizontal BPM orbit readings as a function of turn number: (Left) BPM in a dispersive region; (right) BPM in a non-dispersive region. For this number of bunches at high current the beam was self-excited. The slow oscillation in the left picture corresponds to energy (or synchrotron) oscillations. The fast oscillations are the betatron motion. The corresponding FFT spectra are displayed in Fig. 2.4. (Courtesy U. Wienands, J. Seeman *et al*, 1998.)

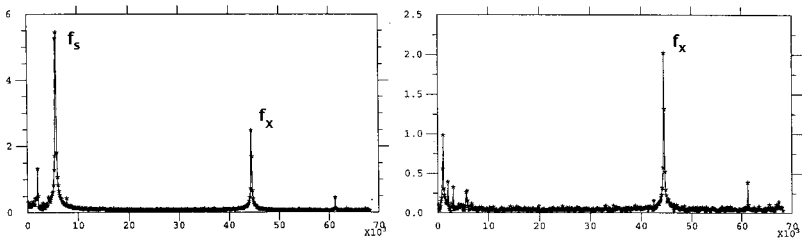

Figure 2.4: FFT spectra for the two BPM measurements of Fig. 2.3 in a dispersive (left) and in a nondispersive region (right). The horizontal scale is in Hz. (Courtesy U. Wienands, J. Seeman *et al*, 1998.)

Interpolated FFT

If we use a simple Fourier analysis based on the peak amplitude of ψ in Eq. (2.2), typically we need about 1000 turns of orbit data to obtain an adequate tune resolution. During this time the beam could filament or the oscillation amplitude could decrease significantly, giving rise to spurious results. Fortunately, interpolating the shape of the Fourier spectrum around the main peak improves the resolution quite dramatically[3]. Thereby the same resolution can be achieved by processing data for a much smaller number of turns.

The basic idea is that the shape of the Fourier spectrum is known, and equal to that of a pure sinusoidal oscillation with tune Q_{Fint},

$$|\psi(Q_j)| = \left| \frac{\sin N\pi(Q_{Fint} - Q_j)}{N \sin \pi(Q_{Fint} - Q_j)} \right| \tag{2.4}$$

The formula for the interpolated tune Q_{Fint} reads[4]:

$$Q_{Fint} = \frac{k}{N} + \frac{1}{\pi} \arctan \left(\frac{|\psi(Q_{k+1})| \sin\left(\frac{\pi}{N}\right)}{|\psi(Q_k| + |\psi(Q_{k+1})| \cos\left(\frac{\pi}{N}\right)} \right) \tag{2.5}$$

where $|\psi(Q_k)|$ is the peak of the Fourier spectrum in Eq. (2.2), and $|\psi(Q_{k+1})|$ its highest neighbor. So, instead of using only the peak value of the FFT, one interpolates between the two highest points. For large N the error is given by

$$|\delta Q| \leq \frac{C_{Fint}}{N^2} \tag{2.6}$$

where C_{Fint} is a numerical constant. So, the resolution improves quadratically with the number of turns, and already from a beam signal recorded over 30–60 turns fairly accurate tune values can be obtained. For $N \gg 1$, Eq. (2.5) may be approximated by the simpler form[3]

$$Q_{Fint} \approx \frac{k}{N} + \frac{1}{N} \arctan \left(\frac{|\psi(Q_{k+1})|}{|\psi(Q_k| + |\psi(Q_{k+1})|} \right) \tag{2.7}$$

Interpolated FFT with Data Windowing

The accuracy of the Fourier analysis can be further improved with data windowing [5,4]. Here, the data $x(n)$ are weighted with filter functions $\chi(n)$ before the interpolated FFT is applied. The Fourier coefficients of the filtered signal are

$$\psi(Q_j) = \frac{1}{N} \sum_{n=1}^{N} x(n)\chi(n) \exp(-2\pi i n Q_j) \tag{2.8}$$

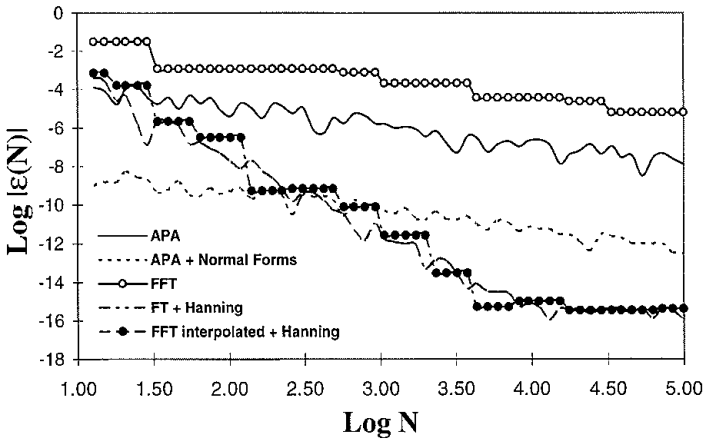

Figure 2.5: Tune precision vs. number of turns, considering different FFT techniques applied to tracking data for the 4-D Hénon map [4]. The abbreviation `APA' refers to a calculation of the average phase advance, which can be computed either in the original phase-space coordinates or in so-called normal-form coordinates. See Ref. [4] for more details on these alternative methods. (Courtesy M. Giovannozzi, 1998.)

Applying a Hanning-like filter of order l, $\chi_l(n) = A_l \sin^l(\pi n/N)$ with A_l some normalization constant, in the limit $N \gg 1$ the interpolated tune reads

$$Q_{Fint} = \frac{k}{N} + \frac{1}{N}\left(\frac{(l+1)\psi(Q_{k+1})}{\psi(Q_k)+\psi(Q_{k+1})} - \frac{l}{2}\right) \tag{2.9}$$

The resolution improves with the $(l+2)$th power of the number of samples N:

$$|\delta Q| \leq \frac{C_{FHan}}{N^{l+2}} \tag{2.10}$$

where C_{FHan} again is a numerical constant.

An example comparing the precision of different FFT procedures is shown in Fig. 2.5 [4], which clearly demonstrates the superiority of the interpolated FFT with data windowing (Hanning filter). Unfortunately, the beneficial effect of the Hanning filter disappears when the signal contains a small noise component [4], in which case the resolution decreases as $\sim N^{-2}$ only, just as with the simple interpolated FFT.

2.1.3 Swept-Frequency Excitation

A different method to measure the tune is to excite the beam with a steady sinusoidal wave and to detect the amplitude and phase of the beam response. The excitation

frequency is increased in steps. The strength of the harmonic excitation is adjusted so as to produce beam oscillations of adequate amplitude at the resonant frequency.

The result of this measurement is a `transverse beam-transfer function', which is the (complex) response of the beam to a harmonic excitation as a function of frequency. The beam-transfer function contains important information, for example, about the transverse impedance or about radiation damping [6]. It is easy to see from Eq. (2.2) that, in frequency domain, the tune signal repeats itself in frequency intervals corresponding to multiples of the revolution frequency f_{rev} (*i.e.*, a spectrum analysis of the signal from one pick up contains no information about the integer part of the tune). If n_b equidistant bunches are stored in a ring and the combined signal of all bunches is detected, the periodicity of the FFT signal is $n_b f_{rev}$. In addition, the tune spectrum from 0 to $n_b f_{rev}/2$ and that from $n_b f_{rev}/2$ to $n_b f_{rev}$ are mirror images of each other. Therefore, for the study of multibunch instabilities, it is sufficient to measure the beam transfer function around each revolution harmonic between zero and $n_b f_{rev}/2$.

The concept of the beam-transfer function can be extended to higher-order beam excitations. At the CERN AA a quadrupole pick-up was used to measure the quadrupole mode beam-transfer function of an antiproton beam [7].

The frequency-sweep method as discussed so far requires a relatively long time in order to measure the response at each frequency with sufficient accuracy. However, there exists a fast version of this method, called a chirp excitation. Here the frequency of the excitation is ramped rapidly across the tune resonance, while the beam response is observed [8]. This is useful to monitor fast tune changes, as, for instance, during acceleration in the SPS [9].

2.1.4 Phase Locked Loop

While exactly at the betatron tune the amplitude of the beam-transfer function has zero slope as a function of excitation frequency, the phase of the beam-response has maximum slope. The phase difference between excitation and beam motion changes from 0 degree to 180 degree when the excitation frequency is ramped through the resonance. Directly at the betatron tune, the phase difference is 90 degrees. The phase can be monitored continually by a phase locked loop circuit (PLL); see, *e.g.*, Ref. [8,10].

The signal flow diagram of a phase locked loop is sketched in Fig. 2.6. The phase detector compares the frequency of a beam position signal, *e.g.*, from a BPM, with the frequency of a local oscillator. The phase-detector output voltage is a measure of the frequency difference of its two input signals. After low-pass filtering and amplification, this signal is used to adjust the frequency of the local oscillator (VCO), such that the oscillator `locks' to the frequency of the input beam signal. The oscillator

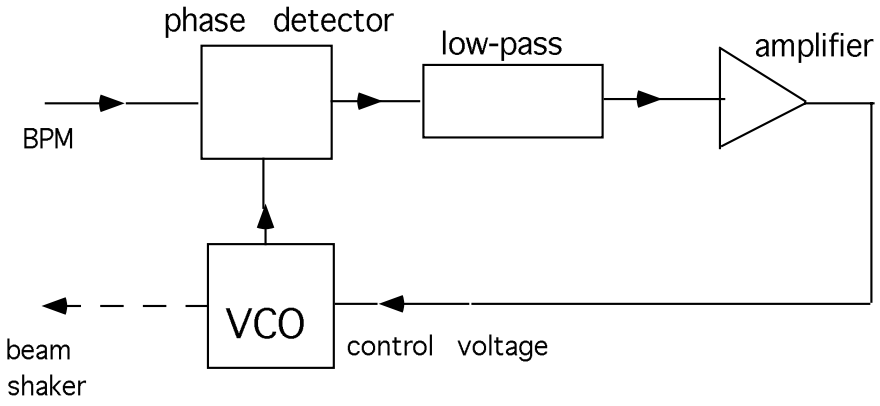

Figure 2.6: Schematic of phase locked loop for continuous tune control.

frequency serves as the betatron tune signal which is displayed or processed by the accelerator control system. Sometimes the oscillator signal is also used to excite the beam, in which case the phase locked loop becomes part of a `lock-in amplifier'. PLL circuits allow a continuous tracking of the time evolution of the betatron tune.

2.1.5 Schottky Monitor

All the techniques reported so far measured the coherent betatron tune, *i.e.*, the oscillation frequency of the beam centroid. In the case of proton beams it is also possible to measure the incoherent betatron tune, *i.e.*, the oscillation frequency of individual particles in the beam (in the absence of centroid motion). The incoherent signal is proportional to $\sqrt{\epsilon N \Delta f}$, where ϵ is the beam emittance, N the number of particles in the beam, and Δf a frequency bandwidth. Though this signal is small, it can be detected with sensitive `Schottky monitors'[11].

Ex.2.1. Schottky signals
The spectrum of a single particle circulating in an accelerator is given by

$$i(t) = ef + 2ef \sum_{n=1}^{\infty} \cos n\omega t, \tag{2.11}$$

where n represents the turn number and $\omega = 2\pi f$ is the angular revolution frequency.
a) Sketch the current spectrum for this particle in both the time and frequency domains.
b) Show that averaging Eq. 2.11 over N particles gives the dc beam current Nef.
c) The power spectrum one would measure with a spectrum analyzer is proportional to the rms current $i_{rms} = \langle i^2 \rangle^{\frac{1}{2}}$. Show that

$$i_{rms} = 2ef\sqrt{\frac{N}{2}}. \tag{2.12}$$

2.1.6 Application: Nonlinear Dynamics Studies

For studies of nonlinear dynamics a multi-turn BPM readout is a great advantage. Three examples may illustrate this point.

Tune Shift with Amplitude: The interpolated FFT with data windowing was applied at LEP and SPEAR to measure the tune shift with betatron amplitude [12]. The latter is of interest since it carries information about the nonlinear fields experienced by the beam, that may affect the beam stability and lifetime. Any nonlinear field can cause a tune shift with amplitude; these nonlinear fields change the average focusing experienced by a particle executing large betatron oscillations.

In the LEP experiment, the beam was kicked in the vertical plane, and the tune was calculated over successive short time windows, of 32 turns each, as the beam oscillation damped rapidly. Figure 2.7 shows a result for LEP at 20 GeV. In Fig. 2.7 (left), the vertical beam position is displayed as a function of time demonstrating the fast damping, over 200 turns. The shift of the horizontal and vertical betatron tune with the vertical action variable, as computed over 32-turns time windows is presented in Fig. 2.7 (right). The vertical action was inferred from the oscillation amplitudes in each time window. The amplitude-dependent tune shifts calculated by an off-line model and the measurement agreed to within 5%.

Higher-Order Resonances and Hamiltonian Reconstruction: Nonlinear magnetic fields not only cause a tune shift with amplitude, they also induce higher-order resonances. These show up as additional lines in the Fourier spectrum.

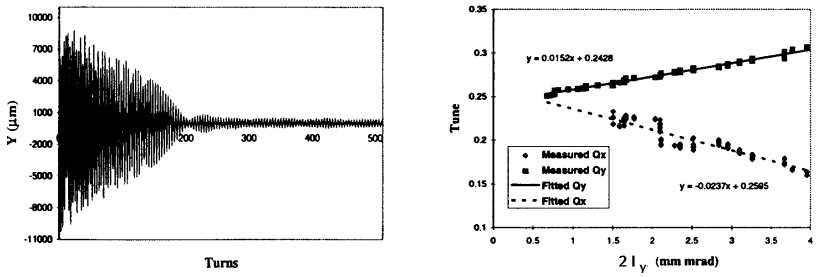

Figure 2.7: Measurement of tune shift with amplitude in LEP at 20 GeV, using a high-precision FFT tune analysis[12]: (left) vertical oscillation amplitude after a kick; (right) horizontal and vertical betatron tunes vs. twice the vertical action variable I_y of the beam centroid motion. The observed tune shift with amplitude was consistent with the expected effect of the sextupole and octupole field components in the dipole magnets. (Courtesy R. Bartolini, 1998.)

In general, betatron resonances are defined by the condition

$$kQ_x + lQ_y = p \tag{2.13}$$

where k, l, and p are integers. Spectral analysis in the presence of nonlinear resonances[13] shows that in the Fourier spectrum of the horizontal coordinate $x(n)$, the above resonance gives rise to lines at the two frequencies $(k \pm 1)Q_x + lQ_y$, and in the Fourier spectrum of the vertical signal $y(n)$ it generates lines at $kQ_x + (l \pm 1)Q_y$. Note that there is no line at $kQ_x + lQ_y$, as one might have naively expected! The amplitude and phase of the higher-order resonance lines in the FFT spectrum can be used to reconstruct the nonlinearities affecting the beam motion[14,15].

Tune Scans: The beam lifetime is often related to the dynamic aperture of the storage ring, where the term `dynamic aperture' denotes the maximum stable betatron amplitude beyond which particles are lost after a certain finite number of turns. In the case of colliding beams, the lifetime is likely limited by the beam-beam interaction. Both dynamic aperture and the beam-beam interaction are sensitive to the value of the betatron tune. Measuring and plotting the beam lifetime as a function of the horizontal and vertical betatron tunes, Q_x and Q_y, yields a tune diagram, in which higher-order resonances, given by Eq. (2.13), are evident as stripes with reduced lifetime. Figure 2.8 compares a typical beam-lifetime tune scan performed during the commissioning of the PEP-II High Energy Ring with the result of a dynamic-aperture simulation[16].

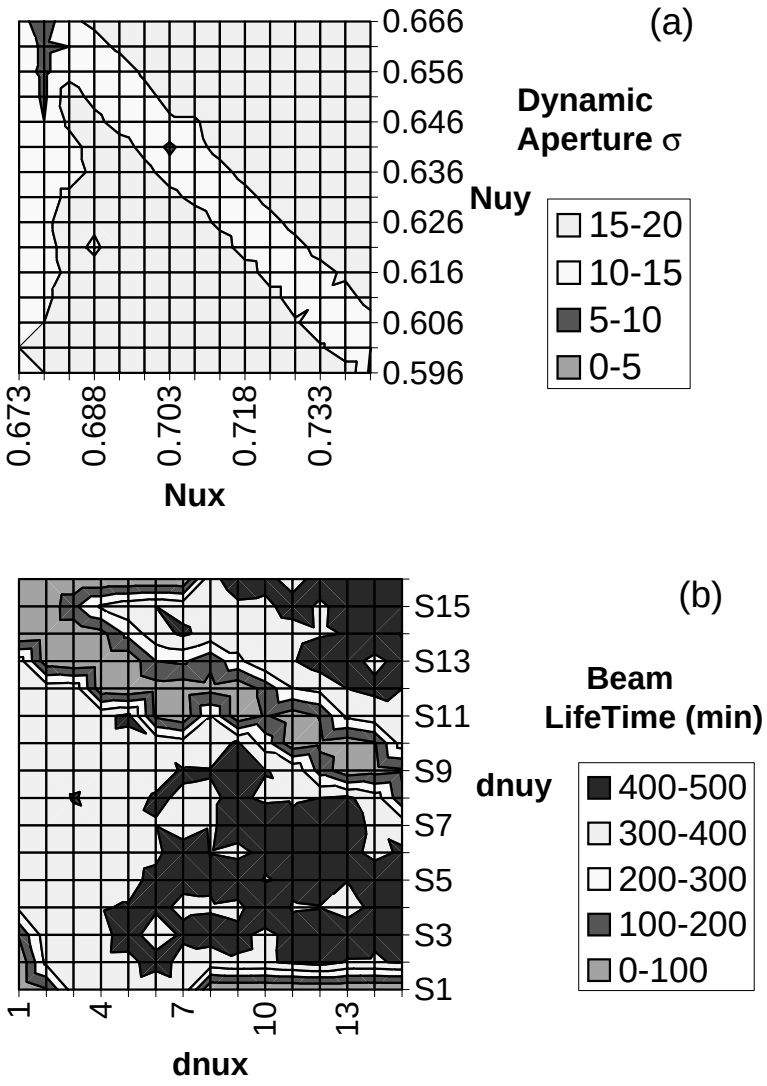

Figure 2.8: Tune scan in PEP-II centered at $Q_x = 24.709$ and $Q_y = 23.634$[16]: (top) simulated dynamic aperture (for a momentum offset $\Delta p/p = 10\ \sigma_\delta$, where δ is the rms momentum spread) as a function of the horizontal and vertical betatron tunes, Q_x and Q_y; (bottom) measured beam lifetime as a function of Q_x and Q_y. Total scan range is ± 0.005 on both axes. The different slope of the resonance line, as compared with the top figure, is attributed to a miscalibration of the tune knobs. (Courtesy Y. Cai, 1998.)

Ex.2.2. Betatron Tunes
The circumference of the PEP-II accelerator is 2200 m.
a) From Fig. 2.4, what is the synchrotron tune?
b) When the quadrupole family for the horizontal tune is increased in strength, the horizontal tune line is observed to move to the right in similar measurements. What is the fractional horizontal betatron tune?
c) After how many turns would a particle with the tunes found in a) and b) return to exactly the same place in phase space?

studies (contains a section on tune shift with amplitude)

Ex.2.3. Application of multipole field expansion
An extremely handy formula for fields produced by a magnet of order n ($n = 0$ represents a dipole) is

$$B_z + iB_x = \Sigma_{n=0}(b_n + ia_n)(x + iz)^n. \tag{2.14}$$

a) For the case of a normal ($a_n = 0$) sextupole, show that the Lorentz force seen by the particle is

$$F_x \propto (x^2 - z^2) \quad \text{and} \quad F_z \propto xz. \tag{2.15}$$

b) For a nondispersive orbit ($x = x_{co} + x_\beta$ and $y = y_{co} + y_\beta$, where the subscripts refers to the closed orbit co and the betatron orbit β), show that a beam off-axis in x at the sextupole experiences a normal quadrupole field while a beam off-axis in z experiences a skew quadrupole field.
c) What transverse-to-longitudinal coupling terms arise if the dispersive contribution to the orbit (x_η and z_η) are also included?

2.2 Betatron Phase

2.2.1 Harmonic Analysis of Orbit Oscillations

By exciting transverse oscillations, sampling the beam position over N turns, and performing a simple harmonic analysis, we can determine the betatron phase at the location of the pick up[17].

The oscillation detected by the BPM is a harmonic function

$$x_{km} = A_k \cos(2\pi Q_x m + \phi_{0k}) \tag{2.16}$$

where the index k specifies the BPM, m is the turn number, and A_k the measured amplitude, which depends on the BPM calibration, on the local beta function, and on the magnitude of the oscillation.

In the limit of large N, the two Fourier sums

$$C_k = \sum_{m=1}^{N} x_{km} \cos(2\pi m Q_x), \qquad S_k = \sum_{m=1}^{N} x_{km} \sin(2\pi m Q_x). \tag{2.17}$$

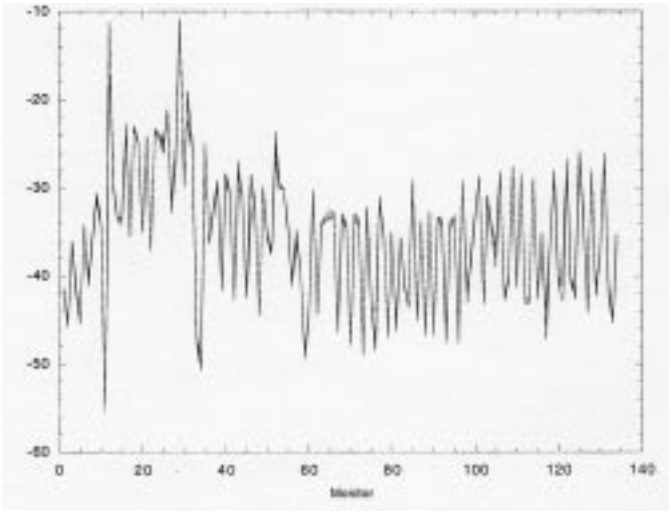

Figure 2.9: Difference between measured and predicted betatron phase advance (in degrees) as a function of position around the PEP-II HER (BPM number) for 5 consecutive measurements; the 5 curves are superimposed. The total phase advance around the ring is about 9000°. (Courtesy M. Donald, 1998.)

approach the asymptotic values

$$C_k \approx \frac{AN}{2} \cos\phi_{0k} \qquad S_k \approx \frac{AN}{2} \sin\phi_{0k}, \tag{2.18}$$

and, thus, the betatron phase at the kth monitor can be expressed as

$$\phi_{0k} \approx \tan^{-1}\left(\frac{S_k}{C_k}\right) \tag{2.19}$$

and the amplitude is given by $A_k \approx 2\sqrt{C_k^2 + S_k^2}/N$. Figure 2.9 shows 5 consecutive measurements of the betatron phase advance around the PEP-II HER. The phase advance predicted by the model was subtracted from the measured phase. The figure demonstrates that the measurement is highly reproducible, and that, for this example, it is in good agreement with the model. The offset of about $40°$ is due to different reference points in model and measurement.

Application: Transverse Impedance Measurement

Measuring the betatron phase advance for different bunch currents provides information about the effective transverse impedance, a quantity which describes the electro-

magnetic coupling of the beam to its environment. A measurement of the current-dependent phase advance around the LEP ring is shown in Fig. 2.10. Clearly visible as step changes are the locations of the rf cavities in the straight sections.

2.3 Beta Function

2.3.1 Tune Shift induced by Quadrupole Excitation

Presumably the simplest beta-function measurement is to detect the shift in the betatron tune as the strength of an individual quadrupole magnet is varied. This shift can be computed using the `thin-lens' approximation of Eq. (1.10). The tune shift induced by a gradient change for a long quadrupole can then be obtained by linear superposition.

With a quadrupole excitation of Δk, the 2×2 transport matrix for the entire ring is the product of the original transport matrix, Eq. 1.12 with $f = i$,

$$\begin{pmatrix} \cos(2\pi Q_{x,y}) + \alpha_{x,y}\sin(2\pi Q_{x,y}) & \beta_{x,y}\sin(2\pi Q_{x,y}) \\ -\sin(2\pi Q_{x,y}) & \cos(2\pi Q_{x,y}) - \alpha_{x,y}\sin(2\pi Q_{x,y}) \end{pmatrix}, \tag{2.20}$$

and a perturbation matrix representing the effect of the change in gradient,

$$\begin{pmatrix} 1 & 0 \\ -(\pm\Delta k) & 1 \end{pmatrix}, \tag{2.21}$$

where Q_x is the original tune, $\beta_{x,y}$ and $\alpha_{x,y}$ the optical functions at the quadrupole, and the plus or minus sign refers to the horizontal and vertical plane, respectively. The function $\beta_{x,y}$ is to be determined.

The trace of the product matrix must be equal to $2\cos(2\pi\bar{Q}_{x,y})$, where $\bar{Q}_{x,y} = (Q_{x,y} + \Delta Q_{x,y})$ is the new tune, and $\Delta Q_{x,y}$ the tune shift induced by a quadrupole excitation of Δk. Explicit evaluation of the trace gives the equation

$$2\cos(2\pi(Q_{x,y} + \Delta Q_{x,y})) = 2\cos(2\pi Q_{x,y}) - \beta_{x,y}(\pm\Delta k)\ \sin(2\pi Q_{x,y}) \tag{2.22}$$

Solving for $\beta_{x,y}$ we find[19]:

$$\beta_{x,y} = \pm\frac{2}{\Delta k}\ (\cot(2\pi Q_{x,y})\{1 - \cos(2\pi\Delta Q_{x,y})\} + \sin(2\pi\Delta Q_{x,y})) \tag{2.23}$$

where the ± sign refers to the horizontal and vertical planes, respectively. For a small tune change, (*i.e.*, $2\pi\Delta Q_{x,y} \ll 1$), far from the integer or half integer resonance (*i.e.*, $\cot(2\pi Q_{x,y}) \leq 1$), we can further simplify and obtain

$$\beta_{x,y} \approx \pm 4\pi\,\frac{\Delta Q_{x,y}}{\Delta k} \tag{2.24}$$

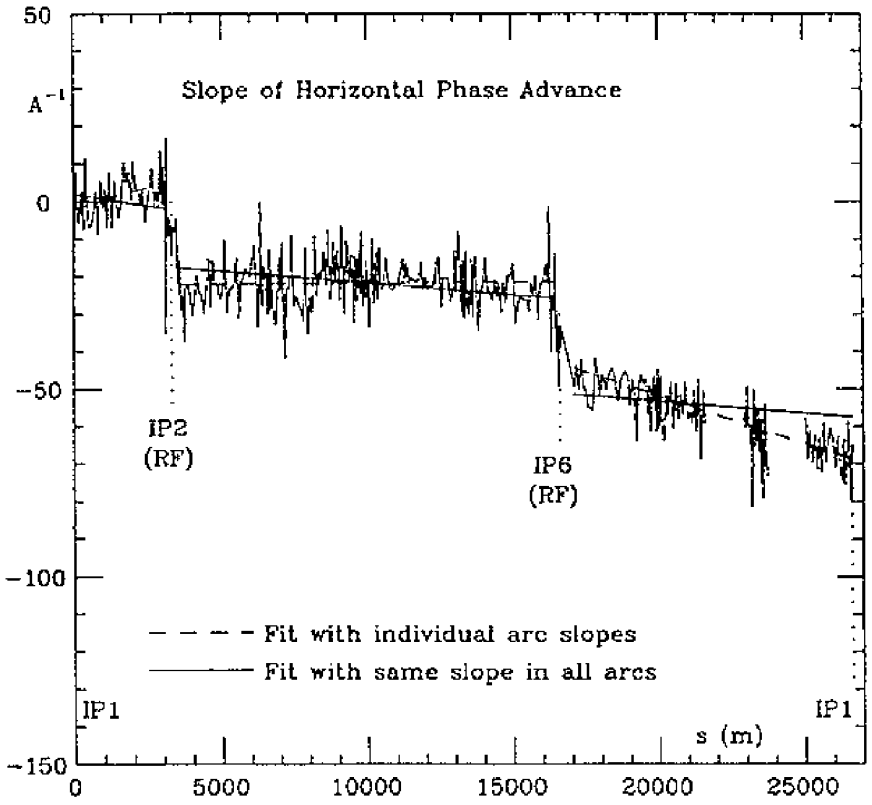

Figure 2.10: Dependence of the horizontal betatron phase advance on the bunch current, $d\phi/dI_b/(2\pi)$ in units of A^{-1}, measured at LEP[18]. (Courtesy A. Hofmann, 1998.)

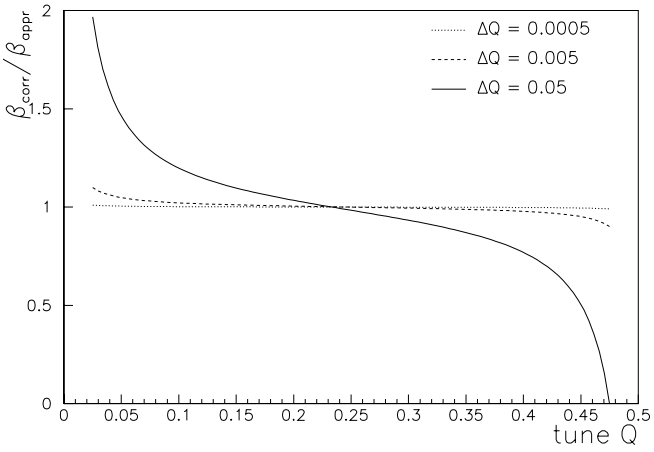

Figure 2.11: The ratio β_{cor}/β_{appr} of the correct beta function, β_{cor}, inferred from Eq. (2.23), to the approximation β_{appr} given in Eq. (2.24), as a function of the nominal tune Q. The three curves correspond to different magnitudes of ΔQ.

Figure 2.11 illustrates the error involved in approximating Eq. (2.23) by Eq. (2.24). The difference between the two expressions becomes important if $Q_{x,y}$ is close to an integer or half integer resonance, and for large changes Δk[19].

Care also has to be taken that the applied change in quadrupole strength does not alter the beam orbit, which happens if the beam is off-center in the quadrupole whose strength is varied. If the orbit changes, part of the measured tune shift could be caused by the closed-orbit variation at the sextupole magnets elsewhere in the accelerator. If a strong effect on the orbit is observed, the orbit should first be corrected with the help of steering correctors before the new (shifted) tune value is measured. Sometimes, several magnets are connected to the same power supply, and then the strengths k_i ($i = 1, ..., m$) of m quadrupoles must be changed simultaneously, all by the same amount Δk. The above result is easily generalized to this case: the induced tune change is related to the average beta function at the m quadrupoles via $< \beta_{x,y} >_m \approx \pm 4\pi \frac{\Delta Q_{x,y}}{m \Delta k}$.

A β function measurement based on the tune shift induced by quadrupole excitations requires independent power supplies (or trim coils, or shunts) for single quadrupoles or groups of quadrupoles, as well as a tune monitor.

2.3.2 Betatron Phase Advance

A different method determines the beta function from betatron oscillations measured with multi-turn beam position monitors (BPMs): the beta function is calculated from the betatron phase advance between three adjacent BPMs. The betatron phase at each BPM can be obtained with a high precision, using Eqs. (2.17) and (2.19)[20]. Since the oscillation amplitude may be subject to calibration errors, it is not used as an input to this calculation. Instead, the computed beta functions can be used to check and correct the BPM calibration.

The first row of the matrix $\mathbf{R}_{fi}$ in Eq. 1.12 can be rewritten as

$$\tan\phi_{fi} = \frac{R_{12}}{R_{11}\beta(s_i) - R_{12}\alpha(s_i)} \tag{2.25}$$

where ϕ_{fi} is the phase advance from monitor i to monitor f, and the R_{kl} are transport matrix elements between the same two locations. These matrix elements can be calculated from the geometry of the beam line assuming that the quadrupole magnets located between the BPMs are at their nominal strength. For a set of three BPMs, there are two independent equations of the form (2.25), which we can solve for the two unknowns α and β[20].

Let us denote the transport matrix from BPM 1 to 2 by $\mathbf{M}$ and the matrix from BPM 1 to 3 by $\mathbf{N}$:

$$\mathbf{M}(1\rightarrow 2) = \begin{pmatrix} m_{11} & m_{12} \\ m_{21} & m_{22} \end{pmatrix} \qquad \mathbf{N}(1\rightarrow 3) = \begin{pmatrix} n_{11} & n_{12} \\ n_{21} & n_{22} \end{pmatrix} \tag{2.26}$$

and denote by ϕ_{21} and ϕ_{31} the phase advances from BPM 1 to 2, and 1 to 3, respectively. Applying Eq. (2.25) twice, we arrive at two expressions for the values of α and β at the first BPM[20]:

$$\beta(s_1) = \left(\frac{1}{\tan\phi_{21}} - \frac{1}{\tan\phi_{31}}\right) / \left(\frac{m_{11}}{m_{12}} - \frac{n_{11}}{n_{12}}\right) \tag{2.27}$$

$$\alpha(s_1) = \left(\frac{n_{11}}{n_{12}\tan\phi_{21}} - \frac{m_{11}}{m_{12}\tan\phi_{31}}\right) / \left(\frac{m_{11}}{m_{12}} - \frac{n_{11}}{n_{12}}\right) \tag{2.28}$$

An example of beta functions obtained by this method is given in Section 2.4.3, Fig. 2.15.

Ex.2.4. Beta-beat
Consider a quadrupole error parameterized by the usual matrix for a quad

$$M_q = \begin{pmatrix} 1 & 0 \\ -\frac{1}{f} & 1 \end{pmatrix}. \tag{2.29}$$

Let the one turn map (OTM) with the field error be given by $M = M_q M M_q$ (where for algebraic convenience we have taken as a reference point the center of the quad), where M is the OTM for the ideal ring:

$$M = \begin{pmatrix} \cos\phi_0 & \beta_0 \sin\phi_0 \\ -\frac{1}{\beta_0}\sin\phi_0 & \cos\phi_0 \end{pmatrix}. \tag{2.30}$$

a) Show that the perturbed phase advance ϕ is given in terms of the unperturbed phase advance ϕ_0 by

$$\cos\phi = \cos\phi_0 - \frac{\beta_0}{f}\sin\phi_0. \tag{2.31}$$

b) From the measurement of phase advance errors in Fig. 2.9, estimate the amplitude of the modulation on the beam size.

2.3.3 Orbit Change induced by a Steering Corrector

A simple method to measure the local beta function at a steering corrector magnet with a nearby BPM is to excite the corrector and to detect the orbit change at that BPM[21].

The formula for the closed-orbit distortion $\Delta x_{c.o.}$ induced by a single dipole kick is

$$\Delta x_{c.o.}(s) = \Delta\theta\, \frac{\sqrt{\beta(s)\beta(s_0)}\ \cos(|\phi(s) - \phi(s_0)| - \pi Q)}{2\ \sin\pi Q} + \Delta\theta\, \frac{\eta(s)\eta(s_0)}{\alpha L} \tag{2.32}$$

where s is the location of the BPM, L the ring circumference, and s_0 the location where the kick $(\Delta\theta)$ is applied. The last term is a small correction reflecting the change in beam energy induced by a kick at a dispersive location, for constant rf frequency. If the locations s and s_0 are the same, and if we ignore the small correction due to the energy change, the formula simplifies, and the beta function at the BPM-corrector pair can be obtained from

$$\beta_{BPM/cor} \approx 2\ \tan\pi Q\, \frac{\Delta x_{c.o.}}{\Delta\theta} \tag{2.33}$$

2.3.4 β^* at Interaction or Symmetry Point

To determine the beta function at the interaction point of a collider ring, or at any other symmetry point (*e.g.*, in a light source), one can excite a pair of symmetrically placed

quadrupoles, by an amount $\pm\Delta k$ (asymmetric excitation), where k is the integrated quadrupole gradient in units of m^{-1}. From Eq. (2.24), the total tune shift is given by

$$\Delta Q_{tot} = \Delta Q_+ - \Delta Q_- \approx \frac{\Delta k}{4\pi} \left[< \beta_+ > - < \beta_- > \right] \tag{2.34}$$

where $< \ldots >$ indicates the average over the quadrupole, and the $\pm$ sign refers to the left or right quadrupole. The advantage of the asymmetric excitation of two quadrupoles is that, if the phase advance between the two quadrupoles is about 180 degree, almost no beta beat is induced. In addition, if the optics is perfect and the beam waist is centered at the collision (or symmetry) point, the beta functions at the two quadrupoles are the same and, to first order, there is no net tune change $\Delta Q_+ - \Delta Q_- = 0$.

The beta function at the collision (symmetry) point β^* is a quadratic function of the ratio

$$\eta = < \beta_+ > - < \beta_- > = 4\pi \, \frac{\Delta Q_+ - \Delta Q_-}{\Delta k} \tag{2.35}$$

which takes the form[22]

$$\beta^* = \beta^*_{design} \left(1 + a_{optics} \eta^2 \right) \tag{2.36}$$

where β^*_{design} is the nominal interaction-point beta function, and the coefficient a_{optics} depends on the optics between the quadrupoles which are being varied and the interaction point, and can be calculated with any optics program, *e.g.*, MAD[23]. For the LEP low-β insertions, $a_{optics} \approx 1/15$[22]. The optics is optimally adjusted, if $\Delta Q_{tot} = 0$.

2.3.5 R Matrix from Trajectory Fit

Consider a set of three BPMs, which are not a multiple of π apart in betatron phase and with nonzero dispersion for at least one. The horizontal orbit readings at these three BPMs, $x^{(1)}$, $x^{(2)}$, and $x^{(3)}$, then contain complete information about the betatron motion (x and x') and the energy offset (δ) of each trajectory. This means we can express the orbit at every other BPM as a linear combination of the orbit reading for these three BPMs:

$$x(s) = B(s)x^{(1)} + C(s)x^{(2)} + D(s)x^{(3)} \tag{2.37}$$

If the three BPMs are adjacent, and the optics between them is known, Eq. (2.37) is equivalent to the more familiar form,

$$x(s) = R_{11}^{s_0 \to s} x(s_0) + R_{12}^{s_0 \to s} x'(s_0) + R_{16}^{s_0 \to s} \delta, \tag{2.38}$$

because then the three variables $x(s_0)$, $x'(s_0)$ and δ are known linear combinations of $x^{(1)}$, $x^{(2)}$ and $x^{(3)}$.

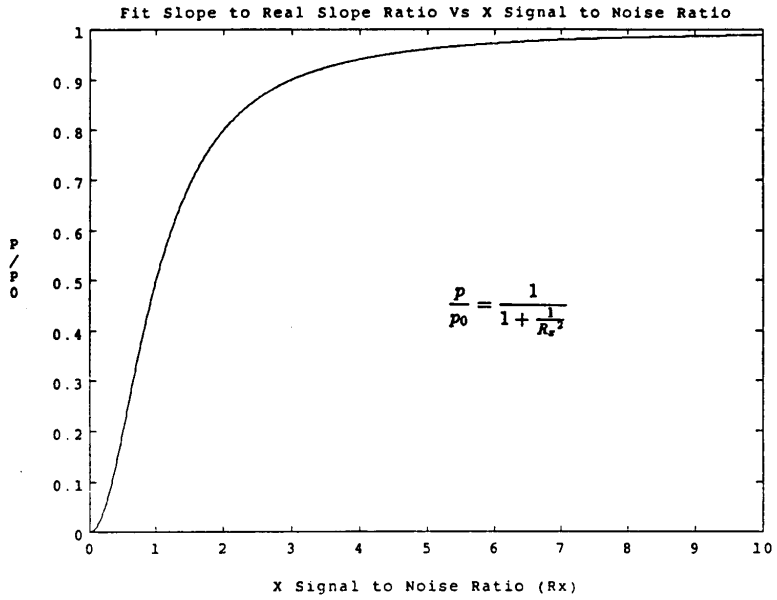

Figure 2.12: Systematic slope error introduced in a linear χ^2 fit of the form $y = px + q$, neglecting the noise smearing in the x measurement[24]. Shown is the reconstructed slope normalized to the true slope as function of signal-to-noise ratio R_x in the horizontal coordinate. (Courtesy P. Emma, 1998.)

If we take data sets for many different turns (in a ring) or for many bunch passages (in a transport line), we can obtain the coefficients $B(s)$, $C(s)$, and $D(s)$, or equivalently the R matrix elements R_{11}, R_{12} and R_{16}, by a fitting procedure. However, care has to be taken: a simple least squares fit may not give the right answer. The reason is that the BPM readings on the left and right side of Eq. (2.38) both have a noise component.

The effect of the noise in the horizontal coordinates can be illustrated by a simple example, taken from Ref.[24]. We consider a linear fit of the form $y = px + q$, where p and q are to be determined, and both x and y are smeared stochastically. Figure 2.12 shows the reconstructed slope normalized to the true slope as a function of the signal to noise ratio in the horizontal coordinate, R_x. Even for a signal-to-noise ratio of 3 the fitted slope still has a 10% error. This result is independent of the noise in the y coordinate.

A better approach, which takes into account the noise in the horizontal coordinates, is schematically to `find the principal axes of the set of data points and then

turn the parameter vector parallel to the principal axis along which the data points fluctuate the least' [24]. The general problem and its solution are as follows. Let x_n be a measured variable which is linearly correlated with $(n-1)$ other measurements $x_1, ..., x_{n-1}$, and suppose there are a total of N data sets. We introduce normalized coordinates:

$$z_i = \frac{x_i - < x_i >}{\sigma_i} \tag{2.39}$$

Using these coordinates, the fit equation (2.37) or (2.38) is rewritten as

$$\mathbf{u}^T \cdot \mathbf{z} = 0 \tag{2.40}$$

Introducing the symmetric covariance matrix

$$C_{ij} = \sum_{l=1}^{N} z_{li} z_{lj} \tag{2.41}$$

Eq. (2.40) is solved in a least squares sense by

$$\mathbf{C} \cdot \mathbf{u} = \lambda u \tag{2.42}$$

$$|\mathbf{u}|^2 = 1 \tag{2.43}$$

$$\chi^2 = \lambda \tag{2.44}$$

where the solution **u** is simply the normalized eigenvector corresponding to the smallest eigenvalue λ of **C**; λ is also the χ^2 of the fit.

If we assume that $\lambda = \lambda_1$ (the smallest eigenvalue) is not degenerate, and cosider a scalar function $f(\mathbf{u})$ of the fit parameters $\mathbf{u}$, the rms fit error in f is given by

$$\sigma(f)^2 = (\nabla_{\mathbf{u}} f)^T \cdot \mathbf{T} \cdot (\nabla_{\mathbf{u}} f) \tag{2.45}$$

where **T** is a symmetric $n \times n$ matrix defined by

$$T_{ij} = \sum_{r=2}^{n} \frac{\lambda_r + \lambda}{(\lambda_r - \lambda)^2} (u_r)_i (u_r)_j \tag{2.46}$$

In particular, the rms error of the coefficient u_i in the normalized equation (2.40) is simply $\sigma(u_i) = \sqrt{T_{ii}}$.

The reconstruction of lattice parameters from orbit and energy fluctuations can be studied by computer simulations. Figure 2.13 presents simulation results for the SLC final focus with an assumed BPM resolution of 20 μm, employing both a standard χ^2 fit and a principal axes transformation. The results of the former differ strongly from the underlying model parameters, despite of good fits and small error bars, while the principal axes method reconstructs the optics almost perfectly.

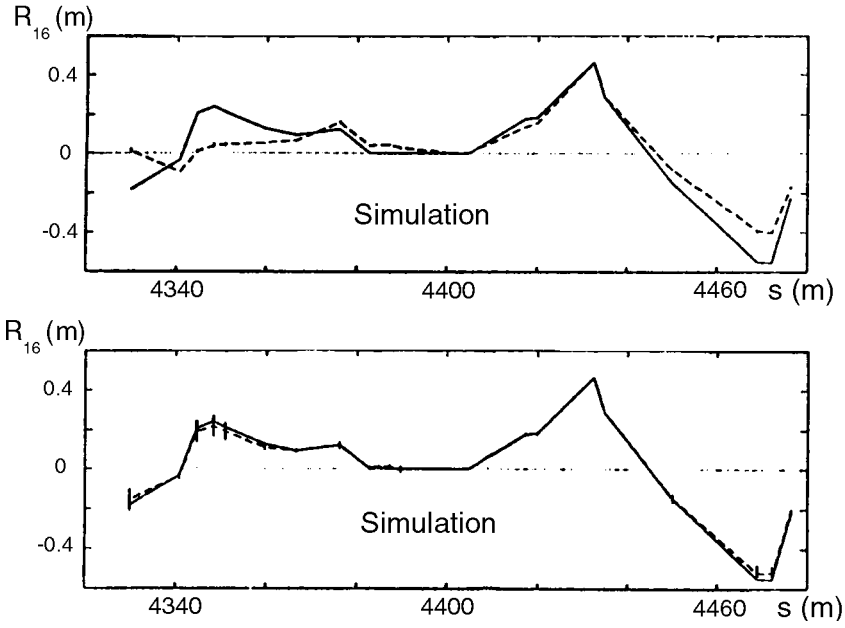

Figure 2.13: Reconstructed final focus R matrix element R_{16}, from a sample of 100 simulated trajectories with fluctuations in betatron orbit and energy, and assuming 20 μm BPM resolution[24]: (top) standard χ^2 fit; (bottom) principal axes transformation. The fit results (dashed) are compared to the model used for the trajectory generation (solid). (Courtesy P. Emma, 1998.)

2.4 Gradient Error Detection and Cures

Once the beta functions have been measured and a significant difference from the model has been found, the source of the discrepancy must be determined. In most cases, the difference from the model beta function will be a beta beat (an oscillation of the measured beta function around the design beta function at twice the betatron frequency) and the source will be a gradient error in one (or more) of the quadrupole magnets.

A gradient error Δk (in units of m^{-1}) at location s_0 will result in a beta beat of the form

$$\Delta\beta(s) = \frac{\beta(s)\beta(s_0)}{2\sin(2\pi Q)}\,\Delta k(s_0)\;\cos(2|\phi(s)-\phi(s_0)|-2\pi Q) \tag{2.47}$$

2.4.1 First Turn Trajectories

A first attempt to find the error may consist in exciting steering correctors (or changing the amplitude of the injection kicker) and fitting first-turn difference trajectories to an on-line or off-line optics model. The difference of two trajectories measured for different injection amplitudes should match a betatron oscillation predicted by the model.

The parameters of the betatron oscillation can be determined by fitting the difference orbit for a few BPMs to the model. The oscillation so obtained is then propagated along the beam line. It will agree with the measured difference trajectory, until it passes the location of a large gradient error, at which point the propagated betatron oscillation and the measurement will start to disagree. The location of the gradient error thus identified can be confirmed by fitting a betatron oscillation backwards starting in a region further downstream. The fit should begin to deviate from the model at the same point as for the forward fit.

In principle, by analyzing first-turn orbits gross optics errors are easily identified. In practice, it is not always so simple, as beam loss, BPM spray (from lost particles), or kicker noise may corrupt the BPM readings on the first couple of turns.

2.4.2 Closed-Orbit Distortion

A variant of this method is to make use of the fact that, except for the location of the corrector, a closed-orbit distortion for a stored beam has exactly the same pattern as a betatron oscillation. Thus, in much the same manner as for the first turn, the model can be used to fit the change in the closed orbit (with and without corrector excitation) to a betatron oscillation, and then to propagate this oscillation around the ring. Again, the location where a noticable disagreement starts identifies the magnet with a gradient

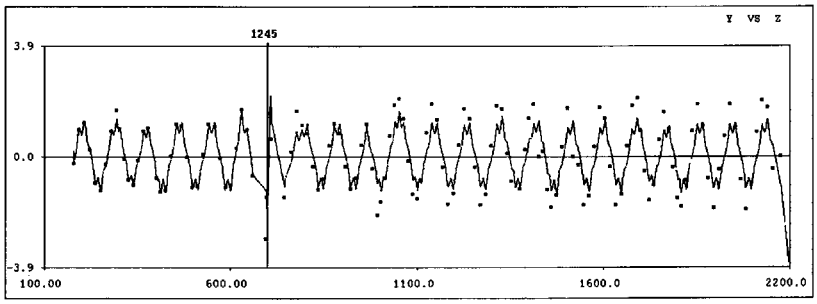

Figure 2.14: Finding quadrupole gradient errors by fitting betatron oscillations to closed-orbit distortions: an example from the PEP-II HER commissioning, using the codes LEGO [25] and RESOLVE [26]. The induced orbit change is fitted to a betatron oscillation over a small number of BPMs (further to the left); the betatron oscillation so obtained is propagated along the beam line using the model optics (solid line) and compared with the actual orbit variation (plotting symbols). In this example, the two agree well up to a region close to the interaction point, near $s = 700$ m on the horizontal axis. It was later verified that two quadrupole pairs in this region had gradient errors of the order of 0.1%. (Courtesy Y. Cai, 1998.)

error. The excitation of this magnet can be changed, and the measurement repeated, until the agreement with the model is satisfactory. Figure 2.14 shows an example of this method from the PEP-II commissioning. A gradient error close to the interaction point was clearly identified.

It is possible to considerably extend this simple closed-orbit distortion scheme. For example, the response of all BPMs to every single steering corrector may be combined into a big matrix, which can be used as an input to a sophisticated statistical fitting program, such as LOCO [27,28]. LOCO then varies the individual gradients of the quadrupoles in a computer model (*e.g.*, MAD [23]) to find the gradients that best reproduce the measured orbit response data.

2.4.3 Phase Advance

Instead of fitting trajectories, we can also use Eq. (2.27) to compute the beta functions from the measured phase advance around the ring. Then we can adjust either the model quadrupoles or change the actual magnet settings of the machine to improve the agreement of measured and predicted phase advance and to identify the source of the discrepancy.

An example from PEP-II is presented in Fig. 2.15 [29]. From left to right we see the improved agreement of model and measurement, when the strength of a quadrupole pair (QF5) in the IP region is changed by a total of 0.15%. For each quadrupole value, the upper row of pictures shows the entire ring, the lower row a close-up view of a particular section. As can be seen, the final quadrupole strength, on the right, yields a

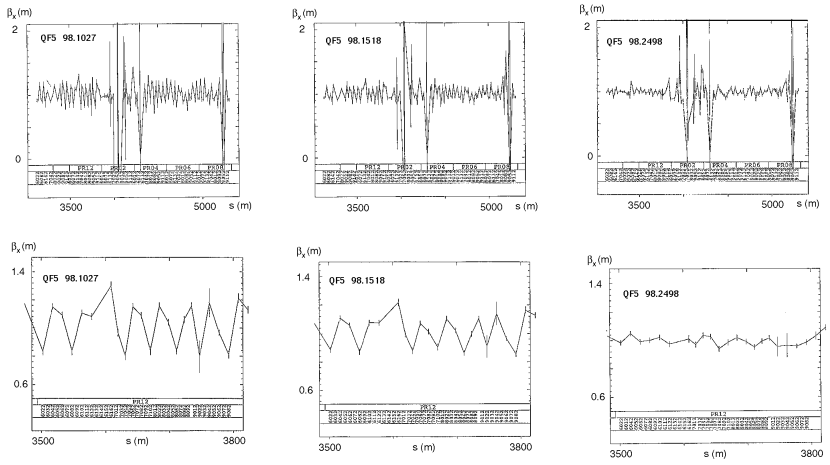

Figure 2.15: Ratio of the horizontal beta function inferred from phase advance measurements to the model beta function: (top row) for the entire PEP-II High Energy Ring (HER); (bottom row) for a limited region only; (left column) with all magnets at nominal strength; (center) for an increased strength of a single quadrupole pair (called QF5) by 0.1%; (right column) for a strength increase of 0.15%. The fliers with large error bars correspond to bad BPMs or to a phase advance between successive BPMs equal to 0 or π. (Courtesy M. Donald, 1998.)

satisfactory agreement with the model.

2.4.4 π Bump Method

Another method which can be used to identify local gradient errors is the π-bump technique, applied at Tristan and at the ATF [30,31,32]. Here, local orbit bumps are induced, one by one, across each quadrupole magnet (or across small groups of quadrupole magnets), so as to cover the entire ring. The non-closure of a theoretically closed bump is indicative of an optics error in this region. Of course, also an error in the calibration of the bump dipole magnets may result in non-closure of the bump, but the effects of dipole errors and optics errors can be separated by their betatron phase. In particular, for an ideal π bump, the bump leakage due to a gradient error and that due to a dipole error are perpendicular to each other. In more complex situations, computer programs can be used to process a large number of measurements for overlapping bumps, so as to determine both the dipole and the focusing errors.

Ex.2.5. Quadrupole with a turn-to-turn short
So-called difference orbit measurements are taken by saving a BPM reference orbit under nominal conditions, perturbing the beam with a single corrector and forming the difference orbit consisting of measurements of the perturbed orbit and the nominal orbit. This difference orbit may be easily compared with model expectation. Suppose such lattice diagnostic measurements are made in an electron accelerator and reveal that the beam is errantly deflected up and outboard (away from ring center) at a focussing quadrupole.
a) Based on these observations, which of the quadrupoles' coils is suspect of a turn-to-turn short?
b) With a position resolution of 10 μm, how well can the relative change in the current through the offending coil be determined?
Ex.2.6. Quadruple gradient errors
a) Design a closed π-bump spanning a focussing quadrupole of strength k assuming perfect calibration of the corrector dipoles.
b) Using this bump, suppose that the orbit is observed not to close with a residual amplitude measured with a BPM of A. Find an expression relating the measured leakage A to the gradient error Δk.

2.5 References

1. F. Zimmermann, P. Krejcik, M. Minty, D. Pritzkau, T. Raubenheimer, M. Ross, M. Woodley, "Ion Effects in the SLC Electron Damping Ring under Exceptionally Poor Vacuum Conditions", Proc. of the International Workshop on Multibunch Instabilities in Future Electron and Positron Accelerators (MBI97), Tsukuba, and SLAC-PUB-7665 (1997).
2. T. Ieiri and K. Hirata, "Observation and Simulation of Nonlinear Behavior of Betatron Oscillations During the Beam-Beam Collision", Proc. of the 1989 IEEE PAC (1989).
3. E. Asseo, CERN PS/85-3 (LEA) (1985).
4. R. Bartolini, M. Giovannozzi, W. Scandale, A. Bazzani, E. Todesco, "Algorithms for a Precise Determination of the Betatron Tune", Proc. of EPAC 96, Sitges, vol. II, p. 1329 (1996). see also CERN report SL/95-84 (1995).
5. F. J. Harris, "On the Use of Windows for Harmonic Analysis with Discrete Fourier Transform", Proc. IEEE Vol. 66, No 1, January 1978.
6. J. Byrd, "Longitudinal Beam Transfer Function Diagnostics in an Electron Storage Ring", Particle Accelerators (1998).
7. G. Carron, D. Möhl, Y. Orlov, F. Pedersen, A. Poncet, S. van der Meer, D.J. Williams, "Observation of Transverse Quadrupole Mode Instabilities in Intense Cooled Antiproton Beams in the AA", CERN/PS/89-18 (1989).
8. H. Schmickler, "Diagnostics and Control of the Time Evolution of Beam Parameters", presented at the Third European Workshop on Beam Diagnostics

and Instrumentation at Particle Accelerators (DIPAC 97) and CERN-SL-97-68 (1997).
9. C. Boccard et al., “Tune Measurements in the SPS as Multicycling machine”, Proc. of EPAC96, Sitges (1996).
10. K.D. Lohmann et al., “Design and functionality of the LEP Q-meter”, Proc. of EPAC90, Nice (1990).
11. J. Borer and R. Jung, “Diagnostics”, CERN Accelerator School on Antiprotons for Colliding Beam Facilities, CERN 84-15, p. 385 (1984)
12. R. Bartolini, M. Giovannozzi, W. Scandale, A. Verdier, C. Pellegrini, P. Tran, E. Todesco, J. Corbett, M. Cornacchia, “Measurements of the Tune Variations Induced by Non-Linearities in Lepton Machines”, Proc. of EPAC 96, Sitges, vol. II, p. 917 (1996).
13. J. Bengtsson, “Spectral Analysis of the Motion at a Single Nonlinear Resonance by Canonical Perturbation Theory”, CERN internal report PS/LEA/Note 87-03 (1987).
14. C.-X. Wang and J. Irwin, “Possibility to measure the Poincaré section map of a circular accelerator”, submitted to Physical Review E, and SLAC-PUB-7547 (1997).
15. R. Bartolini and F. Schmidt, “Normal Form via Tracking or Beam Data”, Part. Accelerators (in press) and LHC Project Report 132 (1997).
16. Y. Cai, “Lattice Performance of the PEP-II High Energy Ring”, presented at the Advanced ICFA Beam Dynamics Workshop on Beam Dynamics Issues for e^+e^- Factories, Frascati, Italy, and SLAC-PUB-7733 (1997).
17. J. Borer, C. Bovet, A. Burns, G. Morpurgo, “Harmonic Analysis of Coherent Bunch Oscillations at LEP”, Proc. of EPAC92, p. 1082 (1992).
18. D. Brandt, P. Castro, K. Cornelis, A. Hofmann, G. Morpugo, G.L. Sabbi, J. Wenninger, and B. Zotter, “Measurements of Impedance Distributions and Instability Thresholds in LEP”, Proc. of 1995 IEEE PAC, Dallas, p. 570 (1995).
19. K. Oide, private communication (1997).
20. P. Castro, “Betatron Function Measurement at LEP Using the BOM 1000 Turns Facility”, SL/Note 92-63 (1992).
21. J. Corbett, private communication (1998).
22. C. Bovet, “The Measurement of some Machine Parameters”, in J. Bosser (ed.), “Beam Instrumentation”, CERN-PE-ED 001-92 (1992), rev. (1994).
23. H. Grote, F.C. Iselin, The MAD Program, Version 8.1, CERN/SL/90-13, 1991.
24. T. Lohse and P. Emma, “Linear Fitting of BPM Orbits and Lattice Parameters”, SLAC Single Pass Collider Memo CN-371 (1989).
25. Y. Cai, M. Donald, J. Irwin, Y. Yan, “LEGO: A Modular Accelerator Design Code”, Proc. of IEEE PAC97, Vancouver, and SLAC-PUB-7642 (1997).
26. The RESOLVE program was written by M. Lee.

27. J. Safranek, “Experimental determination of storage ring optics using orbit response measurements”, Nucl. Instr. and Meth. A388, 27 (1997).
28. J. Safranek, these proceedings.
29. M. Donald, private communication (1998).
30. S. Kamada, “Overview on Experimental Techniques and Observations”, Proc. of workshop on Nonlinear Dynamics in Particle Accelerators: Theory and Experiments”, Arcidosso, Italy (1994).
31. H. Koiso, H. Fukuma, Y. Funakoshi, S. Kamada, S. Matsumoto, K. Oide, and N. Yamamoto, “Beam-Based Measurement of Strength Errors in Quadrupole Magnets with Orbit Bumps”, Proc. of EPAC 96, Sitges, Spain (1996).
32. E.-S. Kim and S. Matsumoto, “Beam-Based Measurement of Focusing Errors in Quadrupole Magnets in ATF Damping Ring”, in the Proc. of the 2nd ATF International Collaboration Meeting”, KEK, Tsukuba, KEK Proceedings 97-9, p. 82 (1997).
33. M. Sands, “A Beta Mismatch Parameter”, SLAC internal report SLAC-AP-85 (1991).
34. W. Spence, private communication (1996).
35. R. Iverson, M. Minty, M. Woodley, private communication, and ATF internal report ATF 12-29 (1997).
36. J.P. Koutchouk, “Linear Betatron Coupling Measurement and Compensation in the ISR”, CERN ISR-OP/80-27, also published in the Proc. XIth Int. Conf. on High Energy Accelerators, CERN, Geneva, Birkhäuser Verlag, Basel, p. 491 (1980).
37. J. Turner, private communication (1998).
38. V. Ziemann, “Corrector Ironing”, SLAC internal report Single-Pass Collider Note CN-393 (1992).
39. W. Press, *et al.*, “Numerical Recipes”, Section 2.9, Cambridge University Press, Cambridge (1986).
40. The MathWorks, Inc. (1994).
41. W.J. Corbett, F. Fong, M. Lee, V. Ziemann, “Optimum Steering of Photon Beam Lines in SPEAR”, Proc. of 1993 IEEE PAC Washington, p. 1483 (1983).
42. M. Minty, C. Adolphsen, L.J. Hendrickson, R. Sass, T. Slaton, M. Woodley, “Feedback Performance at the Stanford Linear Collider”, Proc. of IEEE PAC 95, Dallas (1995).
43. T. Himel, “FEEDBACK: Theory and Accelerator Applications”, Annu. Rev. Nucl. Part. Sci. 47, p. 157 (1997).

Chapter 3

Transverse Optics Measurement and Correction - Part II

3.1 Orbit Measurement and Control

In the next few sections we describe methods used to control the beam orbit. We begin by illustrating the very practical issue relating to the precision to which the beam position can be determined. Next we describe a form of lattice diagnostics, used routinely at almost all accelerators, which serves to identify optical and/or instrumental errors. While such simple checks are absolutely mandatory, to achieve design beam emittances, more advanced tuning algorithms are required. We present a subset of such optimization techniques.

3.1.1 BPM Offsets

In practice, there may be uncertainties associated with the electronic center (and/or mechanical center) of a BPM and the magnetic center of a quadrupole into which BPMs are typically mounted. Consider the case as illustrated in Fig. 3.1. In this case, the deviation from the reference axis [a], the definition of which is still subject to debate, is given by

$$x = x_d + x_b + x_m, \tag{3.1}$$

[a] A famous little-known paper by Courant [1] from the early 60's was titled something like 'Where is Zero?' which we see is still relevant today!

where x_d represents the quadrupole offset, x_b gives the BPM offset, and x_m corresponds to the actual measurement. The reference axis may be chosen to minimize emittance dilutions in a global sense. Neglecting this issue for the moment, we see that even in the ideal case (of perfect local corrections) for which the reference axis is in the center of the quadrupole, a so-called one-to-one steering algorithm designed to zero the BPM readings would still place the beam off-axis in the quadrupole.

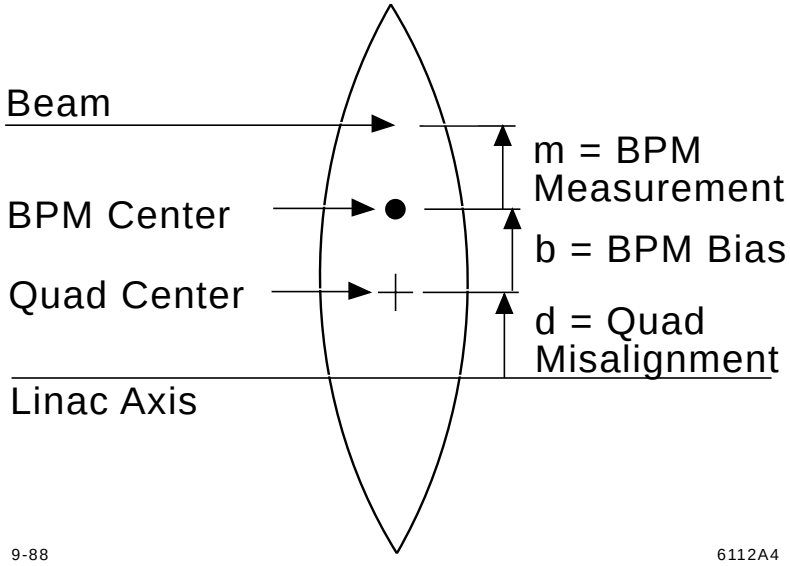

Figure 3.1: Sketch showing relative positions of the BPM, the quadrupole, and the beam position measurement from an ideal reference axis. (Courtesy C. Adolphsen, 1999).

If the orbit is off-center in a quadrupole magnet, dispersion is generated, and, in a ring, also the beam energy may be changed or the depolarization may increase. An orbit that is off-center in a sextupole induces skew coupling and/or beta beating. Thus it is very important to center the orbit in these magnets. The standard tools for correcting the orbit are corrector dipoles. Of course, such an orbit correction will never be perfect. Figure 3.2 shows a typical absolute orbit reading from the PEP-II HER, after moderate orbit correction during commissioning.

We will see that if the BPM offsets are not known, and possibly larger than the alignment errors, a better strategy is to reduce the rms strength of the steering correctors, and to pay less attention to the absolute orbit reading. In several cases, at the SLC and at the ATF, this second approach significantly reduced the magnitude of the residual vertical dispersion[2]. Sometimes other constraints are imposed on the

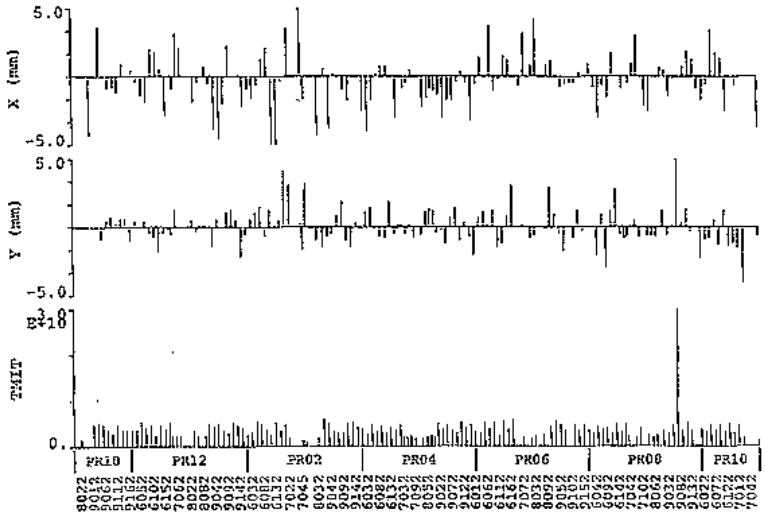

Figure 3.2: Typical commissioning orbit in the PEP-II HER: (top) horizontal orbit in mm; (center) vertical orbit in mm; (bottom) intensity in 10^{10}. (Courtesy U. Wienands, J. Seeman *et al*, 1998.)

orbit. For example, a certain orbit amplitude or a certain angle may be desired near the injection or extraction points, or near a synchrotron light beamline. In such cases, a constant orbit must be maintained at the adjacent BPMs.

3.1.2 Lattice Diagnostics and R Matrix Reconstruction

Consider a beam line with no coupling elements as shown in Fig. 3.3 consisting of dipole and quadrupole magnets, BPMs and corrector magnet dipoles. The point-to-point transfer map between any two points (1) and (2) is given by

$$\begin{pmatrix} x \\ x' \end{pmatrix}_2 = \begin{pmatrix} R_{11} & R_{12} \\ R_{21} & R_{22} \end{pmatrix} \begin{pmatrix} x \\ x' \end{pmatrix}_1 \tag{3.2}$$

Let the initial point (1) be at a corrector and the final point (2) be at a BPM. Two measurements are required to determine R_{12}: $(x, x')_{\rm BPM}$ with the nominal beam trajectory and $(x, x')_{COR}$, and with $(x, x' + \theta)_{COR}$ after the beam is kicked by an angle θ. The difference in x_{BPM} between the two measurements is $R_{12} = \frac{\Delta x}{\theta}$. In practice to decrease sensitivity to measurement error, one introduces a series of large betatron oscillations by varying the corrector in steps. The response of the BPM readings to these perturbations[3] is then measured. The resulting dependence of position on the kick angle θ is fitted with a straight line as shown in Fig. 3.4.

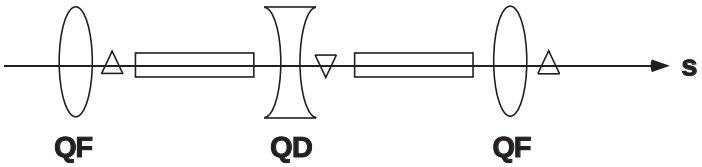

Figure 3.3: Simple FODO lattice. Shown are the focussing quadrupoles (QF), the defocussing quadrupoles (QD), and dipoles (rectangles). The BPMs are usually mounted within the quadrupoles. Corrector magnets are denoted by triangles.

Shown in Fig. 3.5 is an example of a beam trajectory after excitation by a corrector magnet and an amplitude fit using many downstream BPMs. For good viewing conditions the measured trajectory is plotted for the case of a maximum kick angle $\theta = \theta_{max}$. The solid line connects the measurements from each BPM. The dashed line represents the fitted position $x = R_{12}\theta + x_o$ evaluated at θ_{max} where x_o is the offset in the linear fit. To probe all magnetic elements in the beamline, a second measurement is required using a second corrector dipole separated by 90° in betatron phase advance. Discrepancies between the measurement and fit are used to reveal phase errors, which could result from a shorted quadrupole magnet, and/or "bad" BPMs for example. Identification and exclusion of bad BPMs is required for good convergence of steering algorithms.

Assuming the linear transport matrices between the different correctors and the transport matrices between adjacent BPMs are known with sufficient accuracy, the R matrix between the correctors and the BPMs can be determined by a simple least squares fit[3]. Including the additional constraint that the R matrix has to be symplectic eliminates several degrees of freedom, but then the problem must be solved by non-linear regression [3]. Reference [3] describes how a rigorous error analysis allows an estimate of the unknown systematic errors.

Suppose the agreement between the measured data and fit is unsatisfactory. In the absence of hardware errors, this may result from systematic measurement errors or from an incomplete model. Accuracy of the model is vital for basic optics checkout and requires, for example, accurate representations of magnetic field strengths. In a linear accelerator, it may be necessary to take into account the energy dependence of the point-to-point transfer matrix elements. The change in the betatron phase $\Delta\psi$ relative to the expected phase ψ is given by

$$\frac{\Delta\psi}{\psi} = \delta\xi, \tag{3.3}$$

where δ is the relative energy deviation and ξ is the chromaticity. With $\xi = -1/\pi$ for a 90° FODO cell, then a 1% energy error corresponds to a change in phase advance

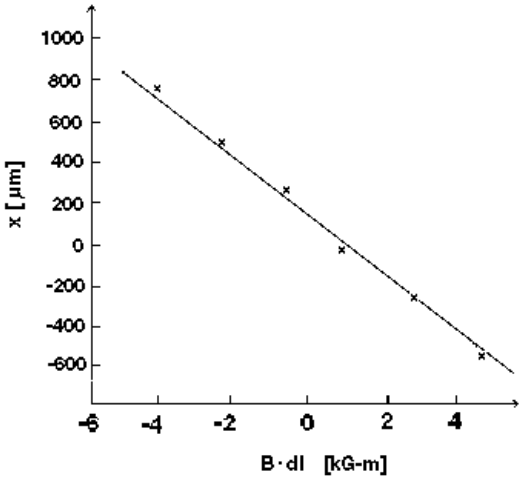

Figure 3.4: Example of an R_{12} measurement: transverse position x versus $B \cdot dl$ where the kick angle, in terms of the magnetic rigidity $B\rho$, is $\theta = \frac{B \cdot dl}{B\rho}$.

of $\Delta\psi = -0.003\psi$ per cell.

To take into account the energy dependence of the transport matrix, the matrix elements may be expanded in a Taylor series. Keeping the linear term only,

$$\begin{pmatrix} x \\ x' \end{pmatrix}_2 = \prod_{k=1}^{N_s} \begin{pmatrix} R_{1,1_k} + \frac{dR_{1,1_k}}{dE_k}\Delta E_k & R_{1,2_k} + \frac{dR_{1,2_k}}{dE_k}\Delta E_k \\ R_{2,1_k} + \frac{dR_{2,1_k}}{dE_k}\Delta E_k & R_{2,2_k} + \frac{dR_{2,2_k}}{dE_k}\Delta E_k \end{pmatrix} \begin{pmatrix} x_0 \\ x'_0 \end{pmatrix}_1 , \quad (3.4)$$

where N_s is the number of regions in which the accelerator has been subdivided. The procedure consists of

1. measuring the transverse position x_m after the beam has been deflected,
2. selecting a set of E_k's,
3. comparing the measured position x_m with the expected, or calculated, position x_c by computing

$$\chi^2 = \sum ({x_m}^2 - {x_c}^2), \quad (3.5)$$

where the sum is over all the BPMs used in the measurement, and
4. iterating steps 2 and 3 to minimize the χ^2.

An example is shown in Fig. 3.6 for the SLAC linear accelerator [5]. In the top plot an amplitude fit was used (as in Fig. 3.5). In bottom plot, the minimum χ^2 corresponded to an energy error of about 30%, which far exceeded the estimated uncertainty in the energy. Possible reasons for the discrepancy might include calibration

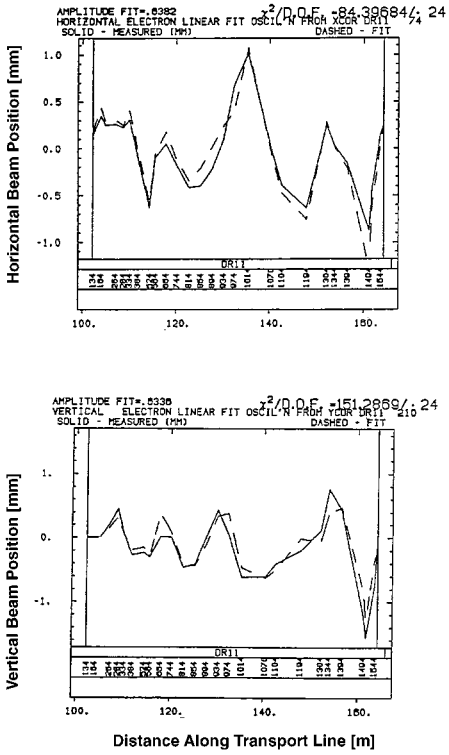

Figure 3.5: Comparison of measured data (solid curve) and amplitude fit (dashed curve). Plotted are the horizontal and vertical beam positions as measured as a function of distance along the transport line. See also ref. [4].

errors in the quadrupoles, random errors in the BPM gains, or wakefields, which are not included in the model. Nonetheless, the dynamics are predictable by incorporating the fitted errors into the accelerator model.

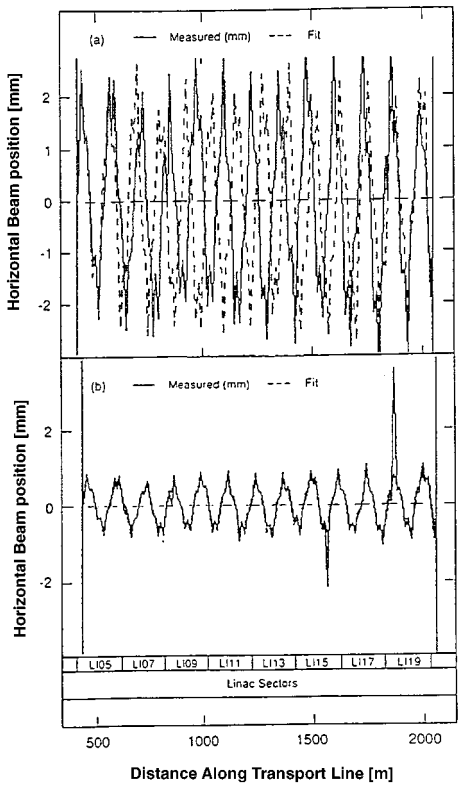

Figure 3.6: Comparison of measured data and fit to betatron amplitude only (a) or fit to both betatron amplitude and energy in the different linac sections (b). Plotted is the horizontal beam position as a function of distance along the linear accelerator. (Courtesy T. Himel, 1999).

3.1.3 Singular Value Decomposition

A common situation is that the BPM offsets are known fairly well and the orbit already fulfills a number of constraints, but many of the corrector magnets are strongly excited with some of them `fighting' (compensating) each other. Fortunately, there exists a very powerful technique to reduce the rms strength of the orbit correctors, while maintaining a set of constraints. This technique is sometimes called `corrector ironing' [6] and it is based on a `singular value decomposition' [7].

Suppose we want to solve the linear equation

$$\mathbf{\Delta x} = \mathbf{A} \cdot \theta \tag{3.6}$$

where the vector $\mathbf{\Delta x} = (\Delta x_1, \ldots \Delta x_M)$ may describe the desired correction (or constraint) at M BPMs, and $\theta = (\theta_1, \ldots, \theta_N)$ are the excitation strengths of N correctors, that we want to determine. If $M \geq N$, we can decompose the matrix $\mathbf{A}$ as

$$\mathbf{A} = \mathbf{U} \cdot \begin{pmatrix} w_1 & 0 & \ldots & 0 \\ 0 & w_2 & \ldots & 0 \\ & \ldots & \ldots & \\ 0 & 0 & \ldots & w_N \end{pmatrix} \cdot \mathbf{V}^t \tag{3.7}$$

The column vectors of the $M \times N$ matrix $\mathbf{U}$ and the $N \times N$ matrix $\mathbf{V}$ are orthonormal

$$\mathbf{U}^t \cdot \mathbf{U} = \mathbf{I}_N \tag{3.8}$$

$$\mathbf{V}^t \cdot \mathbf{V} = \mathbf{I}_N \tag{3.9}$$

where $\mathbf{I}_N$ denotes the $N \times N$ unity matrix. The decomposition of Eq. (3.7) can be performed, for example, using the FORTRAN subroutine described in Ref.[7]. An SVD decomposition is also provided in a convenient form by many mathematical analysis packages, such as MATLAB[8].

We now consider three different cases: First, we suppose the number of correctors is equal to the number of BPMs. In this case the matrix $\mathbf{A}$ is square. We can write down a formal solution

$$\theta = \mathbf{A}^{-1} \cdot \mathbf{\Delta x} = \mathbf{V} \cdot \begin{pmatrix} 1/w_1 & 0 & \ldots & 0 \\ 0 & 1/w_2 & \ldots & 0 \\ & \ldots & \ldots & \\ 0 & 0 & \ldots & 1/w_N \end{pmatrix} \cdot \mathbf{U}^t \cdot \mathbf{\Delta x} \tag{3.10}$$

If none of the w_i is zero, this is the unique solution to the problem. If one or more of the w_i are zero, the equation may not have an exact solution, but for these w_i one can simply replace $1/w_i$ by 0, and with this replacement Eq. (3.10) still gives the solution in a least squares sense. This means it minimizes the distance $r = |\mathbf{A} \cdot \theta - \mathbf{\Delta x}|$.

Furthermore, the solution vector θ so obtained is the (either least-squares or exact) solution with the smallest possible length $|\theta|^2$. In other words, the solution derived from the SVD decomposition also minimizes the rms strength of the correctors.

In addition, it is worthwhile to note that the columns of $\mathbf{U}$ whose same numbered w_i are nonzero are an orthonormal set of basis vectors that span the range of the matrix $\mathbf{A}$ while the columns of $\mathbf{V}$ whose same-numbered elements w_j are zero are an orthonormal set for the nullspace of $\mathbf{A}$.

Next, we consider the case that there are fewer equations than correctors. In this case, we can simply add rows with zeroes to the vectors and matrices of Eq. (3.6) until the matrix is square, and then apply the SVD formalism, as described above. In this case, there is (at least) one zero eigenvalue w_j for every row of zeroes added.

Finally, in the case of more BPM constraints than unknown correctors ($M > N$), SVD works just as well. In general the w_j will not be zero, and the SVD solution will agree with the result of a least-square fit. If there are still some small values w_j, these indicate a degeneracy in $\mathbf{A}$ and the corresponding $1/w_j$ should be set to zero, as before. The corresponding column in $\mathbf{V}$ deserves attention, since it describes a linear combination of corrector excitations, which does not affect the constraints.

The SVD steering algorithm has been used successfully at many accelerators, for example, at the synchrotron light source SPEAR[9] or throughout the SLC.

3.1.4 Beam-Based Alignment

In many modern accelerators, the alignment tolerances on quadrupole and sextupole magnets are so tight that they cannot be achieved by state-of-the art surveying and installation methods with residual errors of 100-200 μm. The standard approach to achieve and maintain tight tolerances is beam-based alignment.

Beam-based alignment determines the relative offset between magnet centers and nearby BPMs. If these offsets are sufficiently stable, a simple orbit correction (steering) can maintain a well-centered orbit, until the alignment measurement is repeated at a later time (after several months).

Quadrupole Excitation

If the beam is not centered in a quadrupole magnet, and the strength of this quadrupole is varied, the beam receives a kick. This causes a change in the beam trajectory, for single-turn measurements, or a change in the closed orbit, for measurements on a stored beam.

For a single-pass measurement, the dipole kick θ can easily be inferred by fitting the difference trajectory to a betatron oscillation including one additional kick at the location of the quadrupole. The dipole kick θ obtained from the fit is proportional to

the quadrupole misalignment x_q and the change in the integrated quadrupole strength:

$$\theta = \Delta k \; x_q \tag{3.11}$$

If beam-based alignment is performed on a stored beam, the additional kick of the closed orbit induced by the change in quadrupole strength is given by the sum of two components, the change in field strength and the change in the closed-orbit offset at the quadrupole. In lowest order, we have[10]

$$\theta \approx \Delta k \; x_q - k \; \Delta x \tag{3.12}$$

where x_q is the original quadrupole offset, Δx the change in closed-orbit position, k the integrated quadrupole gradient, and we have neglected a second-order term $(\Delta k \; \Delta x)$. We can apply the formula for the closed orbit distortion at the location of the dipole kick, Eq. 2.33, and find

$$\Delta x = (\Delta k \; x_q - k \; \Delta x) \; \left(\frac{\beta}{2 \tan \pi Q} \right) \tag{3.13}$$

which we can solve for Δx,

$$\Delta x = \Delta k \; x_q \left(\frac{\beta/(2 \tan \pi Q)}{1 + k\beta/(2 \tan \pi Q)} \right) \tag{3.14}$$

Inserting this back into Eq. (3.12) gives the closed-orbit kick induced by a gradient change Δk:

$$\theta = \Delta k \; x_q \left(\frac{1}{1 + k\beta/(2 \tan \pi Q)} \right). \tag{3.15}$$

This is the stored-beam equivalent of Eq. (3.11).

The precision of this method is much improved by taking difference orbits for several quadrupole-to-beam off-sets, Δx_q, varied with a local bump[11]. One can also define a merit function

$$f(\Delta x_q) = \frac{1}{N_{BPM}} \sum_{i=1}^{N_{BPM}} (x_i(\Delta k) - x_i(-\Delta k))^2, \tag{3.16}$$

where N_{BPM} is the total number of BPMs in the ring, and determine the quadrupole offset by minimizing $f(\Delta x_q)$ as a function of the bump amplitude Δx_q, using a least-squares parabolic fit. At the Advanced Light Source (ALS), this procedure measures the center of the quadrupoles to within ± 5 μm[10] (in case of the ALS, the orbit at the quadrupole is varied with a single corrector and not by a closed bump).

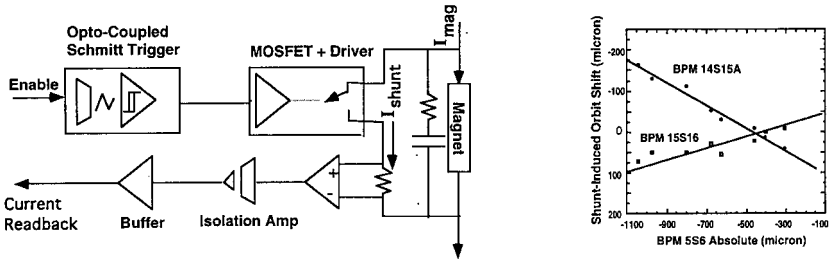

Figure 3.7: Beam-based alignment with quadrupole shunts at SPEAR[12]: (left) electric circuit with shunt resistor; (right) shunt-induced orbit shift at two downstream BPMs as a function of the beam-position read back at the BPM nearest to the quadrupole being varied. (Courtesy J. Corbett, 1998.)

This type of measurement does not require an independent power supply for each quadrupole to be aligned, but, for several magnets in series, a simple switchable shunt resistor across each magnet will suffice. Simultaneously, such shunt resistors allow a measurement of the beta function since

$$\beta_{x,y} \approx 4\pi \frac{\Delta Q_{x,y}}{\Delta k}. \tag{3.17}$$

Figure 3.7 illustrates the application of this technique at the storage ring SPEAR. The left figure shows the circuit diagram for a magnet with shunt resistor, and the right figure presents a typical alignment measurement for a SPEAR quadrupole. Plotted in the right figure is the orbit shift induced by the shunt at two downstream BPMs as a function of the orbit at the shunted quadrupole, which is varied by a local bump. The orbit is centered in the quadrupole when no orbit shift is induced by the shunt (the intersection of the two lines).

If the number of BPMs is small and only groups of quadrupoles can be changed simultaneously, it is still possible to determine the quadrupole misalignments, by applying a statistical fit to a sufficiently large number of trajectories taken for different quadrupole-group excitations, different incoming conditions and different corrector settings. An interesting example of such an analysis can be found in Ref.[13].

Quadrupole Gradient Modulation

A scheme which allows continuous monitoring of quadrupole alignment and BPM offsets was implemented at LEP; see for example Ref.[14]. Here the strength of several quadrupoles is modulated at different frequencies in the range 0.8-15.6 Hz, and the induced oscillation amplitude, of the order of 1 μm is detected. Figure 3.8 shows the FFT over 4096 data points of this detector signal, at a time when four quadrupoles

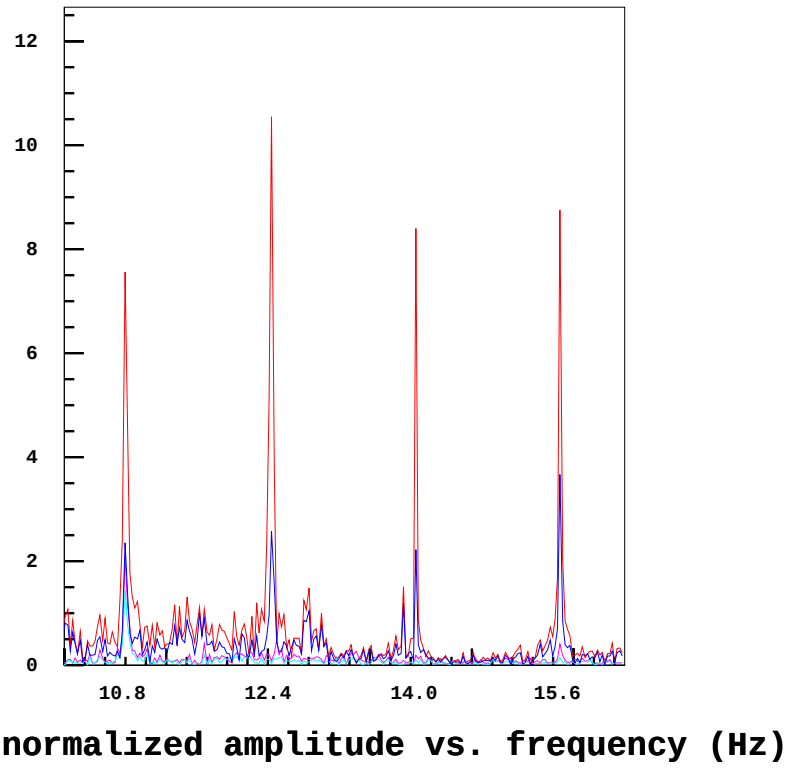

Figure 3.8: FFT spectra with 4 modulated quadrupoles in LEP[14]. The amplitude of the peaks is proportional to the beam displacement in the 4 quadrupoles. (Courtesy I. Reichel, 1998.)

were modulated. Clearly visible are 4 peaks in the frequency sprectrum, corresponding to the four different modulation frequencies. The amplitude of the peak is proportional to the beam offset in that quadrupole.

Using this k modulation technique, one can infer the BPM offsets from the naturally occurring beam-orbit jitter and orbit variation. This is illustrated in Fig. 3.9. The left figure shows a BPM orbit reading in LEP during several hours of a luminosity run. The reasons for the slow changes are not fully understood; the fast steps reflect corrections of the closed orbit. Making use of this natural orbit variation, one can plot the amplitude of the beam response to the quadrupole modulation as a function of the BPM reading for the corresponding quadrupole. The result is a `V plot', as shown in

the right figure. The minimum in this plot determines the BPM reading at which the beam is centered in the quadrupole.

Sextupole Excitation

In present-day storage rings, it is often assumed that the sextupoles are well enough aligned with respect to the quadrupoles that only the quadrupole alignment has to be verified. An orbit off center in a sextupole will result in vertical dispersion, betatron coupling, or beta beating. Although, in principle, also the sextupoles in a storage ring can be aligned by changing their strength and measuring the induced orbit shift (which is a quadratic function of the excitation) there is little experience with such a scheme. To reach the same sensitivity as for the equivalent quadrupole alignment, the change in the sextupole gradient Δk_s would have to be equal to

$$\Delta k_s = \frac{\Delta k_q}{2x_s} \tag{3.18}$$

where x_s is the horizontal orbit offset at the sextupole, and Δk_q the corresponding change in quadrupole gradient. A different approach, which was tested at KEK [15], is to equip the sextupole magnets with additional quadrupole trim windings for beam-based alignment. This is based on the assumption that the magnetic centers of quadrupole trim coil and sextupole will coincide. Sextupole alignment with a precision better than 50 μm was demonstrated[15].

Local orbit bumps across single sextupoles have been used for the purpose of sextupole alignment at KEK[16,17] and DESY[18]. The strength of all sextupoles is changed together and the induced orbit change is measured. Then the measurement is repeated for a different bump amplitude. The horizontal deflection depends quadratically on the horizontal bump amplitude, while the vertical deflection is a linear function:

$$\Delta\theta_x = -0.5\, K_s(x_{bump} - x_s)^2 \tag{3.19}$$

$$\Delta\theta_y = K_s(x_{bump} - x_s)y_s \tag{3.20}$$

where x_{bump} is the amplitude of the bump, and x_s, y_s are the sextupole misalignments. The advantage of this method is that it does not require individual power supplies for the sextupoles.

Alternative approaches are conceivable: one could vary multiple sextupoles at once, and fit for multiple kicks. Also, one could vary the sextupole strength and measure the induced tune variation or the tune separation near the difference resonance [19].

In the final-focus systems of linear colliders, sextupole alignment is essential. At the SLC final focus, the orbit in the sextupoles must frequently be measured and

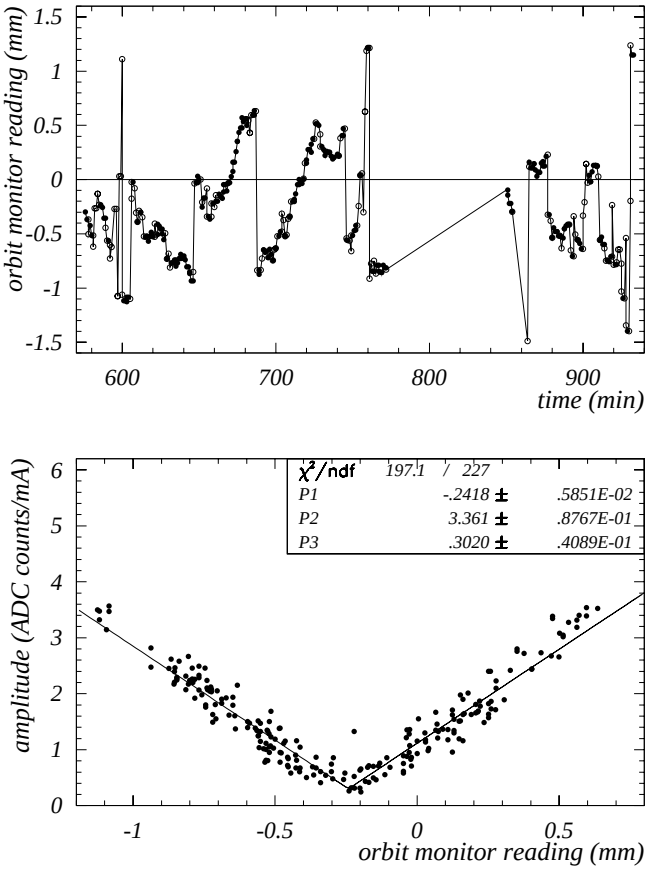

Figure 3.9: Determination of BPM offsets using k modulation and natural orbit variation in LEP[14]: (top) natural orbit drifts and corrections during a LEP luminosity run at one quadrupole; (bottom) amplitude of beam response to k modulation vs. BPM orbit reading for the modulated quadrupole. The minimum of this plot gives the BPM offset. These data were taken continuously during 5 hours of luminosity run. (Courtesy I. Reichel, 1998.)

adjusted to maintain a high luminosity. The SLC sextupole alignment is based on varying the sextupole strength and detecting the induced optics (not orbit) change[20]. If the orbit is off center, the first order effect of the sextupole excitation is a waist shift (change in the beta function), skew coupling, or dispersion at the interaction point. These optics changes can be quantified easily by reoptimizing the spot-size at the collision point, after a change in the sextupole strength. The reoptimization is done by scanning a group of quadrupole and skew quadrupole magnets excited together so that they only affect one optical parameter. For each value of the parameter correction, the IP spot size is remeasured with beam-beam deflection scans, and the magnets are finally set to a value where the beam size is minimum. The change in the optimum waist, dispersion, etc., as a function of the sextupole excitation is proportional to the orbit offset at the sextupole. The measured offsets are corrected by means of closed bumps.

An interesting feature of the SLC final focus is that it has 2 pairs of interleaved sextupoles. The sextupoles in each pair, connected to the same power supply, are separated by an optical $-I$ transform. Thus, the alignment procedure actually consists in generating symmetric or antisymmetric orbit bumps for each sextupole pair, in response to the amount of waist motion or dispersion etc., induced by a change in the sextupole-pair strength[21].

Sextupole Movement

It is also possible to align the sextupole magnets by detecting the second-order effect of the sextupole excitation: the induced orbit kick. This method works well when the sextupoles are installed on precision movers, which can be used for both the measurement and the alignment. The basic idea is straightforward. Measuring the orbit change downstream as a function of horizontal or vertical sextupole-mover position results in a parabolic curve. The sextupole is aligned when the mover position is set to the minimum of this curve. A sample measurement from the FFTB[22] is displayed in Fig. 3.10.

Structure Alignment using Beam-Induced Signals

For future high-gradient linear accelerators it is essential to center the beam orbit in the accelerating structures, thus minimizing the transverse wakefields. Alignment techniques were studied on a test structure for the Next Linear Collider, which was installed in the SLAC linac, as part of the ASSET experiment. These studies demonstrated that the beam-induced dipole-mode signals can be used to center the beam to the level of 40 μm[23]. The result in Fig. 3.11 shows the amplitude and phase (with respect to a reference phase derived from a BPM signal) of a 15-MHz wide slice of the beam-induced dipole mode signal, centered near 15 GHz, as a function of the nominal

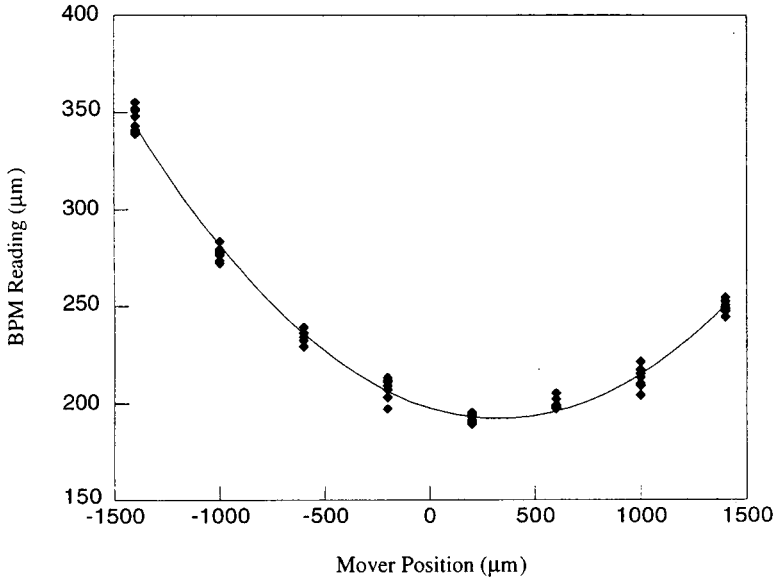

Figure 3.10: Sextupole alignment in the Final Focus Test Beam (FFTB)[22]: downstream orbit variation is measured as a function of sextupole mover position; the sextupole is aligned at the minimum of the parabola. (Courtesy P. Tenenbaum, 1998.)

beam position. The beam position was varied with dipole steering magnets. Clearly visible is a minimum in the amplitude along with a 180 degree phase jump. Steering the beam to the position with minimum signal successfully centered the orbit in the structure as was verified by detecting the deflection experienced by a subsequent witness bunch.

3.1.5 Orbit Feedback

Feedback systems that stabilize the beam orbit are becoming more common in accelerators, both in light sources, such as the APS, and in accelerators for high-energy physics, such as the SLC [24]. A comprehensive overview of orbit feedback systems can be found in Ref. [25]. A simple orbit feedback maintains a constant orbit by adjusting the strength of 2 or 4 steering correctors based on BPM readings. Many orbit feedback systems employ an SVD algorithm which flattens the orbit while at the same time minimizing the strength of the correctors.

Slightly more complicated feedback loops are designed so that they maintain both the beam orbit and the beam energy. Orbit and energy can be separated using BPMs at dispersive locations. The orbit is corrected via steering correctors; the beam energy by adjustments to some upstream rf phase.

The effectiveness of a feedback can be tested by measuring its response to a step change. An example in Fig. 3.12 shows the response of an SLC feedback loop to a sudden step change in energy. The picture illustrates the improvement achieved by increasing the number of feedback BPMs to better constrain the fit.

There are different techniques to calibrate the local transport matrices between correctors and BPMs within each feedback loop, which are used to continually compute the excitation of the feedback steering correctors. For example, the induced change in orbit position and angle can be measured as a function of the individual feedback corrector strengths.

If there are successive feedback loops on a beam line, these loops could interfere with each other, and *e.g.*, cause unwanted orbit oscillations. This interference can be avoided by either one of 4 different approaches [25]: (1) orthogonality, (2) different speed, (3) inter-loop communication (feedback cascades) and (4) integration into one global loop. At the SLC, the orbit feedbacks in the linac are connected by an adaptive cascade. Each feedback passes its information to the loop downstream, in order to avoid overcorrection of the same perturbation. The linear transport matrix between successive loops is measured continuously using natural beam orbit jitter.

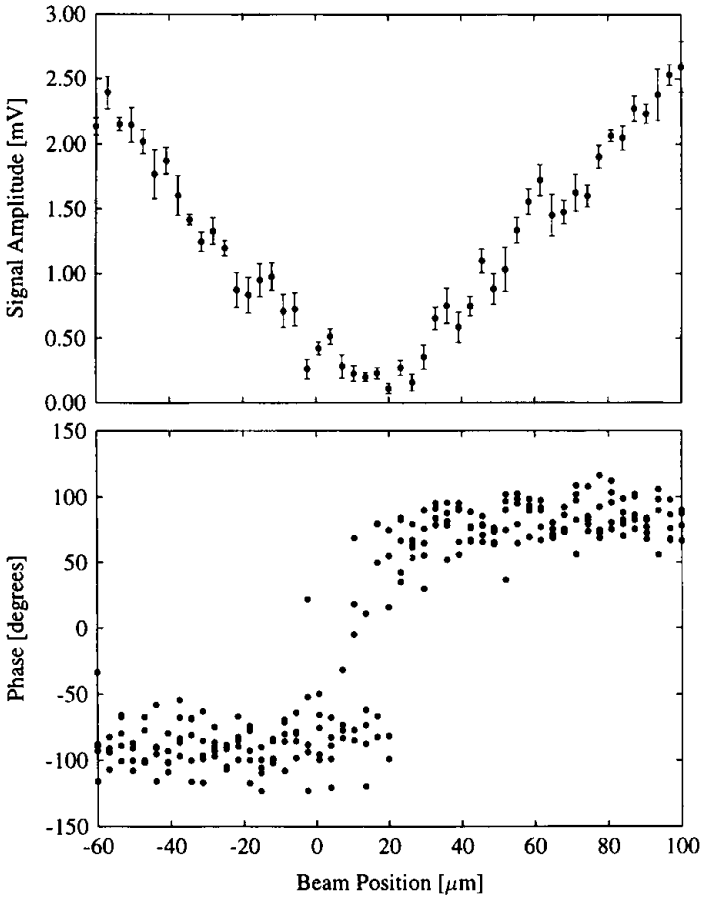

Figure 3.11: Amplitude (top) and phase (bottom) of the beam-induced dipole mode signal in an X-band accelerating structure versus the nominal beam position (arbitrary zero), which was varied by steering correctors[23]. (Courtesy M. Seidel, 1998).

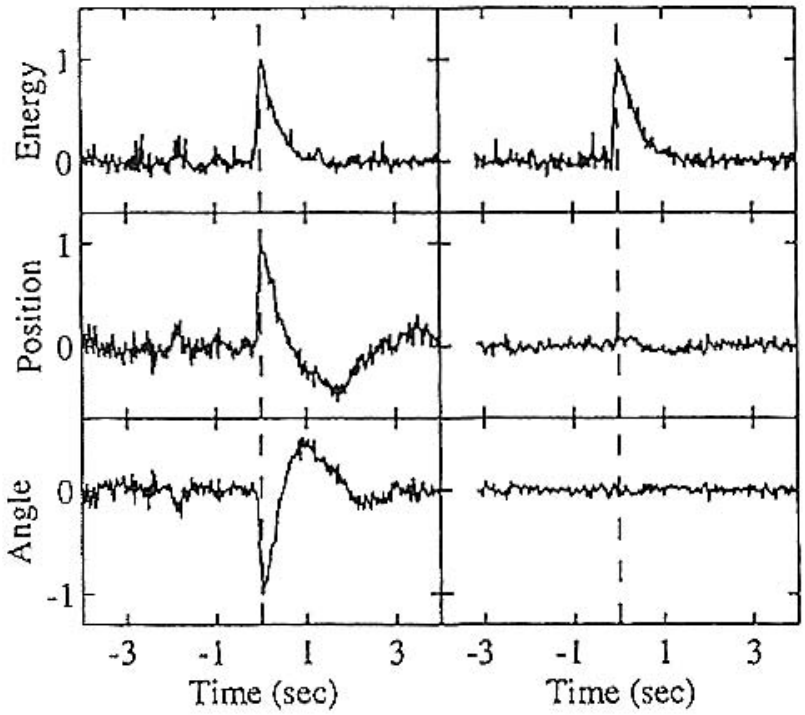

Figure 3.12: Response of the orbit and energy feedback in the ring-to-linac transfer line of the SLC to a fast step change in energy[24]: (left) before and (right) after additional BPMs were included in the feedback loop.

Ex.3.1. Design of an orbit feedback loop *Write an algorithm for orbit correction in one plane assuming uncoupled, linear transport in a transport line. Let the beam position be detected using two BPMs and use two fast corrector dipoles for implementing the desired deflections. Introduce (assumed known) relative phase advances and beta functions as needed to take into account phase differences between the correctors, between the BPMs, and between the correctors and BPMs.*

3.2 Beam Emittance and Emittance Preservation

The beam emittance represents the volume of the beam occupied in the six dimensional phase space $(x, x', y, y', \phi, \delta)$, where x and y are the transverse positions, x' and y' are the transverse angles, ϕ is the time-like variable representing the relative phase of the beam, and δ is the relative beam energy. Often one discusses a beam emittance with implicit reference to a particular plane of interest; i.e. the horizontal, vertical, or longitudinal emittance. In this section we describe not single particle transport, but transport of the beam as a whole. Next we outline methods used to measure the beam emittance and to parametrize the degree of mismatch using very commonly used wire scanners.

3.2.1 Single Wire Measurement of Beam Emittance

An (invasive[b].) measurement of the beam emittance can be performed by varying the field strength of a quadrupole located upstream of a single wire (or screen). The transfer matrix is $M = SQ$, where S is the known transfer matrix between the quadrupole and the wire, and Q is the transfer matrix of the quadrupole:

$$Q = \begin{pmatrix} 1 & 0 \\ k = \pm\frac{1}{f} & 1 \end{pmatrix} \tag{3.21}$$

in the thin-lens approximation for which the length of the quad is short compared to the focal length f. After multiplying the matrices, one obtains

$$M = \begin{pmatrix} S_{11} + kS_{12} & S_{12} \\ S_{21} + kS_{22} & S_{22} \end{pmatrix}. \tag{3.22}$$

Expanding the matrix product $\sigma = (SQ)\sigma_0(SQ)^T$ and equating the (11) element on both sides, the horizontal beam size is

[b] The measurement could be made nonivasive by simultaneously adjusting another quadrupole downstream of the wire scanner, so as to compensate for the change in the beta function induced by the first quadrupole

$$\begin{aligned}\sigma_{11}(=\langle x^2\rangle) &= ({S_{11}}^2\sigma_{11_0} + 2S_{11}S_{12}\sigma_{12_0} + {S_{12}}^2\sigma_{22_0}) \\ &+ (2S_{11}S_{12}\sigma_{11_0} + 2{S_{12}}^2\sigma_{12_0})k + {S_{12}}^2\sigma_{11}k^2, \qquad (3.23)\end{aligned}$$

which is quadratic in the field parameter k.

To make use of these results in an emittance measurement, the following procedure is often used:

1. For each value of quadrupole field strength k, the wire is scanned and the amplitude of the response measured by a detector is obtained as a function of wire position.
2. For each wire scan at fixed k, the distribution is fit with a Gaussian of the form

$$f(x) = f_0 + f_{max}e^{-\frac{(x-\langle x\rangle)^2}{2\langle x^2\rangle}}, \qquad (3.24)$$

where f_0 is the baseline level offset and f_{max} is the peak value of the Gaussian distribution.

3. The fitted beam size $\langle x^2\rangle$ is plotted as a function of k.
4. The result is fit with a parabola. One parametrization for the fit is

$$\begin{aligned}\sigma_{11} &= A(k-B)^2 + C \\ &= Ak^2 - 2ABk + (C + AB^2). \qquad (3.25)\end{aligned}$$

5. The σ matrix is reconstructed by equating coefficients:

$$A = S_{12}^2\sigma_{11}, \qquad (3.26)$$

$$-2AB = 2S_{11}S_{12}\sigma_{11} + 2S_{12}^2\sigma_{12}, \qquad (3.27)$$

$$C + AB^2 = {S_{11}}^2\sigma_{11} + 2S_{11}S_{12}\sigma_{12} + {S_{12}}^2\sigma_{22}, \qquad (3.28)$$

and solve for σ_{11}, σ_{12} $(= \sigma_{21})$, and σ_{22}. The results are

$$\sigma_{11} = \frac{A}{{S_{12}}^2}, \qquad (3.29)$$

$$\sigma_{12} = -\frac{A}{{S_{12}}^2}(B + \frac{S_{11}}{S_{12}}), \qquad (3.30)$$

$$\sigma_{22} = \frac{1}{{S_{12}}^2}[(AB^2 + C) + 2AB(\frac{S_{11}}{S_{12}}) + A(\frac{S_{11}}{S_{12}})^2]. \qquad (3.31)$$

6. The beam emittance is then calculated from the determinant of the beam matrix $\epsilon = \sqrt{\det\,\sigma}$ and the errors are propagated:

$$\det\,\sigma = \sigma_{11}\sigma_{22} - {\sigma_{12}}^2$$

$$= \frac{AC}{{S_{12}}^4} \tag{3.32}$$

so

$$\epsilon = \frac{\sqrt{AC}}{{S_{12}}^2}. \tag{3.33}$$

The above results also give the ellipse parameters α, β, and γ:

$$\beta = \frac{\sigma_{11}}{\epsilon} = \sqrt{\frac{A}{C}}, \tag{3.34}$$

$$\alpha = -\frac{\sigma_{12}}{\epsilon} = \sqrt{\frac{A}{C}}(B + \frac{S_{11}}{S_{12}}), \tag{3.35}$$

$$\gamma = \frac{1}{\epsilon} = \frac{{S_{12}}^2}{\sqrt{AC}}[(AB^2 + C) + 2AB(\frac{S_{11}}{S_{12}}) + A(\frac{S_{11}}{S_{12}})^2]. \tag{3.36}$$

As a check, the ellipse parameters should satisfy $\beta\gamma - 1 = \alpha^2$.

An example of emittance measurements in the two transverse planes x and y is shown in Fig. 3.13. The graphics output shows the square of the measured beam size in μm^2 as a function of the quadrupole field strength in $(\frac{kG}{m})m$. The first two rows in the text display show the measured emittance (ϵ_j) and the normalized emittance ($\gamma\epsilon_j$) with $j = x, y$. The unit designation "M-R" denotes mm-mrad; for example, the measured normalized emittances are $(3.0 \pm 0.4) \times 10^{-5}$ [m-rad] in x by $(4.00 \pm 0.04) \times 10^{-6}$ [m-rad] in y.

3.2.2 Multiple Wire Measurement of Beam Emittance

The beam emittance may be measured (in many applications noninvasively) using 3 wire scanners if there are no coupling elements or using 4 wire scanners wit coupling (in the latter case each wire scanner should be equipped with several wires oriented at different angles in the transverse plane, *e.g.*, a horizontal, a vertical and a 45° wire). The optimum wire locations for maximum sensitivity (without coupling) are such that the separation between wires correspond to a difference in betatron phase advance $\Delta\psi$ of $\frac{90^\circ}{N_w}$, where N_w is the number of wires used in the measurement. Letting σ_i denote the measured σ_{11}'s for wire i, and considering the case of 4 wires, the matrix equation to be solved is

$$\begin{pmatrix} \sigma_1 \\ \sigma_2 \\ \sigma_3 \\ \sigma_4 \end{pmatrix} = \begin{pmatrix} {c_1}^2 & 2c_1s_1 & {s_1}^2 \\ {c_2}^2 & 2c_2s_2 & {s_2}^2 \\ {c_3}^2 & 2c_3s_3 & {s_3}^2 \\ {c_4}^2 & 2c_4s_4 & {s_4}^2 \end{pmatrix} \begin{pmatrix} \sigma_{11} \\ \sigma_{12} \\ \sigma_{22} \end{pmatrix} = M_0 \begin{pmatrix} \sigma_{11} \\ \sigma_{12} \\ \sigma_{22} \end{pmatrix} \tag{3.37}$$

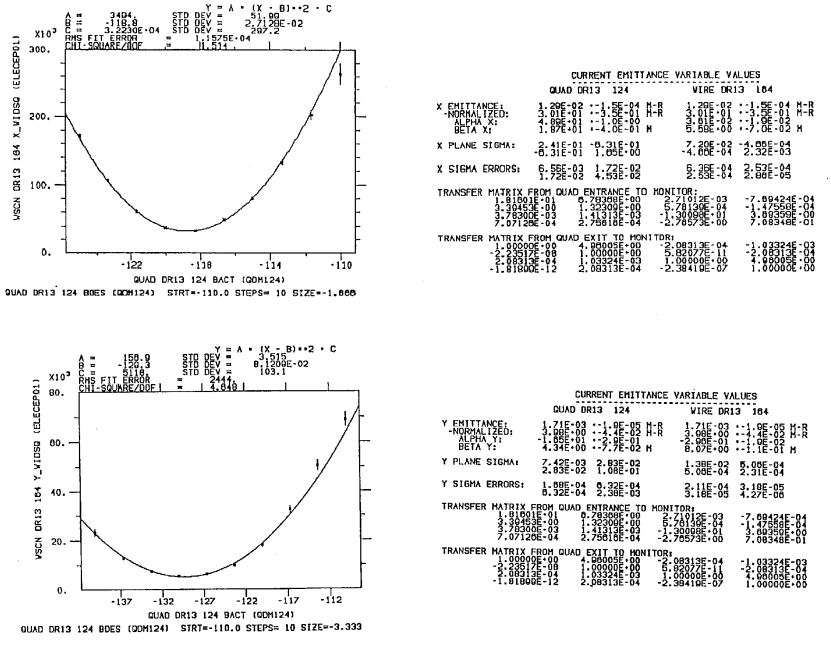

Figure 3.13: Example transverse beam emittance measurements using a single wire.

where c_i and s_i are the R_{11} and R_{12} transfer matrix elements from the point at which the beam matrix is defined to the location of the wire.
Notice that M need not be a square matrix. Rewriting Eq. (3.37) as $A = MC$, then $M^T A = M^T MC$, or $C = (M^T M)^{-1} M^T A$; that is,

$$\begin{pmatrix} \sigma_{11} \\ \sigma_{12} \\ \sigma_{22} \end{pmatrix} = (M^T M)^{-1} M^T \begin{pmatrix} \sigma_1 \\ \sigma_2 \\ \sigma_3 \\ \sigma_4 \end{pmatrix}, \tag{3.38}$$

which in a least-squares sense gives the beam matrix elements (σ_{ij}) in terms of the measured sigmas.

A possible procedure for the multiple wire emittance measurement is as follows:
1. Each wire is scanned to obtain detector counts as a function of wire position x.
2. For each wire scan, the distribution is fit with a Gaussian using Eq. (3.24).
3. The σ matrix is reconstructed using Eq. (3.37), the transfer matrix elements M_i from the model, and the σ_i from the measurements.

4. The emittance is calculated $\epsilon = \sqrt{\det \sigma}$.
5. The ellipse parameters $\alpha = -\frac{\sigma_{12}}{\epsilon}$, $\beta = \frac{\sigma_{11}}{\epsilon}$, and $\gamma = \frac{\sigma_{22}}{\epsilon}$ are calculated, if desired.

3.2.3 Graphics

Increased operational efficiency may be obtained from meaningful graphical representation of the experimental data. In the multiple wire emittance measurement it is useful to project the measurements to a single point along the accelerator and to plot the normalized phase space. The emittance ϵ, multiplied by π, corresponds to the area of the ellipse parametrized by

$$\epsilon = \gamma x^2 + 2\alpha x x' + \beta x'^2. \tag{3.39}$$

Since $\beta\gamma = 1 + \alpha^2$,

$$\begin{aligned} \epsilon &= \frac{1}{\beta}[x^2 + (\alpha x + \beta x')^2] \\ &= \frac{1}{\beta}(x^2 + p_x{}^2), \end{aligned} \tag{3.40}$$

where $p_x = \alpha x + \beta x'$ is the orthogonal coordinate to x.

A useful representation of the data may be obtained with the following procedure. In this representation, the data are shown in normalized phase space for direct viewing of deviations from design. The wire orientations are also plotted to show the phase space coverage by the wires.
1. Plot the design, rms ellipse in the phase space (a circle)

$$\left(\frac{x}{\sqrt{\beta}}, \frac{\alpha x + \beta x'}{\sqrt{\beta}}\right) \tag{3.41}$$

at some reference point s along the trajectory. Normalize the design ellipse to unit radius.
2. Plot also the ellipse obtained from the measurements of the ellipse parameters at the reference point. Apply same normalization as in step 1.
3. Using the lattice model, for each wire project its orientation back to the reference point and add the result to the figure; that is, for each point along the wire $(x, x')_w$, do an inverse mapping to the reference point

$$\begin{pmatrix} x \\ x' \end{pmatrix}_{refpoint} = M^{-1} \begin{pmatrix} x \\ x' \end{pmatrix}_w. \tag{3.42}$$

The display should summarize the measurements which might include the measured and expected beam widths at each of the wires, the measured and design beam emittance, and the beam intensity. Also, a measure of the degree of "mismatch" is useful. This will be further discussed in the next section.

An example of these graphics is shown in Fig. 3.14. The raw data are given in Fig. 3.15. From Fig. 3.14 it is immediately obvious that while the measured ellipse has roughly the same emittance as the design circle (the horizontal emittance is 208.8 ± 9.9 [mm-mrad] compared to the design of 200 [mm-mrad], the vertical emittance is $323 \pm$ 26.7 [mm-mrad] compared to the design of 200 [mm-mrad]), the ellipse orientation is incorrect. As will be shown in the next section, if this beam were allowed to propagate uncorrected, the final emittance titled $B_{mag}\epsilon$ would be $390.0 \pm$ 10.2 [mm-mrad] in x and 543.3 ± 13.2 [mm-mrad] in y. The emittance dilution factor B_{mag} represents the degree of the mismatch. From Fig. 3.14 can be deduced immediately the degree of phase space coverage spanned by the wires. In the horizontal plane, for example, the wire orientations are about $0°$, $-45°$, $-22.5°$, and $-67.5°$, which is ideal for this 4-wire measurement from the SLC linac.

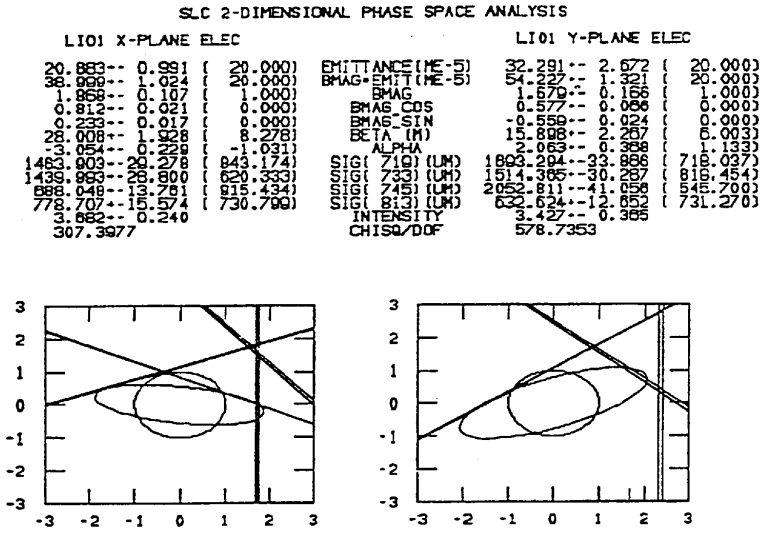

Figure 3.14: Graphics output of multiple wire transverse beam emittance measurement in the SLC linac.

The "measured ellipse", that is the ellipse that was reconstructed from the individual wire scans based on the measured beam widths and the model-dependent transport matrices, does not represent in this case a true rms of the distribution as can be seen by inspection of the raw data shown in Fig. 3.15. For more complex beam distributions, a better characterization is achieved by using an "asymmetric Gaussian" distribution in which the left and right hand sides of the measured beam profile are fit

independently with two separate Gaussians. The fitting function[26] is

$$f(x) = f_0 + f_{max} e^{\left[-\frac{(x-\langle x\rangle)^2}{2\langle x^2\rangle(1+\alpha[\mathrm{sign}(x-\langle x\rangle)])}\right]} \tag{3.43}$$

where α represents an asymmetry factor and is zero for a perfect Gaussian. The σ for the left and right hand sides of the fitted distribution are $\sigma = \langle x^2\rangle(1 \pm \alpha)$. For the ellipse reconstruction the average σ was used. When large tails are present in the raw data this more accurately represents the beam distribution. Based on the raw data it is clear however that even with the more sophisticated fitting algorithm, the fit only marginally represents the actual distributions.

For reasonably well "matched" beams, the graphical summary display is most useful. In this example however, the raw data are more revealing: the "double-humps" in the raw data are characteristic of an upstream error; a beam, if kicked transversely will filament (lose coherency due to the natural spread in the phase advance) resulting in an increased emittance and the double-humps.

If a wire is mounted at 45° with respect to x and y (a "u-plane" wire), then it is also possible to measure the coupling between x and y. The full σ-matrix is

$$\sigma = \begin{pmatrix} \sigma_{11} & \sigma_{12} & \sigma_{13} & \sigma_{14} \\ \sigma_{21} & \sigma_{22} & \sigma_{23} & \sigma_{24} \\ \sigma_{31} & \sigma_{32} & \sigma_{33} & \sigma_{34} \\ \sigma_{41} & \sigma_{42} & \sigma_{43} & \sigma_{44} \end{pmatrix}, \tag{3.44}$$

where for example σ_{14} represents the coupling between between x and y'. Notice that $\sigma_{14} \neq \sigma_{23}$. Whereas for the single plane, uncoupled beam matrix reconstruction a minimum of 3 measurements are required, to fully reconstruct the coupled beam matrix a total of 10 measurements is needed. This includes the 3 measurements in the x plane, 3 in the y plane, and 4 in the u plane. An example of a coupled emittance measurement is presented in Figs. 13-16. In this case the raw data are well fit by a Gaussian. In the text of Fig. 3.16, the parameters ϵ_1 and ϵ_2 represent the emittance one would measure in the absence of coupling. They are in good agreement with the measured projected emittances ϵ_x and ϵ_y, which indicates that, in this example, the coupling is small.

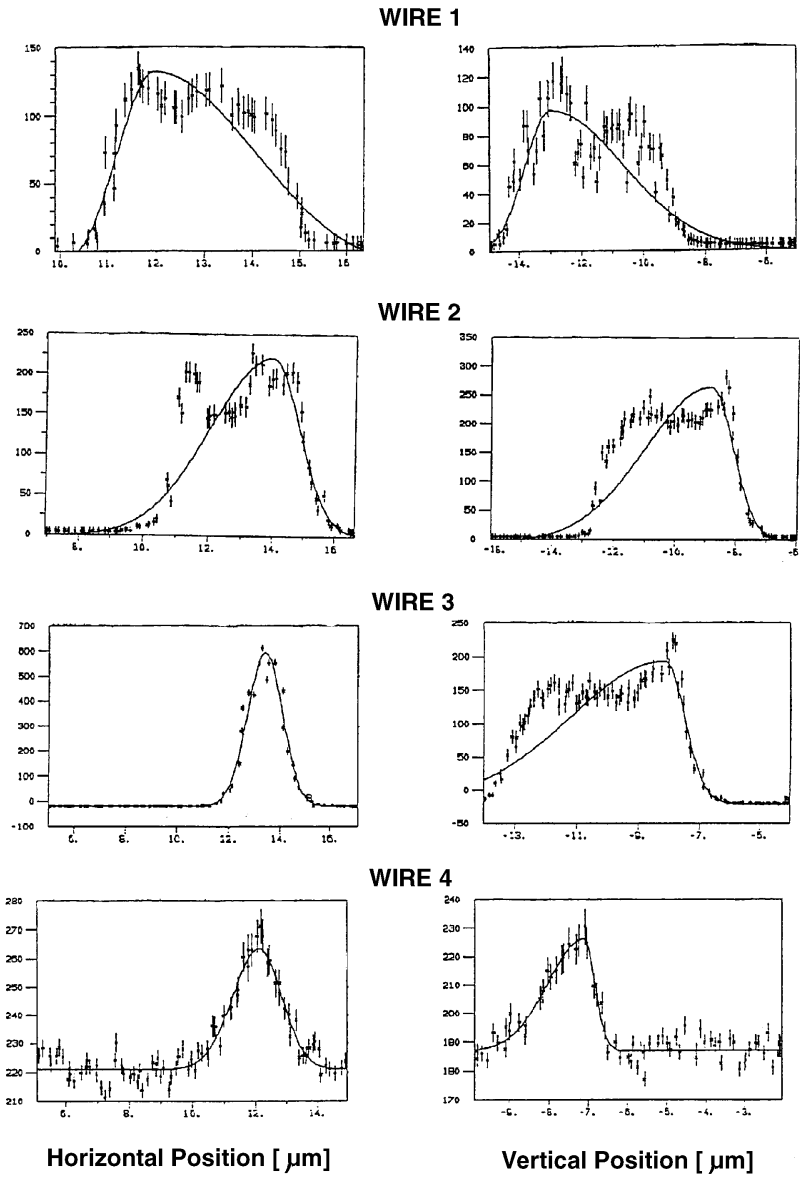

Figure 3.15: Raw data showing individual wire scans used in summary display of Fig. 3.14 and "asymmetric Gaussian" fits (cf. Eq. 3.43).

Four Dimensional Phase Space Analysis — LI02 ELEC 2.9E10/bunch

epsilon_x	= 2.20	+-1.42E-02	epsilon_y	= 1.89	+-1.72E-02
epsilon-b_x	= 2.23	+-1.15E-02	epsilon-b_y	= 1.95	+-2.05E-02
Bmag_x	= 1.01	+-********	Bmag_y	= 1.03	+-3.03E-03
Bmag_cos_x	= 6.355E-02	+-1.13E-02	Bmag_cos_y	= 0.248	+-1.12E-02
Bmag_sin_x	= 0.152	+-1.50E-02	Bmag_sin_y	= 3.112E-02	+-2.90E-02
beta_cos_x	= 1.08	+-1.44E-02	beta_cos_y	= 1.29	+-1.37E-02
beta_sin_x	= 0.154	+-1.41E-02	beta_sin_y	= 3.214E-02	+-3.00E-02
theta_1/deg	= -11.8	+-0.00E+00	theta_2/deg	= -12.6	+-0.00E+00
theta_3/deg	= -20.5	+-0.00E+00	theta_4/deg	= 11.7	+-0.00E+00
tr(CC')	= 0.245	+-0.00E+00	det C	=-0.114	+-0.00E+00
epsilon_1	= 2.13	+-0.00E+00	epsilon_2	= 1.71	+-0.00E+00
-det G+	= 3.265E-02	+-0.00E+00	psi+/deg	= -126.	+-0.00E+00
det G-	= 0.128	+-0.00E+00	psi-/deg	= -89.4	+-0.00E+00
tr(BB')	= 0.358	+-0.00E+00	det B	= 0.104	+-0.00E+00

Figure 3.16: 4-dimensional emittance measurement summary.

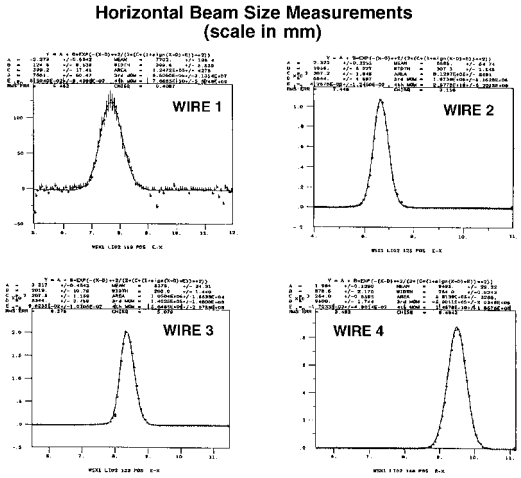

Figure 3.17: Raw data in x-plane corresponding to 4-D measurement of Fig. 3.16.

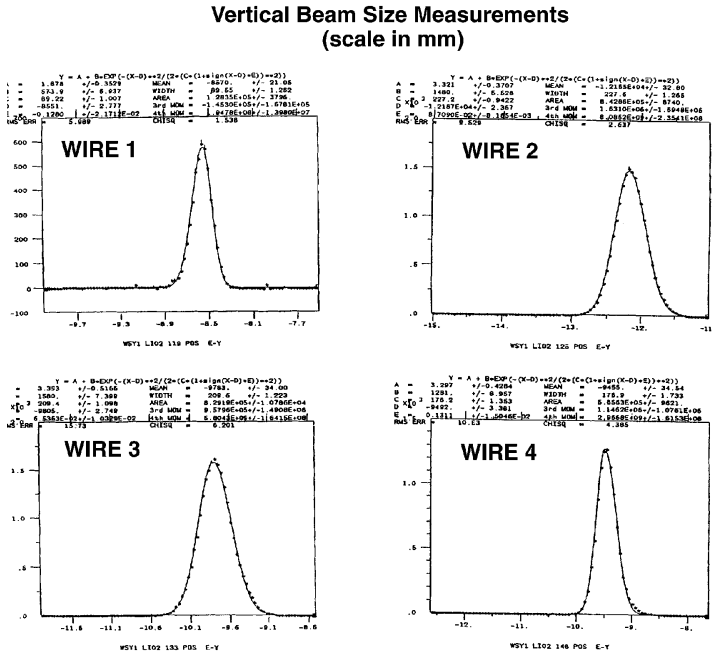

Figure 3.18: Raw data in y-plane corresponding to 4-D measurement of Fig. 3.16.

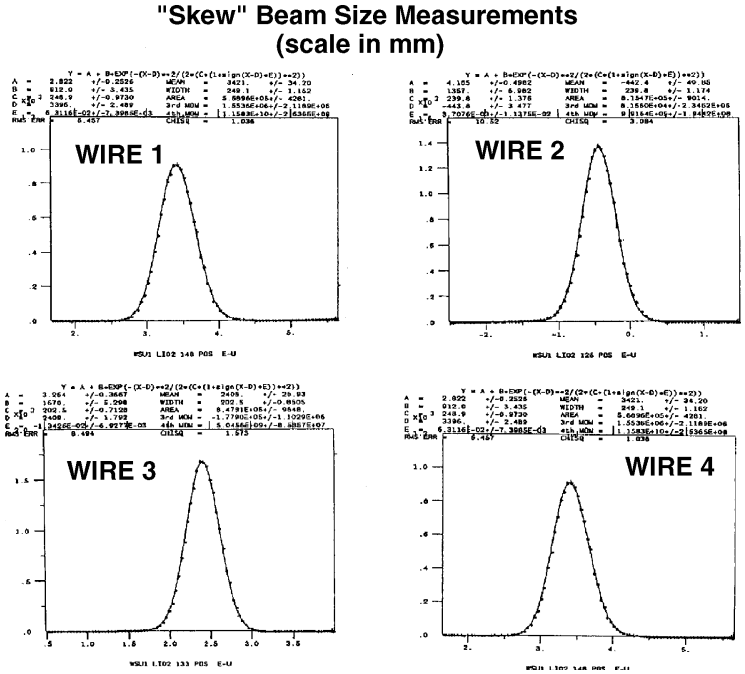

Figure 3.19: Raw data in u-plane corresponding to 4-D measurement of Fig. 3.16.

3.2.4 Emittance Mismatch

In this section we begin by explicitly computing, in two dimensions, the transverse position and angle using the general form of the beam transfer matrix for a periodic lattice. The results are used to calculate the individual elements of the beam transfer matrix and to derive an expression for the mismatch parameter B_{mag}. The mismatch parameter is well suited for analysis in circular machines for which the periodicity is implicit. We will see that the same formalism is useful in describing emittance transport in linear accelerators and transport lines as well.

Derivation of Beam Matrix Elements

Recalling from Eq. 1.18, the beam matrix obtained after subtracting out the contribution from the mean of the beam distribution is

$$\sigma = \begin{pmatrix} \langle x^2 \rangle & \langle xx' \rangle \\ \langle xx' \rangle & \langle x'^2 \rangle \end{pmatrix}. \tag{3.45}$$

The point-to-point transfer matrix is

$$M = \begin{pmatrix} \sqrt{\frac{\beta}{\beta_0}}(\cos\psi + \alpha_0 \sin\psi) & \sqrt{\beta\beta_0}\sin\psi \\ \frac{\alpha_0-\alpha}{\sqrt{\beta\beta_0}}\cos\psi - \frac{1+\alpha\alpha_0}{\sqrt{\beta\beta_0}}\sin\psi & \sqrt{\frac{\beta}{\beta_0}}(\cos\psi - \alpha\sin\psi) \end{pmatrix}, \tag{3.46}$$

where α and β are the ellipse parameters at a point s from the observation point which is denoted by the subscript 0. Here ψ is the phase advance between the reference point and the observation point and is equal to

$$\psi = \int \frac{ds}{\beta}. \tag{3.47}$$

For a periodic lattice for which $\alpha = \alpha_0$ and $\beta = \beta_0$, the periodic point-to-point transfer matrix M_{per} is

$$M_{\mathrm{per}} = \begin{pmatrix} \cos\psi + \alpha_0 \sin\psi & \beta_0 \sin\psi \\ -\gamma_0 \sin\psi & \cos\psi - \alpha_0 \sin\psi \end{pmatrix}. \tag{3.48}$$

The beam matrix elements after n iterations through the periodic lattice are

$$\begin{aligned} \langle x^2 \rangle_n &= \langle x^2 \rangle_0 {M_{11}}^2 + 2\langle xx' \rangle_0 M_{11}M_{12} + \langle x'^2 \rangle_0 {M_{12}}^2 \\ \langle xx' \rangle_n &= \langle x^2 \rangle_0 M_{11}M_{21} + \langle xx' \rangle_0 [M_{11}M_{22} + M_{12}M_{21}] \end{aligned} \tag{3.49}$$

$$+ \quad \langle x'^2\rangle_0 M_{12} M_{22} \tag{3.50}$$

$$\langle x'^2\rangle_n = \langle x^2\rangle_0 {M_{21}}^2 + 2\langle x x'\rangle_0 M_{21} M_{22} + \langle x'^2\rangle_0 {M_{22}}^2. \tag{3.51}$$

After substitution of the matrix elements of Eq. (3.48) into Eqs. (3.50-3.51), and using $\cos 2\psi = \cos\psi^2 - \sin\psi^2$ and $\sin 2\psi = 2\sin\psi\cos\psi$,

$$\begin{aligned}\langle x^2\rangle_n &= \frac{1}{2}[\langle x^2\rangle_0 + \langle(\alpha x_+ \beta x_0')^2\rangle] \\ &+ \frac{1}{2}[\langle x^2\rangle_0 - \langle(\alpha x_0 + \beta x_0')^2\rangle]\cos 2\psi \\ &+ [\alpha\langle x^2\rangle_0 + \beta\langle x x'\rangle_0]\sin 2\psi,\end{aligned} \tag{3.52}$$

$$\begin{aligned}\langle x'^2\rangle_n &= \frac{1}{2}[\langle x^2\rangle_0 + \langle(\alpha x_+ \gamma x_0')^2\rangle] \\ &+ \frac{1}{2}[\langle x^2\rangle_0 - \langle(\alpha x_0 + \gamma x_0')^2\rangle]\cos 2\psi \\ &- [\alpha\langle x'^2\rangle_0 + \gamma\langle x x'\rangle_0]\sin 2\psi,\end{aligned} \tag{3.53}$$

$$\begin{aligned}\langle x x'\rangle_n &= \frac{1}{2}[-\alpha\gamma\langle x^2\rangle_0 - \beta\gamma\langle x x'\rangle_0 - \alpha\beta\langle x'^2\rangle_0] \\ &+ [\frac{\alpha\gamma}{2}\langle x^2\rangle_0 + (1 + \frac{\beta\gamma}{2})\langle x x'\rangle_0 + \frac{\alpha\beta}{2}\langle x'^2\rangle_0]\cos 2\psi \\ &+ \frac{1}{2}[-\gamma\langle x^2\rangle_0 + \beta\langle x'^2\rangle_0]\sin 2\psi.\end{aligned} \tag{3.54}$$

Next, let

$$a = \frac{\beta}{2}[\gamma\langle x^2\rangle_0 + 2\alpha\langle x x'\rangle_0 + \beta\langle x'^2\rangle_0] \tag{3.55}$$

$$b = \frac{\beta}{\gamma}a \tag{3.56}$$

$$c = -\frac{\alpha}{\beta}a \tag{3.57}$$

and use

$$c_1\cos 2\psi + c_2\sin 2\psi = \sqrt{{c_1}^2 + {c_2}^2}\cos(2\psi - \chi), \text{ with } \chi = \tan^{-1}\left(\frac{c_2}{c_1}\right). \tag{3.58}$$

Then,

$$\langle x^2\rangle_n = a + \sqrt{a^2 - \beta^2(\langle x^2\rangle_0\langle x'^2\rangle_0 - \langle x x'\rangle_0^2}\cos(2\psi - \chi_{\langle x^2\rangle_0}), \tag{3.59}$$

$$\langle x'^2\rangle_n = b + \sqrt{b^2 - \gamma^2(\langle x^2\rangle_0\langle x'^2\rangle_0 - \langle xx'\rangle_0^2}\cos(2\psi - \chi_{\langle x'^2\rangle_0}), \text{ and} \quad (3.60)$$

$$\langle xx'\rangle_n = c + \sqrt{(\langle xx'\rangle_0 - c)^2 + (-\frac{\gamma}{2}\langle x^2\rangle_0 + \frac{\beta}{2}\langle x'^2\rangle_0)^2}\cos(2\psi - \chi_{\langle xx'\rangle_0}). \quad (3.61)$$

Note that since $\epsilon = \sqrt{\det\sigma}$ is an invariant in the absence of filamentation,

$$\langle x^2\rangle_n\langle x'^2\rangle_n - \langle xx'\rangle_n = \langle x^2\rangle_0\langle x'^2\rangle_0 - \langle xx'\rangle_0. \quad (3.62)$$

The Mismatch Parameter[27] B_{mag}

Dividing both sides of Eq. (3.59) by $\beta\epsilon_0 = \beta\sqrt{\langle x^2\rangle_0\langle x'^2\rangle_0 - \langle xx'\rangle_0}$, we have

$$\begin{aligned}\frac{\langle x^2\rangle_n}{\beta\epsilon_0} &= \frac{\frac{a}{\beta}}{\sqrt{\langle x^2\rangle_0\langle x'^2\rangle_0 - \langle xx'\rangle_0^2}} \\ &+ \sqrt{\left(\frac{\frac{a}{\beta}}{\sqrt{\langle x^2\rangle_0\langle x'^2\rangle_0 - \langle xx'\rangle_0^2}}\right)^2 - 1}\ \cos(2\psi - \chi_{\langle x^2\rangle_0}) \\ &= \mathrm{B}_{mag} + \sqrt{\mathrm{B}_{mag}^2 - 1}\cos(2\psi - \chi_{\langle x^2\rangle_0}), \end{aligned} \quad (3.63)$$

where the mismatch parameter B_{mag} is defined as

$$\mathrm{B}_{mag} = \frac{\frac{a}{\beta}}{\sqrt{\langle x^2\rangle_0\langle x'^2\rangle_0 - \langle xx'\rangle_0}}. \quad (3.64)$$

With the ellipse parameters α, β, and γ representing those for the steady-state or equilibrium beam distribution, then

$$\mathrm{B}_{mag} = \frac{1}{2}\frac{[\gamma_n\langle x^2\rangle_0 + 2\alpha_n\langle xx'\rangle_0 + \beta_n\langle x'^2\rangle_0]}{\sqrt{\langle x^2\rangle_0\langle x'^2\rangle_0 - \langle xx'\rangle_0}} \quad (3.65)$$

i.e. B_{mag} is the ratio of the area of the decohered beam to the area of the injected beam. The factor of 2 results from the numerator representing an rms area.

Examples of Emittance Dilution due to Mismatch

Emittance dilution results if $\mathrm{B}_{mag} \neq 1$ due to the difference in the transverse phase advance of the particles within the bunch. There are multiple sources of such phase advance variations. The two most commonly considered sources depend on the chromaticity and the amplitude of the betatron oscillations. The chromaticity $\xi = \Delta\psi/\psi\delta$ characterizes the energy dependence of the phase advance where $\Delta\psi$ is the difference in the phase advance of a particle from the mean phase advance of the bunch and δ is the relative energy deviation of that particle compared to the mean energy of the bunch. The amplitude dependence of the phase advance due to sextupole and higher-order magnetic fields is

$$2\pi\psi = 2\pi\psi_0 + \mu a^2, \tag{3.66}$$

where ψ_0 is the phase advance for the on-axis particle, μ characterizes the amplitude of the quadrupole field, and a is the distance from the center of the magnet to the particle. Less commonly considered sources for phase advance variations include wakefield focussing for high current beams, focussing due to ions, and focussing due to the beam-beam tune shift in colliding beam accelerators.

a) Periodic Lattice

Let the length of the lattice period be L. Then, as shown in Fig. 3.20, for $\mathrm{B}_{mag} = 1$, the beam always fills the same area in phase space after each lattice period. The rms area of the ellipse is

$$\langle x^2 \rangle_n = \beta\epsilon_0 \tag{3.67}$$

and the beam is said to be matched. Under these conditions, no emittance dilution will occur. In particular, since $\langle x^2 \rangle_n$ is independent of the phase advance ψ, the phase space area is unchanged even if the phase of each of the particles in the beam advances differently.

For $\mathrm{B}_{mag} > 1$, then

$$\begin{aligned} \epsilon_n &= \frac{\langle x^2 \rangle_n}{\beta} \\ &= \epsilon_0[\mathrm{B}_{mag} + \sqrt{{\mathrm{B}_{mag}}^2 - 1}\cos(2\psi - \chi_{\langle x^2 \rangle_0})] \end{aligned} \tag{3.68}$$

as shown in Fig. 3.21. The solid, small ellipse represents the matched ($\mathrm{B}_{mag} = 1$) ellipse. The shaded ellipse represents the (1σ) rms distribution of the mismatched beam. During the first few traversals of identical lattice segments, the phase advance variations of the different particles may not be obvious. As n approaches infinity, however, the phase advance variations lead to a smearing in the transverse phase space resulting in a larger emittance. This is represented by the area occupied by the shaded ellipse as given by Eq. (3.63).

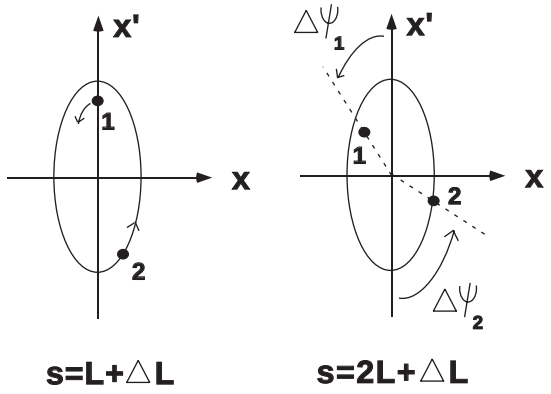

Figure 3.20: Horizontal phase space for a matched beam in a periodic lattice.

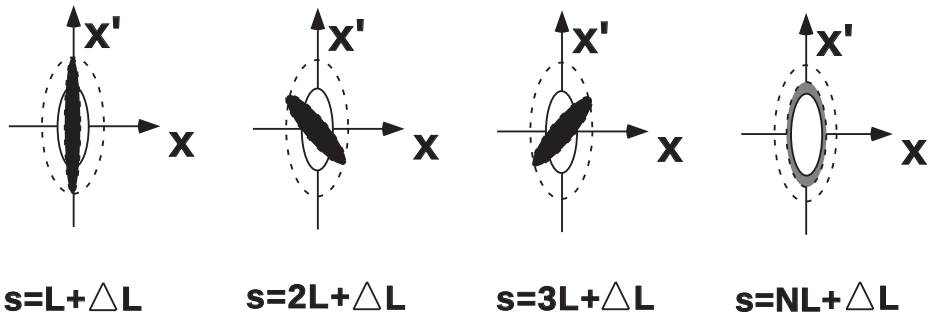

Figure 3.21: Horizontal phase space for a mismatched beam in a periodic linear lattice.

b) Circular Lattice

For a circular accelerator, the periodicity is usually taken to be not the superperiodicity of the machine (i.e. the number of identical lattice sections), but the revolution period. The index n therefore represents turn number. The mismatch B_{mag} most often arises from improper orientation of the beam ellipse at injection. Neglecting the static phase offset $\chi_{\langle x^2\rangle_0}$ in Eq. (3.63), the equilibrium emittance is

$$\epsilon_n = \frac{\langle x^2\rangle_n}{\beta} = \epsilon_0[\mathrm{B_{mag}} + \sqrt{\mathrm{B_{mag}}^2 - 1}]\cos(4\pi\nu), \tag{3.69}$$

where the phase advance per turn is $\nu = 2\pi\psi$. Shown in Fig. 3.22 is the evolution of the transverse phase space for B_{mag} along with the projections onto the horizontal axis. With a turn-by-turn beam size monitor, the consequences of a mismatch can be measured directly by detecting the beam size changes at every turn.

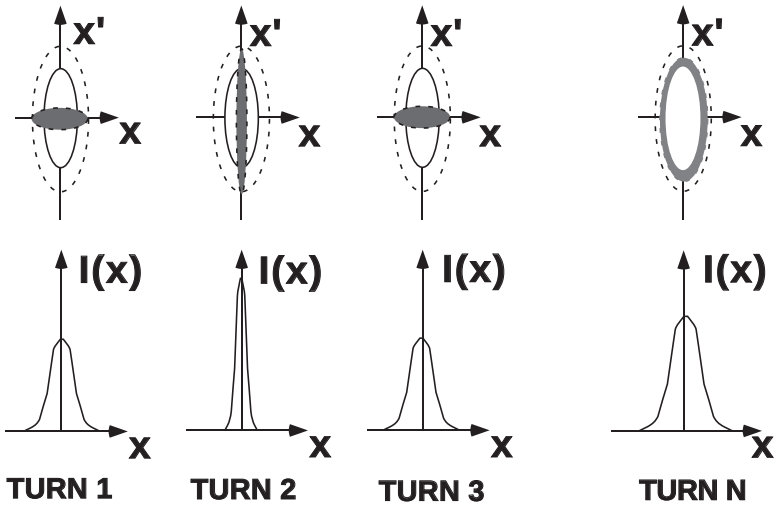

Figure 3.22: Horizontal phase space and x-projection for a mismatched beam in a circular accelerator.

3.3 Beta Matching in a Transport Line or Linac

The beam size (squared) at the location s can be expressed in terms of the α and β functions and the emittance at an upstream location s_0 as

$$< x^2(s) >= R_{11}^2\beta(s_0)\epsilon - 2R_{12}R_{11}\alpha(s_0)\epsilon + R_{12}^2\gamma(s_0)\epsilon \tag{3.70}$$

In a quadrupole scan, the transfer matrix elements R_{11} and R_{12} are varied, by changing the strength of a quadrupole between s_0 and s. Beam-size measurements for at least 3 different quadrupole settings are required in order to solve for the three independent unknown parameters: ϵ, $\beta(s_0)$ and $\alpha(s_0)$. The fourth parameter, $\gamma(s_0)$ is not free, but determined by $\alpha(s_0)$ and $\beta(s_0)$: $\gamma = (1+\alpha^2)/\beta$.

A multi-wire (or multi-screen) emittance measurement is very similar. Here, the quadrupole gradients stay constant, but the R matrices between s_0 and the different wire scanners (or other beam-size monitors) are different. Again, at least 3 measurements are required.

Either case can be described by a matrix equation of the form:

$$\begin{pmatrix} \sigma_x^{(1)2} \\ \sigma_x^{(2)2} \\ \sigma_x^{(3)2} \\ \cdots \\ \sigma_x^{(n)2} \end{pmatrix} = \begin{pmatrix} R_{11}^{(1)2} & 2R_{11}^{(1)}R_{12}^{(1)} & R_{12}^{(1)2} \\ R_{11}^{(2)2} & 2R_{11}^{(2)}R_{12}^{(2)} & R_{12}^{(2)2} \\ R_{11}^{(3)2} & 2R_{11}^{(3)}R_{12}^{(3)} & R_{12}^{(3)2} \\ \cdots & & \\ R_{11}^{(n)2} & R_{11}^{(n)}R_{12}^{(n)} & R_{12}^{(n)2} \end{pmatrix} \begin{pmatrix} \beta(s_0)\epsilon \\ -\alpha(s_0)\epsilon \\ \gamma(s_0)\epsilon \end{pmatrix} \tag{3.71}$$

where the superindex on the right hand-side refers to the different measurements, *i.e.*, it either corresponds to the setting of some quadrupole magnet, in case of a quadrupole scan, or to a different wire scanner or monitor, in case of a multi-wire emittance measurement. At least 3 measurements are required ($N \geq 3$) in order to solve for the three independent parameters ϵ, $\beta(s_0)$ and $\alpha(s_0)$.

To simplify the notation, let us denote the $n \times 3$ matrix on the right-hand side of Eq. (3.71) as $\mathbf{B}$, the n-component vector on the left side by $\mathbf{\Sigma}_x = (\sigma_x^{(1)2}, ..., \sigma_x^{(n)2})$, and the 3-component vector on the far right by

$$\mathbf{o} = (\beta(s_0)\epsilon, -\alpha(s_0)\epsilon, \gamma(s_0)\epsilon). \tag{3.72}$$

The equation then reads:

$$\mathbf{\Sigma}_x = \mathbf{B} \cdot \mathbf{o} \tag{3.73}$$

The problem of determining the elements of the vector $\mathbf{o}$ can be solved by a simple least-squares fit. We have to minimize the sum

$$\chi^2 = \sum_{l=1}^{n} \frac{1}{\sigma^2_{\Sigma_x^{(l)}}} \left(\Sigma_x^{(l)} - \sum_{i=1}^{3} B_{li} o_i \right)^2 \tag{3.74}$$

where $\sigma_{\Sigma_x^{(l)}}$ denotes the rms error of $\Sigma_x^{(l)} = \sigma_x^{(l)2}$. This error is obtained from the fit to the lth wire scan which determines the rms beam size $\sigma_x^{(l)}$.

We find it convenient to normalize the coordinates $\Sigma^{(l)}$ so that the rms error is 1:

$$\hat{\Sigma}_x^{(l)} = \frac{\Sigma_x^{(l)}}{\sigma_{\Sigma_x^{(l)}}} \tag{3.75}$$

$$\hat{B}_{li} = \frac{B_{li}}{\sigma_{\Sigma_x^{(l)}}} \tag{3.76}$$

Forming a symmetric $n \times n$ covariance matrix

$$\mathbf{T} = (\hat{\mathbf{B}}^T \cdot \hat{\mathbf{B}})^{-1} \tag{3.77}$$

the least-squares solution to Eq. (3.73) reads:

$$\mathbf{o} = \mathbf{T} \cdot \hat{\mathbf{B}}^T \cdot \hat{\mathbf{\Sigma}}_x^{(l)} \tag{3.78}$$

and the error of any scalar function $f(\mathbf{o})$ is given by

$$\sigma(f)^2 = (\nabla_{\mathbf{o}} f)^T \cdot \mathbf{T} \cdot (\nabla_{\mathbf{o}} f). \tag{3.79}$$

In particular, the errors of the parameters $\mathbf{o}$ themselves are

$$\sigma_{o_i} = \sqrt{T_{ii}} \tag{3.80}$$

Once the components of $\mathbf{o}$ are known, we still need to perform a simple nonlinear transformation to infer ϵ, β, and α:

$$\epsilon = \sqrt{o_1 o_3 - o_2^2} \tag{3.81}$$

$$\beta = o_1 / \epsilon \tag{3.82}$$

$$\alpha = -o_2 / \epsilon \tag{3.83}$$

The error propagation is straightforward, using Eq. (3.79).

The deviation of the β, α, and γ from the design parameters β_0, α_0 and γ_0 is often characterized in terms of the `B_{mag}' (β matching) parameter[27,28]:

$$\mathrm{B}_{mag} = \frac{1}{2} \left(\beta\gamma_0 - 2\alpha\alpha_0 + \gamma\beta_0\right) \tag{3.84}$$

The parameter B_{mag} has an important physical meaning. If a beam is injected into a ring or linac with a mismatch, the beam will filament until its distribution approaches a shape that is matched to the ring or the linac lattice. However, the filamentation causes the beam emittance to increase, such that, after complete filamentation, the emittance is given by the product of B_{mag} and the initial value of ϵ.

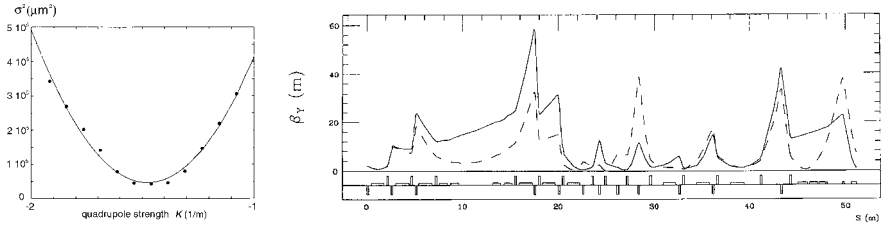

Figure 3.23: Beta matching in the KEK/ATF BT[29]: (left) quadrupole-scan emittance measurement; shown is the square of the vertical beam size on a profile monitor vs. the strength of an upstream quadrupole; (right) the vertical beta function obtained by propagating the measured twiss parameters (solid) through the actual BT optics is compared with the beta function expected for the design optics (dashed).

Ex.3.2. Beta mismatch

Suppose a beam is injected with a distribution characterized by optical functions β, α and γ different from the matched values β_0, α_0 and γ_0. Show that the beam emittance after filamentation is given by $\epsilon = \mathrm{B}_{mag}\ \epsilon_0$, where ϵ_0 is the initial emittance of the injected beam, and B_{mag} was defined in Eq. (3.84). Hint: filamentation corresponds to a randomization of the betatron phase and $\epsilon = \langle I \rangle$.

Once the values of β and α are known, quadrupole magnets can be adjusted so as to match the optical functions at a selected point to their design value, which is equivalent to Bmag=1. The above procedure also provides an absolute measure of the emittance. The SLC has more than 10 multi-wire emittance measurement stations, which monitor the beam emittances in various parts of the machine in hourly intervals, and are indispensable for emittance control and tuning. For example, in the SLC linac transverse orbit bumps are intentionally induced as a global correction which cancels the accumulated local effects of dispersion or wakefields. The bumps are optimized by minimizing the emittance downstream, as calculated by this measurement technique.

Example

To illustrate the beta matching method, Fig. 3.23 shows an example from the KEK/ATF beam transport line (BT), connecting the S-band linac and the ATF damping ring. The left picture shows the result of a typical quadrupole scan at the end of the BT. Plotted is the square of the vertical beam size versus the strength of an upstream quadrupole, as well as a quadratic fit to the data. We can propagate the twiss parameters deduced from such a fit through the BT, using a model derived from the actual or the design magnet settings. The right picture displays the inferred beta functions.

Ex.3.3. Propagation of Twiss parameters
In Fig. 3.16, the Twiss parameters were measured at a single location yet the `measured' values are shown as a function of position along the transport line. Derive the matrix for propagation of the Twiss parameters from a known location to an arbitrary location along the transport line. Hint: use the equation for the phase space ellipse

$$\gamma x^2 + 2\alpha x x' + \beta x'^2 = \epsilon, \tag{3.85}$$

the definition $\beta\gamma - \alpha^2 = 1$ *and the* 2×2 *trasport matrix of the form*

$$\begin{pmatrix} x \\ x' \end{pmatrix} = \begin{pmatrix} C(s) & S(s) \\ C(s)' & S(s)' \end{pmatrix} \begin{pmatrix} x_0 \\ x_0{}' \end{pmatrix} \tag{3.86}$$

3.4 References

1. E. Courant, reference unknown.
2. J. Turner, private communication (1998).
3. T. Barklow, P. Emma, P. Krejcik, N. Walker, "Review of Lattice Measurement Techniques at the SLC", presented at the 5th ICFA Advanced Beam Dynamics Workshop, Corpus Christi, Texas (1991).
4. T. Lohse and P. Emma, "Linear Fitting of BPM Orbits and Lattice Parameters", SLAC Single Pass Collider Memo CN-371 (1989).
5. T. Himel and K. Thompson, "Energy Measurements from Betatron Oscillations", Proc. of the 1989 IEEE Part. Acc. Conf., Chicago, Ill (1989).
6. V. Ziemann, "Corrector Ironing", SLAC internal report Single-Pass Collider Note CN-393 (1992).
7. W. Press, *et al.*, "Numerical Recipes", Section 2.9, Cambridge University Press, Cambridge (1986).
8. The MathWorks, Inc. (1994).
9. W.J. Corbett, F. Fong, M. Lee, V. Ziemann, "Optimum Steering of Photon Beam Lines in SPEAR", Proc. of 1993 IEEE PAC Washington, p. 1483 (1983).
10. D. Robin, G. Portmann, L. Schachinger, "Automated Beam Based Alignment of the ALS Quadrupoles", internal SLAC Report, NLC-Note 18 (1995).
11. R. Brinkmann and M. Böge, "Beam-Based Alignment and Polarization Optimization in the HERA Electron Ring", Proc. of EPAC94, London, p. 938 (1994).
12. J. Corbett, R.O. Hettel, H.-D. Nuhn, "Quadrupole Shunt Experiments at SPEAR", Proc. of 7th Beam Instrumentation Workshop (BIW96), Argonne, Illinois (1996).
13. P. Emma, "Beam-Based Alignment of Sector-1 of the SLAC Linac", Proc. of EPAC 92, Berlin, and SLAC-PUB-5787 (1992).
14. I. Reichel, "Beam Position Measurement by Modulation of Quadrupole Strengths", SL note/95-50 (1995).
15. M. Kikuchi, K. Egawa, H. Fukuma, M. Tejima, "Beam-Based Alignment of Sextupoles with the Modulation Method", Proc. of 1995 IEEE PAC, Dallas, p. 603 (1995).
16. S. Kamada, "Overview on Experimental Techniques and Observations", Proc. of workshop on Nonlinear Dynamics in Particle Accelerators: Theory and Experiments", Arcidosso, Italy (1994).
17. N. Yamamoto, S. Kamada, Y. Kobayashi, H. Koiso, and S. Matsumoto, "Beam-Based Alignment of Sextupole Magnets with a π-Bump Orbit", KEK Preprint 96-74 (1996).

18. S. Herb, G.B. Jaczko, and F. Willeke, “Beam-Based Calibration of Beam Position Monitor Offsets in the HERA Proton Ring using Strong Sextupole Fields”, Proc. of workshop on Beam Diagnostics and Instrumentation for Particle Accelerators, Travemuende, DESY Int. Rep. M-95-07 (1995).
19. T. Raubenheimer, in the Zeroth Order Design Report for the Next Linear Collider, SLAC Report 474, p. 227-228 (1995).
20. P. Emma, J. Irwin, N. Phinney, P. Raimondi, N. Toge, N.J. Walker, V. Ziemann “Beam Based Alignment of the SLC Final Focus Sextupoles”, Proc. of 1993 IEEE PAC, Washington, DC, p. 116 (1993).
21. P. Emma, J. Irwin, N. Phinney, P. Raimondi, N. Toge, N.J. Walker, V. Ziemann, “Beam Based Alignment of the SLC Final Focus Sextupoles”, Proc. of IEEE PAC 93, Washington, D.C. (1993).
22. P.G. Tenenbaum, “Expanded Studies of Linear Collider Final Focus Systems at the Final Focus Test Beam”, SLAC-R-95-475 (1995).
23. M. Seidel, C. Adolphsen, K.L.F. Bane, R.M. Jones, N.M. Kroll, R.H. Miller, D.H. Whittum, “Absolute Beam Position Measurement in an Accelerator Structure”, Nucl. Instr. Methods A 404, p. 231 (1998).
24. M. Minty, C. Adolphsen, L.J. Hendrickson, R. Sass, T. Slaton, M. Woodley, “Feedback Performance at the Stanford Linear Collider”, Proc. of IEEE PAC 95, Dallas (1995).
25. T. Himel, “FEEDBACK: Theory and Accelerator Applications”, Annu. Rev. Nucl. Part. Sci. 47, p. 157 (1997).
26. F.J. Decker, private communication.
27. M. Sands, “A Beta Mismatch Parameter”, SLAC internal report SLAC-AP-85 (1991).
28. W. Spence, private communication (1996).
29. R. Iverson, M. Minty, M. Woodley, private communication, and ATF internal report ATF 12-29 (1997).

Chapter 4

Transverse Phase Space Manipulation

In this chapter we discuss several approaches for manipulating, shaping and preserving the transverse beam emittance. These include the measurement and correction of linear betatron coupling, changes to the equilibrium emittance and to the damping time of stored electron beams, emittance preservation in a linac, compensation of space-charge induced emittance growth in photoinjectors, and collimation of beam halo in linear colliders and storage rings.

4.1 Betatron Coupling

Skew quadrupole field errors and detector solenoids generate betatron coupling between the horizontal and vertical plane of motion. Spurious betatron coupling is a concern, since it may reduce the dynamic aperture[1], and since, in electron machines, it contributes to the vertical equilibrium emittance. The coupling of horizontal and vertical oscillations generates two new eigenmodes of oscillation. These eigenmodes are no longer purely vertical or purely horizontal, but rather they correspond to oscillations whose reference planes are tilted and rotate with the azimuthal position s. In this case, new coupled beta functions can be defined[2,3,4,5].

The important coupling parameters are the two driving terms for the sum and difference resonances, which are given by[5,1,6]:

$$|\kappa_{\pm}| = \left| \frac{1}{2\pi} \oint ds \; K_s(s) \sqrt{\beta_x(s)\beta_y(s)} \; e^{i(\phi_x \pm \phi_y - (Q_x \pm Q_y - q_{\pm}) 2\pi s/L)} \right| \qquad (4.1)$$

where K_s is the normalized gradient of the skew quadrupole (in units of m^{-2}), L is the circumference, $\beta_{x,y}$ are the uncoupled beta functions, and we assume that the betatron tunes are near the resonance:

$$Q_x \pm Q_y + q_\pm = 0 \tag{4.2}$$

where $q_\pm$ is an integer. The dynamic aperture or the beam lifetime of colliding beams can be increased by measuring and minimizing the two driving terms $|\kappa_\pm|$.

In an electron storage ring, the vertical emittance contribution due to weak betatron coupling is[7]

$$\gamma\epsilon_y = \frac{C_q\gamma^3}{16\oint G^2 ds}\oint \mathcal{H}_x|G^3|\left[\sum_\pm \frac{|W_\pm(s)|^2}{\sin^2\pi(\Delta Q_\pm)} + \frac{2\mathrm{Re}\left\{W_+^*(s)W_-(s)\right\}}{\sin\pi(\Delta Q_+)\ \sin\pi(\Delta Q_-)}\right] ds \tag{4.3}$$

where $C_q = 3.84\times10^{-13}$ m, $\mathcal{H}_x$ is the horizontal dispersion invariant, $G = 1/\rho$ the inverse bending radius, $*$ is the complex conjugate, Re gives the real portion of its argument, $\Delta Q_\pm = Q_x + Q_y \pm q_\pm$, and

$$W_\pm(s) = \int_s^{s+L} dz\ K(z)\sqrt{\beta_x\beta_y}e^{i[(\phi_x(s)\pm\phi_y(s))-(\phi_x(z)\pm\phi_y(z))+\pi(Q_x\pm Q_y)]} \tag{4.4}$$

are the driving terms, including all Fourier components. Note that $|W_\pm(0)| \approx |\kappa_\pm|/(2\pi)$.

Equation (4.3) shows that, in order to minimize the vertical emittance, the driving terms $W_\pm(s)$, for the two nearest sum and difference resonances, should be corrected.

4.1.1 First Turn Analysis

Large coupling sources can be identified as locations where a horizontal orbit change generates a vertical kick and vice versa. In order to find such locations, the orbit is changed in one plane, by exciting steering correctors or by changing injection conditions (kicker amplitude), and the effect on the orbit in the perpendicular plane is measured. The same type of analysis can be applied to a transport line.

Large numbers of orbits and BPM data for excitations of different correctors can be fitted to determine the skew quadrupole component of each magnet in the beam line.

4.1.2 Beam Response after Kick

The driving term $|\kappa_-|$ may be measured by first kicking the beam, and then observing its response in the plane of the kick over *many turns*.

In the vicinity of the difference resonance, the envelopes of the oscillations in the horizontal and vertical plane exhibit a beating (energy exchange between the two planes) with a characteristic total modulation amplitude of[8,5]

$$S = \frac{\hat{x}^2_{min}}{\hat{x}^2_{max}}. \tag{4.5}$$

Here $\hat{x}$ denotes the envelope of the betatron oscillation in the plane in which the kick was applied; $\hat{x}_{min}$ is its minimum value, and $\hat{x}_{max}$ its maximum value; these two extreme values are assumed alternately, with a modulation (or beating) period T. The driving term for the difference resonance, $|\kappa_-|$ of Eq. (4.1), is given by[8]

$$|\kappa_-| = \frac{\sqrt{1-S}}{f_{rev}T} \tag{4.6}$$

Thus a measurement of the modulation period T and the squared envelope ratio S after a kick is sufficient to infer $|\kappa_-|$.

An example from the ATF Damping Ring is shown in Fig. 4.1. The frequency spectrum from a horizontal BPM signal is viewed over a wide frequency range on a spectrum analyzer (top figure), and the frequency of the betatron signal is identified as the peak of the spectrum. The span of the spectrum analyzer is then set to zero, and its center set to the betatron frequency. This produces a signal proportional to the square of the betatron-oscillation amplitude. The output signal of the spectrum analyzer can be viewed on an oscilloscope, with results as displayed in Fig. 4.1 (bottom). The slow oscillation in this picture corresponds to synchrotron motion (the BPM is at a dispersive location), while the fast beating reflects the transverse coupling. The picture was taken for a tune separation of $|Q_x - Q_y + q_-| \approx 0.02$. If the two tunes are separated further, the modulation period increases and the modulation amplitude decreases. Using Eq. (4.6) with $T \approx 17.6$ μs and $S \approx$ 0.3-0.7, we infer a coupling term of $|\kappa_-| \approx 0.02$, consistent with other measurements[9].

It is of course possible to perform a much more detailed analysis of multi-turn BPM data. For example, one can determine the evolution of the coupled optical functions (*e.g.*, the tilt angle of the two transverse eigenplanes) around the ring. An example may be found in Ref.[10].

4.1.3 Closest Tune Approach

Near the difference resonance, the tunes of the two coupled eigenmodes in the vertical plane are[5,8]

$$Q_{I,II} = \frac{1}{2}\left(Q_x + Q_y + q \pm \sqrt{(Q_x - Q_y + q)^2 + |\kappa_-|^2}\right) \tag{4.7}$$

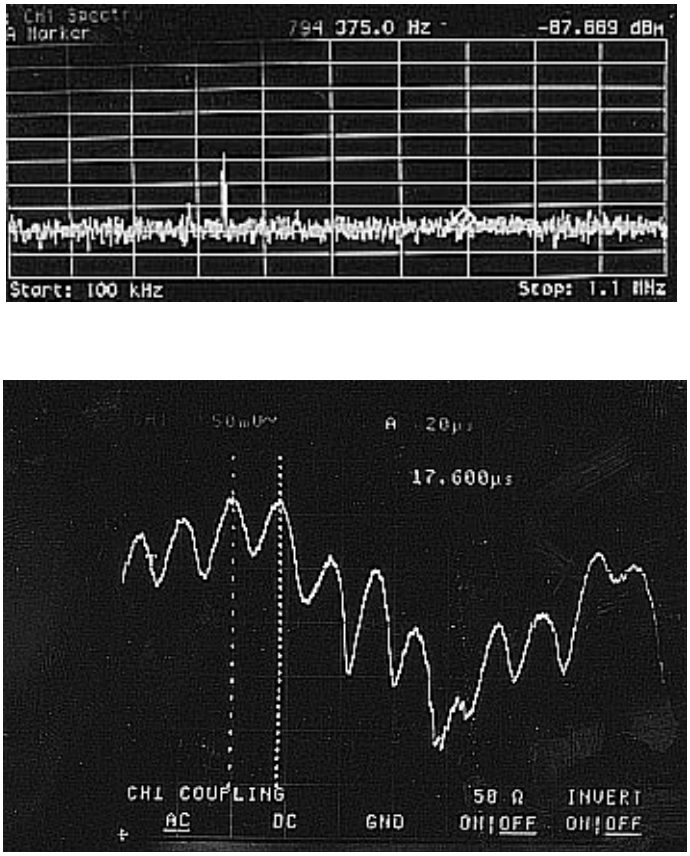

Figure 4.1: Monitoring betatron coupling at the ATF Damping Ring[9]. (Top) frequency spectrum of a horizontal pick up on a spectrum analyzer; (bottom) evolution of the peak signal in the frequency spectrum as a function of time, as viewed on an oscilloscope; the slow variation reflects synchrotron motion, the fast beating with a period of about 17.6 μs is due to the transverse coupling; the amplitude and period of the modulation can be used to determine the driving term $|\kappa_-|$.

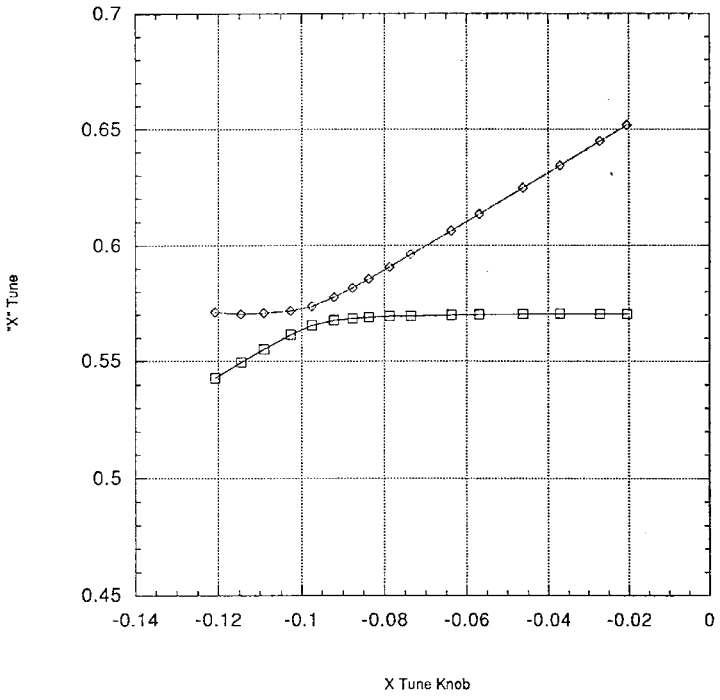

Figure 4.2: Closest tune approach in the PEP-II HER before final correction [11]. Shown are the measured tunes as a function of the horizontal tune `knob' (which would only change Q_x if the machine were uncoupled), in dimensionless units. The minimum tune distance is equal to the driving term $|\kappa_-|$ of the difference resonance. (Courtesy Y. Cai, 1998.)

where Q_x and Q_y are the tunes which one would expect without coupling. A similar formula, with the same fractional values of $Q_{I,II}$, describes the coupled tunes in the horizontal plane. Equation (4.7) shows that the measured tunes, Q_I and Q_{II}, are never exactly equal, but can only approach each other up to a distance $|\kappa_-|$. Figure 4.2 illustrates this with an example from the PEP-II HER. A common technique for correcting the betatron coupling in a storage ring is to minimize the distance of closest approach using at least two skew quadrupole magnets. It is often the only correction necessary, especially if the tunes are close to the difference resonance $Q_x - Q_y + q = 0$ (q integer).

4.1.4 Compensating the Sum Resonance

In the vicinity of the difference resonance, there is a continuous energy exchange between the two transverse planes, but the beam or particle motion remains bounded. By contrast, close to the sum resonance, for $|Q_x + Q_y + q| < |\kappa_+|$, the motion is unstable. The total width of the stop band around the sum resonance is equal to twice the driving term $|\kappa_+|$ of Eq. (4.1) [5]. Although this may be more difficult in practice than to determine the driving term $|\kappa_-|$ for the difference resonance, from the closest-tune approach, the driving term $|\kappa_+|$ can be compensated by adjusting two skew quadrupoles so as to minimize the stop band width of the sum resonance.

Equation (4.3) shows that in order to optimize the vertical emittance in a damping ring, in general it is necessary to correct both driving terms, $|\kappa_-|$ and $|\kappa_+|$. The minimum number of skew quadrupole correctors needed to correct both coupling driving terms as well as the vertical dispersion function is six (one sine-like and one cosine-like corrector are required for each effect).

4.1.5 Emittance near Coupling Resonance

A third approach to determine the coupling parameter $|\kappa_-|$ is to measure the horizontal (or vertical) emittance as a function of distance from the difference resonance [13]. Equation (4.3) does not apply close to the resonance. Instead, near the difference resonance, the horizontal emittance is described by[14]

$$\epsilon_x = \epsilon_{x0}\,\frac{2(|\kappa_-|/\Delta Q_-)^2 + 1}{4(|\kappa_-|/\Delta Q_-)^2 + 1} \tag{4.8}$$

The tune difference $\Delta Q_- = (Q_x - Q_y - n)$ function is related to the measured tune difference $\Delta Q_{I,II} = |Q_{II} - Q_I|$ via

$$\Delta Q_- = \sqrt{\Delta Q_{I,II}^2 - |\kappa_-|^2} \tag{4.9}$$

After inserting this equation for ΔQ_-, Eq. (4.8) is transformed into

$$\epsilon_x = \epsilon_{x0}\,\frac{|\kappa_-|^2 + \Delta Q_{I,II}^2}{3|\kappa_-|^2 + \Delta Q_{I,II}^2} \tag{4.10}$$

In the experiment, the horizontal emittance ϵ_x was inferred from the spot size σ_x measured with the ATF interferometric monitor[15], using the formula $\epsilon_x = (\sigma_x^2 - (\eta\delta)^2)/\beta_x$, where the design beta function ($\beta_x = 0.33$ m) and dispersion ($\eta = 4$ cm) at the point of light emission, and the calculated energy spread of $\delta = 7.14 \times 10^{-4}$ were assumed.

Performing a nonlinear fit to Eq. (4.10) of the emittance ϵ_x obtained for various tune differences $\Delta Q_{I,II}$, the driving term $|\kappa_-|$ can be extracted [13] To this end, we employ the nonlinear regression subroutine RNLIN which is part of the IMSL program library [16]. Figure 4.3 shows the measured horizontal emittance as a function of tune separation $\Delta Q_{I,II}$. The result of the nonlinear fit is also depicted. The coupling strength of $|\kappa_-| \approx 0.037$ inferred from the fit [13] agrees well with the coupling strength $|\kappa_-| \approx 0.042$ obtained from a measurement of the closest tune approach under the same conditions [17].

4.1.6 Coupling Transfer Function

A different method of measuring the coupling is through the `coupling transfer function' [18]. Here, the beam is excited horizontally, while detecting the resulting vertical coherent motion. Such a technique was used to continually monitor and correct the coupling strength during collisions in the CERN ISR [18].

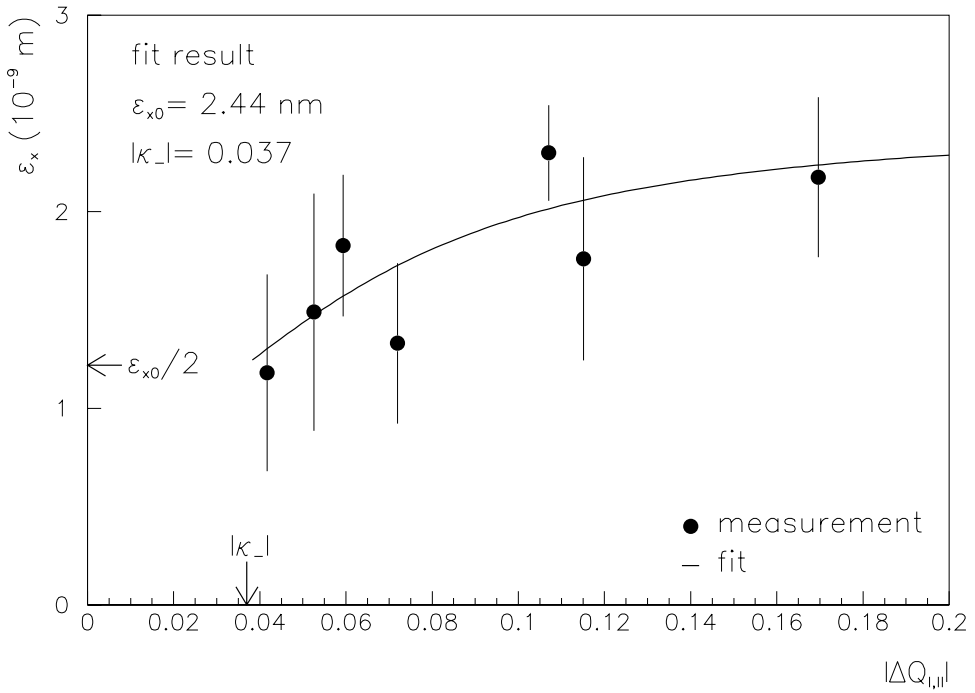

Figure 4.3: Horizontal emittance as a function of the tune separation $\Delta Q_{I,II}$ at the ATF Damping Ring; the measured data[17] as well as the result of a nonlinear fit to Eq. (4.10) are shown; the fitted coupling strength of $|\kappa_-| \approx 0.037$ is consistent with the value $|\kappa_-| \approx 0.042$ inferred from a simultaneous measurement of the closest tune approach[12,13].

4.2 Equilibrium Emittance

We now discuss different methods for changing and controlling the equilibrium emittance in electron or positron storage rings.

Recall the expression for the quantum excitation of the transverse emittance[19]:

$$\frac{d\epsilon_u}{dt} = cC_Q E^5 \left\langle \frac{\mathcal{H}_u}{\rho^3} \right\rangle \tag{4.11}$$

where

$$C_Q = \frac{55}{48\sqrt{3}} \frac{r_e \hbar c}{(m_e c^2)^6} \approx 2 \times 10^{-11}\ \mathrm{m}^2\ \mathrm{GeV}^{-5}, \tag{4.12}$$

$u = x$ or y, and ρ the bending radius. The angular brackets denote an average over the ring. The emittance decrease due to radiation damping is described by

$$\frac{d\epsilon_u}{dt} = -2\epsilon_u C_d J_u E^3 \left\langle \frac{1}{\rho^2} \right\rangle \tag{4.13}$$

where ϵ is the beam emittance,

$$C_d = \frac{c}{3} \frac{r_e}{(m_e c^2)^3} = 2.1 \times 10^3\ \mathrm{m}^2\ \mathrm{GeV}^{-3}\ \mathrm{s}^{-1}, \tag{4.14}$$

and J_u the damping partition number.

The equilibrium emittance is reached when the quantum excitation and the damping are of equal magnitude:

$$\epsilon_{u,\infty} = C_q \frac{\gamma^2}{J_u} \frac{\left\langle \mathcal{H}_\sqcap / \rho^3 \right\rangle}{\langle 1/\rho^2 \rangle} \tag{4.15}$$

where

$$C_q = \frac{55}{32\sqrt{3}} \frac{\hbar c}{m_e c^2} = 3.84 \times 10^{-13}\ \mathrm{m}. \tag{4.16}$$

Thus ϵ_u is inversely proportional to the transverse damping partition number J_u. Similarily, the longitudinal emittance is inversely proportional to J_z.

We obtain the exponential damping time τ_u from $1/\tau_u \equiv d\epsilon_u/dt/\epsilon_u$. Including also the longitudinal degree of freedom, the exponential damping times for all three oscillation modes can be written as[20]

$$\tau_i = \frac{2E_0}{< P_\gamma > J_i} \tag{4.17}$$

where E_0 is the nominal energy, $< P_\gamma >$ the average rate of energy loss. The latter is given by

$$< P_\gamma >= \frac{cC_\gamma}{2\pi} E_0^4 \left\langle \frac{1}{\rho^2} \right\rangle \tag{4.18}$$

where

$$C_\gamma = \frac{4\pi r_e}{3(m_e c^2)^3} \approx 8.877 \times 10^{-5} \text{ m GeV}^{-3} \tag{4.19}$$

as defined by Sands[20].

The factor J_i in Eq. (4.17) is the damping partition number for the ith degree of freedom. A general theorem by Robinson[21] states that the sum of the three partition numbers is a constant:

$$J_x + J_y + J_z = 4 \tag{4.20}$$

If the ring only contains horizontal, but no vertical bending magnets, then $J_y = 1$ and the partition numbers in the other two planes are related by a term $\mathcal{D}$[20]:

$$J_x = 1 - \mathcal{D} \tag{4.21}$$

$$J_z = 2 + \mathcal{D} \tag{4.22}$$

where

$$\mathcal{D} = \frac{\oint \eta/\rho \, \left(1/\rho^2 + 2K_1\right) \, ds}{\oint 1/\rho^2 \, ds} \tag{4.23}$$

For separated function magnets $K_1/\rho = 0$ and the value of $\mathcal{D}$ is typically much smaller than 1.

It is often desirable to increase one of the damping rates or to vary the horizontal emittance. For example, in linear collider applications, a fast horizontal damping and a small horizontal emittance are advantageous, while in storage-ring colliders one may instead want to increase the horizontal emittance near the beam-beam limit, to avoid instabilities.

The damping rate and the equilibrium emittance can be changed by adjusting the value of $\mathcal{D}$ and/or by adding wiggler magnets. Depending on the application, there are various possibilities to do so. We here describe the effect of a change in the ring circumference, and two different applications of wigglers.

4.2.1 Circumference Change

If the geometric circumference of the ring is changed by moving the magnet centers outwards by a step Δx^{mag} while holding the ring rf frequency fixed (so as to maintain synchronization with other systems) the quantity $\mathcal{D}$ changes by

$$\Delta \mathcal{D} \approx - \left(\sum_q K_{q,1}^2 \eta_q L_q \right) \, \frac{2\rho^2}{C} \, \Delta x^{mag} \tag{4.24}$$

where K_1 is the non-integrated quadrupole gradient, L_q the quadrupole length, η_q the dispersion function at the quadrupole, C the ring circumference, and ρ the bending radius of the dipole magnets. The minus sign arises because the orbit moves inwards with respect to the quadrupole magnets (orbit shift: $\Delta x = -\Delta x^{mag}$). Note that the contributions from focusing and defocusing magnets add up, because the effect is quadratic in $K_{1,q}$. The maximum shift Δx is determined by the available aperture, and the beam size at injection.

In 1992, the magnet support girders of the SLC North Damping Ring were pulled outwards by about $\Delta x = 1.5$ mm, increasing the geometric ring circumference by 9 mm. As a result the measured horizontal damping time decreased from 4.11 ± 0.11 ms to 3.41 ± 0.09 ms, consistent with predictions.

An equivalent change in $\mathcal{D}$ can be achieved with a shift of the rf frequency by

$$\frac{\Delta f_{rf}}{f_{rf}} = \frac{2\pi\Delta x}{C} \tag{4.25}$$

More accurately, the orbit shift in the quadrupole is proportional to the local dispersion function

$$\Delta x(s) = -\frac{\eta}{\alpha_C}\,\frac{\Delta f_{rf}}{f_{rf}} \tag{4.26}$$

with α_C the momentum compaction factor, and the change in the partition number reads

$$\Delta\mathcal{D} \approx \frac{\oint 2K_1^2\eta^2 ds}{\oint ds/\rho^2}\,\frac{\Delta p}{p} \equiv C_0\,\frac{\Delta p}{p} \tag{4.27}$$

However, in practice the rf frequency often has to be locked to the rf of the injection (or extraction) system. Therefore, at the SLC damping rings in addition to the static circumference change a dynamic rf frequency shift was implemented[22]. The dynamic rf frequency shift by up to 100 kHz started about 1.33 ms into the store, and it was stopped 200 μs before extraction, in order to stabilize the injected beam and to minimize emittance and extraction jitter, respectively [23]. The total store time was 8.33 ms, equal to about 2.5 nominal damping times. For a dynamic frequency shift of 62.5 kHz the normalized emittance of the extracted beam decreased from 3.30 ± 0.07 m to 2.66 ± 0.06 m. The 20% reduction agreed with SAD calculations[22].

Ex.4.1. Static and dynamic change of partition numbers
Assume parameters typical for the SLC damping rings: 40 quadrupoles, $K_1 \approx 15$ m^{-2}, $\eta_q \approx 0.15$ m, $L_q \approx 18$ cm, $\rho \approx 1/2\ C/(2\pi)$, $C = 35$ m, harmonic number $h = 84$, rf frequency $f_{rf} = 714$ MHz, and momentum compaction $\alpha = 0.0147$.
a) What is the change in $\mathcal{D}$ for an outward shift of all magnets by $\Delta x = 1.5$ mm?
b) What would be the equivalent change in the rf frequency?

From Eq. (4.27) the partition number changes with the particle momentum. If a particle performs synchrotron oscillations

$$\frac{\Delta p}{p} = \delta_{\max} \sin \Omega_s t \tag{4.28}$$

its partition number and damping time vary with the synchrotron period:

$$\frac{1}{\tau} = \frac{1}{\tau_0}(1 - C_0 \delta_{\max} \sin \Omega_s t) \tag{4.29}$$

The equation for the equilibrium emittance of such a particle is then[19]

$$\epsilon(t) = \epsilon_\infty \ \exp\left[\frac{2\delta_{\max} C_0}{\Omega \tau_0}(\cos \Omega t - 1)\right] \tag{4.30}$$

The effect is largest for particles with large synchrotron oscillations.

4.2.2 Wigglers

A wiggler magnet generates additional synchrotron radiation, and thus can enhance the radiation damping or change the equilibrium emittance. The damping time is modified according to

$$\tau_{u,w} = \tau_{u,0} \frac{1}{1 + \frac{<1/\rho^2>_w}{<1/\rho^2>_0>}} \tag{4.31}$$

where the subindex 0 on the right hand side indicates an average over the ring without wiggler magnets, while the subindex w indicates the contribution from the wiggler magnets. On the left, $\tau_{u,x}$ is the damping time in the uth plane, with the effect of the wiggler included, and $\tau_{u,0}$ is the damping time for the ring proper.

Similarily, the relative emittance increase due to the presence of the wiggler is

$$\frac{\epsilon_w}{\epsilon_0} = \frac{1 + \left\langle \mathcal{H}/\rho^3 \right\rangle_w / < \mathcal{H}/\rho^3 >_0}{1 + \left\langle 1/\rho^2 \right\rangle_w / < 1/\rho^2 >_0} \tag{4.32}$$

where the averages are given by, for example,

$$\left\langle \frac{1}{\rho^2} \right\rangle_w = \frac{1}{C} \oint \frac{1}{\rho_w^2} \, ds \tag{4.33}$$

with C the circumference, and ρ_w the bending radius in the wiggler.

In addition to changing the emittance, wigglers also affect the energy spread[19]:

$$\frac{\sigma_{\delta,w}^2}{\sigma_{\delta,0}^2} = \frac{1 + \left\langle 1/\rho^3 \right\rangle_w / < 1/\rho^3 >_0}{1 + \left\langle 1/\rho^2 \right\rangle_w / < 1/\rho^2 >_0} \tag{4.34}$$

Damping Wigglers

If we place a wiggler in a region with no dispersion, $\eta = 0$, we might expect that the equilibrium emittance decreases according to Eq. (4.32) with $< H_w >= 0$. However this is not completely correct, because the wiggler itself generates dispersion. As an example, we consider a sinusoidal wiggler, with field:

$$B(z) = B_w \cos k_p z \tag{4.35}$$

where $k_p = 2\pi/\lambda_p$ and λ_p the wiggler period length. The differential equation for the dispersion function reads:

$$\eta''(z) = \frac{1}{\rho_w} \cos k_p z \tag{4.36}$$

which can be solved as

$$\eta(z) = \frac{1}{k_p^2 \rho_w}(1 - \cos k_p z) \tag{4.37}$$

assuming that $\eta(0) = \eta'(0) = 0$. Using

$$\frac{1}{\rho} = \frac{1}{\rho_w} |\cos k_p z|, \tag{4.38}$$

for each half period of the wiggler we find[19]

$$\int_0^{\lambda_p/2} \frac{\mathcal{H}}{|\rho|^3}\, dz = \frac{36}{15}\frac{1}{\beta}\frac{1}{k_p^5 \rho_w^5} + \frac{4}{15}\frac{\beta}{k_p^3 \rho_w^5} \approx \frac{4}{15}\ \frac{\beta}{k_p^3 \rho_w^5} \tag{4.39}$$

where we assumed $\lambda_p \ll \beta$, and β is the beta function. Introducing the deflection angle per wiggler pole $\theta_w = 1/(\rho_w k_p)$, and the number of wiggler periods N_w, we can rewrite this as

$$\int_w \frac{\mathcal{H}}{\rho^3}\, dz \approx N_w \frac{8}{15}\frac{\beta}{\rho_w^2}\theta_w^3 \tag{4.40}$$

and, similarily,

$$\int_w \frac{1}{\rho^2}\, dz \approx \pi N_w \frac{\theta_w}{\rho_w} \tag{4.41}$$

We finally get for the emittance ratio:

$$\frac{\epsilon_w}{\epsilon_0} = \frac{1 + \frac{8}{30\,\pi} N_w \frac{\beta}{<\mathcal{H}_0>}\frac{\rho_0^2}{\rho_w^2}\theta_w^3}{1 + \frac{1}{2} N_w \frac{\rho_0}{\rho_w}\theta_w} \tag{4.42}$$

where $< \mathcal{H} >_0$ is the average value of $\mathcal{H}$ in the ring magnets, excluding the wiggler magnets. The latter can be re-expressed in terms of the emittance ϵ_{x0} to yield, *i.e.*, with a vertical wiggler field the horizontal emittance

$$\frac{\epsilon_{x,w}}{\epsilon_{x,0}} = \frac{1 + \frac{8C_q}{30\pi J_x} N_w \frac{\beta_x}{\epsilon_{x0}\rho_w} \gamma^2 \frac{\rho_0}{\rho_w} \theta_w^3}{1 + \frac{1}{2} N_w \frac{\rho_0}{\rho_w} \theta_w} \tag{4.43}$$

The emittance is reduced by wiggler magnets if

$$\frac{8}{15\pi} \frac{C_q}{J_x} \frac{\beta_x}{\epsilon_0 \rho_w} \gamma^2 \theta_w^2 \leq 1 \tag{4.44}$$

For a large number of wiggler periods the emittance reaches an asymptotic value

$$\epsilon_{x\,w} \rightarrow \frac{16}{30\pi} \frac{C_q \beta_x}{\rho_w} \gamma^2 \theta_w^2 \tag{4.45}$$

The horizontal damping time with wigglers can be written as

$$\tau_{x,w} = \tau_{u,0} \frac{1}{1 + \frac{1}{2} N_w \frac{\rho_0}{\rho_w} \theta_w} \tag{4.46}$$

and, in the limit of a very long wiggler channel, assuming intermittent re-acceleration:

$$\tau_{x,w} \approx \frac{2\rho_w^2}{C_d J_x E^3} \tag{4.47}$$

Ex.4.2. Effect of wiggler on beam equilibrium emittance
Consider a ring which consists mainly of wiggler magnets, with a peak magnetic field B_w of 40 kG, and a wiggler oscillation period of λ_p of 20 cm. Calculate the equilibrium emittance and the damping time in such a ring, assuming beam energies of 1 GeV and 5 GeV. Compare this with a typical damping-ring design for a future linear collider, where $\gamma\epsilon_x \approx 3$ μm, and $\tau_x \approx 3$ ms.

Robinson wiggler

A "Robinson wiggler" is a wiggler consisting of a series of combined function magnets, arranged such as to increase the horizontal partition number. Such a magnet was first used at the CEA to convert the synchrotron (which because of $\mathcal{D} > 1$ was

horizontally unstable) into a stable storage ring with $0 < \mathcal{D} < 1$ [21]. Such a wiggler will change the partition number according to [24]

$$\Delta\mathcal{D} \approx \frac{\bar{\eta}_x L_{Rob} K_1}{2\pi(1+F_\omega)} \frac{\rho_0}{\rho_{Rob}} \tag{4.48}$$

where L_{Rob} and ρ_{Rob} are the length and the bending radius of the Robinson wiggler, $\bar{\eta}_x$ the average dispersion in the wiggler, ρ_0 the bending radius of the main bends, K_1 the magnitude of the wiggler quadrupole gradient (in units of m^{-2}), and

$$F_\omega \equiv \frac{1}{2} N_w \frac{\rho_0}{\rho_w} \theta_w \tag{4.49}$$

Unfortunately, the Robinson wiggler not only increases the damping but it can also blow up the equilibrium emittance, since it is preferably placed at a location with large dispersion.

Other applications of wigglers include polarization wigglers for electron storage rings. These decrease the polarization time at low beam energies [25] or invert the spin direction [26].

4.3 Linac Emittance Control

4.3.1 Introduction

In a linac, the beam experiences emittance growth due to alignment errors of the accelerator components, which arise from steering the beam through misaligned structures and quadrupole magnets using beam-position monitors with residual offset errors [27]. The resulting transverse wakefields and dispersive effects increase the beam emittance. Some countermeasures that have been developed to minimize linac emittance growth are BNS damping, trajectory oscillations, and dispersion-free steering.

4.3.2 BNS Damping

The wakefield effect can be reduced by proper adjustment of the rf phase profile along the linac. By passing the rf wave off-crest a position-energy correlation is generated along each linac bunch, such that the tail particles have lower energy than the particles in the bunch head. This results in so-called BNS damping [28], where the defocusing due to the wakefields is compensated by the stronger focusing for lower-energy tail particles.

Consider a 2-particle model, each with half the total bunch current and a distance z apart. Let the first particle be at the design energy and assume that the bunch head performs a pure betatron oscillation:

$$y_1(s) = \hat{y} \cos s/\beta \tag{4.50}$$

with β the average beta function, using a smooth approximation. The equation of motion for the second particle with a momentum deviation δ is then[29]

$$\frac{dy_2(s)}{ds^2} + \frac{1}{\beta^2(\delta)} y_2(s) = \frac{N r_e W_1(z)}{2\gamma L} \hat{y} \cos s/\beta \tag{4.51}$$

where $W_1(z)$ denotes the value of the transverse wake function per cavity (in units of cm^{-2}), N is the bunch population, and L the cavity period. We have ignored the effect of acceleration and have assumed an electron beam. There is a value of δ where, in first order, the bunch tail exactly follows the bunch head. Writing $\beta(\delta) = \beta(0) + \Delta\beta(\delta)$ it corresponds to[29]:

$$\frac{\Delta\beta(\delta)}{\beta(0)} = \frac{N_b r_e \beta^2 W_1(z)}{4\gamma L} \tag{4.52}$$

a condition which is also known as `autophasing'. Now the relative change in beta function as a function of energy can be expressed using the linac chromaticity ξ

$$\frac{\Delta\beta}{\beta} = -\xi\delta \tag{4.53}$$

and for a FODO cell:

$$\xi = -\frac{2}{\mu} \tan\frac{\mu}{2} \tag{4.54}$$

where μ is the betatron phase advance per FODO cell. In case of an accelerated beam, the autophasing condition is still given by Eq. (4.52), if we simply replace the factor $1/\gamma$ by $\ln(\gamma_f/\gamma_i)/\gamma_f$ where γ_i and γ_f characterize the initial and final energies in units of the rest mass.

Ex.4.3. BNS at the SLC
For the SLAC linac $\beta \approx 20$ m, $W_1(1\text{ mm}) \approx 1$ cm^{-2}, $L = 3.5$ cm, $N = 4 \times 10^{10}$, $\mu \approx \pi/2$, with an injected beam energy of 1.2 GeV and a final energy of 47 GeV. How large is the BNS energy chirp δ over the bunch length of 1 mm?

In practice, BNS damping can only partially be realized, since the energy spread at the end of the accelerator must be small to fit inside the energy acceptance of the downstream beam delivery system.

4.3.3 Trajectory Oscillations

In addition to BNS damping, empirically distributing a set of short-range oscillations along the accelerator proved indispensable for SLC operation[27]. Examples of induced betatron oscillations in the SLAC linac are shown in Fig. 4.4[27].

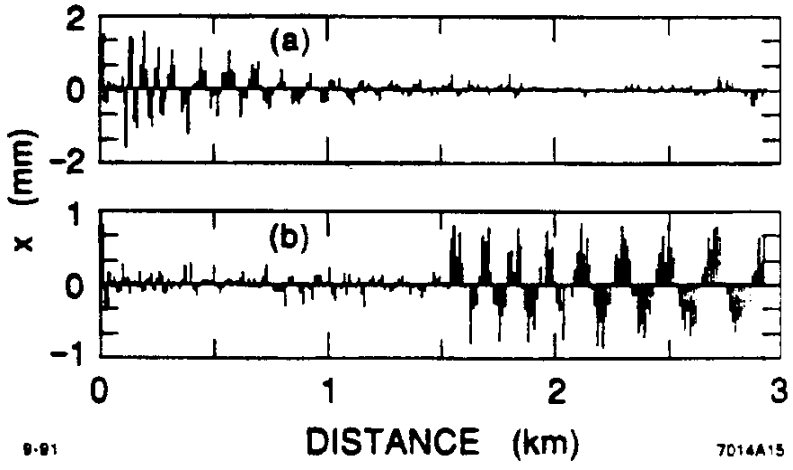

Figure 4.4: Two trajectory ocillations in the SLAC linac, which were used to study the effect on the downstream emittance. (Courtesy F.J. Decker, 1999.)

Wakefields and dispersive effects in the linac generate both emittance growth and a mismatch. Mismatch induced early in the linac has completely filamented at its end, while perturbations near the linac end also result in residual unfilamented tails and in a phase-space mismatch, which is conventionally characterized by the parameter B_{mag} (this factor specifies the emittance growth after filamentation; for a matched beam: $B_{mag} = 1$). Similarily, trajectory oscillations induced in the early parts of the linac only change the beam emittance $\gamma\epsilon$, while those in the later sections also affect the measured betatron mismatch. This is illustrated in Fig. 4.5, which presents the measured normalized emittance versus the amplitude of the two trajectory bumps in Fig. 4.4.

The SLC employs a series of more than 10 orbit feedbacks, with roughly equidistant spacing along the SLAC linac. These feedbacks continually maintain constant values of offset and slope at certain beam-position monitors, by adjusting the strengths of a few steering correctors. The feedback set points for position and slope are set to empirically determined target values.

A closed trajectory oscillation is generated most easily by changing a feedback set point (for either slope or position). The induced trajectory oscillation is then automatically taken out by the next feedback downstream, because the latter attempts to restore the original orbit.

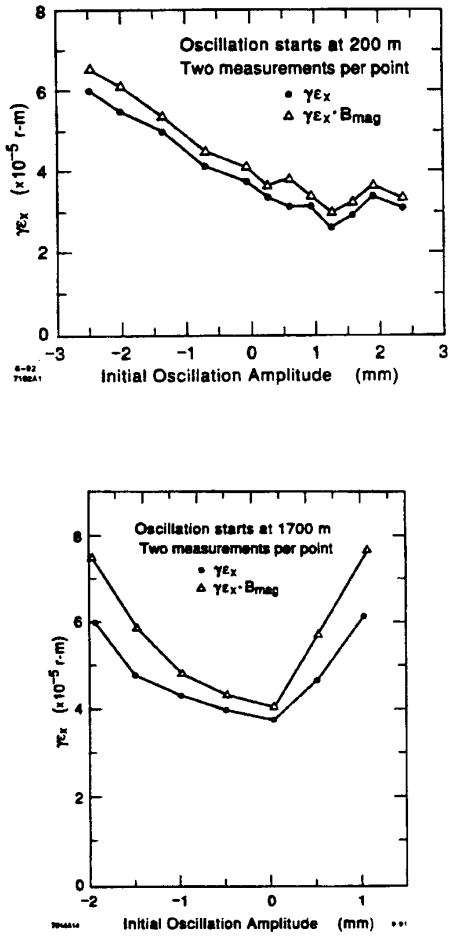

Figure 4.5: Change in the normalized emittance as a function of the amplitude of a trajectory oscillation induced early in the linac (top) and towards the end of the linac (bottom). In the first case, the betatron mismatch is constant, and the normalized emittance decreases by 25% for an oscillation amplitude of about 1.5 mm. On the right, the trajectory oscillation does not reduce the normalized emittance. Instead it enhances the observed betatron mismatch, which is evident by the separation of the two curves representing $\gamma\epsilon$ and $B_{mag}\gamma\epsilon$. (Courtesy F.J. Decker, 1999.)

In the later years of SLC operation, typical oscillation amplitudes were of the order of 100 or 200μm, comparable to the presumed structure misalignments.

4.3.4 Dispersion-Free Steering

A very efficient steering algorithm has been developed in order to minimize the dispersive emittance growth in a linac. By its effect, this method is known as 'dispersion-free steering' [30,31]. The basic idea of the method is to steer the orbit such that the particle trajectories become independent of the particle energy. In practice this can be achieved, for example, by exciting the steering coils in order to minimize the orbit response to a constant relative change of all quadrupole strengths.

In the routine implementation of this method at the SLC, the strength of the quadrupole magnets was not varied, however. Instead, advantage was taken of the fact that both electron and positron bunches traversed the same linac. As far as dispersion is concerned, a change in the sign of the charge is equivalent to a 200% energy error.

The so-called two-beam dispersion free-steering then consisted in measuring the orbit of both electron and positron beams, and correcting the absolute orbit offset of one beam as well the difference to the orbit of the other beam. At the same time, the overall excitation strength of the steering correctors was also constrained. This steering method was implemented in the SLC control system by means of an SVD algorithm, where weighting factors could be assigned to the different minimization constraints.

4.4 Space Charge Compensation in Photoinjectors

Nowadays, photoinjectors, rather than thermionic injectors, are used for all applications requiring the combination of high-peak current and low emittance [32]. After the electron emission from the cathode, at low energies, space charge forces are very important. Scaling arguments, supported by simulations, show that after a drift distance s the transverse emittance growth for a drifting `slug' beam of length L and radius a with peak current I is [33,32]

$$\epsilon_{x\,N} \approx \frac{eIs}{16\pi\epsilon_0 m_0 c^3 \gamma^2 \beta^2}\, G\left(\frac{\gamma L}{a}\right) \tag{4.55}$$

The geometric factor G depends on the longitudinal distribution. In the long-bunch limit, if the radial distribution is uniform, G can be calculated to be 0.556 for a Gaussian longitudinal distribution and 0.214 for a parabolic distribution.

The radial space-charge force is a function of position within the bunch. Following [32] we introduce cylindrical coordinates ρ and ξ within the bunch, $\rho = 1$ defining

the radial edge, and $\xi = \pm 1$ the longitudinal ends. There is no emittance growth if the radial force is linear in ρ and independent of ξ [32],

$$\Lambda(\rho, \xi, t) = \frac{eE_r(\rho, \xi, t)}{m_0 \gamma^3 \beta^2 c^2} = \rho_0 \Lambda_0(t), \tag{4.56}$$

where Λ is the normalized force and E_r the radial electric field in the laboratory frame.

If the longitudinal bunch distribution is not constant, this condition is not fulfilled, and there will be a growth in the transverse emittance because different slices of the beam experience different radial space-charge forces. It is the projected emittance that increases, while the emittance of each short slice remains constant. In phase space the slices rotate against each other.

Now there exists an elegant method by use of a focusing solenoid to realign the different slices in the same phase space direction, and thus to recover the original emittance.

Consider again a slug beam. For simplicity, we assume that the space-charge force does not vary in time. If initially the beam is non-divergent and has a radius r_0, a point in the slug will obey non-relativistic transverse motion:

$$r(\rho, \xi) = \rho r_0 + \Lambda(\rho, \xi) \frac{z^2}{2} \tag{4.57}$$

and

$$r'(\rho, \xi) = \Lambda(\rho, \xi) z \tag{4.58}$$

at a distance z downstream. Now put a lens at a position $z = z_l$ with a focal length of [32]

$$f = \frac{z_d^2}{2(z_l + z_d)} \tag{4.59}$$

Then, at position z_d further downstream from the lens, the ratio of the beam divergence to the radius is

$$\frac{r'(\rho, \xi)}{r(\rho, \xi)} = \frac{2(z_l + z_d)}{z_d(z_d + 2z_l)} \tag{4.60}$$

which is independent of the particle's motion within the bunch. Thus the effect of the lens was to back-rotate the slices along the bunch with respect to each other so that they are re-aligned at a total distance $z_l + z_d$.

Ex.4.4. Solenoidal focussing
Verify Eq. (4.60).

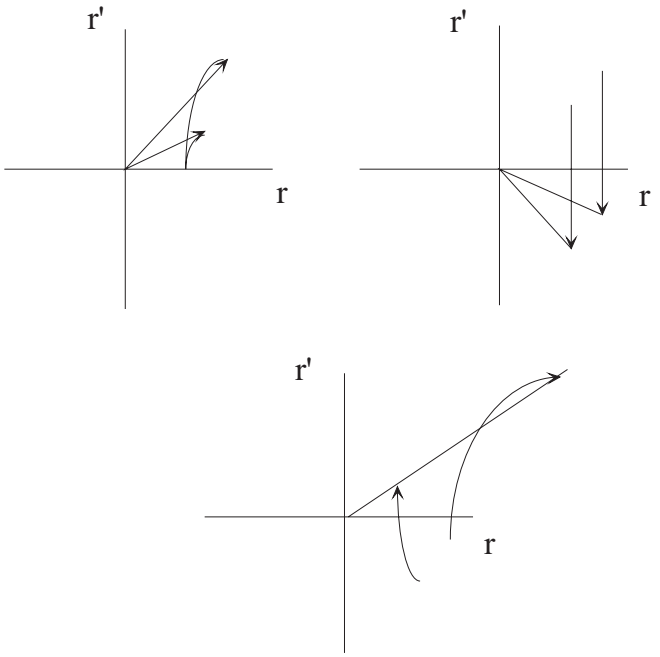

Figure 4.6: Space charge compensation in photoinjectors. The two arrows illustrate the particle motion at the center and at the end of the bunch: (1) after initial drift, (2) after solenoid focusing, (3) after final drift until slice emittances are realigned. [32].

The normalized emittance can be written as[32]

$$\epsilon_{x,y} = \frac{1}{2}\beta\gamma\sqrt{<\Lambda^2><\rho^2> - <\Lambda\rho>^2}\ \left(2r_0(z_l + z_D) - \frac{z_d^2 r_0}{f}\right) \qquad (4.61)$$

which confirms that the emittance can vanish with the proper choice of lens. The compensation recipe is illustrated schematically in Fig. 4.6.

In reality the physics is not quite so simple. In particular, the space-charge force is not constant, resulting in a residual nonzero emittance. Nevertheless, in experiments at Los Alamos[32] the above compensation scheme was shown to reduce the normalized rms emittance by up to an order of magnitude.

Let us assume the beam is focused to a beam-radius minimum. If the space-charge forces are weak, all particles cross through the beam's center. This can be called a *crossover*[32]. On the other hand, for strong space-charge forces, the particles

will be deflected away from the center. This may be called a *waist*[32], but be careful not to confuse this with the notion of beam waist used to describe a generic position of minimum beam radius. In general, parts of the bunch will have a high density and particles there will experience a waist, while particles in the other parts will crossover. Indeed there exist particles at the border between these two regions, which are initially extremely close together and later on will be a finite distance apart. This is called a phase-space *bifurcation*[32].

The space-charge induced emittance growth can only be compensated for those particles which do not cross over, and only for those the above approximations can apply. Therefore, one of the most important design criteria for photoinjectors is to minimize the fraction of the beam crossing over.

The technique described here may be generalized to other situations where one wants to correct a correlated growth in the projected emittances, that is induced by a nonlinear force.

4.5 Collimation and Beam Halo

4.5.1 Linear Collider

In general, the beam entering the beam delivery system of a linear collider is not of the ideal shape, but it can have a significant halo extending to large amplitudes, both transversely and longitudinally. There are many sources of beam halo:

(1) beam-gas Coulomb scattering,

(2) beam-gas bremsstrahlung,

(3) Compton scattering on thermal photons[34],

(4) linac wakefields,

(5) the source or the damping ring

The halo generation due to (1) will be reduced by a higher accelerating gradient, while the halo formation due to (2) and (3) scales with the length of the accelerator. The contributions of (4) and (5) to the halo size depend on many parameters; in a first, very rough approximation, if measured as a fraction of the bunch population, they could be considered as constant, independent of energy. A Monte-Carlo simulation study of beam loss in the NLC beam-delivery system due to the first three processes and the positive effect of additional collimators is described in reference[35].

If halo particles hit the beam pipe or magnet apertures close to the interaction point, or if they traverse the final quadrupole magnets at a large transverse amplitude,

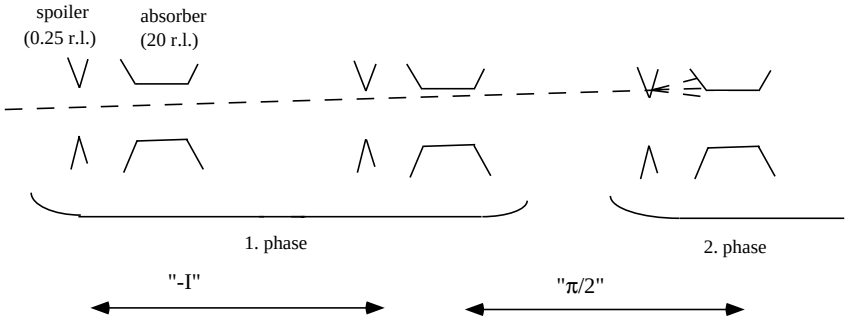

Figure 4.7: Schematic of a conventional collimation system, consisting of a series of spoilers and absorbers. The size of the spoilers and absorbers is approximately 1/4 and 20 radiation lengths, respectively.

they may cause unacceptable background. This background can be due to muons, electromagnetic showers, or synchrotron radiation.

In particular, muons, with a large mean free path length, are difficult to prevent from penetrating into the physics detector. According to the SLC experience, 1 muon per pulse entering the detector corresponds to a marginally acceptable background. Muons are produced when electrons and positrons impinge on apertures. The muon generation occurs by a variety of mechanisms, the most important one being the Bethe-Heitler pair production[36]: $\gamma Z \rightarrow Z\mu^+\mu^-$. On average about one muon is produced for every 2500 lost electrons. Differential cross sections for muon production were derived by Tsai[37], and are used in simulations of the muon-related background [36].

At the Stanford Linear Collider (SLC), collimation upstream of the final focus was found to be essential for smooth operation and for obtaining clean physics events. In addition, large magnetized toroids had to be placed between the location of the collimators and the collision point to reduce the number of muons reaching the detector. When a muon passes through such a toroid it scatters, loses energy, and its trajectory is bent. A complex collimation system and muon toroids will also be indispensable for future linear colliders[38,39].

A conventional collimation system proposed for future linear colliders consists of a series of spoilers and absorbers, which serve two different functions: they remove particles from the beam halo to reduce the background in the detector, and they also protect downstream beamline elements against missteered or off-energy beam pulses. The spoilers increase the angular divergence of an incident beam so that the absorbers can withstand the impact of an entire bunch train[38]. A schematic is shown in Fig. 4.7.

Collimator shape (surface angle) and material should be chosen so as to minimize the fraction of re-scattered particles[46]. A further design criterion are collimator wake fields[50]. An important requirement determining the system length is also that the collimators have to survive the impact of a bunch train. This requires a large spot size, in order that the collimator surface does not fracture or that the collimator does not melt somewhere inside its volume. For the NLC parameters, fracture and melting conditions give rise to about the same spot-size limit (roughly $10^5/\mu\mathrm{m}^2$ for a copper absorber at 500 GeV[38]). While the surface fracture does not depend on the beam energy, the melting limit does, since the energy of an electromagnetic shower deposited per unit length increases in proportion to the beam energy. Therefore, for energies above a few hundred GeV, the beam area at the absorbers must increase linearly with energy. Since, in addition, the emittances decrease inversely proportional to the energy, the beta functions must increase not linearly but quadratically. Assuming that the system length l scales in proportion to the maximum beta function at the absorbers, this results in a quadratic dependence of the system length on energy: $l \propto \gamma^2$. Counting both sides of the IP, the NLC collimation system is 5 km long. At 5 TeV the length of a conventional collimation system could approach 50 km.

Presently, ideas for shorter and indestructible collimation schemes are being pursued, such as laser collimation[40] and nonlinear resonant collimation[41].

4.5.2 Storage Rings

Also the performance of storage rings can be limited by beam halo. At electron or positron rings the halo arises from beam-gas Coulomb scattering, beam-gas bremsstrahlung, beam-beam resonances and at high energies also from Compton scattering on thermal photons. In the case of proton or ion rings, halo may be caused by space-charge forces, injection errors, diffusion driven by magnet nonlinearities or by the beam-beam interaction. A collimation system proved invaluable at the HERA proton ring [42], and an advanced two-stage collimation system is contemplated for the LHC[43]. The halo normally extends in both transverse and in the longitudinal direction, and collimation may be needed in all three planes.

The performance of LEP1 at 45.6 GeV (Z production) was limited by unstable transverse tails generated by the beam-beam interaction. Associated with these tails were a drop in the beam lifetime and background spikes (involving electromagnetic showers and hard synchrotron radiation from low-β quadrupoles), which frequently tripped the experiments. The partial cure consisted in changing tune and chromaticity, increasing the emittance (via a shift in the rf frequency), and opening the collimators. A lesson learnt was that scraping into the beam halo close to the experiments had to be avoided.

For the higher energies and shorter damping times at LEP2 (80–100 GeV), back-

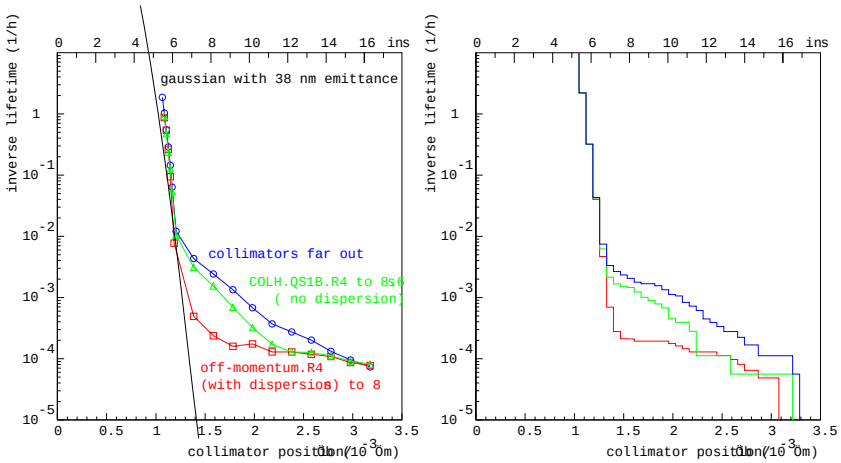

Figure 4.8: Beam tails in LEP2 at 80.5 GeV: (left) measurement using movable scrapers at dispersive and nondispersive locations, and (right) result of Monte-Carlo simulation[44,45]. (Courtesy H. Burkhardt, 1999.)

ground spikes are no longer observed. Stationary tails due to beam-gas scattering and thermal-photon scattering were however still present. Figure 4.8 compares a measurement of the beam tails in LEP using movable scrapers and the result of a Monte-Carlo simulation.

An important scattering process for electron beams is beam-gas bremsstrahlung. The differential cross section for this process is

$$\frac{d\sigma}{dk} = \frac{A}{N_A X_0}\frac{1}{k}\left(\frac{4}{3} - \frac{4}{3}k + k^2\right) \tag{4.62}$$

where k denotes the ratio of the energy of the emitted photon and the beam energy: $k = E_\gamma/E_b$, X_0 is the radiation length ($X_0 \propto A/(Z(Z+1))$ or roughly $\sigma \propto Z^2$). For carbon monoxide molecules: $A/(N_A X_0) = 1.22$ barn, and the total cross section for en energy loss larger than 1% evaluates to 6.5 barn (2.9% barn for an energy loss larger than 10%)[46]. For a gas pressure of 1 nTorr at a temperature of 300 K, the scattering probability is 2×10^{-14} m^{-1}.

The effect of elastic Coulomb collisions can also be significant. Here, the incident particles can scatter off the nucleus or the atomic electrons. In the former case, the energy change of the incident particle is relatively small and the primary effect is an angular deflection that may cause the particle to exceed the beam-pipe aperture. In comparison, the energy change can be significant when scattering off the atomic electrons.

The differential cross-section for Coulomb scattering on atomic nuclei can be written:

$$\frac{d\sigma_{en}}{d\Omega} = \frac{4F^2(q)Z^2r_e^2}{\gamma^2}\frac{1}{(\theta^2+\theta_{min}^2)^2} \tag{4.63}$$

where θ_{min} is a function of the screening due to the atomic electrons, equal to $\theta_{min} \approx \hbar/pa$ where p is the incident particle momentum and a is the atomic radius: $a \approx 1.4\lambda\!\!\!^{-}_e/\alpha Z^{1/3}$. In addition, $F(q)$ is the nuclear form factor which for relatively small scattering angles can be approximated by 1 and we have neglected the recoil of the nucleus; both of these later effects will reduce the large angle scattering and will cause a slight overestimate of the scattering effect.

A further type of Coulomb collision is the elastic scattering with the atomic electrons. Here, the angular deflection can be roughly accounted for by replacing Z^2 with $Z(Z+1)$ in Eq. (4.63); again this will over-estimate the scattering but is a small correction anyway. However, in this case the recoil of the electron cannot be neglected and can result in a significant energy change to the incident particle. The differential cross-section for a relative energy change of δ is[47]:

$$\frac{d\sigma_{ee}}{d\delta} = \frac{2\pi Zr_e^2}{\gamma}\frac{1}{\delta^2} \tag{4.64}$$

and the cross section for scattering beyond a limiting energy aperture δ_{min} is:

$$\sigma_{\delta_{min}} = \frac{2\pi Zr_e^2}{\gamma}\frac{1}{\delta_{min}}\,. \tag{4.65}$$

At ultra-high energies (several 10s of GeV) also the Compton scattering on thermal photons becomes significant[34,48]. The photon density from Planck black-body radiation is

$$\rho_\gamma = \frac{2.4(k_BT)^3}{\pi^2(c\hbar)^3} \approx 20.2\,\left[\frac{T}{\mathrm{K}}\right]^3\,\frac{1}{\mathrm{cm}^3} \tag{4.66}$$

or, at room temperature,

$$\rho_\gamma(T = 300\mathrm{K}) \approx 5\times10^{14}\ \mathrm{m}^{-3}. \tag{4.67}$$

The scattering cross section is of the order of the Thomson cross section, $\sigma_T \approx 0.67$ barn. If all scattered particles are lost, the beam lifetime would be

$$\tau_{beam} \approx \frac{1}{\rho_\gamma c\sigma_T} \tag{4.68}$$

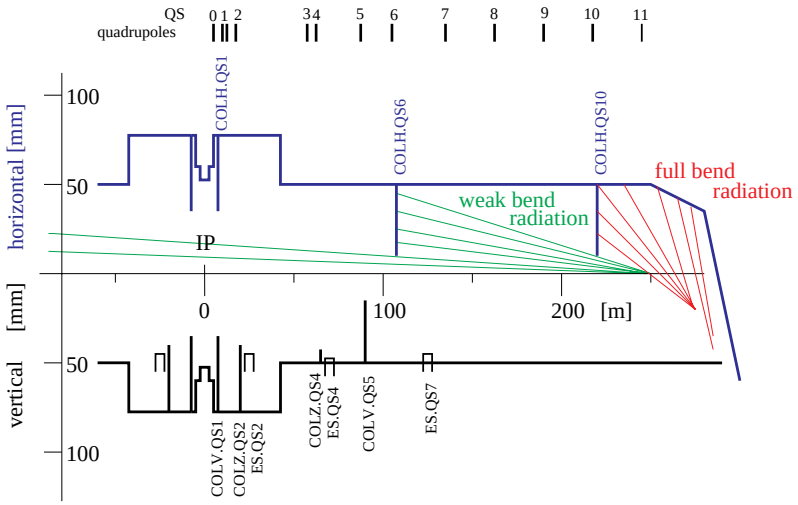

Figure 4.9: Layout of the straight section around IP4 or IP8 in the horizontal and vertical planes. Shown are the quadrupoles (QS), electrostatic separators (ES), and collimators/masks (COLH, COLV, COLZ). The solid lines mark the inner vacuum chamber radii for the LEP1 layout[49,46]. (Courtesy H. Burkhardt, 1999.)

Ex.4.5. Particle loss due to thermal photons
a) Estimate the beam lifetime due to scattering on thermal photons in LEP at $T = 300$ K, and for a storage ring with a vacuum chamber cooled to 4 K.
b) Consider an NLC-like beam with 10^{12} electrons per bunch train. How many particles per train are scattered on thermal photons (T=300K) over a linac length of 10 km?

The synchrotron radiation of electron (or positron) beams has to be kept away from the experiment. Both LEP and SLC achieved this by weakening the last bending magnets closest to the interaction point by a factor $\sim$10, which reduces the critical energy of the emitted photons as well as the number of photons emitted per unit length, and by installing radiation masks, which absorb the synchrotron radiation of the weak bend as well as that from the upstream strong bending magnets. The layout of bends and synchrotron masks for LEP is illustrated in Fig. 4.9.

Radiation collimators and masks around each LEP experiment provide a complete shield against direct photons and also against singly scattered synchrotron radiation, as illustrated in Fig. 4.10. For this reason, at LEP residual background arose mainly from multiply scattered radiation. Specular reflection of soft X rays is close to 100% at angles of incidence smaller than a so-called critical angle θ_c, with the angle measured between the photon direction and the plane of impact. The critical angle is

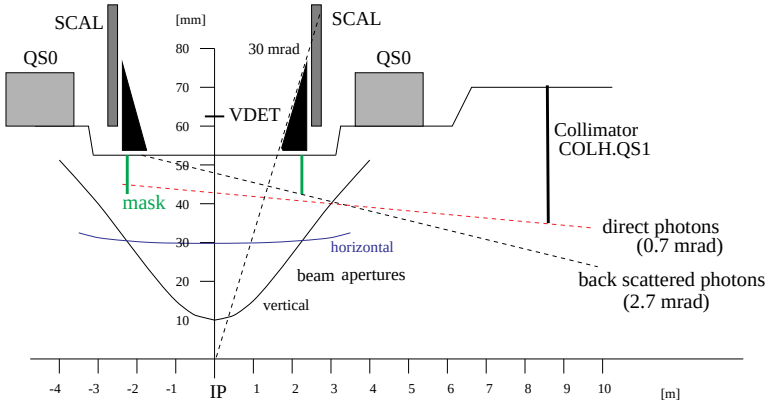

Figure 4.10: Schematic of the synchrotron radiation masks around a LEP IP, indicating the constraints for a mask solutions: (1) to stay outside the required LEP aperture (solid lines), (2) to cast a shadow over the entire unshielded IP beampipe length for small angle backscattered photons (dashed), (3) to stay outside of the very intense beam of direct photyons collimated by the (8.5 m) synchrotron radiation collimator, when closed to 12 σ of the transverse beam distribution[49,46]. (Courtesy H. Burkhardt, 1999.)

roughly

$$\theta_c \approx 30 \text{ mrad } \frac{\text{keV}}{E_\gamma}. \tag{4.69}$$

For a photon energy of 30 keV it is equal to about 1 mrad. Photons of this energy would still have a 95% chance of penetrating through a 1-mm Be layer. Multiple photon reflection can be reduced by coating or roughening of the vacuum chamber surface.

4.6 References

1. G. Ripken, F. Willeke, “On the Impact of Linear Coupling on Nonlinear Dynamics”, DESY 90-001 (1990).
2. G. Ripken, “Untersuchungen zur Strahlführung und Stabilität der Teilchenbewegung in Beschleunigern und Storage-Ringen unter strenger Berücksichtigung einer Kopplung der Betatronschwingungen”, Int. Rep. DESY R1-70/4 (1970).
3. D.A. Edwards and L.C. Teng, “Parametrization of Linear Coupled Motion in Periodic Systems”, IEEE Trans. on Nucl. Sc. 20, p. 885 (1973).
4. L.C. Teng, “Concerning n-dimensional coupled Motion”, Fermilab internal report FN 229 (1971).
5. F. Willeke and G. Ripken, “Methods of Beam Optics”, Cornell Summer School, AIP Proceedings 184, and DESY 88-114 (1988).
6. G. Guignard, “The General Theory of All Sum and Difference Resonances in a Three-Dimensional Magnetic Field in a Synchrotron”, CERN 76-06 (1976).
7. T. Raubenheimer, “Tolerances to Limit the Vertical Emittance in Future Storage Rings”, Part. Acc. 36, p. 75 (1991).
8. P. Bryant, “A Simple Theory for Weak Betatron Coupling”, CERN Accelerator School, CERN 89-05 (1989)
9. M.G. Minty, H. Hayano and F. Zimmermann, “Measurements of Betatron Coupling at the ATF Damping Ring”, ATF internal report, in preparation (1998).
10. G. Bourianoff, S. Hunt, D. Mathieson, F. Pilat, R. Talman, G. Morpugo, “Determination of Coupled-Lattice Properties Using Turn-by-Turn Data”, Proc. of the workshop on the stability of particle motion in storage rings, Upton, NY 1992, AIP Conference Proceedings 292 (1992).
11. J. Seeman *et al.*, unpublished (1997).
12. M. Minty, C. Adolphsen, L.J. Hendrickson, R. Sass, T. Slaton, M. Woodley, “Feedback Performance at the Stanford Linear Collider”, Proc. of IEEE PAC 95, Dallas (1995).
13. F. Zimmermann, M.G. Minty and H. Hayano, ”Measurements of Betatron Coupling at the ATF Damping Ring”, SLAC/AAS-95 and KEK ATF Internal Report ATF 98–22 (1998).
14. G. Guignard, “Adjustment of Emittance Ratio by Coupling Control in Electron-Positron Storage Rings”, Proc. of 11th International Conference on High-Energy Accelerators, Geneva, p. 682 (1980).
15. M. Mitsuhashi, lecture presented at the US-CERN-Japan-Russian School on Beam Measurement, Montreux, Switzerland(1998).
16. IMSL, Inc., “STAT/LIBRARY. FORTRAN subroutines for numerical analysis”, Houston, Texas (1991).

17. M. Minty and M. Woodley, “Summary of Accelerator Physics Studies at KEK/ATF”, ATF-98-12 (1998).
18. J.P. Koutchouk, “Linear Betatron Coupling Measurement and Compensation in the ISR”, CERN ISR-OP/80-27, also published in the Proc. XIth Int. Conf. on High Energy Accelerators, CERN, Geneva, Birkhäuser Verlag, Basel, p. 491 (1980).
19. H. Wiedemann, “Particle Accelerator Physics”, Springer-Verlag, Berlin (1993).
20. M. Sands, “The Physics of Electron Storage Rings”, SLAC-121 (1970)
21. K. Robinson, Phys. Rev. 111, p. 373 (1958).
22. M. Minty, *et al*, “Emittance Reduction via Dynamic RF Frequency Shift at the SLC Damping Rings”, 17th Intnl. Conf. on High Energy Accelerators (Dubna, Russia 1998).
23. R. Akre, F.J. Decker, M.G. Minty, “RF Frequency Shift during Beam Storage in the SLC Damping Rings”, presented at 1999 IEEE PAC New York (1999).
24. T.O. Raubenheimer, L.Z. Rivkin, R.D. Ruth, “Damping Ring Designs for a TeV Linear Collider”, DPF Summer Study Snowmass '88, and SLAC-PUB-4808 (1988).
25. A.M. Kondatenko and B.W. Montague, “Polarized Beams in LEP”, CERN ISR-TH/80-38 (1980).
26. K. Steffen, “An Alternative Interaction Geometry for HERA”, DESY HERA 81/17 (1981).
27. J.T. Seeman, F-J. Decker, I. Hsu, “The Introduction of Trajectory Oscillations to Reduce Emittance Growth in the SLC Linac”, presented at the XV International Conference on High Energy Accelerators, Hamburg, Germany (1992).
28. V. Balakin, A. Novokhatsky, V. Smirnov, Proc. 12th International Conference High Energy Accelerators, Fermilab (1983).
29. A. Chao, “Physics of Collective Beam Instabilities in High Energy Accelerators”, Wiley (1993).
30. T.O. Raubenheimer and R.D. Ruth, “A Dispersion-Free Trajectory Correction Technique for Linear Colliders”, Nucl. Instrum. Meth. A302, p. 191 (1991).
31. T. Raubenheimer, “A New Technique of Correction Emittance Dilutions in Linear Colliders”, Nucl. Instrum. Meth. A306, p. 61 (1991).
32. B.E. Carlsten, “Space-Charge Induced Emittance Compensation in High-Brightness Photoinjectors”, Part. Acc. 49, p. 27 (1995).
33. M.E. Jones and B.E. Carlsten, “Space-Charge Induced Emittance Growth in the Transport of High-Brightness electron Beams”, IEEE Part. Acc. Conf., Washington, D.C., p. 1391 (1987).
34. V.I. Telnov, NIM A260, p. 304 (1987).
35. I. Reichel, F. Zimmermann, T.O. Raubenheimer, P. Tenenbaum “Thermal Photon and Residual Gas Scattering in the NLC Beam Delivery”, International

Computational Accelerator Physics Conference (ICAP 98), Monterey (1998).
36. L.P. Keller, “Calculation of Muon Background in a 0.5 TeV Linear Collider”, contributed to the DPF Summer Study on High Energy Physics, Snowmass, CO (1990).
37. Y. Tsai, Rev. Mod. Phys., 46, 4, p. 815 (1974).
38. Zeroth Order Design Report for the Next Linear Collider, SLAC Report 474, p. 227-228 (1995).
39. S.S. Hertzbach, T.W. Markiewicz, T. Maruyama, R. Messner, “Backgrounds at the Next Linear Collider”, DPF and DPB Summer Study, Snowmass (1996).
40. F. Zimmermann, “New Final Focus Concepts at 5 TeV and Beyond”, invited talk presented at the 8th workshop on Advanced Accelerator Concepts, Baltimore, Maryland, 5 – 11 July, 1998, SLAC-PUB-7883 (1998).
41. P. Emma, R. Helm, Y. Nosochkov, R. Pitthan, T. Raubenheimer, K. Thompson, F. Zimmermann, ”Nonlinear Resonant Collimation for Future Linear Colliders”, presented at the 16th Advanced ICFA Beam Dynamics Workshop on Nonlinear and Collective Phenomena in Beam Physics, Arcidosso, Italy, and SLAC-PUB-7958 (1998).
42. M. Seidel, “The Proton Collimation System of HERA”, DESY-94-103 (1994).
43. J.B. Jeanneret, “Optics of a Two-Stage Collimation System”, Phys.Rev.ST Accel. Beams 1 (1998).
44. I. Reichel, “Transverse Beam Tails at LEP”, ICFA Beam Dynamics Workshop on e^+e^- Factories, Frascati (1997).
45. H. Burkhardt, I. Reichel, G. Roy, “Transverse Beam Tails due to Inelastic Scattering”, to be published.
46. H. Burkhardt, “Machine Background Common to All Machines”, invited talk at the International Workshop on Linear Colliders, Sitges, Barcelona (1999).
47. T.O. Raubenheimer, F. Zimmermann, “Final Focus Systems in Linear Colliders”, Submitted to Rev.Mod.Phys. (1998).
48. B. Dehning et al., Phys. Rev. Lett. B, p. 145 (1990).
49. G. von Holtey, A.H. Ball, et al., NIM A 403, p. 205 (1998).
50. K.L.F. Bane, C. Adolphsen, F.J. Decker, P. Emma, P. Krejcik, F. Zimmermann, “Measurement of the effect of Collimator Generated Wake Fields on the Beams in the SLC”, Proc. of 16th IEEE Particle Accelerator Conference (PAC 95) and International Conference on High Energy Accelerators, Dallas, Texas (1995).

Chapter 5

Longitudinal Optics Measurement and Correction

5.1 Synchronous Phase and Synchrotron Frequency

In a storage ring, a measure of the synchrotron frequency is useful to parameterize the relationship between energy lost and gained by a circulating beam. Relative to the synchronous particle (the hypothetical on-energy and nominal-phase particle), the equations of motion for small perturbations can be expressed in terms of the deviation of a particle within the bunch from the synchronous phase ϕ and the relative momentum deviation

$$\delta = \frac{p - p_0}{p_0}, \tag{5.1}$$

where p_0 is the momentum of the synchronous particle. The equations of motion are

$$\frac{d\phi}{dt} = \left(\alpha_C - \frac{1}{\gamma^2}\right)\omega_{rf}\delta, \tag{5.2}$$

where ω_{rf} is the angular accelerator frequency, $alpha_C$ the momentum compaction factor, γ the particle energy in units of the rest mass, and

$$\frac{d\delta}{dt} = \frac{eV'\beta^2}{\omega_{rf}ET_{rev}}, \tag{5.3}$$

where the derivatives are with respect to time, $\beta = v/c$ the velocity in units of the speed of light. The momentum compaction factor α_C is a property of the magnetic focussing lattice of the accelerator (typically in the range of 10^{-4}, for high brightness

accelerators and future storage rings, to 10^{-2} for existing storage rings). The quantity V' represents the restoring force supplied by the cavity to supress phase oscillations. Specifically, for a low current particle beam, it is the slope of the accelerating voltage evaluated at the particle position: with $V_c(t) = V_c \cos(\omega_{rf} t)$,

$$V' = -\omega_{rf} V_c \sin \phi_b(t), \tag{5.4}$$

where $\phi_b(t)$ denotes the phase of the beam with respect to the cavity voltage which is equal to the synchronous phase in the steady-state; i.e. averaging, $< \phi_b(t) >= \phi_s$.

The physical interpretation of the synchronous phase ϕ_s is shown in Fig. 5.1. In order to store the beam without losses, each particle of charge q must gain an amount of energy qV_c equal to the amount of energy lost. Sketched in the figure is the energy gain curve as a function of time. The cavity voltage V_c is drawn cosine-like: $\vec{V_c} = Re[V_c e^{\phi_c}] = V_c \cos \phi_c$, and the synchronous phase is measured with respect to the crest. The total loss is $\sum U = U_0 + U_{hom} + U_{par}$, where U_0 is the energy loss per turn per particle due to synchrotron radiation, U_{hom} is the loss due to higher order modes in the cavities, and U_{para} represents all other losses arising, for example, from the interaction of the beam with components of the vacuum system. From Fig. 5.1,

$$V_c \cos \phi_s = \sum U \tag{5.5}$$

or

$$\phi_s = \cos^{-1}\Big(\frac{\sum U}{V_c}\Big). \tag{5.6}$$

With this definition of ϕ_s (often the synchronous phase is defined with respect to the zero crossing), $\phi_s = \frac{\pi}{2}$ corresponds to zero energy loss.

The overvoltage factor $q = \frac{eV_c}{\sum U}$ is useful for parametrizing the energy acceptance of the accelerator. From reference[1], the low current energy aperture is given in the limit of a sinusoidal accelerating voltage by

$$\frac{\epsilon}{E_0} = \sqrt{\frac{U_0}{\pi \alpha_C h E_0} F(q)}, \tag{5.7}$$

where $h = \frac{f_{rf}}{f_{rev}}$ is the harmonic number and the aperture function $F(q)$ is

$$F(q) = 2[\sqrt{q^2 - 1} - \cos^{-1}(\frac{1}{q})]. \tag{5.8}$$

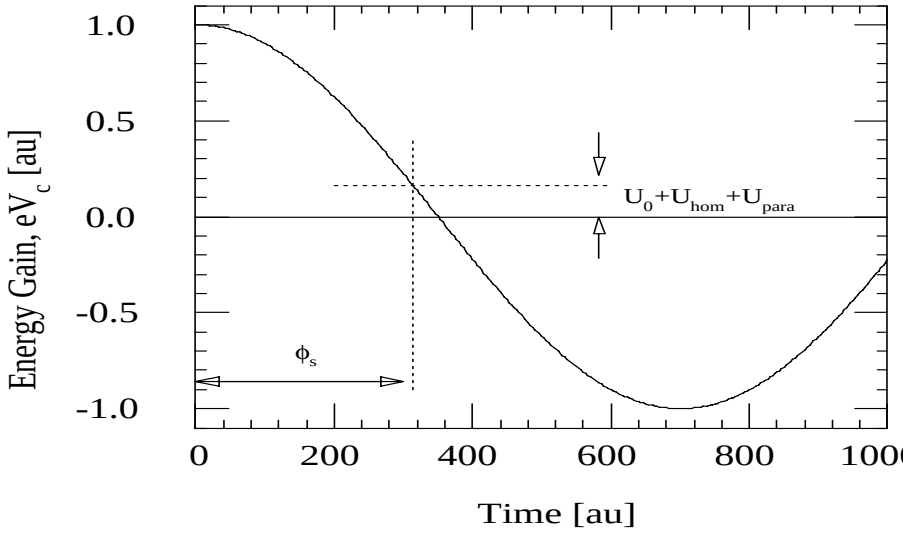

Figure 5.1: Energy gain as a function of time for a particle of charge e traversing a cavity of voltage amplitude V_c. The gain must equal to the total loss per turn, $\sum U = U_0 + U_{hom} + U_{para}$. The phase of the on-energy particle is the synchronous phase ϕ_s.

Ex.5.1. Review of Fourier transformations and application

a) Calculate the Fourier spectrum for two equal charge, macroscopic (i.e. the particle distribution can be represented as a δ-function), unequally spaced, interacting bunches assuming that the bunches have equal synchrotron oscillation amplitudes. That is, in the time domain, take the current distribution to be

$$i(t) = Q \sum_{n=-\infty}^{\infty} \left[\delta(t - nT - \tau_a \cos(\omega_s nT)) + \delta(t - nT - \frac{T}{2} - \Delta t - \tau_a \cos(\omega_s nT + \phi)\right], \tag{5.9}$$

where Q is the individual bunch charge, T is the revolution period, τ_a is the synchrotron oscillation amplitude, ω_s is the angular synchrotron frequency, Δt is the relative timing offset between the bunches, and ϕ is the relative phase between the two bunches. (Some useful properties of Fourier transformations are given below.)

b) Considering dipole mode oscillations only, sketch the frequency spectrum assuming $\Delta t = 0$ for "0-mode" oscillations (bunches oscillate in phase, that is $\phi = 0$) and for "π-mode" oscillations (for which the bunches oscillate out of phase; i.e. $\phi = \pi$). Show that these two normal modes of oscillation can be distinguished from one another by measuring the frequency spectrum.

c) Optional. Suppose you wanted to build a passive cavity to damp the π-mode oscillations. (At high beam currents the 0-mode oscillations are Robinson damped.) Considering cavity resonant frequencies in the range of $f_{rf} < f_0 < f_{rf} + 2f_{rev}$, what would be a suitable choice of resonant frequency for the passive cavity assuming (i) $\Delta t = 0$ or (ii) $\Delta t = \frac{2\lambda}{c}$, where λ is the rf wavelength?

Application of Poisson sum rule

$$\frac{1}{2\pi} \sum_{n=-\infty}^{\infty} e^{-2\pi j n(\frac{\omega}{\omega_r})} = \omega_r \sum \delta(\omega - n\omega_r) \tag{5.10}$$

Delta-function property

$$\int_{-\infty}^{\infty} f(t)\delta(t - x)dx = f(x) \tag{5.11}$$

Bessel function sum rule

$$e^{jz\cos\alpha} = \sum_{k=-\infty}^{\infty} j^k J_k(z) e^{jk\alpha} \tag{5.12}$$

The dc beam current I_{dc} is the amplitude of the zeroth rotation harmonic in the Fourier spectrum of the beam and represents an average beam current. It can be expressed in terms of the number of particles per bunch N_{ppb}, the number of bunches per train N_{bpt}, the number of trains N_t, the particle charge $e = 1.6 \times 10^{-19}$ C, the accelerating frequency f_{rf}, and the harmonic number h:

$$I_{dc} = N_t N_{bpt} N_{ppb} e \frac{f_{rf}}{h}. \tag{5.13}$$

Given the accelerator circumference C and f_{rf}, the harmonic number is known.

Eqns. 5.2 and 5.3 can be combined to give two second order, uncoupled equations:

$$\frac{d^2\phi}{dt^2} + {\omega_s}^2 \phi = 0 \tag{5.14}$$

and

$$\frac{d^2\delta}{dt^2} + {\omega_s}^2 \delta = 0. \tag{5.15}$$

Here $\omega_s = \sqrt{\frac{\alpha_C e V'}{ET}}$ is the angular synchrotron frequency.

The harmonic solutions to Eqs. 5.14 and 5.15 are represented by the small amplitude contours in the phase space ($\phi - \delta$ plane) plot given in Fig. 5.2. The constant energy trajectories are ellipses centered about the synchronous phase and energy. It is convenient to define the synchrotron tune ν_s by normalizing the measurable synchrotron frequency f_s to the beam revolution frequency f_{rev}:

$$\nu_s = \frac{f_s}{f_{rev}} = \sqrt{\frac{\alpha_C h V_c \sin\phi_s}{2\pi E}} \tag{5.16}$$

For the small amplitude oscillations shown in Fig. 5.2, a particle or bunch returns to the same place in this phase space in $\frac{1}{\nu_s}$ turns.

Since the arrival time of the particle at the BPM is modulated by the synchrotron frequency, synchrotron sidebands will appear off any harmonic of the revolution frequency. An example is shown in Fig. 5.3.

In a manner quite similar to the measurement of the betatron tunes, turn-by-turn BPM measurements may be recorded and Fourier analyzed to detect the arrival time modulation of the beam due to synchrotron oscillations provided the selected BPM is in a region of nonzero dispersion. A typical example was shown shown in Fig. 2.3.

5.2 Dispersion and Dispersion Matching

5.2.1 RF Frequency Shift

In most storage rings the dispersion function is inferred from the orbit change induced by a shift in the rf frequency. A frequency shift Δf_{rf} changes the beam energy by an

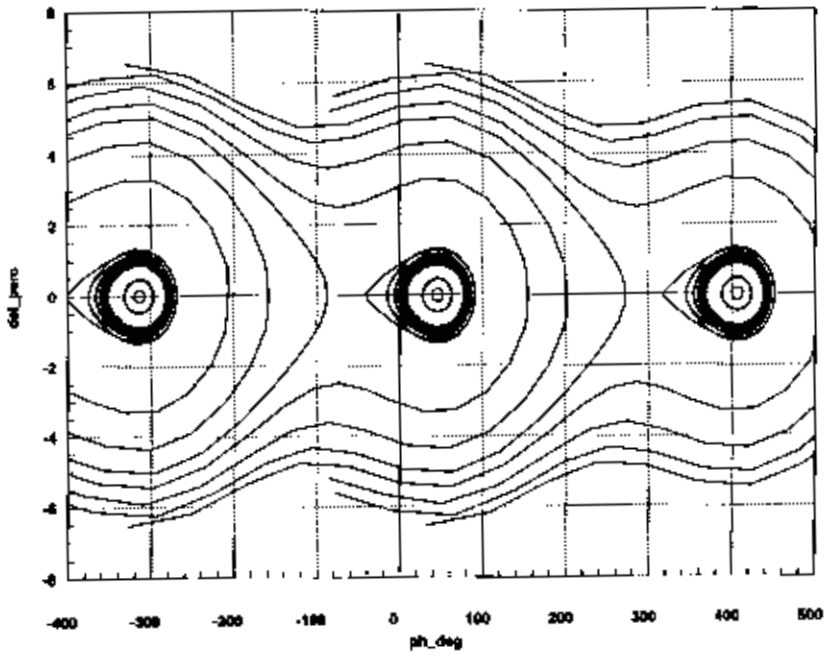

Figure 5.2: Longitudinal phase space for a low current bunch showing three separate rf buckets. The relative energy (in percent) is plotted as a function of phase (in degrees). The oscillator equations, Eqs. 5.14 and 5.15, describe the linear response for which the phase space trajectories are ellipses.

amount

$$\delta = -\frac{1}{\alpha_C - \gamma^{-2}} \frac{\Delta f_{rf}}{f_{rf}} \approx -\frac{1}{\alpha_C} \frac{\Delta f_{rf}}{f_{rf}}. \tag{5.17}$$

The last approximation, which ignores the change in particle velocity, is applicable for all electron rings. Combining Eqs. (5.18),

$$\Delta x(s) = \eta(s)\delta \tag{5.18}$$

and (5.17), we can relate the dispersion to the measured orbit change:

$$\eta(s) = \left(\gamma^{-2} - \alpha_C\right) \frac{\Delta x(s)}{\Delta f_{rf}/f_{rf}} \tag{5.19}$$

This `static' dispersion measurement is quite simple. It requires the capability of stably unlocking the ring rf frequency (*e.g.*, from the injector rf) and a minimum

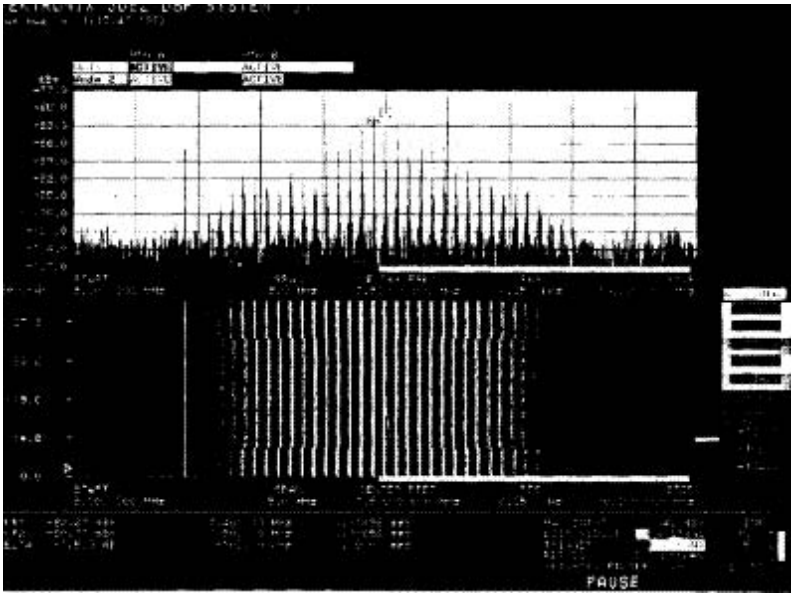

Figure 5.3: Measurement of multiple synchrotron sidebands at injection in the SLAC electron damping ring. The synchrotron frequency is given by the difference in frequency between the fundamental and one of the synchrotron sidebands.

energy aperture; by energy aperture we here mean the range over which f_{rf} can be changed without beam loss. The residual vertical dispersion is obtained from the vertical orbit shift, in quite the same way.

As an illustration, Fig. 5.4 shows a static dispersion measurement at the PEP-II HER.

5.2.2 RF Modulation

In very large rings, operating at high energy, the above method may not be applicable, because of a finite energy aperture and the lack of orbit reproducibility. At LEP, a dynamic measurement is applied[2]: the phase of the rf voltage is harmonically modulated at a frequency close to the synchrotron frequency and the frequency component of the induced (resonant) orbit variation at the synchrotron frequency is used to infer the dispersion function at each BPM.

The result of such a dynamic dispersion measurement is displayed in Fig. 5.5. If the dispersion at the cavities is nonzero, the dynamic measurement will give a result different from the static measurement[3]. The difference has the azimuthal pattern of

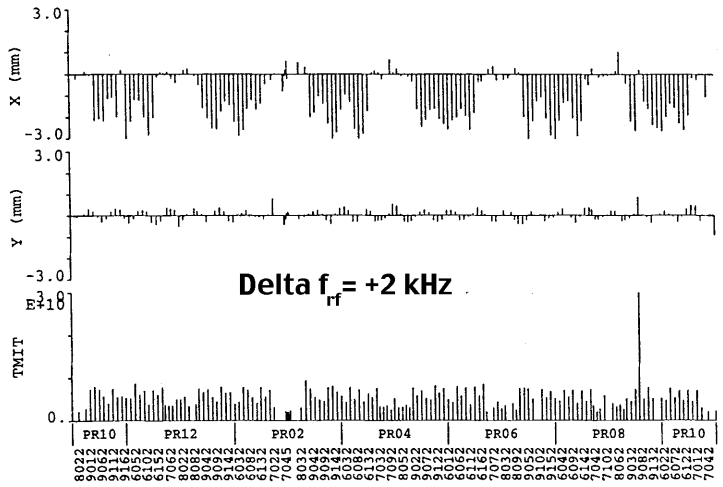

Figure 5.4: Static dispersion measurement on the PEP-II HER: the orbit change induced by a 2-kHz shift in rf frequency. The nominal rf frequency is 476 MHz; the harmonic number $h = 3492$; and the momentum compaction factor $\alpha_C \approx 0.0024$. (Courtesy U. Wienands, J. Seeman *et al*, 1998.)

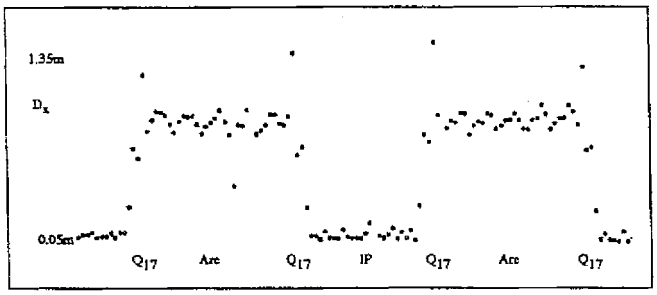

Figure 5.5: Dynamic dispersion measurement at LEP [2]: the rf voltage is modulated at the synchrotron frequency, and the dispersion deduced by a harmonic analysis of the beam response at each BPM. (Courtesy C. Bovet, 1998.)

a betatron oscillation, and it is clearly visible in the figure. At every location s, this component oscillates at the synchrotron frequency, but, in principle, a precise phase measurement from BPM to BPM could be used to correct for this effect.

In the arcs, the maximum value of this spurious dispersion is given by[3]:

$$|\Delta\eta|_{max} = \sqrt{\beta\mathcal{H}_0}\ \left|\frac{\sin(2\pi Q_s)\ \sin(\pi Q)}{\cos(2\pi Q_s) - \cos(2\pi Q)}\right|, \tag{5.20}$$

where Q and Q_s are the betatron and synchrotron tune, respectively, $\mathcal{H}_0$ is the dispersion invariant[1] in the straight section, and β the arc beta function.

5.2.3 RF Amplitude or Phase Jump

Similar dynamic schemes have been tested at the SLC and at the ATF damping rings. In both these rings, a longitudinal oscillation is induced by a shock excitation: either a sudden step-change to the rf voltage (at the SLC[4]) or a fast phase jump (at the ATF [5]). These methods can also give spurious results if there is residual dispersion at the rf cavities.

On the other hand, the dynamic schemes may be used to correct the synchrobetatron coupling by minimizing the spurious dispersion.

5.2.4 Higher-Order Dispersion in a Transport Line or Linac

The dispersion (or, more precisely, the R_{16} matrix element) in a transport line can be inferred from the measured variation of the beam orbit as a function of the incoming beam energy. We can extend the concept of dispersion by including higher-order nonlinear terms, of the form:

$$\Delta x(s) = R_{16}(s)\delta + T_{166}(s)\delta^2 + U_{1666}(s)\delta^3 \tag{5.21}$$

$$\Delta x'(s) = R_{26}(s)\delta + T_{266}(s)\delta^2 + U_{2666}(s)\delta^3 \tag{5.22}$$

Sufficiently large energy changes allow a measurement not only of the first-order dispersion matrix element, R_{16}, but also of the 2nd and 3rd order contributions, $T_{166}(s)$ and $U_{1666}(s)$.

Such measurements have been performed at the North ring-to-linac transfer line (NRTL) of the SLC. Under normal operation, the phase of the rf compressor at the entrance to the RTL is set so that the beam center passes at the zero crossing of the rf wave. For a dispersion measurement, the phase is shifted such that the beam center is positioned at the top of the rf crest, and the beam energy is varied by changing the amplitude of the rf voltage.

Figure 5.6 (top) shows the beam position on one of the RTL BPMs as a function of the beam energy. Clearly visible is a nonlinear dependence, which indicates the

presence of 3rd order dispersion. The value of the 3rd order dispersion at this BPM can be obtained by fitting a 3rd order polynomial to the measurement. Plotted in the bottom figure is the 3rd order dispersion function so obtained as a function of position along the RTL and the early part of the SLAC linac.

The large 3rd order dispersion led to undesired and irrecoverable emittance growth. To correct this, in 1991 two octupole magnets were installed which cancel the U_{1666} and U_{2666} terms. The optimum octupole strength was found by minimizing the linac emittance as a function of the octupole excitation. Such a measurement is shown in Fig. 5.7. The octupole setting for minimum emittance and the corresponding U_{1666} value are in good agreement with the 3rd order dispersion inferred from the BPM readings, which was depicted in Fig. 5.6 (bottom).

Ex.5.2. Adjusting the incoming beam energy

An off-energy beam will have orbit contributions $x_\eta = \eta\delta$ not unlike that shown in Fig. 5.4. For a proton beam, the dispersive offset will persist, whereas for electrons, the beam will naturally radiation damp to the on-energy equilibrium orbit. In either case, describe a procedure using difference orbits at fixed rf frequency for correcting the energy of the incoming beam. Hint: consider a beam injected perfectly into the center of an rf bucket and determine, at which turn one is maximally sensitive to beam energy deviations.

5.3 Momentum Compaction Factor

It is sometimes of interest to measure the momentum compaction factor α_C, Eq. (5.23),

$$\alpha_C = \frac{\Delta L/L}{\delta} = \frac{1}{L}\oint \frac{\eta(s)}{\rho(s)}\, ds., \tag{5.23}$$

for example, in storage rings operating near $\alpha_C = 0$.

5.3.1 Synchrotron Tune

If the rf voltage is well calibrated, one can use Eq. (5.24),

$$Q_s = \frac{f_s}{f_{rev}} = \sqrt{\frac{(\gamma^{-2} - \alpha_C)he\hat{V}\cos\psi_s}{2\pi c p_0}}, \tag{5.24}$$

where α_C is the momentum compaction factor, and $\hat{V}$ the amplitude of the rf voltage, to infer the momentum compaction factor from the measured synchrotron tune, taking into account that the synchronous phase angle ψ_s is also a function of the rf voltage. However, often the rf voltage calibration is not very accurate. In addition, if the ring accommodates several rf cavities, these may be not optimally phased with respect to

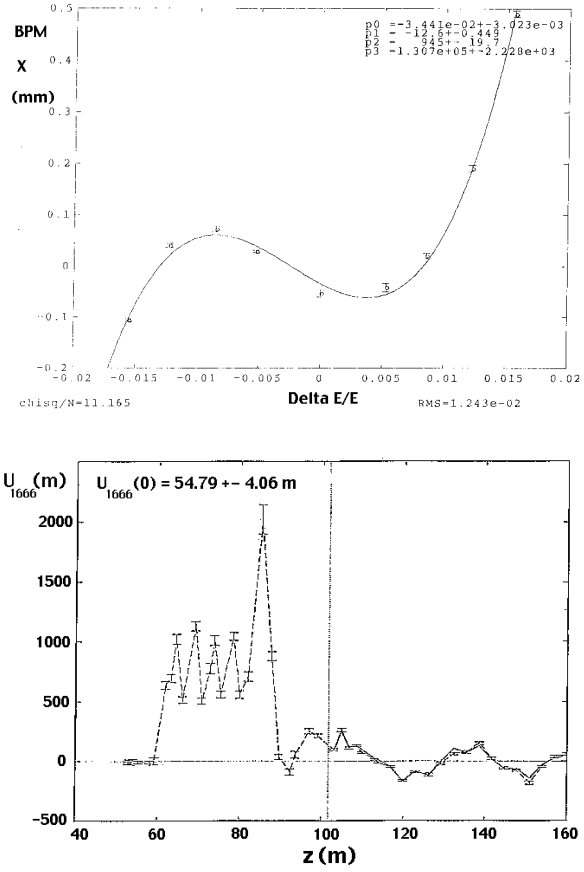

Figure 5.6: Evidence of 3rd order dispersion in the SLC ring-to-linac transfer line (RTL)[6]: (Top) BPM reading vs. beam energy; (bottom) 3rd order dispersion inferred for all BPMs in the RTL and in the early linac; the 3rd order dispersion in the linac is fitted to calculate the magnitude of the U_{1666} and U_{2666} matrix elements. (Courtesy P. Emma, 1998.)

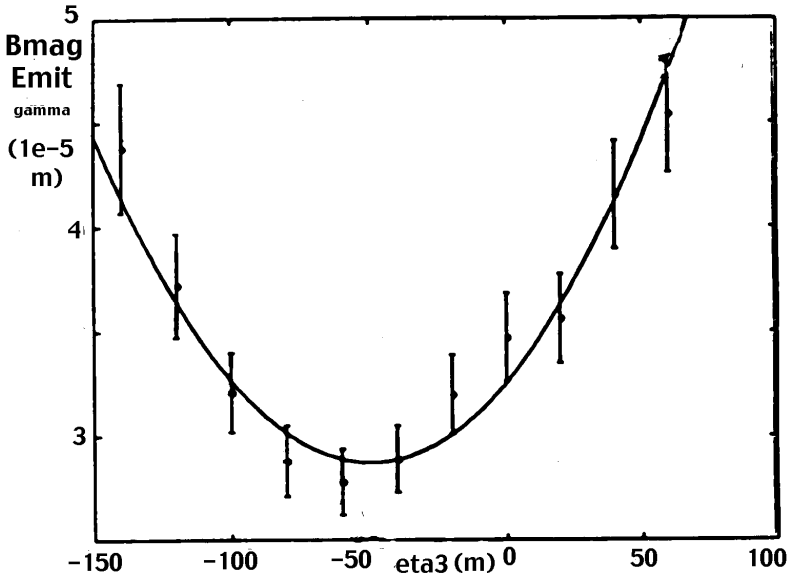

Figure 5.7: RTL emittance minimization with an octupole correcting the 3rd order dispersion. Shown on the horizontal axis is the octupole strength in units of the generated 3rd order dispersion (U_{1666}). The vertical axis represents the product of Bmag and normalized emittance in units of 10^{-5} m. The octupole strength for which the emittance is minimum agrees with the magnitude of U_{1666} estimated from the fit in Fig. 5.6 (bottom). (Courtesy P. Emma, 1998.)

each other, complicating the calculation of the total rf voltage. It is then advantageous to confirm the momentum compaction without having to assume a value for the rf voltage.

5.3.2 Bunch Length

The rms bunch length in an electron ring is proportional to α_C and to the rms energy spread[1], namely

$$\sigma_z = \frac{c\alpha_C}{2\pi Q_s f_{rev}}\sigma_\delta, \tag{5.25}$$

where c is the speed of light, and f_{rev} the revolution frequency. The rms energy spread can either be deduced from the measured decoherence of a transverse oscillation due to nonzero chromaticity and its subsequent recoherence after one synchrotron period [7], or it can be calculated from[1]

$$\sigma_\delta^2 = \frac{C_q < G^3 > \gamma^2}{J_\epsilon < G^2 >} \tag{5.26}$$

where $C_q = 3.84 \times 10^{-13}$ m, $G = 1/\rho$ the inverse bending radius, $< \ldots >$ indicates an average over the ring, γ is the beam energy in units of the particle rest mass, and J_ϵ the longitudinal damping partition number. The theoretical value for the latter could be verified by measuring either the horizontal emittance (which determines the horizontal partition number $J_x = 3 - J_\epsilon$) or the longitudinal damping time.

Plotting the bunch length as a function of the inverse synchrotron tune immediately gives the value of α_C as the slope [8]. Note that the synchrotron frequency $f_s = \omega_s/(2\pi)$ can be measured very precisely. Figure 5.8 shows a measurement of bunch length vs. synchrotron tune in PEP-II.

5.3.3 Lifetime

A different approach, also applicable for electron rings, is to measure the quantum lifetime[8], which in an electron storage ring is given by[1]

$$\tau_q = \frac{\tau_\delta}{2}\,\frac{e^\xi}{\xi}, \tag{5.27}$$

where τ_δ is the longitudinal damping time, and ξ is given by the ratio of the energy aperture δ_{max} and the relative rms energy spread σ_δ:

$$\xi = \frac{\delta_{max}^2}{2\sigma_\delta^2} \tag{5.28}$$

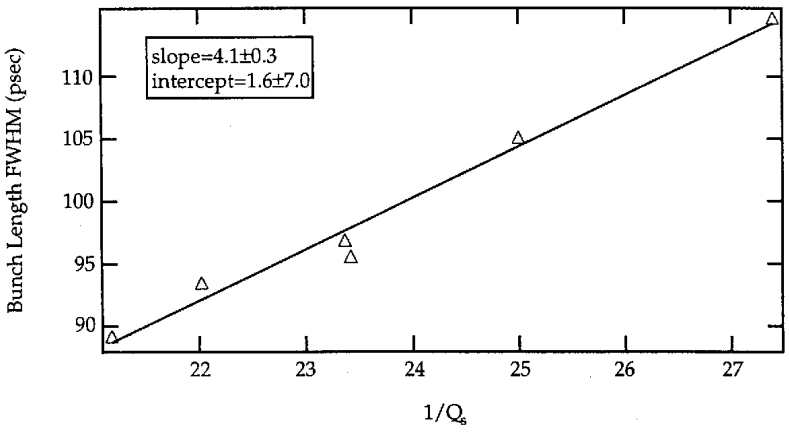

Figure 5.8: Rms bunch length in the PEP-II HER as a function of the inverse synchrotron tune[9]. The fitted slope determines the momentum compaction factor α_C, if the rms energy spread is known. (Courtesy U. Wienands, A. Fisher, J. Seeman *et al*, 1998.)

The energy aperture, if limited by the rf bucket size, is[1]

$$\delta_{max}^2 \approx \frac{eU_0}{\pi \alpha_C h E_0} F(q) \tag{5.29}$$

with

$$F(q) = 2\left(\sqrt{q^2-1} - \cos^{-1}(1/q)\right). \tag{5.30}$$

and

$$q = \frac{e\hat{V}}{U_0} \tag{5.31}$$

The term $U_0 = C_\gamma E_0^4 L < G^2 > /(2\pi)$, is the energy loss per turn, and $C_\gamma = 8.85 \times 10^{-5}$ m GeV^{-3}. A formula for the rms relative energy spread σ_δ was given in Eq. (5.26).

We may express σ_δ in terms of σ_z using Eq. (5.25), and in addition replace the rf voltage $\hat{V}$ in the definition of q by Q_s and α_C, making use of Eq. (5.24). We then arrive at an equation for the quantum lifetime τ_q in terms of the measurable quantities Q_s and σ_z, and the unknown parameter α_C. The latter can then be obtained from a fit to data taken at different rf voltages[8].

5.3.4 *Path Length vs. Energy*

The momentum compaction factor, or R_{56} matrix element, can also be measured directly by changing the beam energy at the entrance to the beam line of interest, and observing the shift in arrival time at the end of that section.

Such measurements were performed to fine-tune the optics in the nominally achromatic arc of the KEKB linac. The time of arrival at the exit of the arc was measured by a streak camera. The streak camera converts the time structure of a pulse of synchrotron radiation from a bend, or of optical transition radiation from a target, into vertical deflection at the CCD camera.

For the KEKB linac commissioning, the streak camera trigger signal was locked to the linac rf frequency upstream of the arc. The beam energy was varied by adjusting the voltage of the last klystrons prior to the arc. Figure 5.9 shows two measurements of the R_{56}, performed before and after the strengths of a few quadrupoles were adjusted to match the dispersion, as inferred from the energy dependence of the orbit. Figure 5.9 demonstrates that the dispersion match also eliminated the linear component of the R_{56}. The remaining path length dependence on energy is purely quadratic. In the future, it is planned to reduce this quadratic component, as well as the second order dispersion, by adjusting sextupole magnets.

5.3.5 *Beam Energy via Resonant Depolarization*

In electron storage rings with polarization the beam energy can be determined with a very high precision, using a resonant depolarization technique. The spin tune is given by

$$\nu_0 = a_e \gamma = \frac{E\,[\mathrm{MeV}]}{440.6486(1)\,[\mathrm{MeV}]} \tag{5.32}$$

where a_e is the electron anomalous magnetic moment. If a radially oscillating field generated by a coil is in resonance with the fractional part of the spin tune, the effect of the field adds up over many turns and the spin vector can be brought into the horizontal plane. The exact value of the resonance frequency determines the beam energy via Eq. (5.32).

With this technique, it is possible to very precisely measure the energy variation induced by a change in the rf frequency. The slope of this measurement gives the momentum compaction factor:

$$\frac{\Delta p}{p} = \frac{1}{\gamma^{-2} - \alpha_C} \frac{\Delta f_{rf}}{f_{rf}} \approx -\frac{1}{\alpha} \frac{\Delta f_{rf}}{f_{rf}} \tag{5.33}$$

An application of this technique at LEP is shown in Fig. 5.10

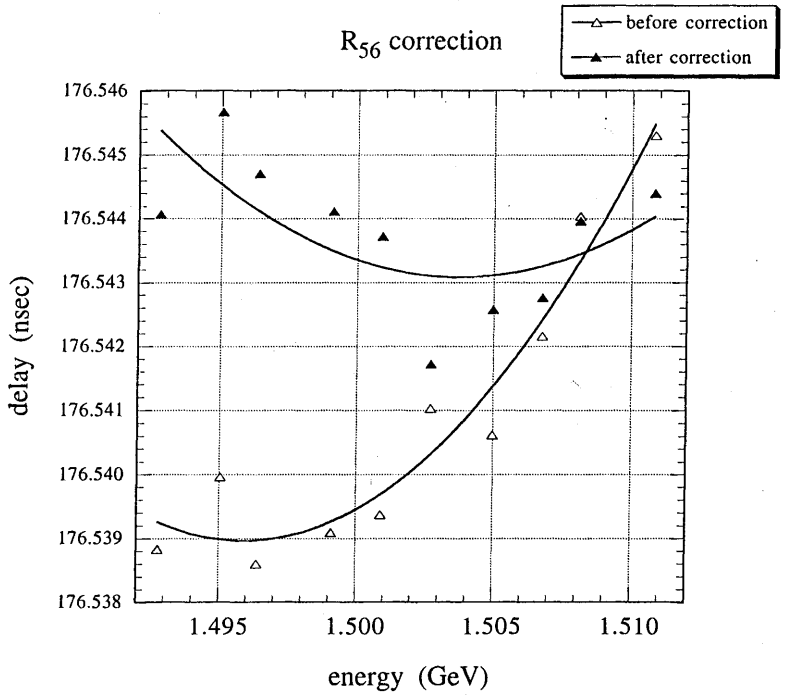

Figure 5.9: R_{56} measurement for the asynchronous arc of the KEKB linac, before and after dispersion correction, A streak camera was used to measure the arrival time (vertical axis) as a function of the beam energy. (Courtesy H. Koiso and K. Oide, 1998.)

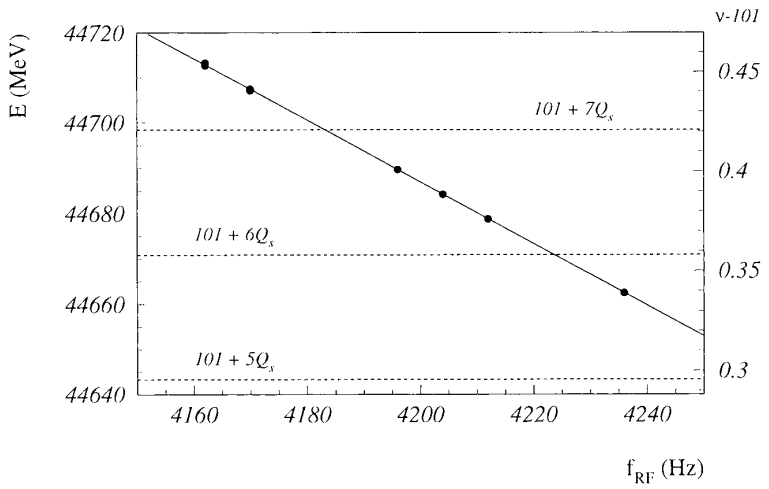

Figure 5.10: Change of beam energy, E, as a function of the rf frequency, f_{rf}, in LEP[10]. Only the last four digits of the rf frequency are shown (the nominal value is $f_{rf} = 352\ 254\ 170$ Hz). Several strong spin resonances are indicated by the dotted lines. From this measurement the momentum compaction factor was determined to be $(1.86 \pm 0.02) \times 10^{-4}$, which compared well with the calculated value of 1.859×10^{-4}. (Courtesy R. Assmann, 1998).

Ex.5.3. Resonant depolarization application
Resonant depolarization at the IUCF cooler ring was initially observed at a driving frequency slightly different from expectation assuming the beam energy. Using well-known kinematic reactions with an internal target, the beam energy was precisely determined. Show that the apparent discrepancy can be explained by a small adjustment to the assumed orbit circumference.

5.3.6 Change in Field Strength for Unbunched Proton Beam

The energy of an unbunched proton beam is constant. If the strength of all magnets (dipoles and quadrupoles) is increased by a factor $\Delta B/B$, the orbit moves inwards and the revolution time is reduced. This change in revolution period can be detected with a Schottky monitor[11]. The momentum compaction factor α then simply follows from the relation

$$\frac{\Delta T}{T} = -\alpha \frac{\Delta B}{B} \tag{5.34}$$

where T denotes the revolution period.

Ex.5.4. Approximate expression for α
Using the approximate formula for the average dispersion function

$$\langle \eta \rangle \approx \frac{\langle \beta \rangle}{\nu}, \tag{5.35}$$

and Eq. 1.15,
a) show that a good approximation for the momentum compaction factor is given by $\alpha \approx 1/\nu^2$. Give a numerical example.
b) Find an analogous expression for the transition energy γ_t using these approximations.

5.4 Chromaticity

5.4.1 RF Frequency Shift

The dependence of the focusing force on beam energy is generically referred to as chromaticity. In a storage ring this is characterized by the energy dependence of the betatron tunes, which is denoted as ξ.

The natural chromaticity due to the energy dependence of the quadrupole focusing is usually compensated by means of two or more sextupole families. Usually a total chromaticity close to zero is desired, as this minimizes the tune spread induced by chromaticity and finite energy spread, and also the amount of synchrobetatron coupling. The chromaticity should be slightly positive to avoid the head-tail instability. Since a positive chromaticity gives head-tail damping, sometimes ξ is intentionally increased in order to counteract beam instabilities.

The total chromaticity can easily be determined by measuring the tune shift as a function of the rf frequency f_{rf}.:

$$\xi_{x,y} = \frac{\Delta Q_{x,y}}{\Delta p/p} = \left(\gamma^{-2} - \alpha\right) \frac{\Delta Q_{x,y}}{\Delta f_{rf}/f_{rf}} \tag{5.36}$$

where α is the momentum compaction factor. As an example, Fig. 5.11 shows a chromaticity measurement performed at LEP.

5.4.2 Head-Tail Phase Shift

Recently, a new technique to measure the chromaticity was successfully tested at the CERN SPS [13]. A bunch was kicked transversely, and the linear head-tail phase shift $\Delta\phi_\beta$ as a function of arrival time Δt was measured half a synchrotron period later. The chromaticity is then obtained from the relation

$$\xi = -\frac{\omega_s \left(\alpha - \gamma^{-2}\right)}{2\omega_0} \frac{\Delta\phi_\beta}{\Delta t} \tag{5.37}$$

The advantage of this method is that it is very fast.

5.4.3 Natural Chromaticity

The natural chromaticity is the chromaticity that derives from the energy dependence of the quadrupole focusing. In other words it is the chromaticity the ring would have without sextupole magnets. Fortunately it is not necessary to turn off the sextupoles to measure the natural chromaticity. Rather the latter can be obtained by detecting the variation of the betatron tune as a function of the main dipole field strength. In this case, since the rf frequency and, hence, the total path length are unchanged, the orbit in the sextupoles remains approximately the same, and the sextupoles thus do not contribute to any tune change. (This is a good assumption for FODO lattices. However, it is conceivable that for certain low-emittance lattices, the orbit in the sextupoles might change when the dipole field strength is varied. This effect can be estimated with computer codes. One can also monitor the orbit stability at the sextupoles when the dipole field is varied.) However, the absolute beam energy E is changed in proportion to the field change: $\Delta E/E = \Delta B/B$. Thus, the natural chromaticity $\xi_{x,y}^{nat}$ is given by

$$\xi_{x,y}^{nat} \approx \frac{\Delta Q_{x,y}}{\Delta B/B} \tag{5.38}$$

A typical measurement is depicted in Fig. 5.12.

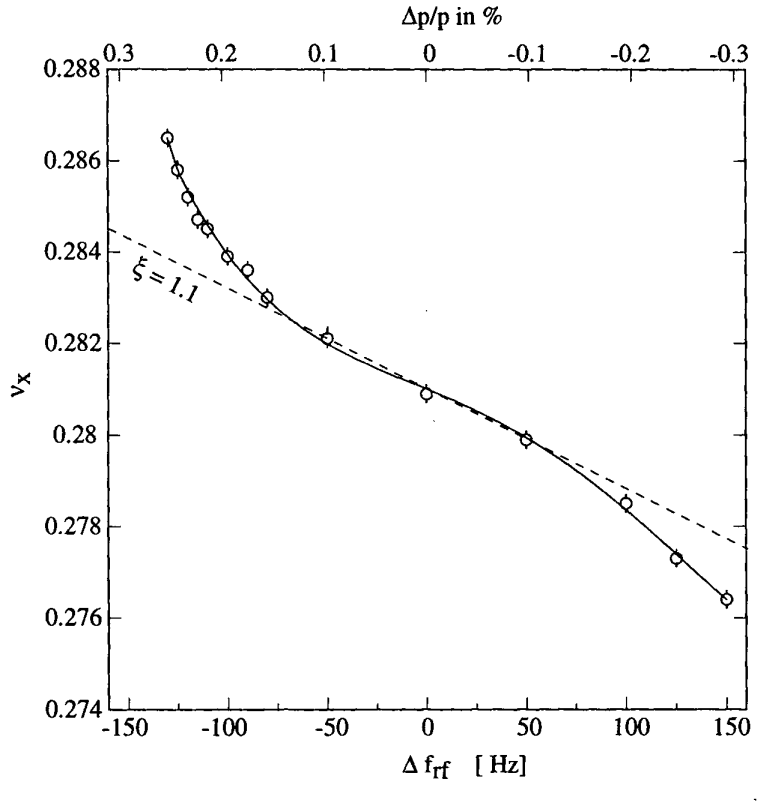

Figure 5.11: Horizontal tune as a function of the rf frequency change in LEP. Plotting symbols with error bars are the data. The dashed line is the linear chromaticity as calculated from tune measurements at $\Delta f_{rf} = \pm 50$ kHz. (Courtesy H. Burkhardt, 1998.)

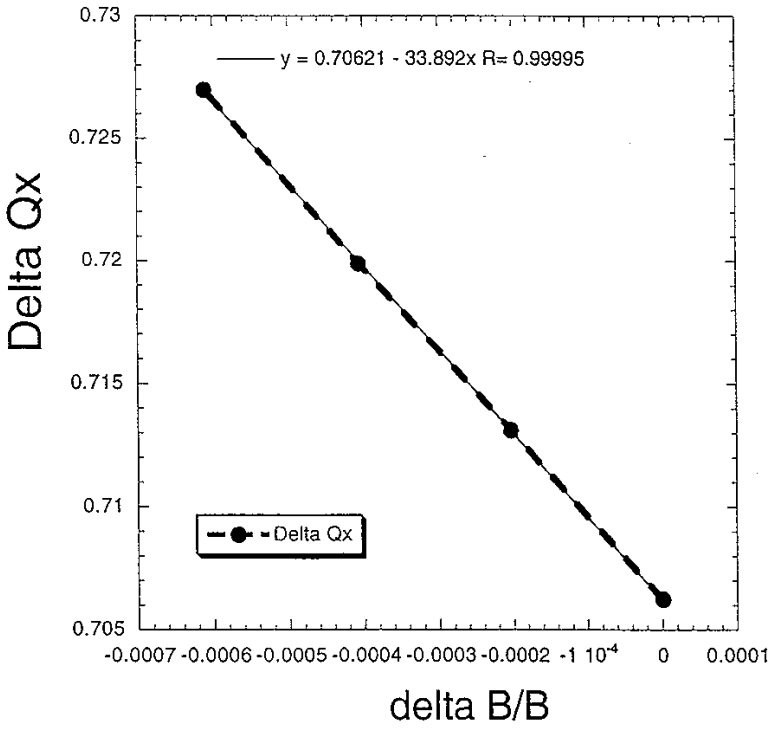

Figure 5.12: Measurement of the natural chromaticity in the PEP-II HER. Shown is the horizontal tune as a function of a relative variation in the main dipole field. The slope is the natural chromaticity. (Courtesy U. Wienands, J. Seeman *et al*, 1998.)

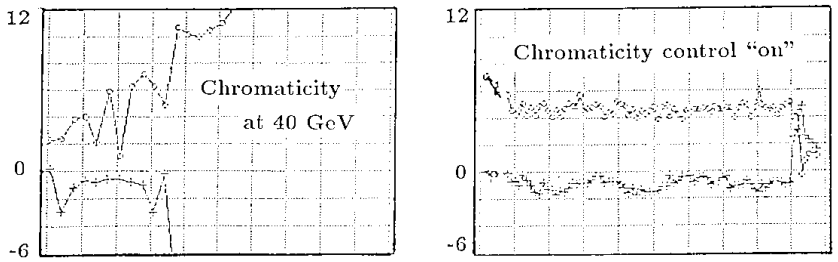

Figure 5.13: Variation of chromaticity in time, due to persistent-current decay without (left) and with (right) chromaticity control based on continuous measurements of the sextupole fields in two dipole reference magnets at the HERA proton ring. The horizontal axis is the time in units of 3 minutes per division. The vertical axis refers to the horizontal (upper trace) and vertical chromaticity (lower trace) in dimensionless units. (Courtesy B. Holzer, 1998.)

5.4.4 Local Chromaticity: $d\beta/d\delta$

Measuring the beta functions (*e.g.*, with the tune shift method of Eq. (5.39)),

$$\beta_{x,y} \approx \pm 4\pi \, \frac{\Delta Q_{x,y}}{\Delta k}, \tag{5.39}$$

for different values of the rf frequency yields informations on the local chromaticity. This can help to identify the origin of chromatic errors or to find sources of chromatic nonlinearities.

5.4.5 Chromaticity Control in Superconducting Proton Rings

In superconducting proton rings the natural chromaticity is small compared with the chromaticity arising from the persistent-current sextupole components in the dipole magnets. For example, in the HERA proton ring the sextupole component in the dipoles contributes a chromaticity that is 5 times larger than the natural chromaticity. At injection energy, a significant part of the persistent current decays in time, causing a large variation in chromaticity. This is illustrated in Fig. 5.13, which also demonstrates the effect of an automatic correction system. The correction is done locally, by exciting sextupole correction coils mounted inside all bending magnets. The excitation for these correction magnets is determined from the instantaneous sextupole field measured by rotating coils in two reference magnets, which are connected in series with the main superconducting magnet circuit.

The persistent-current sextupole field in the dipole magnets decays during injection at 40 GeV. It is reinduced at the start of acceleration, resulting in large variations

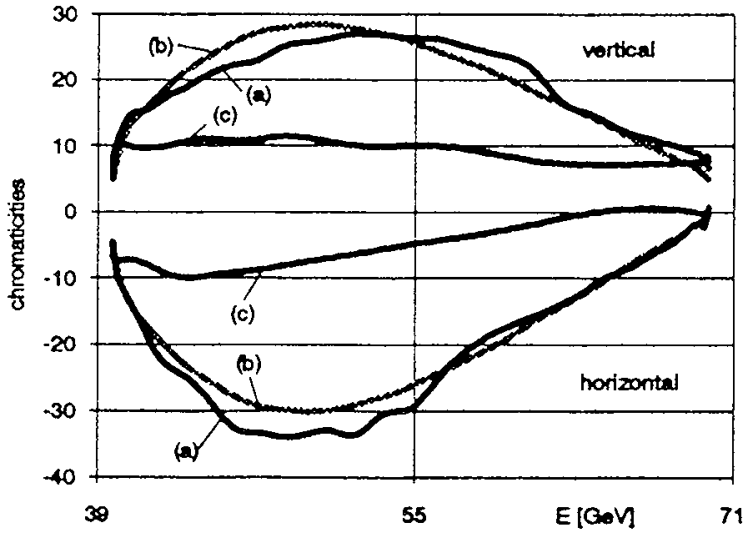

Figure 5.14: Variation of the chromaticity in the HERA proton ring during acceleration from 40 GeV to 70 GeV[15]: (a) measured chromaticity without correction; (b) change in chromaticity derived from the reference-magnet measurements; (c) measured chromaticity with correction. (Courtesy O. Meincke, 1998.)

of the chromaticity. Figure 5.14 shows the change in chromaticity during acceleration from 40 GeV to 70 GeV. The figure compares the actual chromaticity, *i.e.*, the change in tune detected per relative rf frequency change, Eq. (5.36)[15], measured without continuous correction; the chromaticity predicted by the reference magnets; and the chromaticity measured with a correction derived from the reference magnets.

Another noteworthy feature of the persistent-current sextupole field is that it is not very reproducible from cycle to cycle. An example of the nonreproducibility is depicted in Fig. 5.15. After each magnet cycle, when the ring is back at injection energy, the chromaticity is first corrected by means of a direct measurement (tune shift versus rf frequency). Subsequently, the chormaticity is held constant using the automatic control based on the reference magnets.

5.4.6 Application: Measuring the Central Frequency

Measuring the chromaticity for different sextupole strengths determines the `central frequency'. This is the rf frequency for which the orbit on average passes through the

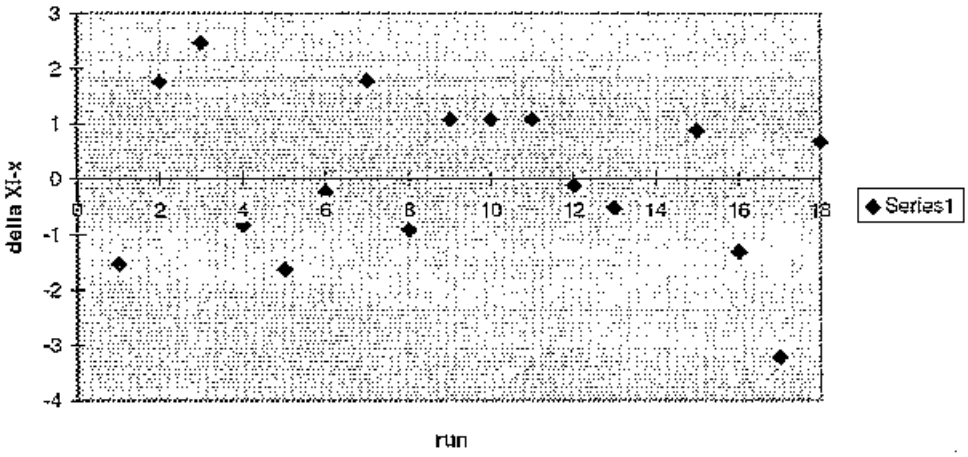

Figure 5.15: (Ir)reproducibility of the chromaticity for different machine cycles of the HERA proton ring. (Courtesy B. Holzer, 1998.)

center of all sextupoles [16,17]. An example of such a measurement is shown in Fig. 5.16. Usually adjacent sextupoles and quadrupoles are well aligned with respect to each other, so that one can expect that at the central frequency the beam also passes (on average) through the center of the quadrupoles.

On close view, four different center frequencies can be measured by changing the strength of the horizontal or vertical sextupole families and by measuring the resulting change in the horizontal or vertical tune, respectively. In most cases, the four central frequencies so obtained are found to be the same, supporting the hypothesis that the magnets are usually well aligned on short length scales.

This method allows one to monitor changes of the beam energy, using the relation

$$\frac{\Delta p}{p} = \left(\frac{1}{\gamma^{-2} - \alpha} \right) \frac{\Delta f_{rf}}{f_{rf}} \tag{5.40}$$

and the fact that the quadrupoles and sextupoles are well aligned with respect to each other. This energy-monitoring technique was applied at BEPC[18] and LEP[19].

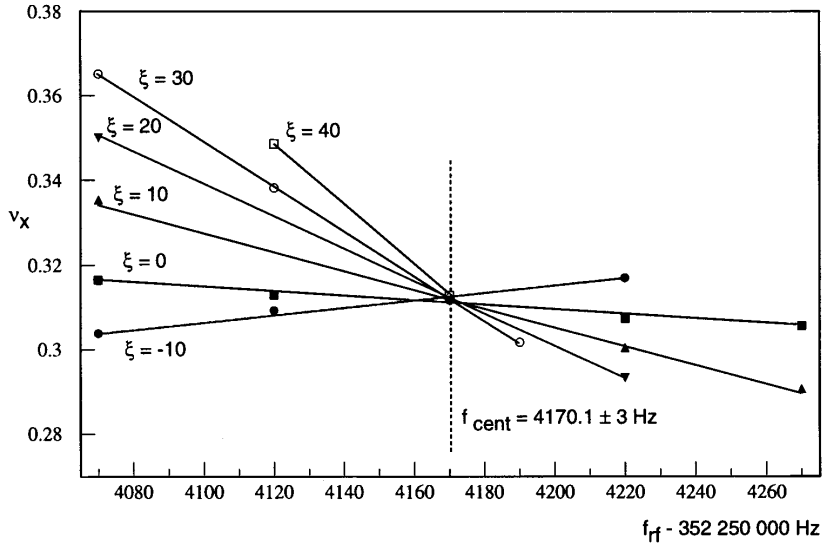

Figure 5.16: LEP chromaticity measurements for different sextupole excitation patterns, with net chromaciticities in the range $\xi = -10$ to $+40$. The intersection of the different lines determines the central frequency, where the orbit is on average centered in the sextupoles. (Courtesy H. Burkhardt, 1998.)

Ex.5.5. Achieving design parameters in the presence of unknowns
Suppose upon initial commissioning of an accelerator, the beam energy E, the ring circumference C, and main dipole field B are known to only about $\pm 1 - 2\%$. Describe a strategy for setup that ensures the desired beam energy, dipole field strengths matched to this energy, and dictates the required rf frequency to center the beam in the quadrupoles.

Ex.5.6. Chromatic Phase Advance
Maintaining the second order driving terms in Hill's equations for the particle motion, we have

$$\begin{aligned} x'' + kx &= kx\delta - \frac{b_2}{2}(x^2 - z^2) \\ z'' - kz &= -kz\delta + b_2 xz, \end{aligned} \tag{5.41}$$

where b_2 is the sextupole coefficient from the multipole field expansion of Ex. 2.3.
a) Assuming horizontal dispersion (η) only show that

$$\begin{aligned} {x_\beta}'' + kx_\beta &= (k - b_2\eta)x_\beta\delta \\ {z_\beta}'' - kz_\beta &= -(k - b_2\eta)z_\beta\delta, \end{aligned} \tag{5.42}$$

where the higher-order, so-called geometric aberrations, have been set to zero.
b) Noting that the perturbation in betatron tune may be expressed as

$$\delta\nu = -\frac{\beta_0}{4\pi}\int e(s)ds, \tag{5.43}$$

where $e(s)$ represents the focussing error (for example, you can convince yourself that $e = \frac{1}{f}$ in the previous exercise), show that the chromatic tune shifts are given by

$$\begin{aligned} \Delta\phi_x &= -\frac{\delta}{2}\int_s^{s+l} \beta_x(k - b_2\eta)ds \\ \Delta\phi_y &= \frac{\delta}{2}\int_s^{s+l} \beta_z(k - b_2\eta)ds. \end{aligned} \tag{5.44}$$

c) Using the definition of chromaticity, show that

$$\begin{aligned} \xi_x &= -\frac{1}{4\pi}\int \beta_x(k - b_2\eta)ds \\ \xi_z &= \frac{1}{4\pi}\int \beta_x(k - b_2\eta)ds \end{aligned} \tag{5.45}$$

The first term on the right-hand side of the last two equations gives the natural chromaticity while the second term shows the additive contributions arising from the sextupoles.

5.5 References

1. M. Sands, “The Physics of Electron Storage Rings”, SLAC-121 (1970)
2. J. Borer, C. Bovet, A. Burns, G. Morpurgo, “Harmonic Analysis of Coherent

Bunch Oscillations at LEP", Proc. of EPAC92, p. 1082 (1992).
3. F. Ruggiero, "Effect of Residual Dispersion at the RF Cavities on the Dynamic Measurement of Dispersion in LEP", CERN SL/91-38 (1991).
4. M. Minty, unpublished (1997).
5. K. Kubo and T. Okugi, "Dispersion Measurement in ATF DR", ATF Internal Report ATF-97-19 (1997).
6. P. Emma and W. Spence, Proc. of the SLAC/KEK Linear Collider Workshop on Damping Ring, Tsukuba, KEK Proceedings 92-6 (1992).
7. E. Perevedentsev, US-CERN-Russia-Japan Accelerator School, Montreux (1998).
8. U. Wienands, private communication (1998).
9. A. Fisher, A. Lumpkin, B. Zotter, J. Byrd, J. Hinkson, R. Assmann, unpublished (1998).
10. R. Assmann, *et al.*, "The Energy Calibration of LEP in the 1993 Scan", submitted to Zeitschrift für Physik, CERN-SL/95-02 (1995).
11. A. Hofmann, private communication (1998).
12. H. Burkhardt, private communication (1998).
13. H. Schmickler, "Diagnostics and Control of the Time Evolution of Beam Parameters", presented at the Third European Workshop on Beam Diagnostics and Instrumentation at Particle Accelerators (DIPAC 97) and CERN-SL-97-68 (1997).
14. These figures are a courtesy of B. Holzer, DESY (1998).
15. O. Meincke, S. Herb, and P. Schmüser, "Chromaticity Measurements in the HERA Proton Storage Ring", Proc. of EPAC 92, Berlin, p. 1070 (1992).
16. A. Piwinski, S. Herb, *et al.*, measurements at DORIS-I and HERA.
17. For LEP this measurement was proposed by A. Hofmann.
18. C. Zhang, W.F. Du, Z.G. Cai, "Beam Energy Stabilization and Online Measurement in BEPC", Proc. of the XVth International Conference on High Energy Accelerators, Hamburg, p. 409 (1992).
19. H. Schmickler, "Measurement of the Central Frequency of LEP", CERN LEP performance note 89 (1993).

Chapter 6

Longitudinal Phase Space Manipulation

In this chapter we describe various techniques used to control the longitudinal properties of particle beams. We concentrate on manipulation of the second moments of the longitudinal distribution; that is, on the bunch length and energy spread. As will be shown, the bunch length can be varied using both existing and additional rf cavities to compress, coalesce, split, and lengthen stored bunches. The energy spread of the beam can also be adjusted (usually for a minimum) by proper phasing of the rf, by invoking cancellations between the applied and beam-induced rf, and by more sophisticated techniques for the case of long bunch trains. A practical application of the use of rf systems to affect the beam's transverse emittance is presented lastly.

6.1 Bunch Length Compression

Bunch length compression using dedicated accelerating structures and beamlines is common to all linear collider designs [1,2,3]. Compression is usually performed in two or more steps. First an rf section (for example an accelerating structure) is used to introduce a correlation between the particle energy and position within a bunch. In the second stage the beam passes through a transport line with nonzero dispersion (i.e. bends) where the actual compression occurs due to the energy dependence of the particle trajectory.

The longitudinal phase space through the compressor evolves as follows. Let z_1, δ_1, z_2, δ_2, and z_3, δ_3 denote the longitudinal position z and relative energy δ into the compressor, downstream of the compressor structure, and at the end of the compressor, respectively. A particle within the bunch is transported through the compres-

sor cavity as

$$\begin{aligned} z_2 &= z_1 \\ \delta_2 &= \delta_1 + \frac{eV}{E}\cos\phi, \end{aligned} \tag{6.1}$$

where e is the particle charge, V is the compressor voltage, E is the beam energy, and ϕ is the relative phase of the particle with respect to the zero crossing of the compressor voltage. After the dispersive downstream arc,

$$\begin{aligned} z_3 &= z_2 + R_{56}\delta_2 \\ \delta_3 &= \delta_2. \end{aligned} \tag{6.2}$$

Combining Eqs. 6.1 and 6.2, the particle position and energy at the end of the compressor are given in terms of its initial conditions by

$$\begin{aligned} z_3 &= z_1 + R_{56}(\delta_1 + \frac{eV}{E}\cos\phi) \\ \delta_3 &= \delta_1 + \frac{eV}{E}\cos\phi. \end{aligned} \tag{6.3}$$

Phase errors may be critical particularly if the compression takes place upstream of a linear accelerator with tight injection phase tolerances. For the (single-stage) compressor scheme described above with $\phi = \frac{\omega}{c}z$, the resulting beam phase ϕ_3 in terms of the initial beam phase ϕ_1 is

$$\begin{aligned} \phi_3 &= \phi_1 - R_{56}\frac{\omega}{c}[\delta_1 + \frac{eV}{E}\sin(\phi_1 - \phi_c)] \\ &\approx [1 - R_{56}\frac{\omega}{c}(\delta_1 + \frac{eV}{E})]\phi_1 - R_{56}\frac{\omega}{c}\frac{eV}{E}\phi_c, \end{aligned} \tag{6.4}$$

where ω is the angular accelerating frequency of the structure. Assuming that the errors in the injected beam phase ϕ_i and the compressor phase ϕ_c are independent, and that $\frac{d\delta_1}{d\phi_1} = \frac{d\delta_1}{d\phi_c} = 0$, then

$$\frac{d\phi_3}{d\phi_c} = \eta \text{ and } \frac{d\phi_3}{d\phi_1} = 1 - \eta \text{ with } \eta = R_{56}\frac{\omega}{c}\frac{eV}{E}. \tag{6.5}$$

Combining the contributions in quadrature gives

$$(d\phi_3)^2 = \eta^2(d\phi_c)^2 + (1-\eta)^2(d\phi_1)^2. \tag{6.6}$$

Ex.6.1. Phase tolerances in bunch compressors

a)Sketch as a function of compressor voltage the injection phase tolerance for a 1.2 GeV electron beam passing through a 2856 MHz compressor cavity and a transport line with $R_{56} = 0.6$ m.

b) At what compressor voltage is the phase of the beam at extraction of the compressor region minimially sensitive to phase errors at injection?

An example bunch compressor designed for the Next Linear Collider[4] is shown in Fig. 6.1. There is two-fold compression in this design. The principle of the first compressor (BC1) is as described above with the energy-dependent path length generated by a wiggler magnet. At high energy, the second compressor stage (BC2) is applied. It consists of an arc, a second rf section, and a magnet chicane. In BC2 a net 360° phase space rotation is used to minimize sensitivity to incoming phase errors.

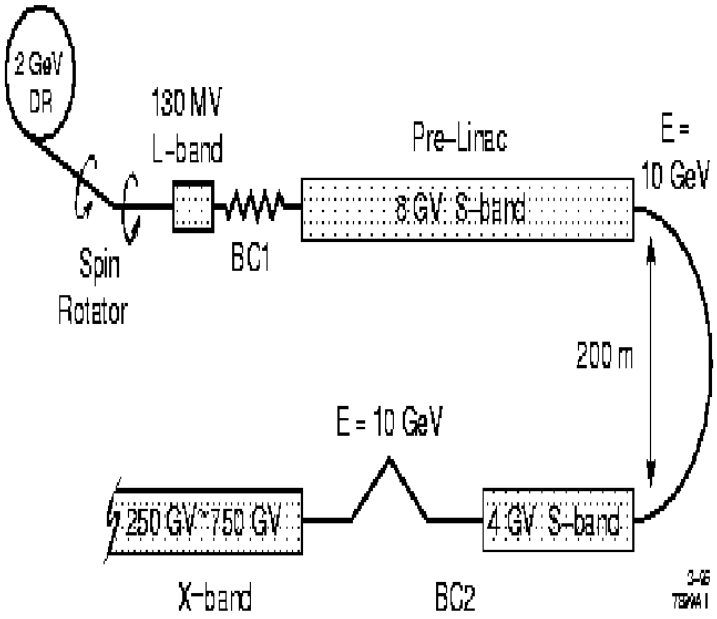

Figure 6.1: Schematic of the NLC bunch compressor.

6.2 Bunch Length Precompression

Bunch precompression using rf systems is frequently used for reducing the bunch length (at the expense of increased energy spread) for transferral of hadron beams from one accelerator to a downstream, higher frequency accelerator. Bunch precompression has also been used to reduce the consequences of current-dependent bunch lengthening (i.e. beam loss) in lepton accelerators.

The equations of motion for the beam phase ϕ and the beam energy δ are:

$$\dot{\phi} = \alpha\omega\delta \tag{6.7}$$

and

$$\dot{\delta} = -\frac{e\dot{V}}{E\omega T}\phi, \tag{6.8}$$

where α is the momentum compaction factor, E is the beam energy, ω is the angular rf frequency, and T is the revolution period. Combining the equations gives the harmonic solution:

$$\ddot{\phi} + \frac{\alpha\omega e\dot{V}}{E\omega T}\phi = 0. \tag{6.9}$$

The longitudinal emittance ϵ is given by

$$\epsilon^2 = \langle\phi^2\rangle\langle\delta^2\rangle - \langle\phi\delta\rangle^2. \tag{6.10}$$

Since

$$\begin{aligned} \langle\dot{\phi^2}\rangle &= 2\langle\phi\dot{\phi}\rangle = 2\alpha\omega\langle\phi\delta\rangle, \\ \langle\dot{\phi}\delta\rangle &= \langle\phi\dot{\delta} + \dot{\phi}\delta\rangle, \\ \langle\dot{\delta^2}\rangle &= 2\langle\delta\dot{\delta}\rangle \end{aligned} \tag{6.11}$$

then

$$\begin{aligned} \langle\ddot{\phi^2}\rangle &= 2\alpha\omega\langle\dot{\phi}\delta\rangle \\ &= -\frac{2\alpha e\dot{V}}{ET}\langle\phi^2\rangle + 2(\alpha\omega)^2[\frac{1}{\langle\phi^2\rangle}(\epsilon^2 + \frac{\langle\dot{\phi^2}\rangle^2}{(2\alpha\omega)^2})] \\ &= -\frac{2\alpha e\dot{V}}{ET}\langle\phi^2\rangle + \frac{2(\alpha\omega)^2}{\langle\phi^2\rangle}\epsilon^2 + \frac{1}{2}\frac{\langle\dot{\phi^2}\rangle^2}{\langle\phi^2\rangle}. \end{aligned} \tag{6.12}$$

From the second moment of the distribution (i.e. the bunch length)

$$\sigma_\phi = \langle\phi^2\rangle^{\frac{1}{2}}, \tag{6.13}$$

and since

$$\frac{d}{dt^2}\sigma_{\phi^2} = 2(\sigma_\phi \ddot{\sigma_\phi} + \dot{\sigma_\phi}^2), \tag{6.14}$$

then the equation of motion for the bunch length is

$$\ddot{\sigma_\phi} = -\frac{\alpha e \dot{V}}{ET}\sigma_\phi + \frac{(\alpha\omega)^2\epsilon^2}{{\sigma_\phi}^3}, \tag{6.15}$$

where

$$\dot{V} = \omega V(t) \sin\phi_b \tag{6.16}$$

with ϕ_b equal to the synchronous phase measured with respect to the rf crest. A similar analysis for the rms energy spread is likewise calculable. The results are summarized as

$$\begin{aligned} \ddot{\sigma_\phi} + {\omega_s}^2\sigma_\phi &= (\alpha\omega_s)^2\frac{\epsilon^2}{{\sigma_\phi}^3} \\ \ddot{\sigma_\delta} + {\omega_s}^2\sigma_\delta &= \frac{(e\dot{V})^2}{E\omega T}\frac{\epsilon^2}{{\sigma_\phi}^3}. \end{aligned} \tag{6.17}$$

Bunch rotations are used for better capture efficiency of the proton beam at HERA [5,6]. There two schemes were tried to shorten the bunch at extraction from the upstream PETRA ring. Initially, the bunch rotation was made by introducing a 180° phase jump in the accelerating rf, waiting for the bunch to lengthen, then restoring the phase to its original setting, and extracting the beam about a quarter of a synchrotron period later. Beam loading effects however caused bunch shape distortions during the phase jump[5].

Presently bunch precompression at HERA is achieved by amplitude modulating the rf system to induce a quadrupole mode oscillation. A similar scheme was used at the SLC primarily for reducing transmission losses within the transport line. A single step change in requested cavity voltage in the storage ring results in a longitudinal phase space mismatch which elongates the bunch. The resulting beam phase oscillation is then eliminated while amplifying the bunch length oscillation by application of a second, appropriately timed, step change to the cavity voltage.

An example in Fig. 6.2 shows measurements from the SLC of the cavity voltage (measured using a diode detector), bunch length (obtained from a peak current measurement, which is inversely proportional to bunch length, using a single stripline of a position monitor), and mean energy of the beam during precompression. The centroid energy was measured using a horizontal beam position monitor in a region of high dispersion in the damping ring.

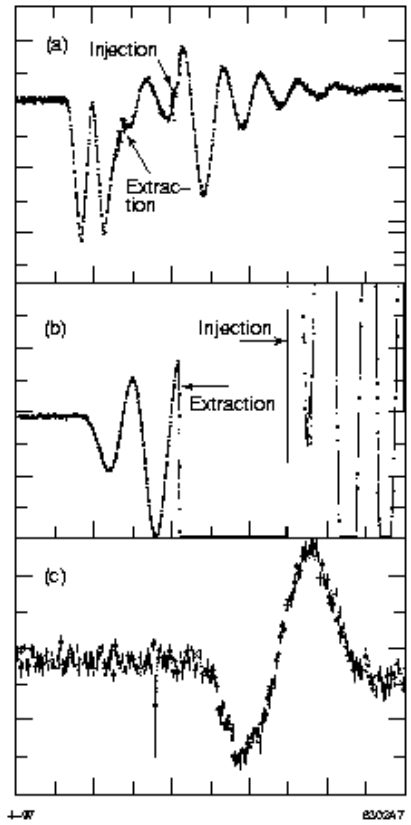

Figure 6.2: Measured cavity voltage [50 kV/dvsn, 10 μs/dvsn] (a), peak current [10%/dvsn, 5 μs/dvsn] (b), and centroid energy [50 μm or 0.77%/dvsn, 20 turns or 2.34 μs/dvsn] (c) during bunch precompression in the SLC damping rings.

Ex.6.2. Bunch precompression
a) Sketch the motion of the beam centroid using phase space diagrams for the following process:

$$\begin{aligned} V_c &= V_0 \text{ for } t < t_0 \\ &= 0.75V_0 \text{ for } t_0 < t < t_1 = \frac{\tau_{s,l}}{8} \\ &= V_0 \text{ for } t_1 < t < t_2 = \frac{\tau_{s,h}}{4} \\ &= 0.75V_0 \text{ for } t_2 < t < t_3 = \frac{\tau_{s,l}}{8} \\ &= V_0 \text{ for } t_3 < t < t, \end{aligned} \tag{6.18}$$

where $\tau_{s,l}$ is the synchrotron period at the lower voltage and $\tau_{s,h}$ is the synchrotron period at the higher voltage.

b) Taking into consideration a multiparticle beam, sketch the particle distribution in phase space during the process given. Show that the the bunch length is compressed (at the expense of increased energy spread).

6.3 Bunch Coalescing

Bunch coalescing, used primarily in hadron accelerators, consists of combining multiple bunches into a single bunch for high peak intensity. At Fermilab two types of coalescing are used[7]: standard coalescing for the low intensity antiprotons and `snap' coalescing for high intensity proton beams.

Experimental data from the Fermilab Main Ring are shown in Fig. 6.3 which demonstrate the bunch coalescing concept. The different traces correspond to different times. Initially there are 9 bunches in 53 MHz rf buckets. The vector sum of the rf voltages is then adiabatically reduced, or `paraphased' by shifting the relative phases between the accelerating cavities, to lengthen the bunch while preserving the longitudinal beam emittance. The bunches are next subjected to a higher voltage 2.5 MHz rf system. The bunches rotate with the synchrotron frequency in this low frequency rf potential. In practice[8], a 5 MHz rf is also applied to help linearize the rotation. When the bunches are vertically aligned in the 2.5 MHz rf bucket, they are then captured in a single 53 MHz rf bucket.

The snap coalescing scheme replaces the adiabatic voltage reduction with a phase space rotation. Here the coalescing procedure is initiated with a fast reduction of the primary rf amplitude. The beam is then longitudinally mismatched and shears in longitudinal phase space. After one quarter synchrotron oscillation the low frequency rf systems are turned on and the bunches are recaptured back into the primary rf bucket as before. Simulations[7] have shown that the capture efficiency of snap coalescing is about 10% less than with the adiabatic coalescing. However, at high currents, beam instabilities have been observed during adiabatic paraphasing of the 53 MHz

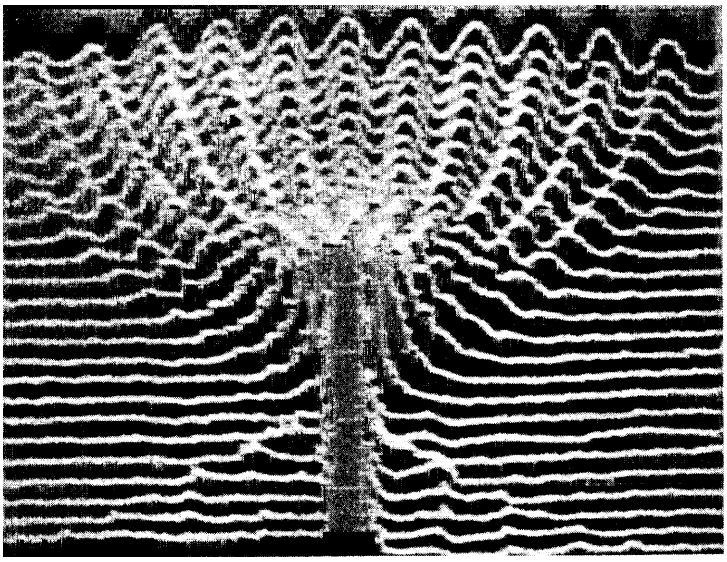

Figure 6.3: Experimental data from the Fermilab main ring showing multiple bunches being coalesced into a single bunch. Successive traces occur at 6.8 ms intervals. (Courtesy P. Martin, 1999.)

rf systems. This is avoided with snap coalescing and is therefore the implemented technique for the high intensity proton beams in the Fermilab Main Ring.

Two practical issues associated with bunch coalescing are increased longitudinal emittance (optimized by adjusting the amplitude of the rf during initial bunch lengthening) and the production of satellite bunches which can arise from nonlinearities in the rf of the capturing bucket. The latter, which can cause detector backgrounds, may be eliminated using a longitudinal damper to discard the offending bunches[9].

6.4 Bunch Splitting

The splitting of bunches using additional harmonic cavities has been proposed for the LHC. Basically, preexisting injectors are modified to include higher harmonic cavities to allow for the production of multiple bunches as required by the LHC[10]. To produce as many bunches as possible, the bunches will be split in the upstream PS accelerator in a 2 step process. First, at low energy (3.57 Gev/c) each of the 6 bunches from the booster ring will be split into 3 as shown in Fig. 6.4. Then, after ramping to high energy (26 Gev/c) the bunches will be further split into 4 as shown in Fig. 6.5. On the left of these figures is shown the relative amplitude of each of the different harmonic

rf systems as a function of time during the bunch splitting process.

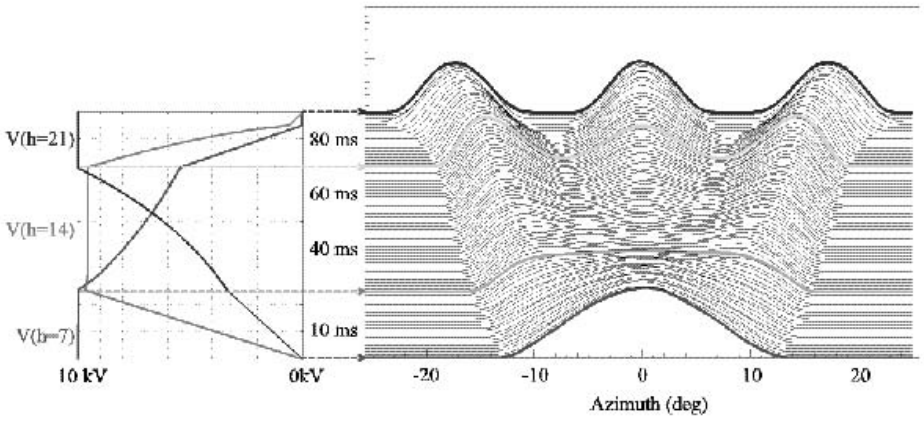

Figure 6.4: Bunch splitting in the CERN PS at low energy (3.57 GeV/c) in preparation for injection into the LHC. (Courtesy R. Garoby, 1999.)

Bunch splitting has been experimentally demonstrated [11] in the PS booster at CERN in application to ongoing neutrino experiments. Shown in Fig. 6.6 is the measured evolution of the longitudinal distribution using tomographic measurement techniques [12,13] from the CERN PS [10,13]. Plotted is the phase space at the indicated times and distribution of primary and harmonic cavity voltages.

In a series of dedicated experiments at the IUCF Cooler Ring, proton bunches were split by application of phase [14] or amplitude [15,16] modulations of the rf cavities. An example is shown in Fig. 6.7. In this case, longitudinal modulation resulted from application of a sinusoidal variation to a transverse dipole located in a region of high dispersion. Since the time of these data further experiments at the ALS [17] with electron beams have included the use of streak camera to more directly measure the evolution of the bunch length.

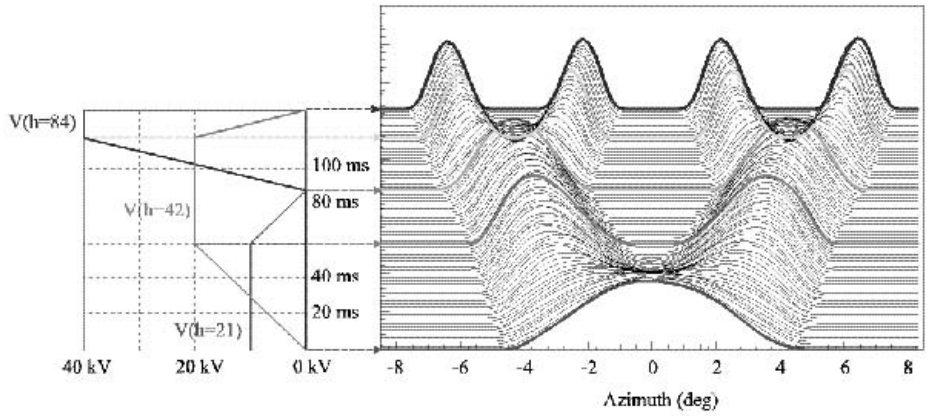

Figure 6.5: Further bunch splitting in the CERN PS at high energy (26 GeV/c) in preparation for injection into the LHC. (Courtesy R. Garoby, 1999.)

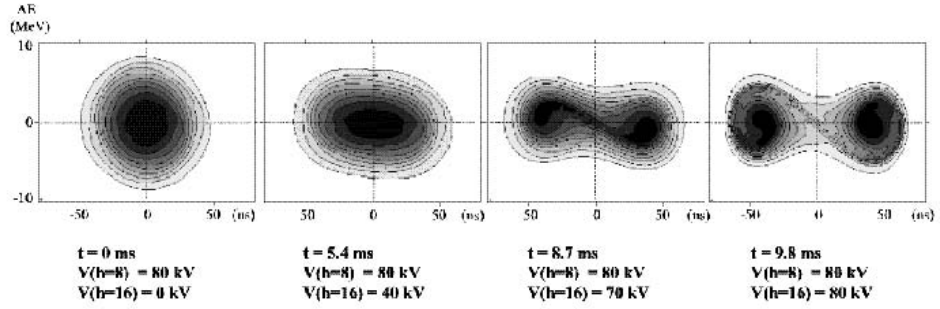

Figure 6.6: Bunch splitting in the CERN PS booter ring after acceleration with 3×10^{12} protons. (Courtesy R. Garoby, 1999.)

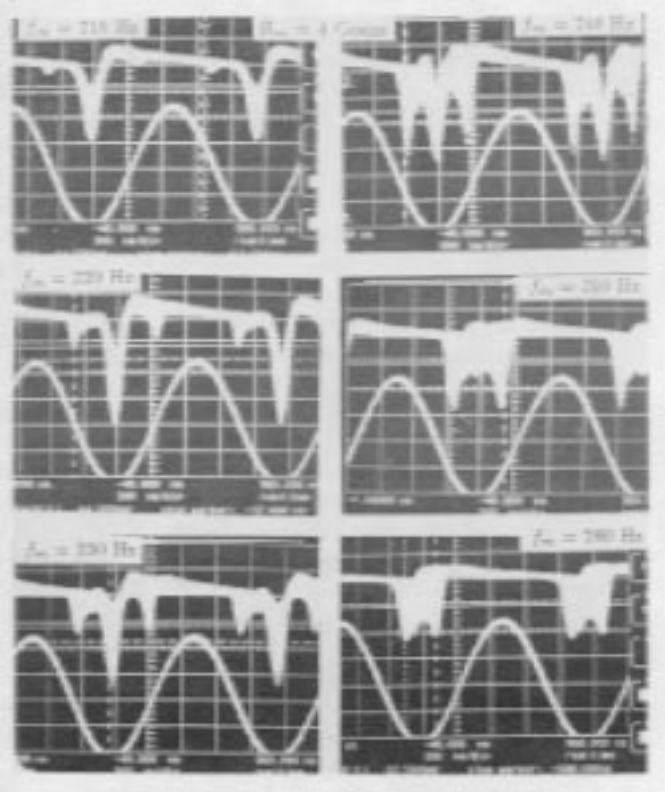

Figure 6.7: Longitudinal beam profile observed using an oscilloscope (top) and the rf wave form (bottom) during rf modulation of proton bunches in the IUCF Cooler Ring. (Courtesy S.Y. Lee, 1999.)

6.5 Harmonic Cavities

The use of additional rf cavities for longitudinal phase space manipulation has a variety of applications - we have already seen two such examples for bunch coalescing and splitting. Applications of harmonic cavities to reduce emittance growth when crossing transition has been demonstrated at the Fermilab main ring[18,19] and at BNL[20]. In this section we describe the use of harmonic cavities for lengthening the bunch. This approach has been adopted at various synchrotron light sources[21] to increase beam lifetime or to increase the bunch length to avoid longitudinal beam instabilities, for example, at DAPHNE [22,23] and as once proposed at LEP[24,25].

Low energy ($\approx GeV$) electron beam lifetimes may be dominated by large angle intrabeam scattering otherwise known as Touschek[26] scattering. The lifetime τ is given by

$$\frac{1}{\tau} = \frac{\sigma}{N} \int \rho^2 dV, \tag{6.19}$$

where σ is the probability for scattering beyond the momentum acceptance, ρ is the volume charge density, and V represents the volume. For a fixed beam energy and charge, the lifetime can be increased by increasing the bunch length (nominally independently of the transverse emittances so that the transverse brightness is unchanged).

Increasing the bunch length via addition of a higher harmonic rf system can be easily understood from Fig. 6.8. Here a third harmonic cavity is added to the primary rf such that the vector voltage seen by the beam is constant over the length of the bunch.

For electrons with nonzero synchronous phase, the total voltage is given by

$$V(t) = V_{rf}\left[\sin\omega_{rf}t + k\sin\big(n(\omega_{rf}t+\phi)\big)\right], \tag{6.20}$$

where ω_{rf} and V_{rf} are the angular rf frequency and voltage of the fundamental rf, n is the ratio of frequencies, k is the desired net voltage ratio for the two rf amplitudes, and $n\phi$ is the relative phase between the two systems. For optimum bunch lengthening, $V(0) = U_0$, where U_0 is the energy loss per turn (taken here to be dominated by synchrotron radiation), and both the slope and curvature of the net voltage at the position of the bunch is zero; i.e.

$$\frac{dV}{dt} = 0 \ \text{ and } \ \frac{d^2V}{dt^2} = 0. \tag{6.21}$$

The potential seen by the beam with and without a third harmonic rf system is shown in Fig. 6.9.

Satisfying these conditions, Eqs. 6.20 and 6.21 give the optimum amplitude and

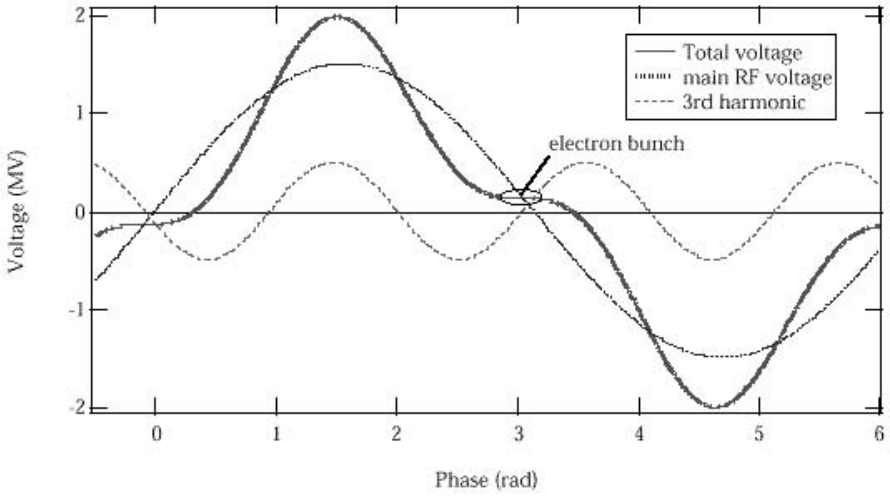

Figure 6.8: Conceptual illustration of bunch lengthening with a higher harmonic cavity. (Courtesy J. Byrd, 1999.)

phase of the harmonic cavity:

$$\begin{aligned} k^2 &= \frac{1}{n^2} - \frac{(\frac{U_0}{V_{rf}})^2}{n^2-1} \\ \sin(n\phi) &= -\frac{\frac{U_0}{kV_{rf}}}{n^2-1}. \end{aligned} \tag{6.22}$$

Simulations for the expected longitudinal density distribution are shown for the case of the ALS in Fig. 6.10.

Ex.6.3. Harmonic cavities

a) Verify the equations given in 6.22.

b) Sketch the relative phase between the two rf systems of Fig. 6.8 as the ratio of radiative losses to primary rf voltage varies from zero (proton beam limit) to slightly less than one.

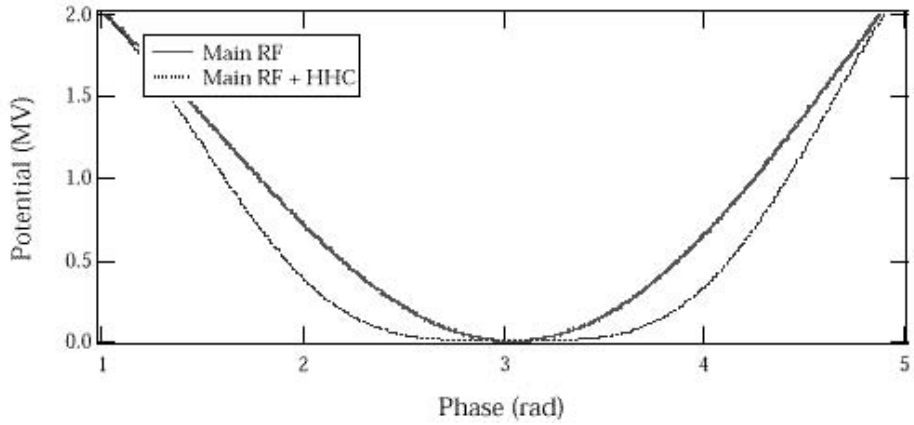

Figure 6.9: Potential seen by circulating bunch with and without a harmonic cavity for the parameters of the ALS. (Courtesy J. Byrd, 1999.)

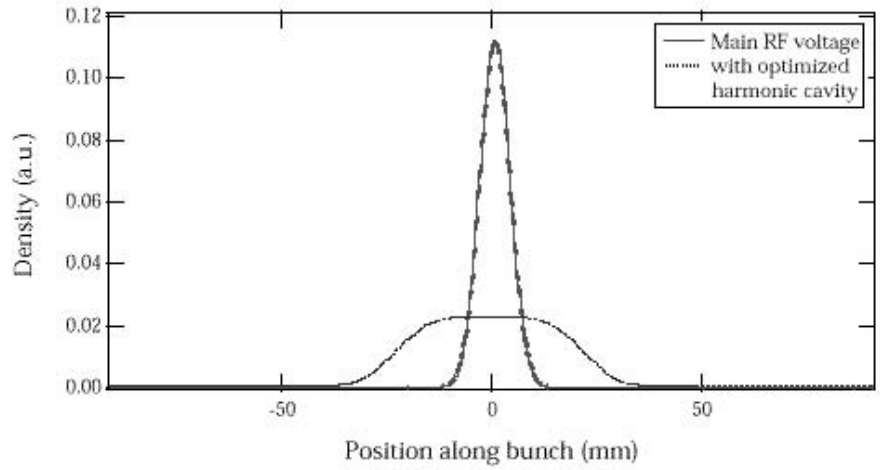

Figure 6.10: Bunch length with and without a third harmonic cavity at the ALS. (Courtesy J. Byrd, 1999.)

Ex.6.4. Minimum voltage required to store a beam
The power P_γ radiated due to synchrotron radiation per turn by an electron or positron may be expressed[27] *as*

$$P_\gamma = \frac{cC_\gamma}{2\pi}\frac{E^4}{\rho^2}, \tag{6.23}$$

where c is the speed of light, $C_\gamma = 8.85 \times 10^{-5}$ m-GeV^{-3}, E is the beam energy in GeV, and ρ is the local radius of curvature of the bending magnets.
a) For an accelerator (without insertion devices) with $\rho = 2$ m and $E = 1$ GeV, what is the total radiated power for 10^{11} particles?
b) With a 100 ns particle revolution period, at what voltage could the beam no longer be captured? What is the synchronous phase at this voltage? Assume that there are no other energy loss sources.
c) For low current beams, the bunch length scales with total accelerating voltage V as $V^{-\frac{1}{2}}$. What is the disadvantage of lowering the cavity voltage for increased bunch length compared with the use of harmonic cavities?

6.6 Energy Spread

As compared with the other 5 dimensions of a beam's phase space, the second moment corresponding to the beam energy spread is perhaps the most difficult to measure and control. In circular accelerators, lepton beams are naturally radiation damped to the limit of quantum fluctuations. Hadron beams on the other hand experience emittance dilutions particularly if subjected to internal targetry. For this reason various cooling mechanisms (see chapter 8) have been devised to combat large energy spreads.

Experience with lepton accelerators with high beam currents has shown that as the currents are increased, single-bunch instabilities, dominated by the so-called microwave instability, can lead to increased beam energy spreads. Measurements made with a downstream wire in a region of high dispersion are shown in Fig. 6.11 which demonstrated a dramatic increase beyond currents of about 1.5×10^{10} particles per bunch[28]. While relatively unimportant provided that the distribution remains stable from pulse-to-pulse, observations have shown that increased energy spread is associated with random turbulent bunch lengthening. Detailed analyses of this yet not fully understood phenomenon are beyond the scope of this lecture. Rather we will focus on methods for preserving, controlling, and minimizing the beam energy spread assuming a constant incoming energy spread in linear accelerators and transport lines. We have already seen one example whereby the energy spread of a beam is increased as the bunch length is decreased using bunch precompression and bunch compression.

In linear accelerators with high current bunches the longitudinal density profile can be further adjusted (so-called bunch shaping) to minimize transverse emittance dilutions arising from short-range wakefields and/or dispersion. This is particularly

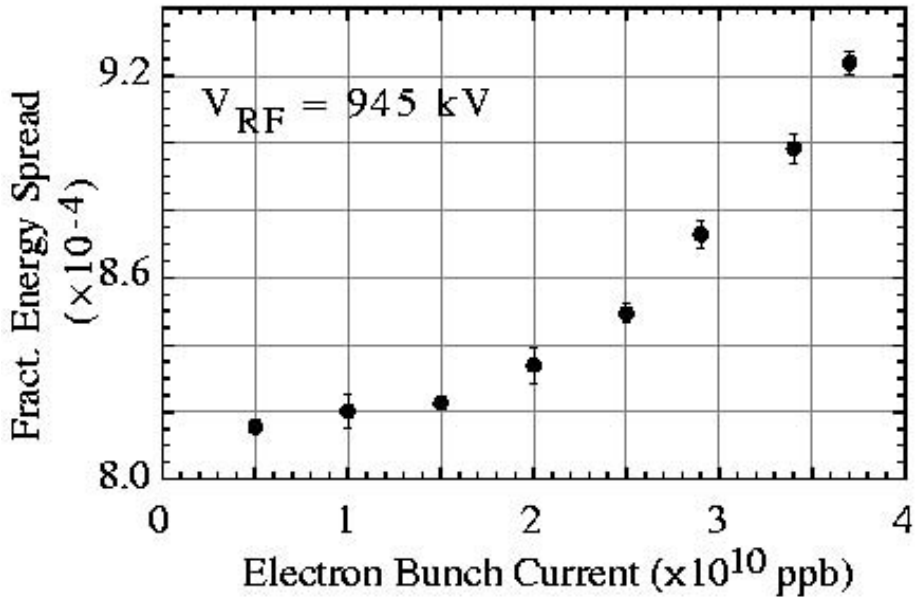

Figure 6.11: Measured energy spread of beams exiting the SLAC electron damping ring as a function of beam current.

useful since the outgoing energy spread, and especially energy `tails', often cause even further emittance dilutions in downstream final focus systems arising from chromatic aberrations.

Minimization of the energy spread depends critically on the single-bunch charge. In the single particle approximation, the energy gained is given by

$$eV = E_0 L \cos\theta, \tag{6.24}$$

where E_0 is the accelerating gradient, L is the length of the accelerating region, and θ is the time-like variable representing the phase of the particle relative to the crest of the rf.

For a bunch of particles, the energy seen by a given particle is reduced due to loading of the accelerating structure by leading particles within the bunch. Letting θ_0 represent the phase at the head of the bunch, the energy gain becomes

$$eV(\theta) = E_0 L \cos\theta - \int_0^{\theta_0-\theta} f(\theta') W_L(\theta_0 - \theta - \theta') d\theta', \tag{6.25}$$

where $f(\theta')$ represents the bunch charge distribution, and W_L is the wake function for the entire accelerator and is given by the product of the single-bunch wakefield times the number of accelerating structures.

Minimum energy spread within the bunch requires that $V(\theta)$ is independent of θ; that is

$$\frac{\partial V(\theta)}{\partial \theta} = 0. \tag{6.26}$$

It has been shown[29] that there exist solutions for the bunch charge distribution which satisfy this criterion. The solution is

$$f(x) = \frac{E_0 L}{W_L(0)} \sin(\theta_0 - x) - \int_0^x \frac{\frac{\partial W_L}{\partial dx}(x - \theta') f(\theta')}{W_L(0)}, \tag{6.27}$$

where $x = \theta_0 - \theta$. The interpretation of Eq. 6.27 is quite analogous to that shown in Fig. 6.8 where the voltage provided by the higher harmonic cavity is replaced by the decelerating voltage induced by beam loading of leading particles.

The solution given in Eq. 6.27 is shown in Fig. 6.12 for the case of the SLC linac. The horizontal axis shows the phase angle of particles within the bunch with the leading bunch at zero phase angle. The different curves correspond to different BNS phase angles and the points marked "T" indicate where the integrated bunch charge reaches the design single bunch charge of 5×10^{10} particles per bunch. As can be seen, for minimum energy spread, the prefered charge distributions tend in general to have a steep rising edge.

The tradeoff between bunch length and energy spread in a linear accelerator is shown in Fig. 6.13 which shows the effect of the combined voltages from the power source $\mathrm{E_{RF}}$ and the longitudinal wakefield $\mathrm{W_{Long}}$. On the left is depicted the longitudinal phase space of a long bunch while the projection onto the energy axis is given on the right. In the limit of long bunches one can see that a 'double-horned' distribution produces the minimum rms energy spread.

Measured energy spread profiles taken at the end of the SLAC linac are shown in Fig. 6.14. A wire scanner located in a dispersive region of a downstream transport line was used to measure the profile σ_w - after subtracting out, in quadrature, the contribution from the beam size σ_β, the energy spread σ_η was measured:

$$\sigma_\eta = \sqrt{{\sigma_w}^2 - {\sigma_\beta}^2}. \tag{6.28}$$

The angle ϕ denoted in the figure shows the BNS phase angle at the time of the measurement. These data show clearly the effects of not only misphasing the linac, but the additive contributions of the short-range longitudinal wakefield and have been used together with simulation[30,31] to determine the longitudinal bunch distribution.

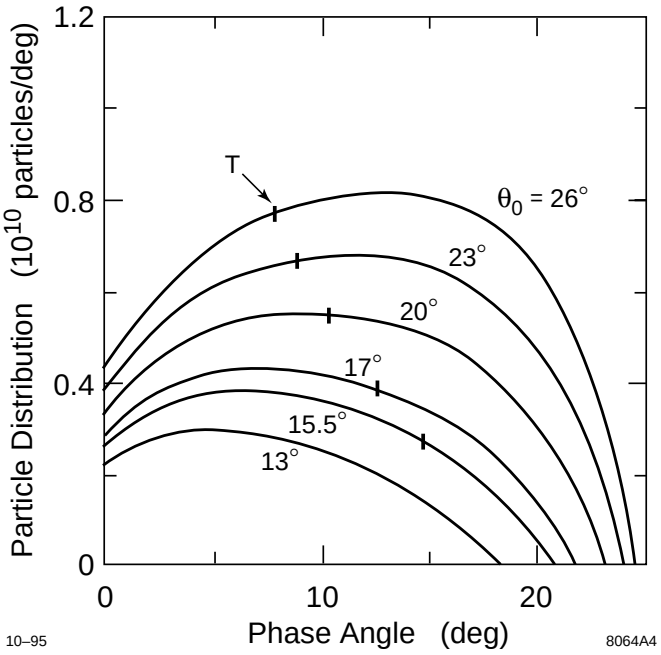

Figure 6.12: Optimum bunch shape for beam loading compensation in the SLC linac. (Courtesy G. Loew, 1999.)

A clever technique to avoid the undesirable energy spread tails (see Fig. 6.14) useful particlularly for the case of long bunches was devised using overvoltaging the upstream energy compressor[32]. A conceptual drawing illustrating the effect is shown in Fig. 6.15. While perhaps nonintuitive, simply by `overcompressing' the bunch, the tails in the energy spread distribution could be eliminated without diluting the longitudinal beam emittance.

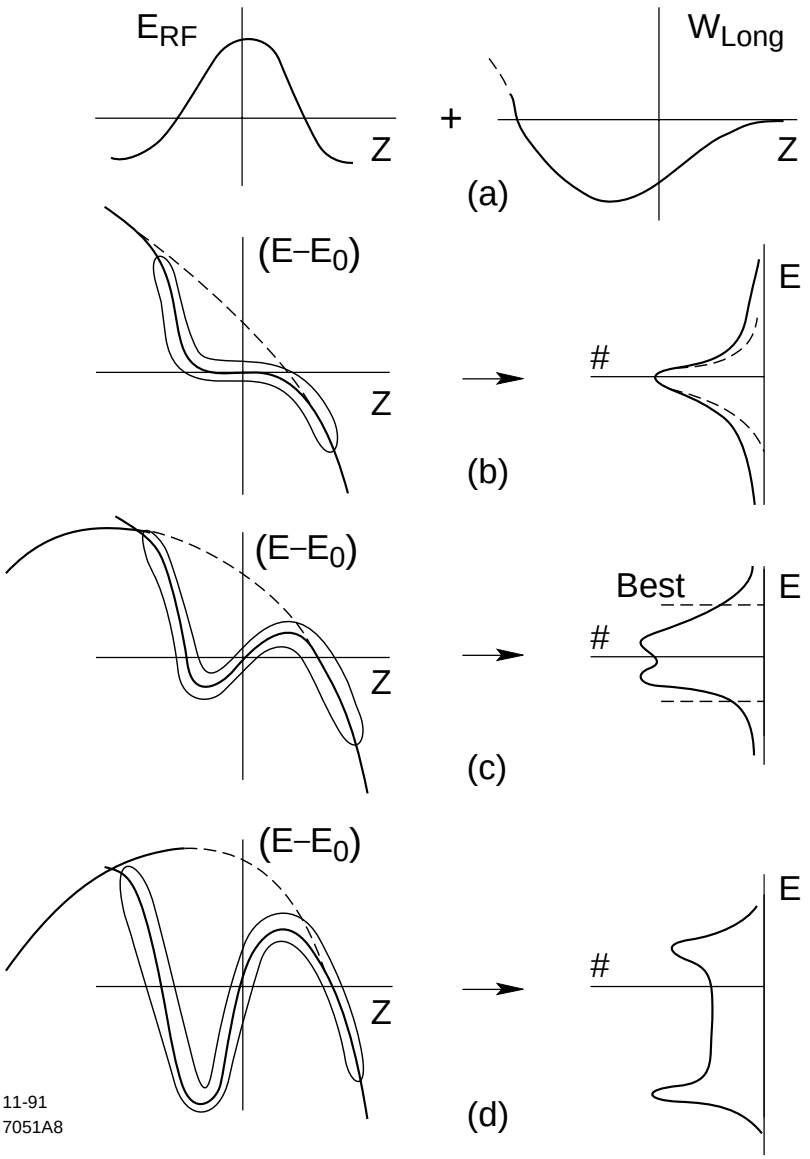

Figure 6.13: Conceptual illustration for optimizing the relative phase of the beam for the case of long bunches. (Courtesy J. Seeman, 1999.)

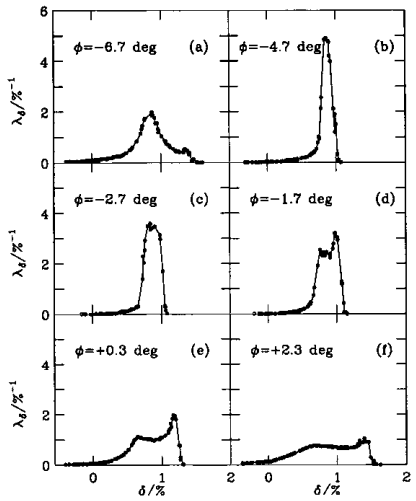

Figure 6.14: Energy spread measurements taken at the end of the SLAC linac for different BNS phases (ϕ). (Courtesy K. Bane, 1999.)

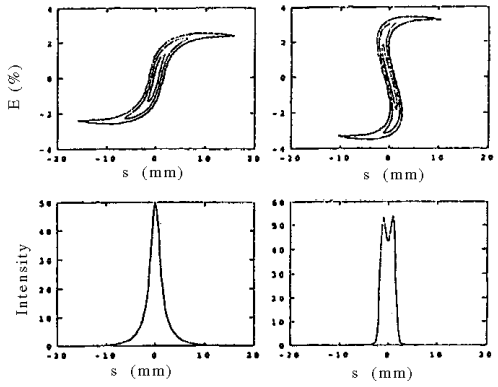

Figure 6.15: Longitudinal phase space (top) and projections onto time axis (bottom) with and without overcompression. (Courtesy F.-J. Decker, 1999.)

6.7 Energy Compression

The energy spread of a single bunch can be made smaller (at the expense of increased bunch length) using reverse application of a bunch length compressor. In this case, the beam passes through a region with an energy-dependent path length followed by an accelerating section which decelerates and accelerates the high and low energy particles respectively. Energy compression for single bunches was designed and implemented[33] for the positron transport line into the SLAC positron damping ring. The net increase in particle yield was observed to be about 10%.

6.8 Beam Loading

In the quest for obtaining ever-increasing total beam currents, both newly constructed and future accelerators have in common bunch trains consisting of multiple high current closely spaced bunches. In both linear and circular accelerators this may lead to a relative phase shift between the bunches of a bunch train.

When a beam passes through an accelerating cavity, it induces a voltage $V_{b,m}$ in each mode m of the cavity. The induced voltage is always retarding; that is, the beam-induced voltage always acts to decelerate the beam. Expressed another way, the beam always takes energy away from the cavity. This is refered to as beam loading.

The fundamental theorem of beam loading[34] is relevant on very short time scales (i.e. for a single pass through an accelerating cavity). The theorem states that the voltage that a test particle would experience when trailing a (point) source particle at time $t_0 > 0$ is exactly twice its beam induced voltage at $t_0 = 0$. More generally, the induced voltage, or wake potential, V_δ is given by

$$\begin{aligned} V_\delta(t_0) &= 0 \text{ for } t_0 < 0 \\ &= -kq \text{ for } t_0 = 0 \\ &= -2kqe^{-\frac{t_0}{\tau_f}} \cos\omega t_0 \text{ for } t_0 > 0, \text{ where } \tau_f = \frac{2Q}{\omega}. \end{aligned} \tag{6.29}$$

This function is illustrated in Figure 6.16. Here the variable

$$k = \frac{\omega}{2}\left(\frac{R}{Q}\right) \tag{6.30}$$

is called the loss parameter which tends to be determined by the structure geometry close to the beam. In practice, k is often calculated for each cavity mode using numerical programs (e.g. MAFIA). The wake potential describes the electromagnetic field that the point-like beam generates as it interacts with its surroundings and how this field acts back on the beam thus perturbing its motion.

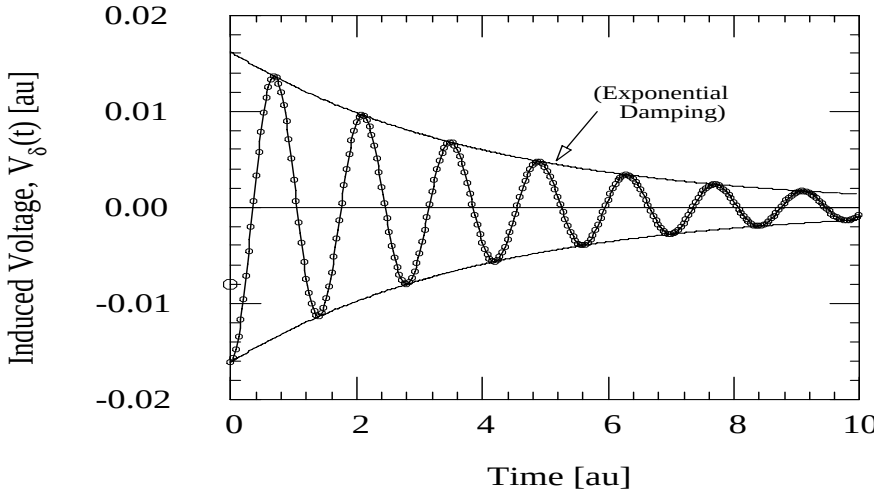

Figure 6.16: Wake potential. This function shows the voltage that would be experienced by a particle trailing a point-like test particle by time t_0 after passing a resonant structure.

In a circular accelerator containing a single accelerating cavity and a single particle bunch, the steady-state ($t >> \tau_f$) beam-induced voltage V_b is given by summing over the contribution from all previous turns. Using Eq. 6.29 with T_r denoting the bunch revolution frequency,

$$\begin{aligned} V_b &= -kq - 2kq\sum_{n=1}^{\infty} e^{-\frac{t_0}{\tau_f}}\cos\omega t_o\,\delta(t_0 - nT_r) \\ &= -2kq\Big[\sum_{n=0}^{\infty} e^{-\frac{t_0}{\tau_f}}\cos\omega t_o + \frac{1}{2}\Big]\delta(t_0 - nT_r) \\ &= -2kq\Big[\sum_{n=0}^{\infty} e^{-\frac{nT_r}{\tau_f}}\cos n\omega T_r + \frac{1}{2}\Big]. \end{aligned} \tag{6.31}$$

Driving the cavity near its resonance frequency (i.e. taking $\omega = \omega_{rf}$), and noting that $\cos n\omega T_r = 1$ for all n, then

$$\begin{aligned} V_b &= -2kq\Big[\sum_{n=0}^{\infty} e^{-\frac{n\omega_{rf}}{2Q}T_r} + \frac{1}{2}\Big] \\ &= -2kq\Big[\frac{1}{1 - e^{-\frac{n\omega_{rf}}{2Q}T_r}} + \frac{1}{2}\Big] \end{aligned} \tag{6.32}$$

Neglecting the small self-loading term, and applying

$$\frac{1}{1-e^{-x}} \approx \frac{1}{x} \text{ for } x = \frac{\omega_{rf} T_r}{2Q} << 1, \tag{6.33}$$

then

$$\begin{aligned} V_b &= -2kq(\frac{2Q}{\omega_{rf} T_r}), \;\; k = \frac{\omega_0}{2}(\frac{R}{Q}) \\ &= -2qf_{rev}R \\ &= -I_b R. \end{aligned} \tag{6.34}$$

This simple result shows that with the cavity tuned to resonance, the beam-induced voltage is simply given by the beam current at the resonance frequency ($I_b = 2I_{dc}$) times the cavity impedance. (Note that this is the loaded impedance since the expression for the cavity fill time used the loaded quality factor.) The minus sign, again, indicates that the beam takes energy away from the accelerating cavity.

Application of Eq. 6.29 to transport of high current particle beams is a subject of great interest in modern accelerators. In the extreme short-range limit, the variable t_0 above may represent the time interval between particles within a single bunch in which case, by causality the charge q represents the charge of all preceeding charges within the bunch. As the beam current is increased, eventually, as many experimental and theoretical studies have shown, the ensuing motion can become unstable.

One way to achieve high beam currents while avoiding intrabunch beam instabilities arising from increased single-bunch beam currents, would be to introduce multiple bunches (often called a bunch train) each with lower single-bunch beam currents. In this case, t_0 in Eq. 6.29 refers to spacing between appropriate bunches; here the beam-induced voltage experienced by a particular bunch is given by the sum of the voltages induced by all preceeding bunches each obtained by evaluation of Eq. 6.29 at the appropriate time t_0. In recent years, much effort has been devoted in carefully designing and testing new cavity designs (such as ARES or super conducting cavities) in order to minimize the net 'wakefield' experienced by all bunches within a bunch train.

6.9 Multibunch Energy Compensation

Two methods, known as Δf and Δt compensation have been proposed to combat multibunch phase transients in linear accelerators. Shown in Fig. 6.17 is the principle of Δt compensation [35]. Here the voltage V_k represents the voltage response of a finite bandwidth accelerating structure to a step function input pulse. The lower curve labeled V_b represents the beam-induced voltage of the entire bunch train. By injecting the beam prior to the time the linac structure is at peak voltage, the vector sum is

observed to be flat over the duration of the bunch train. The projected energy spread is therefore minimized and the phase relationship between the bunches is constant.

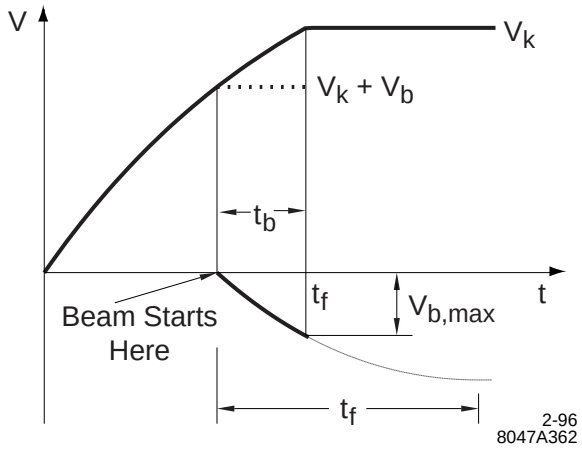

Figure 6.17: Conceptual diagram illustrating multi-bunch, ΔT beam loading and energy compensation.

Beam loading compensaton using the Δt method may be advantageous since the correction may be applied locally at each accelerating section. On the other hand it is anticipated[35] that about 10% more power is required relative to the Δf compensation scheme.

The principle of the Δf compensation is illustrated[36] in Fig. 6.18. In this design from the ATF in Japan, some fraction of the many accelerating structures are slightly detuned by $\pm\delta f$ which changes the net accelerating field seen by each of the bunches within the train.

Ex.6.5. Phase shift along a bunch train
The cavity fill time τ_f describes, in the absence of feedback, the time evolution of the cavity voltage in response to a step function. For example, if a cavity initially at amplitude V_0 has suddenly its power source turned off, then the cavity voltage decays as

$$V_c(t) = V_0 e^{-\frac{t}{\tau_f}}, \quad \text{where } \tau_f = \frac{2Q}{\omega_{rf}}. \tag{6.35}$$

For the case of a storage ring, estimate the change in synchronous phase across a 500 ns long bunch of 100 mA dc beam current and cavities with $Q = 30000$, a total impedance of 50 MΩ, and an rf frequency of 476 MHz.

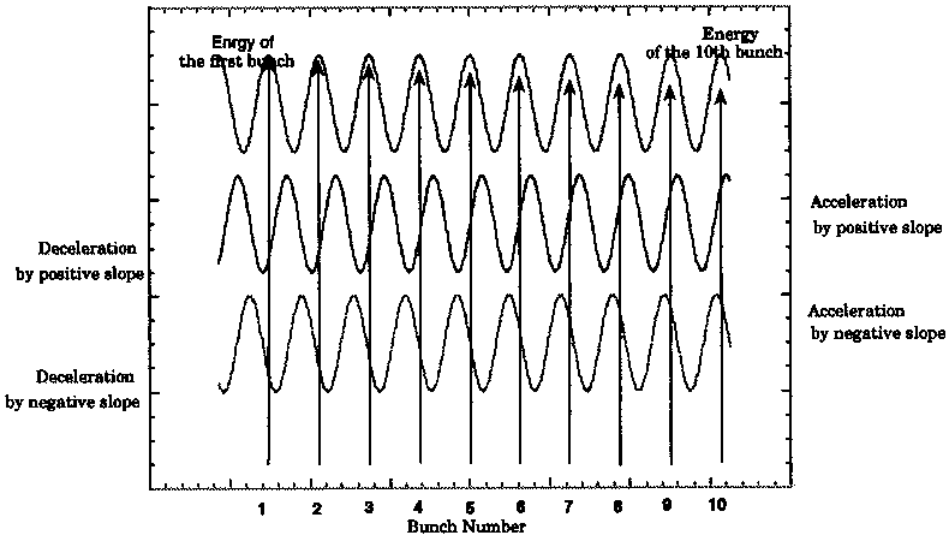

Figure 6.18: Conceptual diagram illustrating multi-bunch, Δf beam loading and energy compensation. (Courtesy J. Urakawa, 1999.)

6.10 Damping Partition Number Change via RF Frequency Shift

The generation of small emittance beams is a key issue for synchrotron light sources, collider rings, and for future linear colliders. Dedicated accelerators have been designed to produce such beams, but techniques to further reduce the design emittances would yield immediate improvements. At injection into such accelerators, the transverse beam emittances are large and often fill a large fraction of the dynamic aperture. For lepton beams, at later times after the beam has radiation damped, the horizontal damping time and equilibrium emittance may be reduced by shifting the rf frequency, such that the particle orbit moves inwards. By passing off-center through the quadrupoles in regions of nonzero dispersion, the horizontal partition number J_x is changed. This reduces both the horizontal damping time and equilibrium emittance. In addition, to the extent that the vertical emittance is determined by betatron coupling, the reduction in horizontal emittance may be accompanied by a corresponding reduction in vertical emittance.

The horizontal damping time and beam emittance are both inversely proportional

to the horizontal partition number $J_x = 1 - D$, where[27]

$$D = \frac{\int \eta G(G^2 + 2K_1) ds}{\int G^2 ds}. \tag{6.36}$$

Here η is the horizontal dispersion, G and K_1 describe properties of the magnetic guide field, and the integrals are evaluated around the ring circumference. For the non-combined function SLC damping ring dipole magnets, $GK_1 \approx 0$.

For an orbit offset Δx in the quadrupoles, the change in D is given approximately by

$$\frac{2{K_1}^2 \eta_q L_g N_q}{2\pi/\rho} \Delta x, \tag{6.37}$$

where $K_1 = \frac{ec}{E}(\frac{\partial B}{\partial x})$ with $e = 1.6 \times 10^{-19}$ C, $c = 3 \times 10^{10}$ m/s, $E = 1.19$ GeV, ρ is the local bending radius, η_q is the dispersion at the quadrupoles, and L_q and N_q are respectively the quadrupole length and number of quadrupoles.

The orbit may be offset in the quadrupoles by either changing the accelerating frequency or by physically displacing the magnet support girders. Emittance optimization using the accelerating frequency has been used in $e+/e-$ storage rings previously[37] and is used routinely at LEP[38]. The circumference adjustment is applicable provided that the transverse acceptance is not limited and that the injected beam energy spread is small compared to the energy acceptance. At the SLC, the electron damping ring was 'stretched'[39] in 1992 by 9 mm for a 15% increase in J_x. In doing so, the energy aperture at injection was reduced without any loss in transmitted beam current. For the case of the positron ring, the incoming beam filled the entire aperture so stretching the accelerator was not an option.

Shown in Fig. 6.19 is a calculation of the horizontal emittance $\gamma\epsilon_x$ as a function of time for 4 different frequency offsets for the case of the SLC damping rings. It is assumed that the beam is injected at the nominal rf frequency of 714 MHz with an initial emittance of 20×10^{-5} m-r. The accelerating frequency is increased after 1 ms (dashed line) for which the longitudinal emittance has damped by about a factor of 2. The simulations (using SAD[40]) with a trapezoidal approximation for the bending magnet fringe fields show a half unit reduction (i.e. 15-20%) in normalized emittance with a 100 kHz frequency change while the damping time reduces from 3.4 ms to 3.0 ms.

At storage rings and colliders there is no tight tolerance on maintaining the desired rf frequency. In a damping ring, the time required to reset the frequency and relock the beam phase to the desired extraction phase is critical since the frequency must be ramped back to nominal just before extraction in order not to introduce any energy and/or phase errors in downstream subsystems (in this case bunch compressor and SLC linac). Minimizing this time is critical since reverting to the nominal rf frequency is associated with corresponding antidamping of the beam.

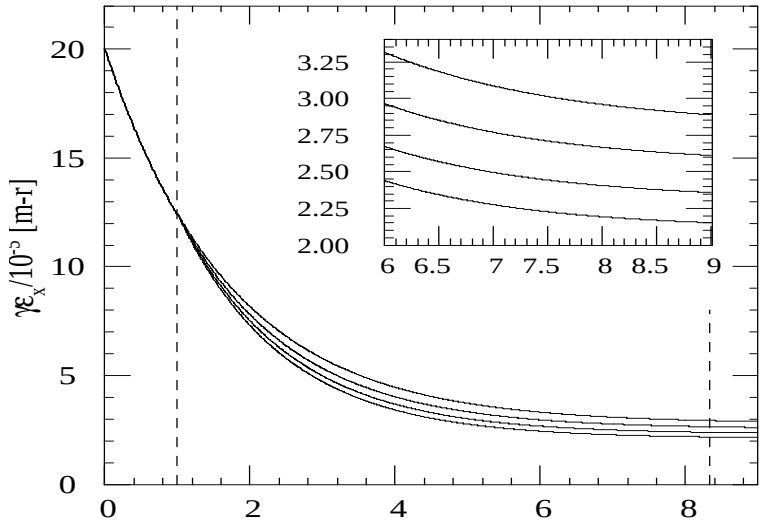

Figure 6.19: Normalized horizontal beam emittance as a function of store time for different frequency shifts calculated for the SLC damping rings. The full store time is shown with an expanded view near beam extraction at 8.33 ms shown in the insert. The curves, when viewed from top to bottom, correspond to frequency shifts of 0, 50, 100, and 150 kHz, respectively.

As a practical point, with a change in accelerating frequency, the accelerating cavities are detuned by an amount characterized by the tuning angle ϕ_z which is given by

$$\phi_z = \tan^{-1}\left[2Q\left(\frac{f_0 - f_{\rm rf}}{f_0}\right)\right], \tag{6.38}$$

where Q is the loaded cavity quality factor, f_0 is the resonant frequency of the cavity, and f_{rf} is the frequency of the applied rf. With the cavity tuners *fixed*, the new tuning angle ${\phi_z}'$ corresponding to the new applied rf frequency ${f_{rf}}' = f_{rf} + \delta f_{rf}$ is given by

$$\tan {\phi_z}' = 2Q\left[1 - (1 - \frac{1}{2Q}\tan\phi_z)\frac{{f_{rf}}'}{f_{rf}}\right]. \tag{6.39}$$

An example is shown in Fig. 6.20(a). Typically, the tuning angle is set for minimum reflected power:

$$\phi_z|_{\phi_l=0} = -\frac{I_b R}{V_c}\sin\phi_b, \tag{6.40}$$

where I_b is twice the dc beam current, R is the total loaded impedance, V_c kV is the total cavity voltage, and ϕ_b is the synchronous phase measured with respect to the crest of the accelerating rf. The loading angle ϕ_l is related to the tuning angle ϕ_z by

$$\tan\phi_z = \left(1 + \frac{I_b R}{V_c}\cos\phi_b\right)\tan\phi_l - \frac{I_b R}{V_c}\,\sin\phi_b. \tag{6.41}$$

In the case of the SLC, the cavity detuning exceeded the power capabilities of the power source as shown using a solid curve in Fig. 6.20(b).

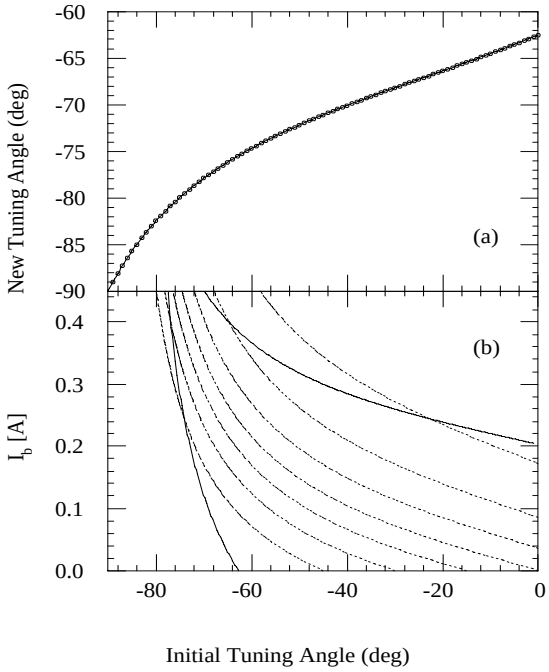

Figure 6.20: Cavity tuning considerations. The initial and final tuning angles at f_{rf} and $f_{rf}{}' = f_{rf} + 100$ kHz, respectively, are shown in Fig. 6.20(a). The stability boundary for cavity voltage regulation at 600 kV is given by the solid curve in Fig. 6.20(b). The dashed curves show the loading angle ϕ_l which is measured and regulated by the tuner feedback loops. At zero beam current, the loading angle is equal to the tuning angle.

Assuming sufficient frequency aperture, which may be limited *e.g.* by transverse betatron resonances that can be encountered during the frequency ramp with nonzero

chromaticity, the maximum frequency change may be limited by either available rf power as discussed above or by the damping poles[41] at which the damping rate becomes zero.

Measurements[42] showing the effect of a frequency ramp in the SLC positron ring are given in Figs. 6.21 and 6.22. In this experiment, the downstream compressor was turned off in order to more cleanly detect the effect of the frequency shift on beam emittance. From Fig. 6.22, with a 62.5 kHz shift, the reduction in normalized emittance was from 3.30 ± 0.07 m-r to 2.66 ± 0.06 m-r. For the electron damping ring, the reduction with the frequency shift was from 3.22 ± 0.08 m-r to 2.93 ± 0.07 m-r. Using the 1997 SLC interaction point parameters of $\theta_x, \theta_y = 450, 250$ μr angular divergence, and $\gamma\epsilon_x, \gamma\epsilon_y = (5.2, 1.1) \times 10^{-5}$ m-r normalized emittances measured in the final focus, the corresponding rms beam sizes are $\sigma_x, \sigma_y = 1.3, 0.5$ μm. With a 1 mm bunch length and 4×10^{10} particles per bunch, the luminosity is estimated from guinea-pig[43] to be 4.28×10^{32} m^{-2} per collision. This corresponds to an estimated increase of over 40% in luminosity by application of the frequency shift in the damping rings.

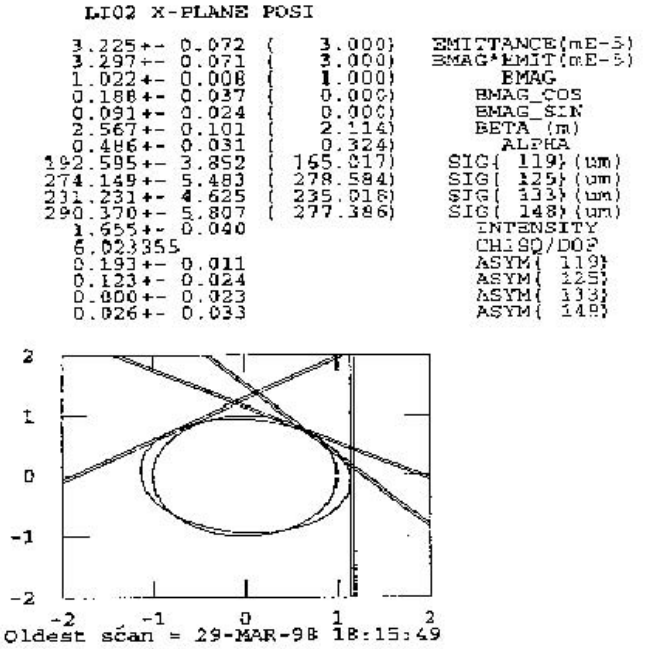

Figure 6.21: Nominal emittance measured in the downstream linear accelerator. The measured normalized emittance was 3.30 ± 0.07 m-r.

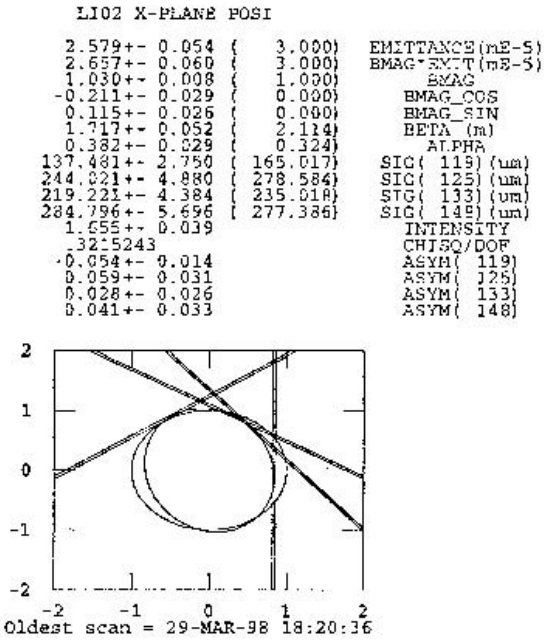

Figure 6.22: Emittance measurement with a 62.5 kHz frequency shift. The normalized emittance was reduced from 3.30 ± 0.07 m-r to 2.66 ± 0.06 m-r.

Decreasing the beam emittance by changing the damping partition numbers is also part of the HERA luminosity upgrade[44]. To maintain matched beam sizes, with a reduced proton beam size resulting from modified optics at the interaction points of HERA, the electron beam size must be reduced. The approach to be taken is twofold - both stronger focusing in the arcs and a +200 Hz frequency shift.

6.11 References

1. `The SLC Design Handbook', Ed. R. Erickson (1984).
2. `Zeroth-Order Design Report for the Next Linear Collider', LBNL-PUB-5424, SLAC Report 474, UCRL-ID-124161 (1996).
3. `JLC Design Study', N. Akasaka *et al*, KEK-REPORT-97-1.
4. P. Emma, T. Raubenheimer, F. Zimmermann, `A Bunch Compressor for the Next Linear Collider', IEEE Part. Acc. Conf., Dallas, Texas, 704-706 (1995); SLAC-PUB-6787 (1995)
5. W. Kriens, `Petra Bunch Rotation', DESY-M-97-10N (1997).
6. G. Wiesenfeldt, `Untersuchungen zur longitudinalen Strahlanpassung beim Protonentransfer von PETRA nach HERA', Diplomarbeit, Universitaet hamburg, March 1995.
7. I. Kourbanis, G.P. Jackson, X. Lu, `Performance and Comparison of the Different Coalescing Schemes Used in the Fermilab Main Ring', IEEE Part. Acc. Conf., Washington, DC 3799-3801 (1993).
8. P.S. Martin and D.W. Wildman, `Bunch coalescing and Bunch Rotation in the Fermilab Main Ring: Operational Experience and Comparison with Simulations', FERMILAB-Conf-88/87 (1988).
9. V. Bharadwaj, private communication (1999).
10. R. Garoby, `Status of the Nominal Proton Beam for LHC in the PS', presented at the 1999 Charmonix workshop.
11. see for example A. Blas, R. Cappi, R.Garoby, S. Hancock, K. Schindl, J-L. Vallet, `Beams in the CERN PS Complex after the rf upgrades for LHC', EPAC98
12. G. Jackson, `Phase Space Tomography (PST) Monitor for Adjusting Bunch Rotation during Coalescing', FERMILAB-FN-469 (1987).
13. S. Hancock, P. Knaus, M. Lindroos, `Tomographic Measurements of Longitudinal Phase Space Density', CERN/PS 98-030 (RF) (1998).
14. H. Huang *et al*, `Experimental Determination of the Hamiltonian for Synchrotron Motion with RF Phase Modulation', Phys. Rev. E48, 4670-4688 (1993).
15. D. Li *et al*,, `Experimental Measurement of REsonance Islands Induced by the RF Voltage Modulation', Phys. Rev. E48, 1538-1641 (1993).
16. D. Li *et al*, `Effects of RF Voltage Modulation on Particle Motion', Nucl. Instr. Meth. A364, 205-223 (1995).
17. J.M. Byrd, W.H. Cheng, F. Zimmermann, `Nonlinear Effects of Phase Modulation in an Electron Storage Ring', Phys. Rev. E57, 4706-4712 (1998).
18. J.E. Griffin, `New Method for Control of Longitudinal Emittance During Transition in Proton Synchrotrons', IEEE Part. Acc. Conf., Washington, DC 408-410 (1993).

19. C.M. Bhat, J. Dey, J. Griffin, I. Kourbanis, J. MacLachlan, M. Martens, K. Meisner, K.Y. Nig, J. Shan, and D. Wildman, `Operational Expereience with Third Harmonic RF Cavity for Improved Beam Acceleation Through Transition in the Fermilab Main Ring', IEEE Part. Acc. Conf., Washington, DC 405-407 (1993).
20. J.M. Kats and W.T. Weng, `Effects of the Second Harmonic Cavity on RF Capture and Transition Crossing', 15th Intl. Conf. on High-Energy Acc., Hamburg, Germany vol. 2, 1052-1054 (1992).
21. `Conceptual Design of the ALS 3rd Harmonic RF System' (1998).
22. S. Bartalucci, M. Migliorati, L. Palumbo, B. Spartaro, M. Zobov, `A 3rd Harmonic Cavity for Daphne', 4th Eur. Part. Accel. Conf. (EPAC94), London, England (1994).
23. M. Migliorati, L. Palumbo, M. Zobov, `Bunch Length Control In Daphne by a Higher Harmonic Cavity', Nucl. Insr. Mth. A **354** 215-223 (1995).
24. P. Bramham, A. Hofmann, P.B. Wilson, CERN-LEP-70/25 (1977).
25. P.B. Wilson, `Rough Design of a Third Harmonic RF Cavity for LEP', CERN-LEP-70/60 (1978).
26. C. Bernadini *et al*, `Lifetime and Beam Size in a Storage Ring', Phys. Rev. Lett. **10**, 407-409 (1963).
27. M. Sands, "The Physics of Electron Storage Rings", SLAC-121 (1970).
28. K. Bane *et al*, `High Intensity Single Bunch Instability Behavior in the New SLC Damping Ring Vacuum Chamber', IEEE Part. Acc. Conf., Dallas, TX 3109-3111 (1995).
29. G.A. Loew and J.W. Wang, `Minimizing the Energy Spread within a Single Bunch by Shaping its Charge Distribution', SLAC/AP-025 (1984).
30. K.L.F. Bane, F.-J. Decker, J.T. Seeman, F. Zimmermann, `Measurement of the Longitudinal Wakefield and the Bunch Shape in the SLAC Linac', IEEE Part. Acc. Conf., Vancouver, Canada (1997).
31. K.L.F. Bane, F.-J. Decker, F. Zimmermann, `Obtaining the Bunch Shape in a Linac from Beam Spectrum Measurement', IEEE Part. Acc. Conf., New York, NY (1999).
32. F.-J. Decker, R. Holtzapple, T. Raubenheimer, `Over-Compression, a Method to Shape the Longitudinal Bunch Distribution for a Reduced Energy Spread', 17th Intl. Lin. Acc. Conf., Tsukuba, Japan (1994).
33. J.E. Clendenin, R. H. Helm, R. K. Jobe, A. Kulikov, and J.C. Sheppard, `Energy Matching of 1.2 GeV Positron Beam to the SLC Damping Ring', XIV Intl. Conf. on High Energy Accelerators, Tsukuba, Japan (1989).
34. P. Wilson, "High Energy Electron Linacs; Application to Storage Ring RF Systems and Linear Colliders", SLAC-PUB-2884 (1982).
35. T. Raubenheimer, in the Zeroth Order Design Report for the Next Linear Col-

lider, SLAC Report 474, p. 227-228 (1995).
36. F. Hinode *et al.*, "Accelerator Test Facility–Design and Study Report", KEK Internal Report 95-4 (1995).
37. R.D. Kohaupt and G.A. Voss, 'Progress and Problems in Performance of $e+/e-$ Storage Rings', Ann. Rev. Nucl. and Part. Sci., **33**, (1983) 67.
38. I. Reichel, talk at SLAC, May 1997.
39. M.G. Minty *et al*, the measured damping times before and after the ring circumference adjustment are given in "Using a Fast-Gated Camera for Measurements of Transverse Beam Distributions and Damping Times", AIP Conf. Proc., **281** J.A. Hinkson and G. Stover eds., Accelerator Instrumentation Workshop, (Berkeley, 1992) 158.
40. SAD accelerator modeling code by K. Oide.
41. G. Hoffstätter, private communication (1999).
42. M.G. Minty, R. Akre, F.-J. Decker, J. Frisch, S. Kuroda, F. Zimmermann, `Emittance Reduction via Dynamic RF FRequency Shift at the SLC Damping Rings', 17th Intl. Conf. on High-Energy Acc., Dubna, Russia (1998).
43. D. Schulte, "Study of Electromagnetic and Hadronic Background in the Interaction Region of the TESLA Collider", Ph.D. thesis, University of Hamburg (1996).
44. G. Hoffstätter, F. Willeke, `Electron Dynamics in the HERA Luminosity Upgrade Lattice of the Year 2000', to be published in proc. IEEE Part. Acc. Conf., New York, NY (1999).

Chapter 7

Polarization Issues

In this chapter spin transport in circular accelerators and transport lines is described. We begin with a review of the Thomas-BMT equation[a]. The spin equation of motion will be given in terms of the SU(2) spinor representation. Basic concepts of spinor algebra will be introduced and applied in the description of techniques used for preserving the spin of polarized beams up to very high beam energies. Lastly we present a few concepts from spin resonances theory.

7.1 Thomas-BMT Equation

The concept of particle spin was first introduced by Uhlenbeck and Goudsmit in 1926. In 1927 Thomas[1] showed that a purely kinematic precession governs the behavior of relativistic accelerated particles which possess a magnetic moment. This helped to explain an outstanding discrepancy in describing both the anomalous Zeeman effect and the fine structure splittings of the Coulombic energy levels in the hydrogen spectrum. In 1959, Bargmann, Michel, and Telegdi[2] expressed the magnetic field in terms of its transverse and longitudinal components. The resultant Thomas-BMT equation describes the spin motion in the presence of electromagnetic fields experienced by an orbiting particle in the laboratory frame.

Uhlenbeck and Goudsmit presupposed that the (in this case) electron of mass m and charge e, possessed both a magnetic moment $\vec{\mu}$ and spin angular momentum $\vec{S}$ related to one another by

$$\vec{\mu} = \frac{ge}{2mc}\hbar\vec{S}, \tag{7.1}$$

[a] Here BMT stands for Bargman, Michel, and Telegdi.

where $c = 2.9979 \times 10^8$ m/s, $\hbar$ is Planck's constant (normalized by 2π), S again is the three-dimensional particle `spin', and g is the gyromagnetic ratio. For spin transport calculations one defines the deviation of the gyromagnetic ratio, or Lande' g-factor g, from 2 as

$$\begin{aligned} G &= \frac{g-2}{2} = 1.7928 \text{ for protons, and} \\ a &= \frac{g-2}{2} = 0.00115966 \text{ for electrons.} \end{aligned} \tag{7.2}$$

The equation of motion for the spin in an external magnetic field[3] is given, in the particle rest frame, by

$$\begin{aligned} \frac{d\vec{S}}{dt} &= \vec{\mu} \times \vec{B} \\ &= \vec{\Omega} \times \vec{S}, \end{aligned} \tag{7.3}$$

where the angular velocity of the spin precession is simply

$$\vec{\Omega} = -\frac{ge}{2mc}\vec{B}. \tag{7.4}$$

The kinematic solution for the precession frequency for a relativistic particle in external electromagnetic fields is given by the Thomas-BMT equation:

$$\frac{d\vec{S}}{dt} = -\frac{e}{mc}\big[(a+\frac{1}{\gamma})\vec{B} - \frac{a\gamma}{1+\gamma}\vec{\beta}(\vec{\beta}\cdot\vec{B}) - (a+\frac{1}{1+\gamma})\vec{\beta}\times\vec{E}\big], \tag{7.5}$$

where $\vec{\beta} = \frac{\vec{v}}{c}$ with $\vec{v}$ the particle velocity, and $\gamma = 1/\sqrt{1-\beta^2}$ is the Lorentz factor or ratio of the particle energy to mass. For many practical applications there are no significant electric fields[b], and the Thomas-BMT equation reduces to

$$\frac{d\vec{S}}{dt} = \frac{e}{\gamma mc}\vec{S} \times [(1+G\gamma)\vec{B}_\perp + (1+G)\vec{B}_\parallel], \tag{7.6}$$

where $\vec{B}_\perp$ and $\vec{B}_\parallel$ represents the magnetic fields perpendicular and parallel to the particle velocity respectively.

[b] More precisely, in transforming the electromagnetic fields, the term $\vec{\beta} \times \vec{E}$ is nearly zero since the electric fields in an accelerator are usually parallel to the particle velocity

Ex.7.1. Electrostatic lenses and muon storage rings[a]
The muon anomolous magnetic moment, now recognized to be about 0.001166, can be measured very accurately using electrostatic lenses with a transverse electric field. In the rotating reference frame, the spin precession is given by

$$\vec{\Omega} = -\frac{e}{mc}\Big(\frac{\vec{B}}{\gamma} - \frac{\gamma}{\gamma^2 - 1}\vec{\beta} \times \vec{E}\Big). \tag{7.7}$$

Show that even the transverse electric field $\vec{E}$ does not contribute to spin precession when the Lorentz factor is

$$\gamma = \sqrt{1 + \frac{1}{a}}. \tag{7.8}$$

[a] Adapted from lecture notes of A. Chao (1999)

From Eq. 7.6 notice that the amount of spin `kick' due to a transverse magnetic field depends on the particle energy through the factor $1 + G\gamma$ while the amount of spin precession due to a longitudinal magnetic field is energy independent. We will see later that this has implications on spin rotator design.

7.2 Spinor algebra using SU(2)

While we first present an entirely classical approach [4] to spin dynamics calculations, we can still use quantum mechanics formalisms to more easily describe spin dynamics. It is mathematically advantageous to do so since transporting 2×2 spinors (Ψ) is simpler than transporting the 3-dimensional spin polarization vector $\vec{S}$. The relationship between the two is given by the expectation value of the Pauli spin vector $\vec{\sigma}$; i.e.

$$S_i = \Psi^\dagger \sigma_i \Psi, \tag{7.9}$$

with the Pauli matrices defined[c] as

$$\sigma_x = \begin{pmatrix} 0 & 1 \\ 1 & 0 \end{pmatrix} \quad \sigma_s = \begin{pmatrix} 0 & -i \\ i & 0 \end{pmatrix} \quad \sigma_y = \begin{pmatrix} 1 & 0 \\ 0 & -1 \end{pmatrix}. \tag{7.10}$$

Together with the identity matrix these 4 matrices generate an irreducible representation of the SU(2) group.

[c] Caution–different authors adopt different conventions; here we adopt the convention (often used by high energy physicists) that x is radial, s is longitudinal, and y is vertical. A cyclic permutation may be used to transform between conventions.

Ex.7.2. Spinors
For practice, these exercises are informative.
a) Using Eq. 7.9 find the spinor wave function for the spin basis $\vec{S} = [\vec{S}_x, \vec{S}_s, \vec{S}_y]$ *with* $\vec{S}_x = [1\ 0\ 0]$, $\vec{S}_s = [0\ 1\ 0]$, *and* $\vec{S}_z = [0\ 0\ 1]$.
b) Show that the Pauli matrices are unitary ($\sigma_j {\sigma^\dagger}_j = I$*) and Hermitian (*${\sigma^\dagger}_j = \sigma_j$*) with* $\vec{\sigma}^\dagger \cdot \vec{\sigma} = 3I$.
c) Verify the compact form of the commutation relations:

$$\sigma_j \sigma_k = \delta_{jk} I + i \Sigma_m \epsilon_{jkm} \sigma_m, \tag{7.11}$$

where

$$\begin{aligned} \sigma_{jk} &= 1 \text{ if } j = k \\ &= 0 \text{ if } j \neq k \end{aligned} \tag{7.12}$$

and ϵ_{jkm} *is the Levi-Civita tensor defined by*

$$\begin{aligned} \epsilon_{jkm} &= 0 \text{ if any two indices are equal} \\ &= +1 \text{ for even permutation of indices} \\ &= -1 \text{ for odd permutation of indices.} \end{aligned} \tag{7.13}$$

Ex.7.3. Spin precession in solenoidal fields
Consider a vertically polarized beam traversing ($\vec{\beta} = \beta \hat{s}$*) a longitudinal solenoid of field* $\vec{B} = B_z \hat{s}$ *of length* l *in the absence of any electric fields.*
a) Show that the spin precession ϕ *after traversal of the solenoid is given by*

$$\phi = -\frac{e}{\gamma m c^2} \frac{l}{\beta} (1 + G) B_z. \tag{7.14}$$

b) Suppose this solenoid is in a circular accelerator. By equating the centrifugal and Lorentz forces on the particle show that the magnetic rigidity is

$$B\rho = \frac{\beta E}{e} \tag{7.15}$$

and reexpress Eq. 7.14 in terms of the rigidity.
c) For spin polarization in a storage ring we will see that spin precession by π *per turn helps cancel various spin resonances. For the case of a 100 MeV proton beam specify the required integrated field strength to achieve this.*

7.3 Spin Equation of Motion

For generality we can reexpress the spin equation of motion for spinor wave function, Eq. 7.3, in terms of a time-like variable θ defined as

$$\theta = \int_0^s \frac{ds'}{\rho(s')} \tag{7.16}$$

which is equal to the accumulated bending angle or so-called orbital angle. Then the equation of motion is

$$\frac{d\Psi}{d\theta} = \frac{i}{2} H \Psi, \tag{7.17}$$

where H denotes the spin precession matrix which in the absence of depolarizing resonances is

$$H = \begin{pmatrix} -\kappa & 0 \\ 0 & \kappa \end{pmatrix}, \tag{7.18}$$

with $\kappa = G\gamma$ for protons and $\kappa = a\gamma$ for electrons.

If the spin precession matrix H is time-independent, or equivalently independent of the orbital angle, θ, and there are no perturbing fields, then the 2×2 unitary matrix can be written as a linear combination of the three components of the Pauli matrix vector. Eq. 7.17 may then be expressed as

$$\frac{d\Psi}{d\theta} = -i\frac{\lambda}{2}(\vec{\sigma} \cdot \hat{n})\Psi, \tag{7.19}$$

in which λ depends on the particle coordinates (to emphasize the basic underlying principles, we defer the explicit expressions until needed in section 7.9), and $\hat{n}$ is a unit vector. The solution, which defines the spinor transformation matrix M is

$$\Psi(\theta) = M\Psi(0), \tag{7.20}$$

where

$$M = e^{-i(\frac{\lambda}{2})(\vec{\sigma}\cdot\hat{n})\theta}. \tag{7.21}$$

By expanding the exponential, the solution is then

$$\Psi(\theta) = \left[\cos\left(\frac{\lambda\theta}{2}\right) - i(\vec{\sigma} \cdot \hat{n}) \sin\left(\frac{\lambda\theta}{2}\right)\right] \Psi(0). \tag{7.22}$$

To complete this section we give also the spin equation of motion for the polarization vector $\vec{S}$ which serves also to illustrate some of the algebraic conversions

presented to far. Since the components of the polarization are given by the expectation value of the Pauli spin matrices ($\vec{\mathrm{S}} = \Psi^\dagger \vec{\sigma} \Psi$), the spin equation of motion for the vector polarization is obtained by taking the derivative of the last expression

$$\frac{d\vec{\mathrm{S}}}{d\theta} = \frac{d\Psi^\dagger}{d\theta}\vec{\sigma}\Psi + \Psi^\dagger\vec{\sigma}\frac{d\Psi}{d\theta}. \tag{7.23}$$

Using Eq.7.19 and its Hermitian conjugate, $\frac{d\Psi^\dagger}{d\theta} = i\frac{\lambda}{2}\Psi^\dagger(\vec{\sigma}\cdot\hat{n})$, one finds

$$\frac{d\vec{\mathrm{S}}}{d\theta} = i\frac{\lambda}{2}\Psi^\dagger[(\vec{\sigma}\cdot\hat{n})\vec{\sigma} - \vec{\sigma}(\vec{\sigma}\cdot\hat{n})]\Psi = i\frac{\lambda}{2}\Psi^\dagger[2i(\hat{n}\times\vec{\sigma})]\Psi. \tag{7.24}$$

Using $\sigma_i\sigma_j = 1$ for $i = j$ and $\sigma_i\sigma_j = i\epsilon_{ijk}$ for $i \neq j$, one can show that

$$[\vec{\sigma}\cdot\vec{\mathrm{n}}, \vec{\sigma}] = 2i(\vec{\mathrm{n}}\times\vec{\sigma}). \tag{7.25}$$

Then,

$$\frac{d\vec{\mathrm{S}}}{d\theta} = -\lambda\Psi^\dagger(\hat{n}\times\vec{\sigma})\Psi = -\lambda\hat{n}\times(\Psi^\dagger\vec{\sigma}\Psi) = -\lambda(\hat{n}\times\vec{\mathrm{S}}). \tag{7.26}$$

7.4 Periodic Solution to the Spin Equation of Motion

For a circular accelerator we seek a periodic solution to the spin equation of motion. Here we write the spin transfer matrix M as a product of n precession matrices, each of which characterizes a spin precession field; i.e. $M = M_1 M_2 \cdots M_n$. The one turn spin transfer map is the transfer matrix corresponding to one revolution around the accelerator. Because spin is conserved, the matrix M is unitary. It may therefore be expressed as

$$M = e^{-i\pi\nu_s(\sigma\cdot\hat{n}_s)} = \cos\pi\nu_s - i(\sigma\cdot\hat{n}_s)\sin\pi\nu_s \tag{7.27}$$

or

$$M = \begin{pmatrix} \cos\pi\nu_s - i\sin\pi\nu_s\cos\alpha_y & -\sin\pi\nu_s\cos\alpha_s - i\sin\pi\nu_s\cos\alpha_x \\ \sin\pi\nu_s\cos\alpha_s - i\sin\pi\nu_s\cos\alpha_x & \cos\pi\nu_s + i\sin\pi\nu_s\cos\alpha_y \end{pmatrix} \tag{7.28}$$

Here the directional cosines are used to specify the stable spin direction

$$\hat{n}_s = (\cos\alpha_x, \cos\alpha_s, \cos\alpha_y). \tag{7.29}$$

The directional cosines satisfy the normalization

$$\cos^2\alpha_x + \cos^2\alpha_s + \cos^2\alpha_y = 1. \tag{7.30}$$

The stable spin direction, is defined as the axis[d] that returns to the same place in every turn around the ring. The spin tune, ν_s, is the number of times the spin precesses about the stable spin direction in one turn around the ring. It may be obtained from the trace of the spin precession matrix:

$$\begin{aligned} \mathrm{Tr}\ M &= 2\cos\pi\nu_x \ \text{ or} \\ \nu_s &= \frac{1}{\pi}\cos^{-1}\left(\frac{\mathrm{Tr}\ M}{2}\right). \end{aligned} \tag{7.31}$$

Ex.7.4. Periodic spin motion
Using the expansion of the exponential

$$e^{i\alpha\sigma_j} = \cos\alpha + i\sigma_j \sin\alpha \ \text{ where } j = x, s, y \tag{7.32}$$

verify Eq. 7.28.

7.5 Depolarizing Resonances

Depolarizing resonances occur whenever the spin tune, ν_s, equals a resonance tune, ν_{res}, by satisfying

$$\nu_s = \nu_{res} \equiv n + mP + q\nu_x + r\nu_y + s\nu_{syn}, \tag{7.33}$$

where P is the superperiodicity (the number of identical lattice sections) of the accelerator, ν_x and ν_y are the horizontal and vertical betatron tunes, ν_{syn} is the synchrotron tune, while $m, n, q, r,$and s are integers. In the absence of any longitudinal and radial error fields, the spin tune, ν_s, is equal to $G\gamma$ or $a\gamma$ for protons or electrons, respectively.

The general resonance condition specifies the criteria for many first order resonances. Imperfection depolarizing resonance, for which

$$\nu_s = \nu_{res} = n = \text{integer}, \tag{7.34}$$

arise from horizontal magnetic fields experienced by the orbiting particle due to magnet imperfections, dipole magnet rotations about the beam direction, and to vertical quadrupole magnet misalignments. Gradient error resonances and intrinsic resonances, which result from the horizontal fields of quadrupoles, occur if

$$\nu_s = \nu_{res} = n + r\nu_y \text{ and } \nu_s = \nu_{res} = mP + r\nu_y, \tag{7.35}$$

[d] the existence of this axis hold true for conservative force fields only

respectively. Synchrotron depolarizing resonances due to the coupling between transverse and longitudinal particle oscillations occur if

$$\nu_s = \nu_{res} = n + s\nu_{syn} \text{ or } \nu_s = \nu_{res} = mP + s\nu_{syn}. \tag{7.36}$$

Finally, betatron coupling resonances, given by

$$\nu_s = \nu_{res} = n + q\nu_x + r\nu_y \tag{7.37}$$

can also result in spin depolarization. Other higher order spin depolarizing resonances may occur for any combination of integers which satisfy Eq. 7.33.

Resonant spin motion was observed in the SLC collider arcs[5]. The 1 mile arcs were used to transport 45.6 GeV polarized electrons from the linac to the interaction point where they collided headon with positrons. The arc consists of 23 achromatic sections with a 108° phase advance per cell. The vertical beam trajectory and the components of the spin (denoted here by S_y for vertical and S_z for longitudinal) is shown in Fig. 7.1 assuming an initial vertical offset of 0.5 mm. The equal orbit and spin phase advance is seen to contribute to a net spin precession as evidenced by the increase in vertical polarization along the arc. In practice, vertical bumps were used to optimally align the spin to be longitudinal at the interaction point.

Ex.7.5. SLC `3-state experiment'
Assuming no resonant depolarization (that is pure spin precession) in the SLC arcs, show that the magnitude of the polarization at the interaction point (IP) can be obtained from three successive measurements of the longitudinal polarization at the IP by proper orientation of the incoming polarization with each measurement.

7.6 Polarization Preservation in Storage Rings

The first requirement of maintaining a beam's polarization is preserving this polarization at injection into a downstream accelerator. This is easily achieved by orienting (using upstream spin rotators) the beam polarization so that it is aligned with the stable spin direction of the downstream transport line or storage ring.

A mismatch at injection results in a cosine-like reduction of the beam polarization. The injected polarization is replaced by

$$\vec{S} = \vec{S}_{inj}(\cos\beta_x, \cos\beta_s, \cos\beta_y), \tag{7.38}$$

where the directional cosines for the injected beam are $(\cos\beta_x, \cos\beta_s, \cos\beta_y)$. The resultant polarization is given by the projection of the injected polarization vector on the stable spin vector, $\vec{n}_s$; i.e.

$$\|\vec{S}\| = \vec{S}_{inj}(\cos\beta_x\cos\alpha_x + \cos\beta_s\cos\alpha_s + \cos\beta_y\cos\alpha_y), \tag{7.39}$$

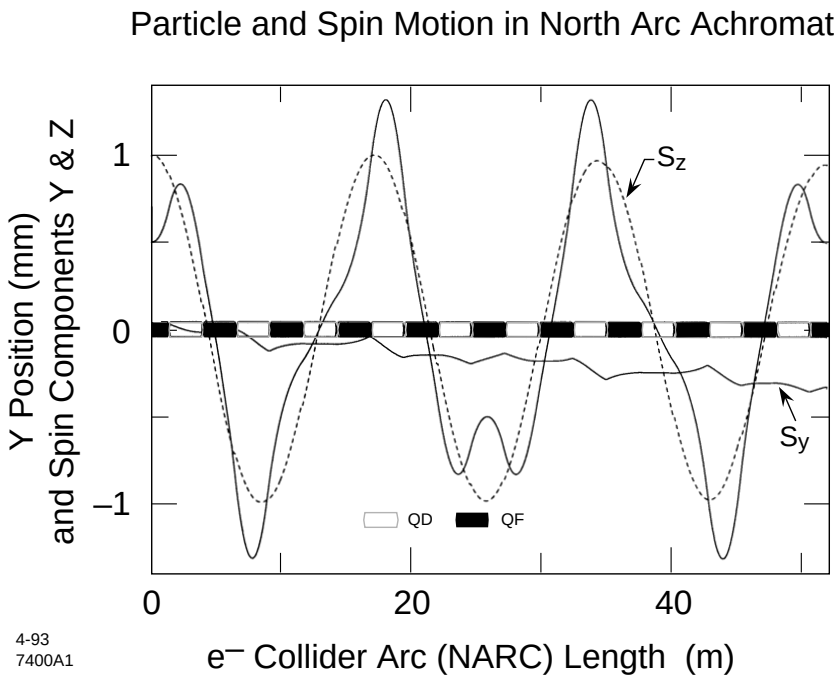

Figure 7.1: Polarization transport in the SLC collider arc. (Courtesy P. Emma, 1999).

where α_j with $j = x, s, y$ are the directional cosines corresponding to the one turn map of Eq. 7.28. The components of the resultant polarization vector are then obtained by projecting the polarization onto the three coordinate axes:

$$S_y = \|S\| \cos \alpha_y; \quad S_x = \|S\| \cos \alpha_x; \quad S_z = \|S\| \cos \alpha_s. \tag{7.40}$$

A conceptual illustration is given in Fig. 7.2.

Once the beam is successfully injected without loss of polarization, it must be ramped to high energy thereby encountering numerous depolarizing resonance along the energy ramp. With considerable effort, polarized proton beams were accelerated through many intrinsic and imperfection depolarizing resonances to GeV energies at the ZGS [6], Saturne [7], the AGS [8], and KEK [9]. The methods employed were based on overcoming each depolarizing resonance individually. In this section we review the physics and techniques used to overcome these resonances. In the next section we describe so-called 'Siberian snakes', the use of which has recently been successfully demonstrated experimentally and is now the prefered technique for all newly

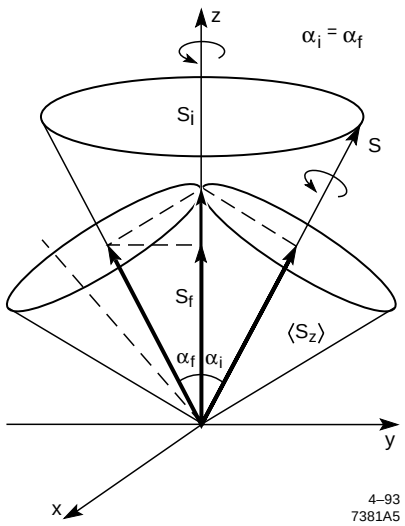

Figure 7.2: Graphical representation showing projection of (drawn purely vertical) injected polarization S_i onto stable spin direction S resulting in average projection $\langle S_z \rangle$.

constructed and future high energy accelerators.

7.6.1 Harmonic correction

The concept of harmonic correction of imperfection depolarizing resonances was used at the AGS to ramp polarized proton beams to about 22 GeV. There 96 correction dipoles were employed whose currents were programmed to be proportional to $a_n \cos n\theta + b_n \sin n\theta$, where n is the resonance harmonic and θ is the orbital location of the correction dipole. As will be shown later, the resonance strength depends on the vertical beam displacement (in quadrupoles, for example, the nominally vertical polarization experiences a radial precession field with an off-axis beam). To eliminate depolarization, the coefficients a_n and b_n were experimentally adjusted to cancel the horizontal magnetic fields causing each imperfection resonance.

Harmonic correction methods were successfully applied for the cases of high energy electron beams at both HERA [10] and, deterministically, at LEP [11]. Instead of empirically varying the closed orbit, closed orbit bumps were used to minimize the strength of the nearest imperfection resonances.

7.6.2 Adiabatic spin flip

The method of adiabatic spin flip, which was also used at the AGS, is based on the results of Froissart and Stora [12]. The Froissart-Stora formula, which describes the spin transport through a single, isolated resonance, is

$$S_z(\infty) = 2e^{-\frac{\pi\epsilon^2}{2\alpha}} - 1, \tag{7.41}$$

where the resonance strength (see section 7.9) is parameterized by ϵ, and α is the rate of spin precession $\frac{d\nu_s}{d\theta}$.

The Froissart-Stora formula mandates that the spin of the orbiting particle will flip if the passage is slow and the resonance is strong. This behavior has also been verified by experiment [13,14,15]. An example taken from the IUCF cooler ring [15] is shown in Fig. 7.3. Here a solenoid was used to produce a sinusoidally varying longitudinal field to induce a depolarizing resonance at frequencies related harmonically to the revolution frequency of the orbiting proton beam. For a fixed frequency range of 2 kHz, the rate of the frequency change, or ramp rate, was varied for different peak magnetic fields proportional to the voltage given on the horizontal axis. The curve shows the Froissart-Stora equation with the measured resonance strength and variable ramp rate.

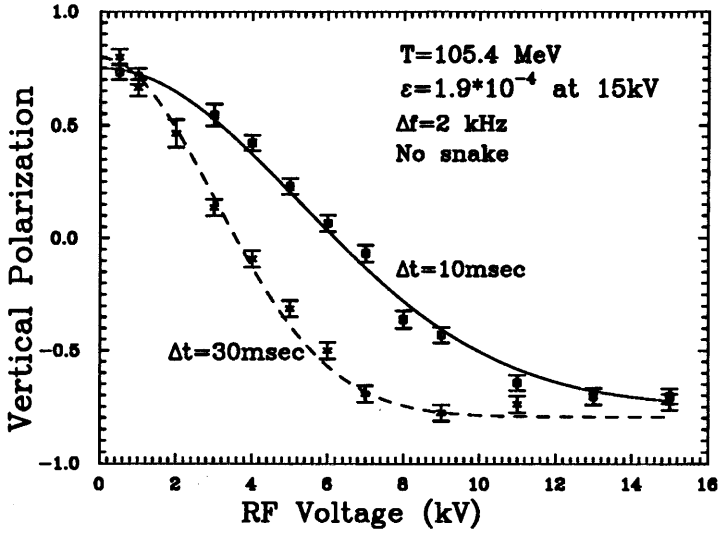

Figure 7.3: Spin flip of a vertically polarized beam. (Courtesy A. Krisch, 1999).

7.6.3 Tune jump

Intrinsic depolarizing resonances were overcome at the AGS using the method of tune jump[16]. As γ increases during acceleration, the resonance condition can be rapidly traversed by rapidly shifting the vertical betatron tune, ν_y. A classic example[16] is shown in Fig. 7.4. To achieve this, strong pulsed quadrupoles and special ceramic beam pipes (to allow passage of the field) were required.

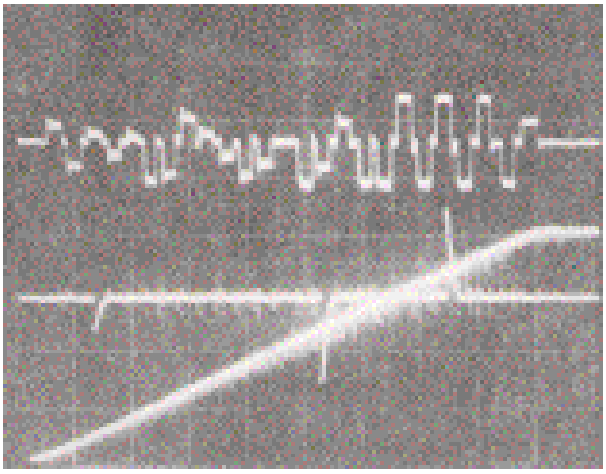

Figure 7.4: Oscilloscope traces showing pulsed devices during the energy ramp to 16.5 GeV/c at the AGS. Shown are the pulsed dipoles (top), the pulsed quadrupoles (middle), and the dipoles fields (bottom). (Courtesy A. Krisch, 1999).

7.7 Siberian Snakes

The above mentioned correction schemes were anticipated to be of limited applicability when accelerating polarized beams to very high energies. The harmonic correction employed at the AGS was complicated and time consuming; the empirically found corrections also depended on the closed orbit of the accelerator, which were seen to drift with time and change between running periods. At very high energies, where the resonances will be overlapping, the method of adiabatic spin flip fails[17]. The method of tune jump is stopband limited since, for a very strong intrinsic resonance, the vertical betatron tune shift required to overcome the resonance may exceed the separation between the machine betatron resonances. Finally, the number of resonances increases with increasing energy. At the SSC, where there would have been more than

10^4 depolarizing resonances, overcoming each resonance individually clearly would become impractical.

An ingenious arrangement of magnets was proposed [18] by Derbenev and Kondratenko in 1976. This technique [e] would simultaneously overcome all depolarizing resonances by making the spin tune to be energy independent. A so-called Type-1 snake rotates the spin of each proton by 180 degrees about the longitudinal axis on each turn around the ring without changing the closed orbit outside of the snake. This forces the spin tune to be $\frac{1}{2}$. The resonance condition of Eq. 7.33 is therefore never satisfied regardless of the beam energy: the integer spin tune imperfection resonance criterion is never satisfied and, for betatron tunes not equal to $\frac{1}{2}$ (corresponding to half integer orbit resonances), imperfection resonances are also avoided. A type-2 Siberian snake precesses the spin about the radial direction. A type-3 Siberian snake, which has not been considered to date as a means to preserve polarization, precesses the spin about the vertical direction.

The best construction of a Siberian snake depends upon the energy range of interest. A longitudinal Siberian snake consists of a solenoidal field and quadrupoles used for coupling correction. The required field strength is

$$\int B_{long} \cdot dl = \frac{mc\beta\gamma}{(1+G)e}\psi \quad (\text{longitudinal snake}) \tag{7.42}$$

in which ψ ($= \pi$ for a full Siberian snake) is the angle through which the spin is precessed. Notice that the required field integral depends linearly on γ. Due to technical constraints the field strength and magnet length cannot be increased indefinitely. Therefore longitudinal Siberian snakes are better suited for low energy operation. A transverse Siberian snake conventionally consists of eight transverse field dipoles each of which precesses the spin by $\frac{\pi}{2}$. The required field strength for a transverse Siberian snake is

$$\int B_{tran} \cdot dl = \frac{mc\beta}{Ge}\psi \quad (\text{transverse snake}) \tag{7.43}$$

which is independent of γ. Transverse Siberian snakes therefore have the advantage that a single set of dipole operating currents suffices for all beam energies once β is close to 1. However, the orbit displacement angle is $\frac{\psi}{G\gamma}$. For low beam energies ($\gamma < 10$), transverse Siberian snakes would require the construction of large and costly dipoles. Transverse Siberian snakes are therefore more suitable for operation at high beam energies.

The spin equation of motion with a type-1 Siberian snake, which precesses the spin about the longitudinal direction by an amount η, is

$$M = e^{-i\pi\nu_s(\vec{n}_s\cdot\vec{\sigma})} = [e^{-i\frac{G\gamma}{2}(\pi-\theta)\sigma_{\mathbf{y}}} e^{-i\frac{\eta}{2}\sigma_{\mathbf{s}}}][e^{-i\frac{G\gamma}{2}(\pi+\theta)\sigma_{\mathbf{y}}}], \tag{7.44}$$

[e] dubbed 'Siberian snake' by Courant

where θ is the orbital angle representing the location of the polarization monitor, and η gives the spin precession about the longitudinal in radians. Taking the trace of Eq. 7.44, the particle spin tune is

$$\cos \pi\nu_s = \cos(\pi G\gamma)\cos\left(\frac{\eta}{2}\right). \tag{7.45}$$

If the Siberian snake is off ($\eta = 0$), then $\nu_s = G\gamma$ as expected.

The use of transverse magnetic fields acting on the spin have the unfortunate consequence of also deflecting the particle orbit. Optical transparancy must be maintained usually at the expense of increased snake length. Many different snake designs[19,20,21] have been proposed. Shown in Fig. 7.5 is one such design consisting of alternating horizontal and vertical dipoles. This design is conveniently expressed as

$$\mathrm{H}(\frac{\pi}{2})\mathrm{H}(-\frac{\pi}{2})\mathrm{V}(\frac{\pi}{2})\mathrm{H}(-\frac{\pi}{2})\mathrm{V}(-\pi)\mathrm{H}(\frac{\pi}{2})\mathrm{V}(\frac{\pi}{2}), \tag{7.46}$$

where H and V represent horizontal and vertical dipoles rotating the spin through the angle of the argument.

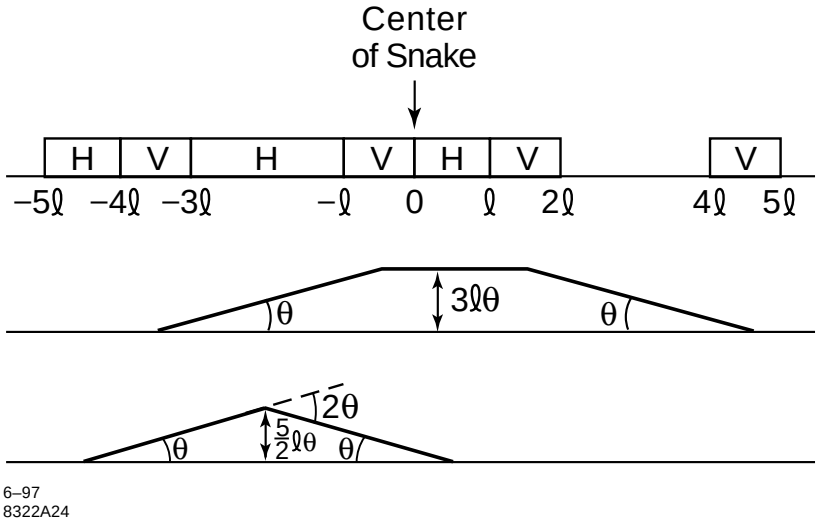

Figure 7.5: A design of a type-1 Siberian snake showing the geometry (top) and the mean trajectories in the horizontal (middle) and vertical (bottom) planes. (Courtesy A. Chao, 1999).

Ex.7.6. Type-3 snakes
With L representing a precession about the longitudinal axis
a) show that the configuration

$$[\mathrm{H}(-\frac{\phi}{2})\mathrm{L}(+\frac{\chi}{2})\mathrm{H}(+\frac{\phi}{2})]\ \mathrm{L}(-\frac{\chi}{2})\ [\mathrm{H}(-\frac{\phi}{2})\mathrm{L}(+\frac{\chi}{2})\mathrm{H}(+\frac{\phi}{2})] \qquad (7.47)$$

is optically transparant but produces a net spin precession about the vertical axis.
b) Draw the spin orientation and the particle orbit for the given magnet configuration.

In addition to preserving the spin, it is often desirable to rotate the spin from vertical to longitudinal at one of possibly many interaction points in a storage ring as is done at HERA [22], for example. An optically transparant spin rotator which does that was proposed by Montague [23] in 1976. The spin rotation matrix R is given by

$$\mathrm{R} = \mathrm{V}(\alpha)\mathrm{V}(-\alpha)\mathrm{V}(-\frac{\pi}{4})\mathrm{H}(-\pi)\mathrm{V}(\frac{\pi}{4}) \times \mathrm{V}(-\frac{\pi}{4})\mathrm{H}(\pi)\mathrm{V}(\frac{\pi}{4}). \qquad (7.48)$$

For transverse magnetic fields, the orbital bending angles are obtained by the precession angle divided by $G\gamma$. The contribution of each magnet to orbital displacements, which commute, is seen to sum to zero. Since the time of this invention numerous other schemes have been proposed and some implemented. Some novel designs of Steffen exhibit also the highly desirable feature of energy-independent spin precession.

Interestingly, it was not until 1989 that the Siberian snake concept was tested experimentally [24,25]. Shown in Figs. 7.6 and 7.7 are measurements of the vertical and radial polarization taken at different beam energies in the vicinity of the $G\gamma = 2$ imperfection resonance. The horizontal axis shows the error field introduced 180° opposite of the Siberian snake. With the snake turned off, the polarization of the injected beam was vertical to match the stable spin direction in the ring. With the snake on, the incoming polarization was oriented in the plane of the accelerator at an angle consistent with the prefered longitudinal orientation at the Siberian snake.

It is worth mentioning that the presence of a Siberian snake in an accelerator may introduce a new kind of resonance dubbed a snake resonance [26]. The snake resonance condition is given by $u\nu_{res} = t\nu_s + n$ in which ν_s (=$\frac{1}{2}$) is the spin tune determined by the snake, ν_{res} is defined in Eq.7.33, and u, t and n are integers. Depolarization may occur if the spin precession frequency is modulated by the frequency at which the depolarizing precession elements are encountered by the orbiting particle. Experimental verification of the presence of the snake resonance is given in ref. [27]

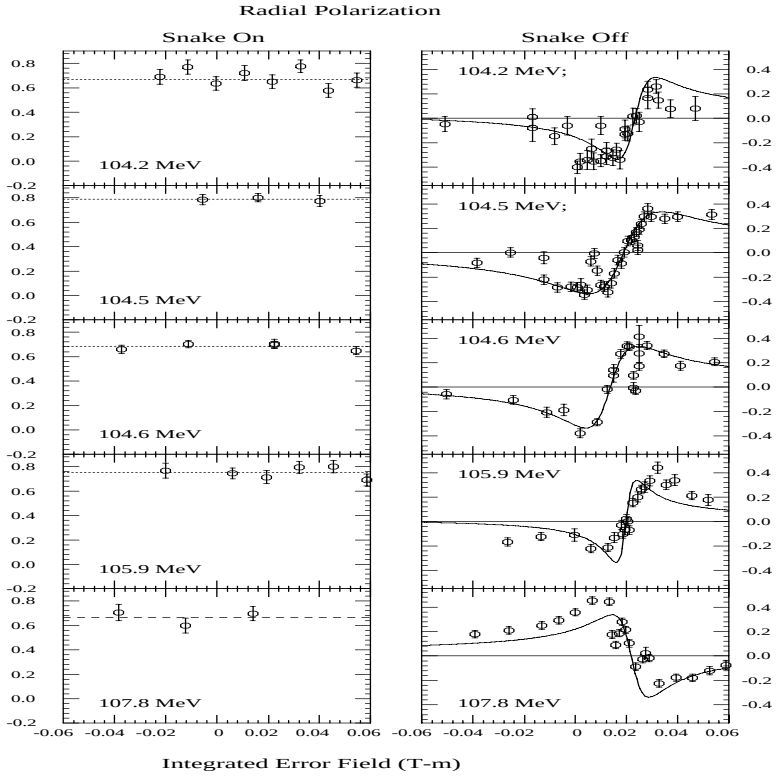

Figure 7.6: Measurements of radial polarization near a $G\gamma = 2$ imperfection resonance (at about 106.4 GeV) at 5 different beam energies with a 100% Siberian snake on (left) and off (right).

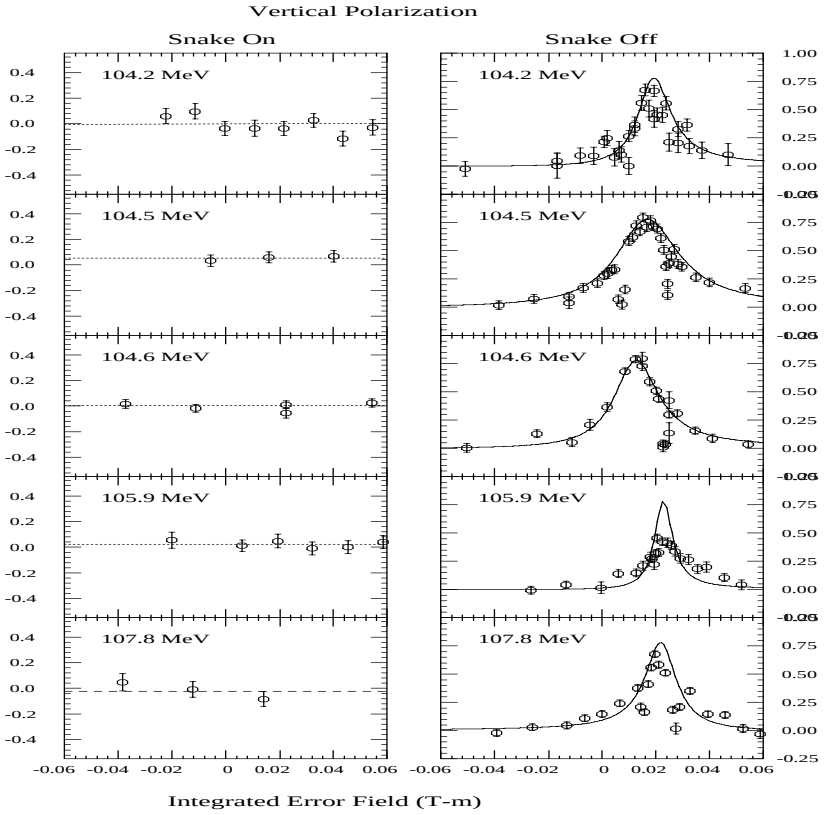

Figure 7.7: Measurements of vertical polarization near a $G\gamma = 2$ imperfection resonance (at about 106.4 GeV) at 5 different beam energies with a 100% Siberian snake on (left) and off (right).

7.8 Partial Siberian Snakes

In 1989 T. Roser[28] proposed an elegant and intuitive variant of the Siberian snakes called partial Siberian snakes. With the benefit of reduced cost and required space, at lower beam energies partial snakes may be used place the spin tune (not at $\frac{1}{2}$ as in the case of full snakes) at a desired value thus avoiding known locations of imperfection and/or intrinsic resonances. The expression for the spin tune versus energy was given in Eq. 7.45 and is shown in Fig. 7.8 for different percentages of applied longitudinal field ($\eta = \pi$ denotes a full snake which is designated in the figure by 100%). The diagonal line shows the spin tune with no snake. As can be seen, even a relatively weak ($\sim$ few $\%$) snake can be used to avoid the imperfection resonance at $\nu_s =$integer. Moreover, once the betatron tunes are known, the snake strength can be set such that intrinsic resonances are also avoided.

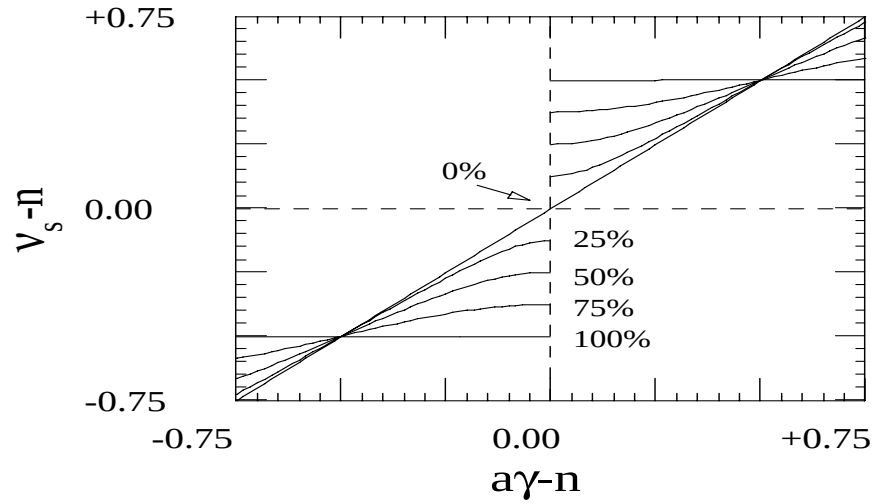

Figure 7.8: The dependence of the spin tune on $G\gamma$ for various strengths (indicated by percentage of full 180 degree spin precession).

An example showing the first demonstration of the ability of partial Siberian snakes to avoid depolarizing resonances is shown in Fig. 7.9. With a 10% snake full polarization was maintained. Since the time of these data, partial snakes have been installed and successfully used[29] to ramp polarized protrons to high energy ($\sim$ 22 GeV) at the Brookhaven AGS in preparation for high energy spin physics in RHIC.

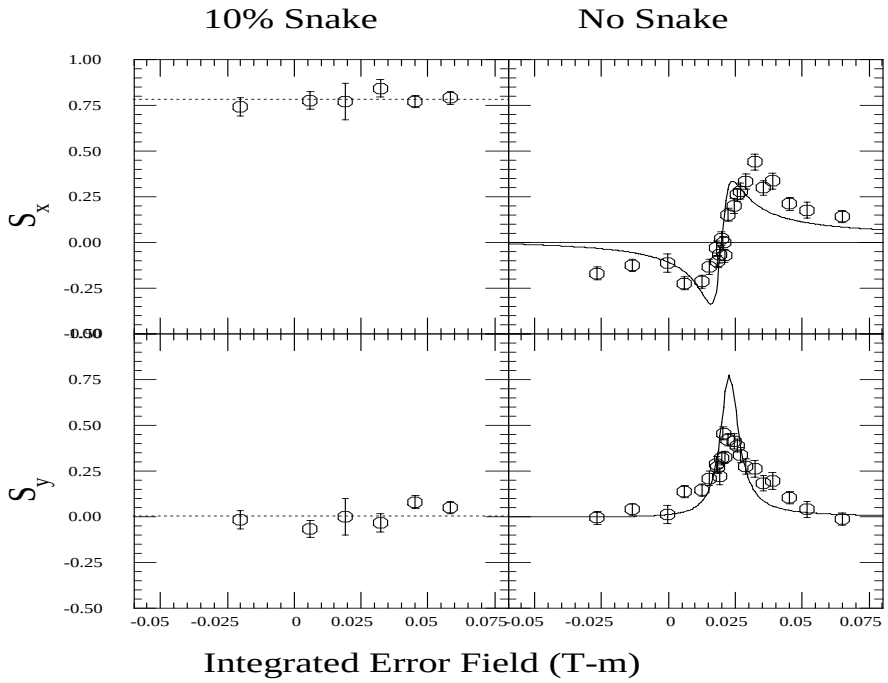

Figure 7.9: Demonstration of polarization preservation in the vicinity of an imperfection resonance using a partial Siberian snake.

7.9 Spin resonance theory

Until now we have avoided the use of complicated formulas and have presented basic concepts one needs in practical applications of spin transport and preservation. In particular the resonance criterion of Eq. 7.33 was simply stated without proof. Here we expand on the Thomas-BMT equation and demonstrate explicitly the resonance conditions of spin motion.

We rely on the work of Courant and Ruth[30], who expressed the magnetic fields in the Thomas-BMT equation in terms of the particle coordinates. They found that the spin equation of motion reduces to

$$\frac{dS_x}{d\theta} = -\kappa S_s - r S_y; \quad \frac{dS_s}{d\theta} = +\kappa S_x - t S_y; \quad \frac{dS_y}{d\theta} = +r S_x + t S_s, \qquad (7.49)$$

where κ, r, and t are functions of the transverse coordinates of the particle orbit. In the cartesian coordinate system (with $\hat{x}$ radially outward, $\hat{s}$ along the beam direction, and

$\hat{y}$ vertical) and ρ the local radius of curvature of the reference orbit, these variables are given by[30]

$$\begin{aligned} \kappa &= G\gamma - (1+G\gamma)\rho x'' \approx G\gamma \\ r &= (1+G\gamma)y' - \rho(1+G)\left(\frac{y}{\rho}\right)' \\ t &= (1+G\gamma)\rho y'', \end{aligned} \tag{7.50}$$

with the derivatives taken with respect to the longitudinal coordinate, s.

Eq. 7.49 can then be transformed into an equivalent spinor representation, for which

$$\frac{d\Psi}{d\theta} = \frac{i}{2} H \Psi. \tag{7.51}$$

Here H is the spinor precession matrix given by

$$H = \begin{pmatrix} -\kappa & -t - ir \\ -t + ir & \kappa \end{pmatrix}, \tag{7.52}$$

and Ψ is a two component complex spinor. As before the polarization components are obtained by taking the expectation value of the Pauli matrix vector, $\vec{\sigma}$; i.e.

$$S_i = \Psi^\dagger \sigma_i \Psi. \tag{7.53}$$

The off diagonal matrix elements in H characterize the effect of spin depolarization due to the coupling between the up and down components of the spinor wave function. Due to the periodic nature of a synchrotron, the coupling term of Eq. 7.52 may be expanded in terms of the Fourier components; i.e.

$$t + ir = \sum \epsilon_i e^{-i\nu^i{}_{res}\theta} \tag{7.54}$$

in which θ is the particle's orbital angle, $\nu^i{}_{res}$ is the value of the resonant tune for the i^{th} resonance from Eq. 7.33, and ϵ_i is the resonance strength and is given by the Fourier amplitude

$$\epsilon_i = \frac{1}{2\pi} \int (t + ir) e^{i\nu^i{}_{res}\theta} d\theta. \tag{7.55}$$

The resonance strength, which may be calculated by summing over error fields encountered by the particle in one turn around the ring, is approximately

$$\epsilon_i \approx \frac{1+G\gamma}{2\pi} \sum \frac{\partial B_y/\partial x}{B\rho} y e^{i\nu^i{}_{res}\theta}. \tag{7.56}$$

This corresponds to summing over the precession angles due to each radial error field. The function H is uniquely determined by the properties of the synchrotron. In the

analyses of previous sections we have assumed that the function, H, is piecewise constant.

As an illustration of the previous results, we now show that a transverse imperfection resonance can also shift the spin tune. In the single resonance approximation[26,31], the spin equation in the particle rest frame is given by

$$\frac{d\Psi}{d\theta} = -\frac{i}{2}\begin{pmatrix} G\gamma & -\zeta \\ -\zeta^* & -G\gamma \end{pmatrix}\Psi, \quad \text{with} \quad \zeta = \epsilon \cdot e^{-i\nu_{res}\theta}, \tag{7.57}$$

in which ϵ is the resonance strength, ν_{res} is the resonance tune, and θ is the particle orbital angle around the accelerator. Transforming the spin equation to the resonance precession frame (the reference frame in which the polarization vector does not precess) using

$$\Psi_k = e^{i\frac{\nu_{res}\theta}{2}\sigma_y}\Psi, \tag{7.58}$$

we obtain

$$\frac{d\Psi_k}{d\theta} = \frac{i}{2}(\delta\sigma_y + \epsilon_R\sigma_x - \epsilon_I\sigma_s)\Psi_k, \tag{7.59}$$

where σ_i are the Pauli matrices and $\epsilon = \epsilon_R + i\epsilon_I$. Eq. (90) can be integrated easily to obtain

$$\Psi_k(\theta_f) = e^{\frac{i}{2}(\delta\sigma_y + \epsilon_R\sigma_x - \epsilon_I\sigma_s)(\theta_f - \theta_i)}\Psi_k(\theta_i). \tag{7.60}$$

Transforming back to the particle rest frame, we obtain then

$$\begin{aligned} \Psi(\theta_f) &= e^{-i\frac{\nu_{res}\theta_f}{2}\sigma_y} e^{\frac{i}{2}(\delta\sigma_y + \epsilon_R\sigma_x - \epsilon_I\sigma_s)(\theta_f - \theta_i)} e^{i\frac{\nu_{res}\theta_i}{2}\sigma_y}\Psi(\theta_i) \\ &= T(\theta_f, \theta_i)\Psi(\theta_i). \end{aligned} \tag{7.61}$$

By expanding the exponential, the spin transfer matrix $T(\theta_f, \theta_i)$ for a single resonance may be calculated[26,31]:

$$T(\theta_f, \theta_i) = \begin{pmatrix} ae^{i(c - \frac{\nu_{res}(\theta_f - \theta_i)}{2})} & ibe^{-i(d + \frac{\nu_{res}(\theta_f + \theta_i)}{2})} \\ ibe^{i(d + \frac{\nu_{res}(\theta_f + \theta_i)}{2})} & ae^{-i(c - \frac{\nu_{res}(\theta_f - \theta_i)}{2})} \end{pmatrix} \tag{7.62}$$

with

$$\begin{aligned} b &= \frac{|\epsilon|}{\lambda}\sin\frac{\lambda(\theta_f - \theta_i)}{2}, \quad a = \sqrt{1 - b^2}, \\ c &= \arctan[\frac{\delta}{\lambda}\tan\frac{\lambda(\theta_f - \theta_i)}{2}], \quad d = \arg\epsilon^*, \\ \delta &= \nu_{res} - G\gamma, \quad \lambda = \sqrt{\delta^2 + |\epsilon|^2}. \end{aligned} \tag{7.63}$$

The spin tune can be obtained from the trace of the one turn transfer map, $T(\theta + 2\pi, \theta)$ of Eq. 7.62, i.e.

$$\cos\pi\nu_s = a\cos(c - \nu_{res}\pi). \tag{7.64}$$

Figure 7.10 shows the effect of the spin tune shift, $\nu_{res} - G\gamma$, as a function of $G\gamma - 2$ for the special cases where $|\epsilon| = \sqrt{\epsilon_R^2 + \epsilon_I^2} = 0.0008$ and $|\epsilon| = 0.0015$. In both cases, for $G\gamma$ far away from the resonance tune, ν_{res}, $\delta >> |\epsilon|$ and $a \approx 1$ so $\nu_s \approx G\gamma$. As $G\gamma$ approaches the resonance tune, the spin tune is shifted from $G\gamma$ by $\Delta\nu_s = -|\epsilon|$ below the resonance and by $\Delta\nu_s = |\epsilon|$ above the resonance; i.e. the spin tune is always shifted away from the resonance tune. Therefore at a given energy, the observed width of the vertical polarization would always be increased when the effect of the imperfection resonance is included. The observed slope of the radial polarization through the fully compensated field value would also be lessened in magnitude. Figure 7.10 indicates that the effect of the imperfection resonance becomes important only in very close proximity to the resonance.

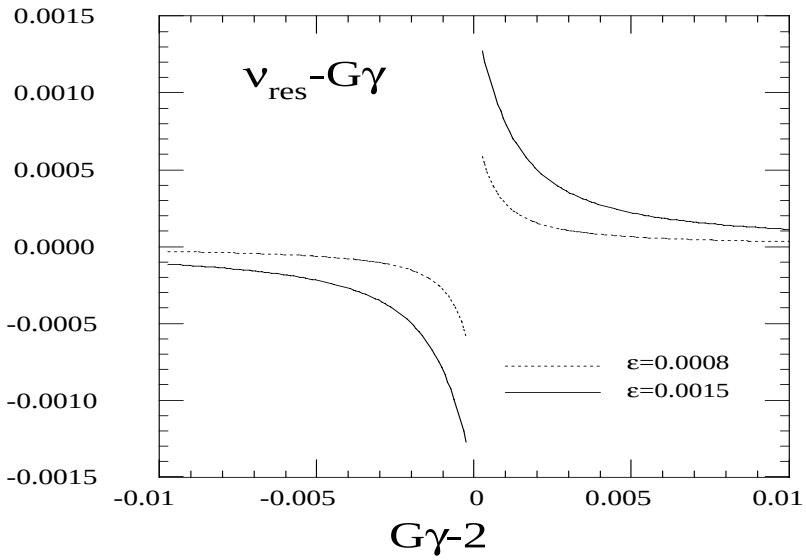

Figure 7.10: Spin tune shift vs. $G\gamma - 2$ near an imperfection resonance. From Eq. 7.64 the dependence of the shift in the spin tune on $G\gamma - 2$ due to an imperfection resonance is plotted. The dashed curve corresponds to a resonance strength of magnitude 0.0008. The solid curve results for a resonance strength of 0.0015.

Near the imperfection resonance, the spin motion can be seen by transforming to the resonance precession frame by letting

$$\Psi_1 = e^{-\frac{i}{2}\kappa\theta\sigma_y}\Psi \tag{7.65}$$

with $\delta = \kappa - G\gamma$ in Eq. 7.57. Then

$$\frac{d\Psi_1}{d\theta} = -\frac{i}{2}\begin{pmatrix} -\delta & \epsilon \\ \epsilon^* & \delta \end{pmatrix}\Psi_1. \tag{7.66}$$

The solution, decomposed into two eigenmodes, is

$$\Psi_\pm = e^{\pm i\frac{\lambda\theta}{2}}\begin{pmatrix} \frac{\epsilon}{|\epsilon|}\sqrt{\frac{\lambda\pm\delta}{2\lambda}} \\ \mp\sqrt{\frac{\lambda\mp\delta}{2\lambda}} \end{pmatrix}, \tag{7.67}$$

where $\lambda = \sqrt{\delta^2 + |\epsilon|^2}$. The particle spin is given by a linear combination of the eigensolutions:

$$\Psi_1(\theta) = C_+\Psi_+ + C_-\Psi_- \tag{7.68}$$

normalized such that $|C_+|^2 + |C_-|^2 = 1$. The component along the y axis is

$$\begin{aligned} S_y &= \Psi^\dagger\sigma_y\Psi \\ &= {\Psi_1}^\dagger\sigma_y\Psi_1 \\ &= \frac{\delta}{\lambda}(|C_+|^2 - |C_-|^2) + \frac{2|\epsilon|}{\lambda}\mathrm{Re}[C_+{C_-}^* e^{i\lambda\theta}]. \end{aligned} \tag{7.69}$$

For an initially vertically polarized particle, the time averaged vertical polarization is found to be

$$\langle S_y\rangle = \frac{\delta}{\lambda}(|C_+|^2 - |C_-|^2) = \frac{\delta^2}{\lambda^2} = \frac{\delta^2}{\delta^2 + |\epsilon|^2} \tag{7.70}$$

which is less than the initial polarization by an amount that depends on the resonance strength ϵ.

7.10 References

1. L.H. Thomas, Philos. Mag., 3 (1927) 1.
2. V. Bargman, L. Michel, V.L. Telegdi, Phys. Rev. Lett.,2(1959)435.
3. J.D. Jackson, `Classical Electrodynamics', John Wiley and Sons, Inc. (1975).
4. B.W. Montague, "Polarized Beams in High Energy Storage Rings", Phys. Rep. 113 (1984)
5. T. Limberg, P. Emma, and R. Rossmanith, `The North Arc of the SLC as a Spin Rotator', IEEE Part. Acc. Conf., Washington, DC, 429-431 (1993).
6. T. Khoe *et al.*, Part. Accel., 6(1975)213.
7. J.L. Laclare *et al.*, Jour. de Phys., 46(1985)C2-499.
8. F.Z. Khiari *et al.*, Phys. Rev., D39(1989)45.
9. H. Sato *et al.*, Nucl. Instr. and Meth., A272(1988) 617.
10. M. Böge and R. Brinkmann, `Optimization of Electron Spin Polarization by Application of a Beam Based Alignment Technique in the HERA Electron Ring', DESY Int. Rep. MEA-95-02; Proc. 1995 Conf. in Accelerator Alignment, Tsukuba, Japan (1995) 412-420; R. Brinkmann and M. Boege, `Beam Based Alignment and Polarization Optimization in the HERA Electron ring', DESY Int. Rep. M-94-03-D; proc. EPAC London (1994) .
11. R. Assmann *et al*, `Deterministic Harmonic Spin Matching in LEP', 4th Eur. Part. Acc. Conf. (EPAC94), London, England (1994) 932-934.
12. M. Froissart and R. Stora, Nucl. Instr. Meth., 1(1960)
13. J.L. Laclare *et al.*, Jour. de Phys., 46(1985)C2-499.
14. Y. Cho, A.D. Krisch, L. Ratner *et al.*, ` `Proceedings of High Energy Spin Symposium", AIP Conf. Proc., 35, No. 12, (1976) 396.
15. D.D. Caussyn *et al*, `Spin Flipping a Stored Polarized Proton Beam', Phys. Rev. Lett. **73** (1994) 2857-2859.
16. F.Z. Khiari *et al*, Phys. Rev., D39 (1989) 45.
17. S. Tepikian, S.Y. Lee, E.D. Courant, ` `On Multiple Spin Resonances for the Polarized Proton", Part. Accel., 17(1986)1.
18. Ya.S. Derbenev and A.M. Kondratenko, *Proc. of the* 10^{th} *Intl. Conf. on High Energy Accel.,* Protvino, *v.*2(1977)70; Ya.S. Derbenev, Part. Accel., 8(1978)115.
19. K. Steffen, `Note on the choice of Siberian Snake Configurations in Proton Rings', DESY HERA 85-24 (1985).
20. K. Steffen, `Design of an Orthogonal Snake Pair for Proton rings in the Few Gev Energy Range', DESY HERA 97-11 (1987).
21. K. Steffen, `How to Avoid Imperfection Spin Resonances in a Protron Ring with Snakes', DESY 89-024 (1989).
22. D.P. Barber, `Longitudinal Electron Spin Polarisation at 27.5 GeV in HERA',

DESY-98-096B (1998).
23. B.W. Montague, rpt. CERN/ISR-LTD/76-2 (1976).
24. A.D. Krisch *et al*, "First Test of the Siberian Snake Magnet Arrangement to Overcome Depolarizing Resonances in a Circular Accelerator," *Phys. Rev. Lett.*, **63** (1989) 1137.
25. J.E. Goodwin *et al*, "Overcoming Intrinsic and Synchrotron Depolarizing Resonances with a Siberian Snake," *Phys. Rev. Lett.*, **64** (1990) 2779.
26. S.Y. Lee, S. Tepikian, Phys. Rev. Lett., **56** (1986) 1635-1638.
27. R.A. Phelps *et al*, `First Observation of a Snake Depolarizing Resonance', Phys. Rev. Lett. **78** 2772-2774 (1997).
28. R. Roser, 1990 Partial Siberian Snake Workshop, Brookhaven, NY (1990).
29. H. Huang *et al*, `Preservation of Protron Polarization by a Partial Siberian Snake', Phys. Rev. Lett. **73**, 2982-2985 (1994).
30. E.D. Courant, BNL Report EDC-45 (1962); E.D. Courant, R.D. Ruth, "The Acceleration of Polarized Protons in Circular Accelerators," BNL 51270, 1980.
31. S.Y. Lee, Prospects for Polarization at RHIC and SSC, AIP Conf. Proc., No. 224, (1991) 35.

Chapter 8

Injection and Extraction

Injection into a storage ring or linac is the final part of beam transfer from one accelerator to another. Injection should be accomplished with minimum beam loss and emittance dilution. Single-turn injection is straightforward. In many cases, one also wishes to accumulate beam, in a storage ring, by reinjecting different beam pulses into the same rf bucket. This is called multi-turn injection. In addition to conventional schemes, there are several new or more exotic injection techniques, devised to control and improve the properties of the stored beam.

Extraction refers to the removal of beam from an accelerator. It is roughly the reverse process of injection. One difference is that usually at extraction the beam energy is higher. Thus space charge effects are less important, but the hardware requirements are more challenging. A high extraction efficiency is necessary to avoid activation of accelerator components and to make optimum use of the accelerated beam. Which extraction procedure is chosen depends on the specific application. Fast one-turn extraction is used for transfering bunches between different circular machines in an accelerator chain. For fixed-target experiments, slow extraction by the controlled excitation of nonlinear betatron resonances is a common technique, which provides a slow uniform spill. Again, several novel extraction schemes are being studied, for example, extraction using a bent crystal.

A good overview of conventional beam injection and extraction can be found in Refs.[1] and[2].

8.1 Transverse Single-Turn Injection

In single-turn injection, the beam is brought onto the central orbit using a septum magnet and a fast kicker element, as illustrated in Fig. 8.1. In the following, we

assume that the injection is performed horizontally. The expressions derived can be extended easily to the vertical case, or to a combined horizontal and vertical injection.

At the exit of the septum, the injected beam must be at a horizontal distance x_{sep} from the center of the machine aperture:

$$x_{sep} \geq n_x(\sigma_{xi} + \sigma_{xs}) + \eta_x \left(\frac{\Delta p}{p}\right)_i + x_{co,\mathrm{rms}} + x_{i,\mathrm{rms}} + d_{sep} \qquad (8.1)$$

where σ_{xi}, σ_{xs} are the rms beam sizes of the incoming beam and of the stored beam, respectively, n_x is the required beam stay-clear for sufficient beam lifetime or negligible injection losses (*e.g.*, reasonable values may be $n_x \geq 8$ for electron rings, and $n_x \geq 4$ for proton rings), $(\Delta p/p)_i$ the relative momentum deviation of the injected beam with respect to the ring energy, η_x the dispersion function, $x_{co,\mathrm{rms}}$ the rms closed-orbit offset at the location of the septum, $x_{i,\mathrm{rms}}$ the rms orbit variation of the injected beam, and d_{sep} the thickness of the septum. For simplicity in Eq. (8.1) we assumed that the injected and the stored beam have the same beam stay-clear, in units of their rms beam size.

The injected beam must be at the center of the aperture when it reaches the kicker. Let R denote the 2×2 transport matrix between the septum and the kicker. The condition $x_{kic} = R_{11}x_{sep} + R_{12}x'_{sep} = 0$ determines the correlation of angle x'_{sep} and offset x_{sep} of the injected beam at the exit of the septum:

$$x'_{sep} = -\frac{\alpha_{sep} + \cot\mu}{\beta_{sep}} x_{sep} \qquad (8.2)$$

where μ denotes the phase advance from septum to kicker, and α_{sep} and β_{sep} are the beta and alpha function at the septum. The angle can be adjusted by changing the strength of the septum magnet. The kicker must then apply an angular deflection of

$$\theta_{kic} = -\frac{x_{sep}}{\sqrt{\beta_{sep}\beta_{kic}}\sin\mu} \qquad (8.3)$$

A large value of β_{kic} reduces the kicker strength, and also reduces the relative contribution to θ due to the septum thickness.

In case of a FODO lattice, septum and kicker are best placed downstream of a focusing quadrupole, where the beta functions are close to maximum. In the particular case that the phase advance μ is $\pi/2$, the above formulae simplify to $x'_{sep} = -\alpha_{sep}x_{sep}/\beta_{sep}$, $\theta_{kic} = -x_{sep}/\sqrt{\beta_{sep}\beta_{kic}}$.

Ex.8.1. Required septum fields for injection and extraction
Suppose that the minimum beam separation at the septum is $x_{sep} > n_s\sigma_x$. Derive an expression for the integrated kick strength $B_{kic}L_{kic}$, with B_{kic} the kicker magnetic field and L_{kic} its length, as a function of normalized emittance $\epsilon_{x,N}$ and energy.
Assume $n_s = 10$, $\beta = 100$ m, $\mu = \pi/2$, a kicker length of $L_{kic} = 5$ m, and a normalized emittance $\epsilon_{x,N} = 4$ μm. Compute the magnetic field B_{kic} required at a beam energy of 10 GeV and at 10 TeV.

The septum units can be either dc septum magnets or dc electrostatic wires. In either case, the stray or leakage fields of the septum are a concern. These nonlinear fields can affect the quality of the stored beam, if too large and improperly shielded.

The kicker magnets must be fast, since their rise and fall time determines the size of the gaps between bunches or between bunch trains in the ring. Typical time constants are tens of nanoseconds, and voltage and current levels of 80 kV and 5000 A, with fields of 500 Gauss, are not uncommon. Frequently ferrites are used for field containment, and sometimes a ceramic vacuum chamber is inserted between ferrite and the beam, with a conducting layer deposited on the inside of the ceramic. It is remarkable that the conducting layer can be much smaller than the skin depth and still provide adequate shielding of the beam fields. Shielding occurs when the thickness of the metal coating is larger than the square of the skin depth divided by the thickness of the ceramic[3]. The coupling impedance experienced by the beam should be measured prior to installation of the kicker chamber; as an example, measurements for a prototype LHC kicker chamber are documented in Ref.[4].

Other injection issues are transient beam loading and phase-space matching. Ref. [5] gives a thorough review of beam loading compensation in storage rings, including a discussion of direct rf feedback and of problems that can arise from klystron power limititions. Horizontal and vertical dispersion and beta functions, as well as the ratio of bunch length and energy spread must be matched to the ring (or linac) optics. The latter can be achieved via bunch rotation, bunch compression, or energy compression.

Ex.8.2. Emittance dilutions from injection errors
Consider injection into a storage ring with a 1 mm orbit error at $\beta = 100$ m, in both betatron phases.
a) Estimate the corresponding (growth in) normalized emittance after complete filamentation for proton, muon and electron beams at 10 GeV and at 1 TeV. Compare this with the design normalized emittances of the LHC (3.75 μm), the multi-TeV Muon Collider (50 μm), and the NLC (3 nm vertically). Note that $m_e c^2 = 511$ keV, $m_p c^2 = 938$ MeV, and $m_\mu c^2 = 105.7$ MeV.
b) In general the orbit error results in emittance growth comparable to the design emittance when it is of the same order as the rms beam size. Calculate the rms beam sizes for a 7-TeV proton beam (LHC), a 500-GeV electron beam (NLC) and a 2-TeV muon beam (MC) at $\beta = 100$ m.

It is also possible and indeed more elegant, to install two kickers in the ring, powered in parallel by the same pulser. They are arranged such that only the second kicker of the pair deflects the injected beam, while both kickers act on the stored beam. If the phase advance between the two kickers is π or 2π, and the sign of the kick appropriately chosen, the kicker deflections generate a closed bump for the circulating beam. The advantage is that in this case the rise and fall times of the kicker do not have to be smaller than the bunch spacing, but can be on the order of the revolution time. The requirements on the kickers can be further alleviated by a dc orbit bump, which brings the stored beam closer to the septum prior to the injection. Such a scheme is used at PEP-II [6]. The PEP-II injection process is illustrated in Fig. 8.2.

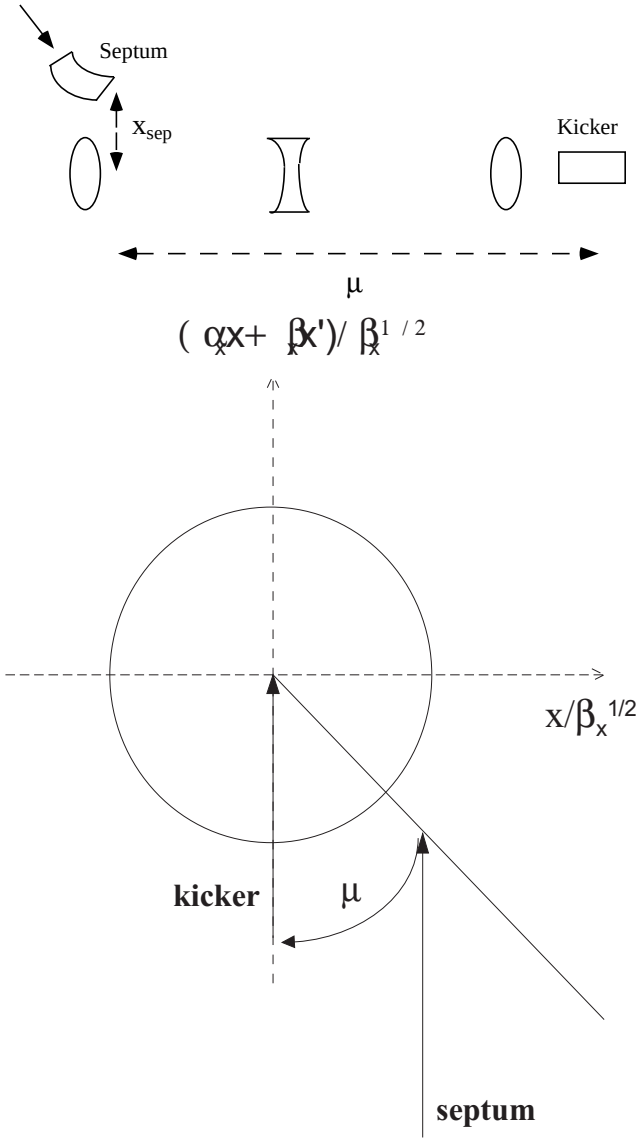

Figure 8.1: Schematic of single-turn injection with septum and kicker: (top) magnet arrangement, (bottom) phase-space diagram.

(a) nominal situation

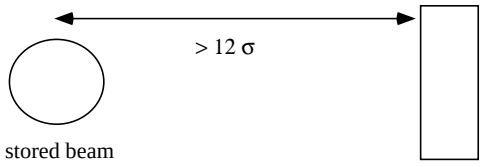

(b) dc orbit bump

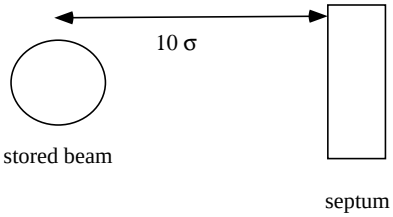

(c) displaced orbit plus incoming beam

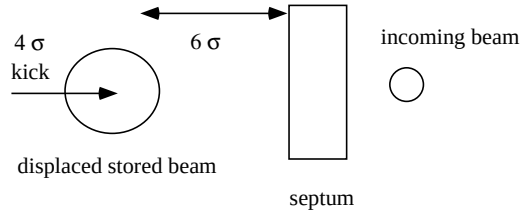

(d) pre-kick orbit restored, incoming beam kicked

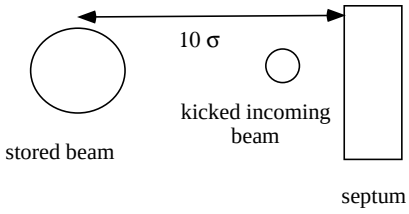

Figure 8.2: Injection process for PEP-II[6].

8.2 Multi-Turn Injection

8.2.1 Transverse Multi-Turn Injection

Multi-turn injection usually employs a programmed orbit bump in the vicinity of the septum, instead of a fast kicker. The injection scheme is different for electrons and for protons or heavy ions.

In case of electron rings, radiation damping is utilized. First, a single bunch is injected. Then the orbit bumps is reduced over a few revolution periods. After a few damping times, when the beam size has shrunk to its small equilibrium value, the orbit bump is reintroduced, and another bunch is injected into the same bucket. Similar schemes, though usually in the synchrotron phase space, are employed for accumulation of stochastically cooled antiproton beams.

For proton or heavy ions beams, the orbit bump is reduced slowly in time, and bunches are injected into different regions of the ring acceptance, so that the early bunches occupy the central region, and the later ones the outer parts of the acceptance. Some emittance dilution is inherent to this scheme. For N turn injection, the final emittance can be estimated from the rough formula[1]:

$$\epsilon_s > 1.5 N \epsilon_i \tag{8.4}$$

Much larger emittance dilutions arise when space charge effects are important.

8.2.2 Longitudinal and Transverse Multi-Turn Injection

The accumulation efficiency can be increased by combining transverse and longitudinal injection. This option is being studied for LEAR[7]. As in the purely transverse multi-turn injection scheme, a local orbit bump is created and then decreased during the injection of successive linac bunches. At the same time the linac energy is ramped such that, at the injection septum, the closed orbit corresponding to the instantaneous linac energy remains constant. In other words, the change in the bump amplitude $x_{bump}(t)$ and the simultaneous variation of the momentum $\delta(t)$ are related by

$$\eta\delta(t) = -x_{bump}(t) + x_0 \tag{8.5}$$

where x_0 is a constant and η the dispersion at the injection septum. In this scheme, the final transverse emittance is smaller than for the conventional multi-turn injection at the expense of an increased momentum spread. Figure 8.3 compares simulated phase space distributions[7] for transverse and combined injection into LEAR. Figure 8.4 shows the predicted improvement in the accumulation efficiency[7].

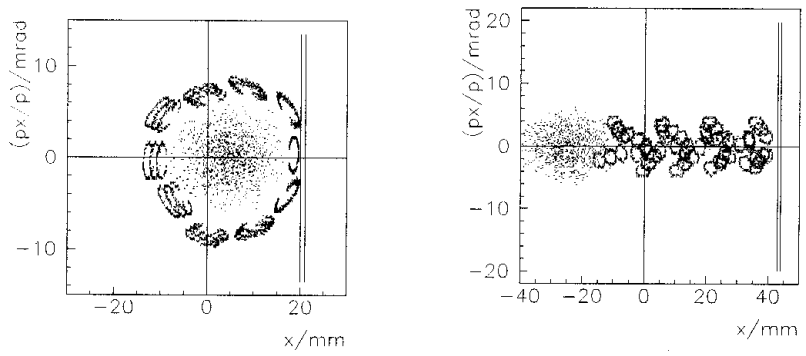

Figure 8.3: Plots of the simulated horizontal phase space for multiturn injection into LEAR[7]: (left) 10 turns after start of purely transverse injection and (right) 20 turns after start of combined longitudinal transverse injection. Each bunch is represented by three ellipses with slightly different momentum deviations.

8.2.3 Longitudinal Multiturn Injection

If for an electron ring the time between subsequent injections is short compared with the radiation damping time, multiturn transverse injection becomes difficult. In such a case, longitudinal injection offers a solution. Here the circulating beam is brought close to the septum with an ac bump and the incoming beam is injected with a negative energy offset such that the product of this offset in energy and the dispersion is equal to the distance between the newly injected and the stored beam. The injected bunches conduct slow synchrotron oscillations.

Consider as an example the case of LEP[8]. Half a synchrotron period after the first bunch is injected, the next injection occurs. At this time, the first bunch is at its maximum distance from the septum. The situation is illustrated in Fig. 8.5. Similarily one could conceive injecting every 1/4 oscillation period, thus accumulating 4 injected bunches in one rf bucket. An advantage of longitudinal injection is a factor two faster damping of the injection oscillations. A possible disadvantage is that the acceptable time separation of successive injections is constrained by the synchrotron frequency.

8.2.4 Phase-Space Painting

For proton and ions beams, the multi-turn injection is often described as “phase-space painting”[9,10]. This term refers to the injection of many small (linac) bunches into different spots of a 2- or 6-dimensional storage-ring phase space, so as to generate a desired beam distribution, *e.g.*, an approximately uniform distribution with reduced

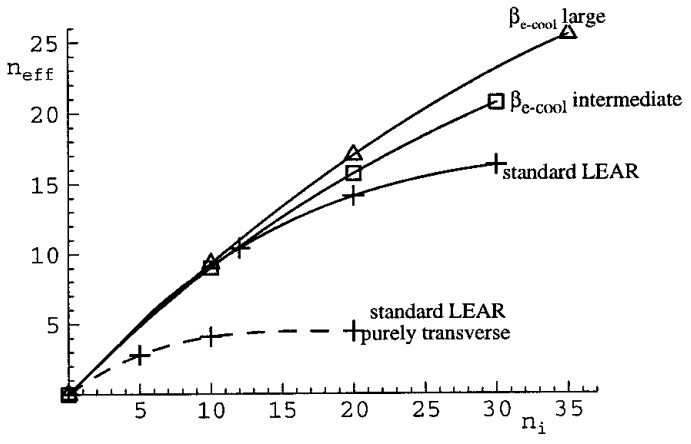

Figure 8.4: Effective number of turns stored in LEAR as a function of the number of injected turns [7]. The solid lines represent the combined transverse longitudinal injection scheme, for three different LEAR optics. For comparison, the dashed line is for a purely transverse injection.

space-charge effects. The combined longitudinal-transverse injection into LEAR discussed in subsection 8.2.2 can be considered as an example of phase-space painting.

In the simplest case the beam is injected at a fixed locus in the longitudinal (or transverse) phase space, and the painting is done automatically by the synchrotron oscillations.

The locus can also be moved in time at a speed slow compared with the synchrotron oscillations. The injected phase-space density $P(r)$ and its projection $p(x)$ are related via

$$p(x) = 2 \int_x^R \frac{rP(r)dr}{\sqrt{r^2 - x^2}} \tag{8.6}$$

where R denotes the maximum radius in phase space at which bunches are injected.

Ex.8.3. Filamentation
Consider a point bunch which is injected somewhere in phase space at a radius r. Compute the projected beam density $p(x)$, normalized to unity, after filamentation.

From a desired function $p(x)$, the corresponding radial density $P(r)$ can be com-

puted. The radial increment between two successive bunches is[9]

$$\Delta r \approx \frac{1}{2\pi r P(r) N_{inj}} \tag{8.7}$$

with N_{inj} the total number of injected bunches.

More complicated schemes are frequently used. Similar to the above horizontal-longitudinal injection for LEAR, one can also combine horizontal and vertical painting. For example, at RAL, a vertical steering magnet in the injection line is ramped, while the guide field in the ring is decreased[10]. Initially, there are small horizontal and large vertical oscillations, while at the end of the injection the situation is reversed. Instead of the vertical steering in the injection line, a programmable vertical orbit bump in the ring could be employed.

8.3 H^- Charge Exchange Injection

The idea of H^- exchange injections originated in Novosibirsk[11]. It is now the preferred injection scheme for proton machines[1]. In this scheme H^- ions are accelerated by a linac and are stripped to protons, when they traverse a thin foil during injection into the ring[1,12], as illustrated in Fig. 8.6.

Since the stripping of the H^- ions to protons occurs within the ring acceptance, Liouville's theorem does not apply, and, in principle, a very high proton density could be attained by injecting successive bunches into the same region of phase space. In most practical applications, however, vertical steering in the injection line is combined with a ramped horizontal orbit bump in the ring in order to provide a very uniform filling of the phase space and to minimize space charge effects.

The heating of the stripping foil and stripper scattering effects limit the foil thickness. Typical thicknesses range between 50 and 200 μg cm^{-2} (less than 1 μm), with stripping efficiencies of 98% for 50 MeV protons[1]. As foil materials, polyparaxylene, carbon and aluminum oxide have been used. The rms scattering angle for a single foil traversal is typically on the order 0.2 mrad. The total scattering angle increases as the square root of the average number of passages through the foil. The stripping foils are supported at three edges, so that vertical beam motion cannot be exploited to reduce the number of foil traversals.

Stacking simultaneously in both betatron and synchrotron phase space reduces the number of foil traversals. This can be achieved by changing the magnitude of an orbit bump, while also ramping the frequency and phase of the rf system during the injection cycle. The following lattice parameters at the location of the foil are advantageous[1]: $\eta' = 0$, $\alpha_x = 0$, and $\eta(\Delta p/p) > \sqrt{A\beta}$, where $\Delta p/p$ is the momentum acceptance and A is the transverse acceptance (in emittance units). A location be-

tween two symmetric defocusing quadrupoles is suitable. The quadrupole assists in deflecting the unstripped H^- ions.

Stripping foils are used for heavy ions as well. The final charge distribution of the ions depends on the foil thickness and on the particle energy [13]. In the extreme case, the ions can be fully stripped.

Foils are also used for extracting H^0 atoms or protons from H^- storage rings. A gas jet or a laser beam [14] would facilitate extraction in a similar way.

8.4 Resonant Injection

Another injection schemes worth mentioning is a proposal for resonant injection [15]. Here bumper magnets with dipole, quadrupole and octupole fields are excited to produce a separatrix with two stable regions in phase space; the stored beam is in one region, and a bunch is injected into the other region. Afterwards, the fields are adjusted to merge the two parts of the beam. Then the injection condition is reestablished.

8.5 Continuous Injection

Continuous injection has been proposed as a means for maximizing the luminosity of a circular collider [16]. The motivation is obvious. If the stored beam could be continually replenished so that the current per bunch stays constant, then the average luminosity would roughly equal the peak luminosity. Continuous injection would also reduce fill-to-fill variations and avoid transient events, thereby establishing quasi-static conditions. Finally, at the beam-beam limit, the beam lifetime decreases exponentially with the luminosity. Thus, continuous injection supporting a much reduced lifetime could provide a substantial gain in peak luminosity.

As an example, taking all these effects together, continuous injection is estimated [16] to potentially increase the average luminosity of the PEP-II B factory by about a factor of 5, assuming that each bunch in both rings can be replenished every 2.1 s. In this example, a 67-ns long orbit bump would move the injected bunches transversely to about 4σ from the stored beam core. This is done so that the injected bunches have an unobstructed passage through the physics detector. The effective minimum beam lifetime which can be supported is given by [16]

$$\tau = \frac{N}{\Delta N}\,\Delta t, \tag{8.8}$$

where N is the nominal number of particles per bunch, ΔN is the number of particles added into a single bunch per injection, and Δt the time period between successive injections into the same bunch. Extreme parameters for PEP-II are [16] $N \approx 1.2 \times 10^{11}$,

$\Delta N \approx 10^9$, and $\Delta t \approx 2.1$ s, yielding a minimum supportable beam lifetime of $\tau \approx 4.2$ minutes.

8.6 Injection Envelope Matching

At injection into a storage ring, if the incoming beam distribution is not properly matched to the ring optics, the beam envelope in phase space will rotate around the matched design envelope. This oscillation will result in turn-to-turn beam-size variations, which can be measured on a synchrotron light monitor using a gated camera.

An injection-mismatch measurement from the SLC damping ring[17,18] is shown in Fig. 8.7. The different pictures correspond to successive turns after injection, starting with turn number one. Each picture is an average over 8 individual images. Clearly visible is a variation of the bunch shape from turn to turn.

In case of the SLC damping ring, the matching of the injected beam distribution consists of minimizing the measured beam size after 1250 turns, by varying several quadrupoles at the end of the injection beam transport line. A number of 1250 turns was chosen, because at this time the initial beta and dispersion mismatch has completely filamented. Since, on the other hand, the time scale is much shorter than the radiation damping time, the emittance is given directly by $(\mathrm{Bmag} \cdot \epsilon)$, where ϵ is the emittance of the injected beam.

It is interesting to note that, in much the same manner as for the centroid motion measured with BPMs, the beam size variation can be analyzed in the frequency domain by a Fourier transform. A beta mismatch will appear as a frequency line at twice the betatron tune, while a dispersion mismatch will be evident as a line at the betatron tune itself[18]. If only a beta mismatch is present, the ratio ρ of the dc Fourier component and the component at $2Q_x$ is equal to $(\mathrm{Bmag}/\sqrt{\mathrm{Bmag}^2 - 1})$. From this, $\mathrm{Bmag} = 1/\sqrt{1 - \rho^{-2}}$ can be determined[18,19].

Figure 8.8 shows the beam size for the first 100 turns after injection, as well as the FFT (multiplied with γ/β where γ is the relativistic Lorentz factor and β the beta function). Clearly visible are peaks at $2Q_x$ in the horizontal signal and at $(1 - 2Q_y)$ in the vertical one. The final emittance after filamentation, $\mathrm{Bmag}\epsilon$, is given by the dc component of the FFT.

The standard matching procedure reduces the FFT signals at $2Q_x$, $(1-2Q_y)$ and Q_x, as illustrated in Fig. 8.9.

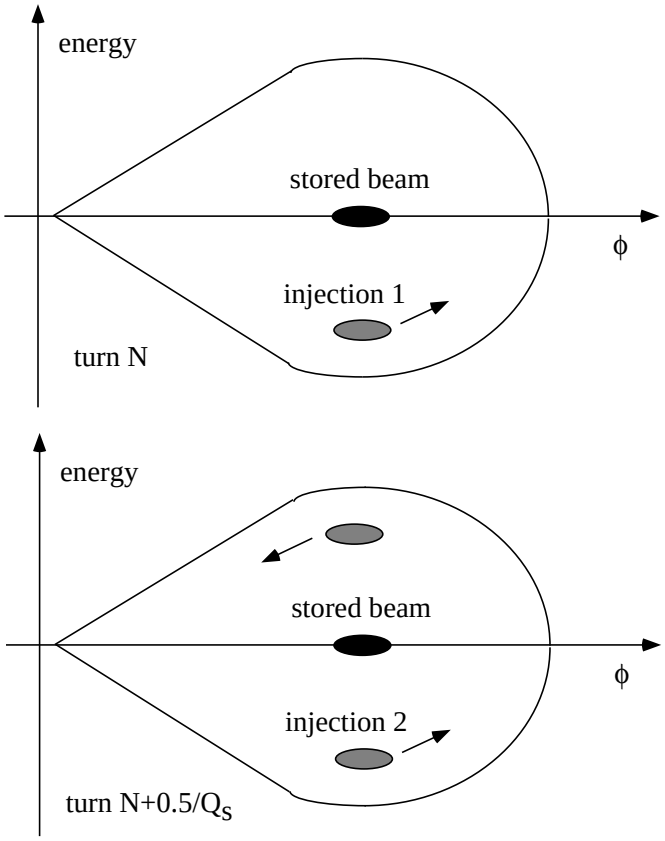

Figure 8.5: Double injection into the same rf bucket; bunches are injected off-energy at a point with dispersion. Time between the two injections is half a synchrotron oscillation period modulo a full period. This picture is copied from Ref.[8].

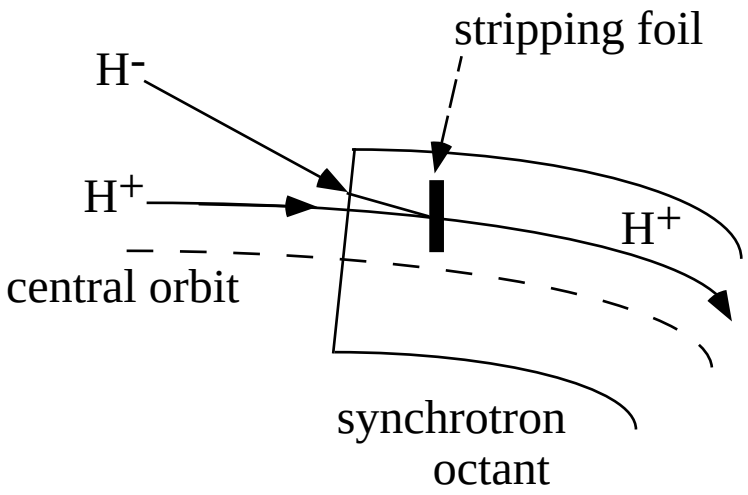

Figure 8.6: Schematic of H^- stripping injection.

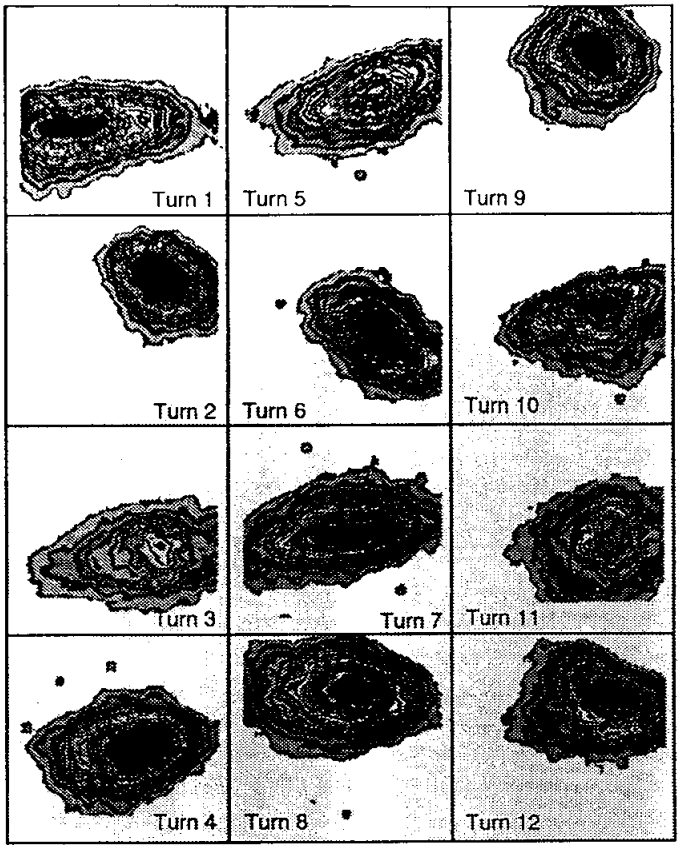

Figure 8.7: Beam images on the first twelve turns after injection into the SLC Damping rings, illustrating the effect of an injection mismatch[17,18]. These are pictures from a synchrotron light monitor taken with a gated camera. Each image is an average over 8 beam pulses. The beam-size variation from turn to turn is an indication of injection mismatch.

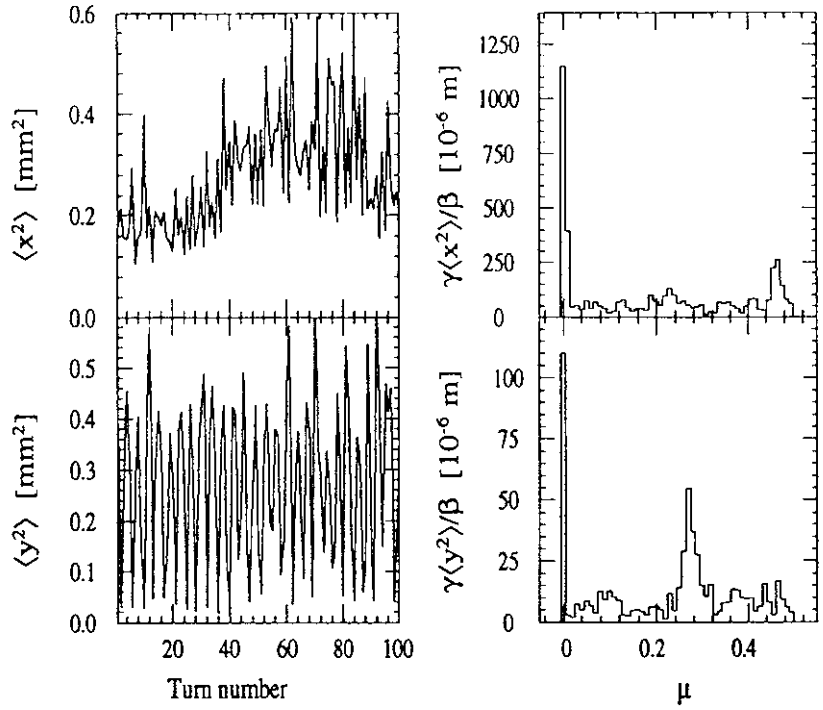

Figure 8.8: Horizontal (top) and vertical (bottom) beam sizes for the first 100 turns after injection into the SLC damping ring (left) and their FFT (right)[18]. Clearly visible in the frequency spectra are lines at $2Q_{x,y}$ (top) and at $1 - 2Q_y$ (bottom), whose amplitude is a measure of the amount of beta mismatch.

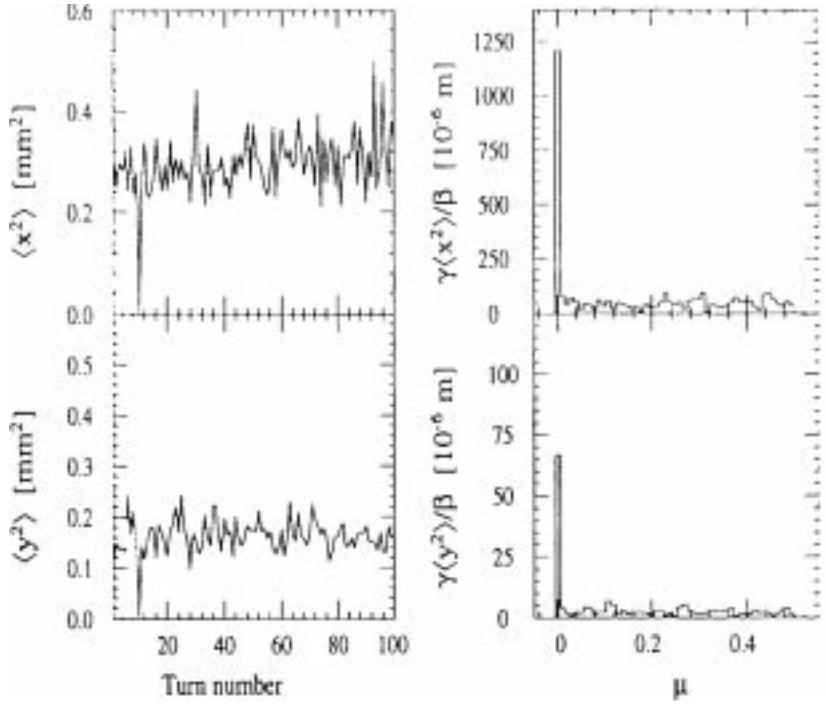

Figure 8.9: Same as Fig. 8.8, after beta matching[18]. The peaks at twice the betatron tune have disappeared.

8.7 Fast Extraction

Fast extraction is similar to single-turn injection. Orbit bumps are generated which move the stored beam close to a septum magnet. Then a fast kicker is fired, which deflects the next bunch, or group of bunches, into the extraction channel. If only one kicker is used, the kicker rise time must normally be smaller than the separation between two circulating bunches. The pulse length and fall time of the kicker are determined by the number of bunches to be extracted, and by the ring fill pattern. The minimum deflection angle required is

$$\theta_{kic} = \frac{x_{sep}}{\sqrt{\beta_{sep}\beta_{kic}}\sin\mu} \tag{8.9}$$

where β_{sep} and β_{kic} are the beta functions at septum and kicker, μ is the phase advance between these two elements, and x_{sep} is the minium displacement at the septum required for clean extraction. The initial orbit bump reduces the value of x_{sep}. In a FODO lattice, the kicker can be positioned just upstream of the focusing quadrupole, and the septum at the identical position one cell downstream. This gives the maximum values for the beta functions, and thus minimizes the deflection angle from the kicker.

For extraction from the damping ring of a linear collider, it is extremely important that the deflection imparted by the kicker has a very small pulse-to-pulse fluctuation (`jitter') and is sufficiently flat over the length of a bunch train. In order to confine the IP orbit variation at the interaction point to $0.1\sigma^*$ (σ^* is the IP spot size), the orbit variation at the septum should be smaller than $0.1\sigma_{sep}$. The tolerance on the relative deflection error is $\Delta\theta_{kic}/\theta_{kic} < 0.1\sigma_{sep}/x_{sep}$, where σ_{sep} is the rms beam size at he septum, and x_{sep} the transverse displacement of the kicked beam. This can also be rewritten as[20]

$$\frac{\Delta\theta}{\theta} \leq \frac{(0.1)\sqrt{\epsilon_{ext}\beta_{sep}}}{d_{sep} + n_s\sqrt{\epsilon_{inj}\beta_{sep}}} \tag{8.10}$$

where ϵ_{ext} and ϵ_{inj} are the injected and extracted beam emittances, β_{sep} the beta function at the septum, and n_s the distance between the closed orbit and the injection plate in units of the injected rms beam size, when the beam is largest. For electron rings, one must have $n_s \geq 7$. Using typical parameters, the jitter tolerance for the kicker is on the order of a few 10^{-4}, and it is mainly determined by the ratio of the extracted beam emittance to the injected emittance[20]. A possible solution is the use of a double kicker system, separated by a betatron phase advance of π, to cancel the jitter[20,21]. This compensation scheme is illustrated in Fig. 8.10. One kicker would be placed before the septum and one in the extraction line. If a pulser feeds both kickers in parallel, with appropriate cable delays, kicker pulse errors in the first magnet are

canceled by the second magnet. A double-kicker system of this type has been built and installed at the KEK ATF[22].

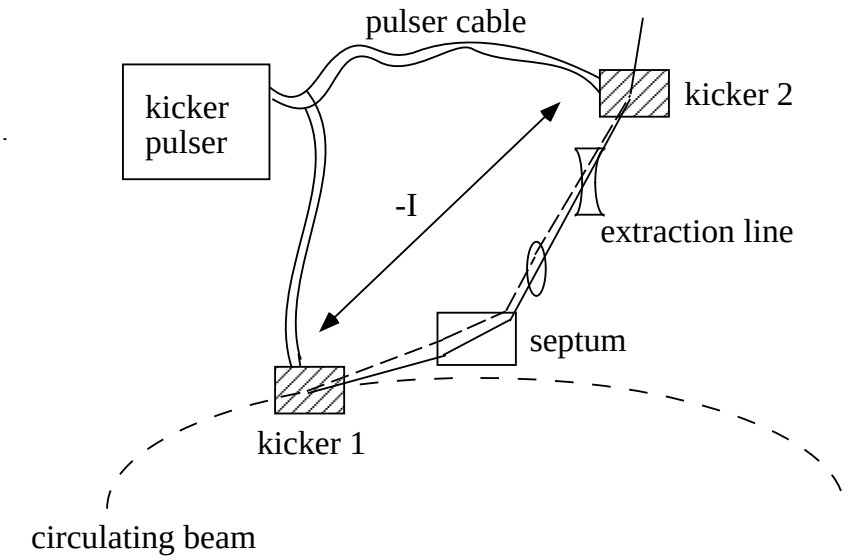

Figure 8.10: Damping ring extraction with double kicker system, for reduced beam orbit fluctuation downstream. A change in the pulse shape alters the deflection from both kickers equally. The R matrix between the two kickers and cable delay times are chosen such that the effects of the two deflection errors cancel exactly, and the final beam trajectory is unchanged.

Similar techniques can be applied to compensate for drifts of the septum field. So contemplates the NLC design the use of a compensating bending magnet in the extraction line, which is powered in series with the septum and placed such that field fluctuations will cancel[21].

8.8 Kickers and Septa

There are several different types of kicker magnets such as[23,6]: (1) current loop inside the vacuum, (2) terminated transmission line inside the vacuum, (3) ferrite magnet outside the vacuum, and (4) multi-cell transmission lines with ferrite flux returns[21]. As an example, Fig. 8.11 shows the ferrite kicker and the kicker pulser circuit adopted for PEP-II[6].

Typical kicker rise and fall times are 50-150 ns (SLC and NLC design: 60 ns, PEP-II: 120 ns). For a fast horizontal kicker with ferrite yoke, the characteristic time constant of the kicker scales as lw/g, where l is the length, w the width, and g vertical

gap of the kicker. This time constant can be reduced by dividing the kicker into several shorter length segments. The kicker magnets are powered by kicker pulsers, usually based on thyratron cable discharges. The pulse shape can be modified by adding filters and capacitors in parallel with the charge line. Spark gaps and solid-state FETs, such as in Fig. 8.11, are thyratron alternatives with potentially shorter rise and fall times[21].

For many future applications with closely spaced bunch trains, shorter kicker time constants are desired. A very fast counter-traveling wave kicker was designed and built for the TESLA project[24]. This kicker scheme uses two parallel conducting plates or electrodes. These are excited by short pulses from a generator, generating an electromagnetic wave which travels in a direction opposite to the beam, and produces a horizontal kick. At the end of the kicker plates, the wave passes into two ceramic outputs, in which ideally it is fully damped. For a beam traveling opposite to the wave the magnetic and electric forces add, while they cancel each other for a beam moving in the same direction. The maximum integrated kicker strength in units of voltage is given by

$$S_0 \approx \frac{2U_m l}{a} \tag{8.11}$$

where U_m is the maximum pulse voltage at each plate, a is the half aperture, and l the length. A kicker was tested with $U_m = 2$ kV, $a = 25$ mm, and total length l of 0.5 m. Figure 8.12 shows output pulses measured on this kicker prototype, demonstrating a zero-to-zero pulse length of about 6 ns. The maximum pulse height corresponds to the predicted kick strength of 80 kV, or 2.76 Gm. For $E = 3.3$ GeV, this would amount to a deflection angle of 24 μrad.

An ultrafast beam-beam kicker was proposed[25], which could provide even faster kicker pulses. Here, a wide high-charge low-energy bunch traverses the beam pipe either parallel to the beam direction or perpendicular to it. The electro-magnetic or electric field of this bunch is used to deflect (and extract) a bunch circulating in the ring. The pulse length of the beam-beam kicker is determined by the length of the low-energy bunch and can be on the order of 2 ns. Figure 8.13 illustrates the two different geometries for a beam-beam kicker.

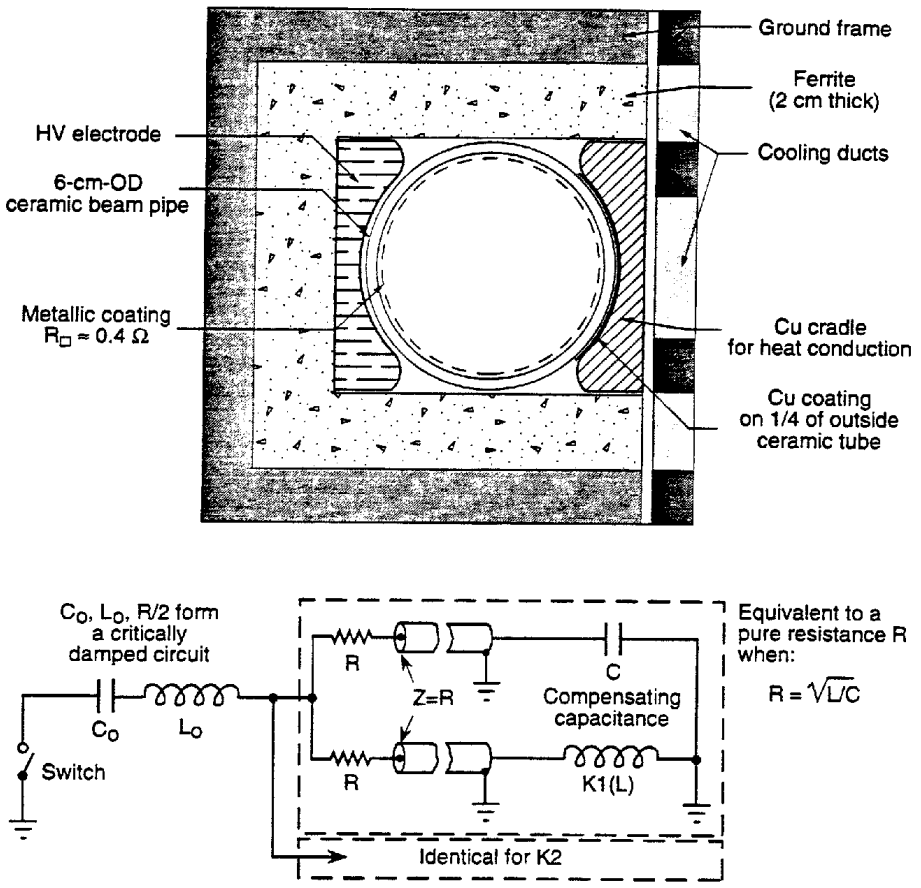

Figure 8.11: Schematic of PEP-II kickers [6]: (top) kicker magnet cross section; (bottom) pulsing circuit with FET switch.

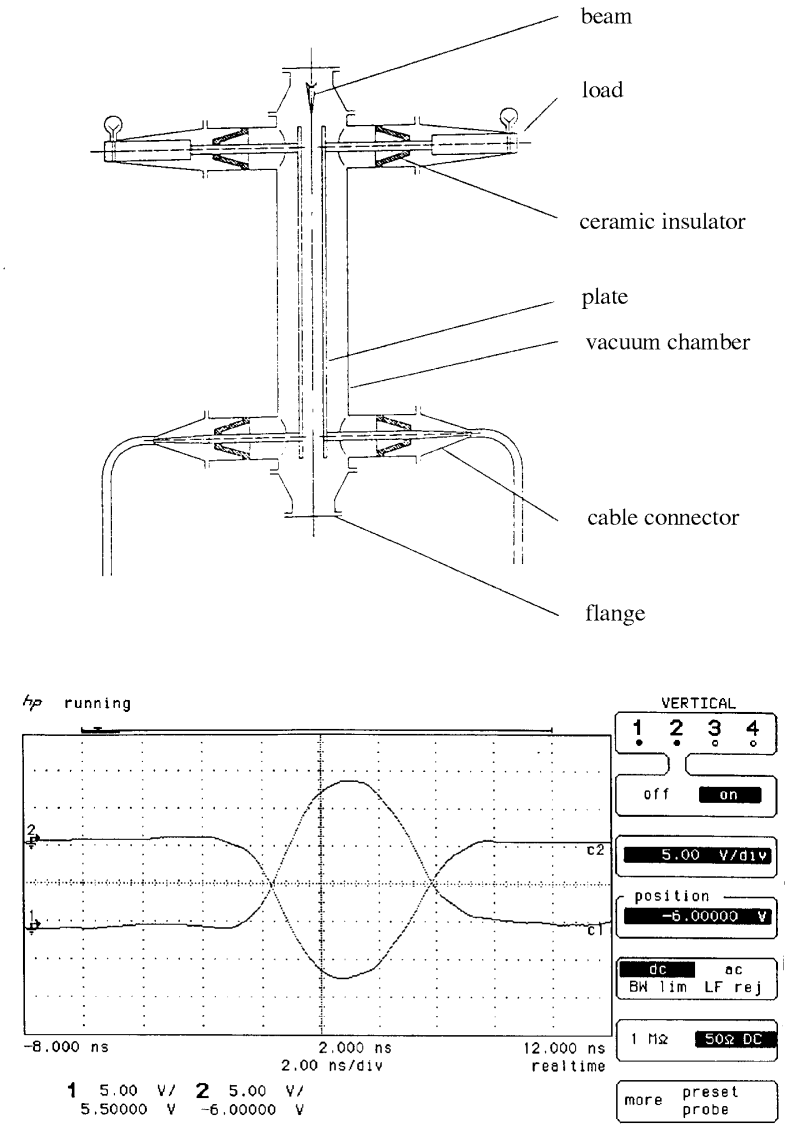

Figure 8.12: Very fast kicker prototype[24]: (top) layout; (bottom) measured output rf pulses. (Courtesy V. Shiltsev, 1998).

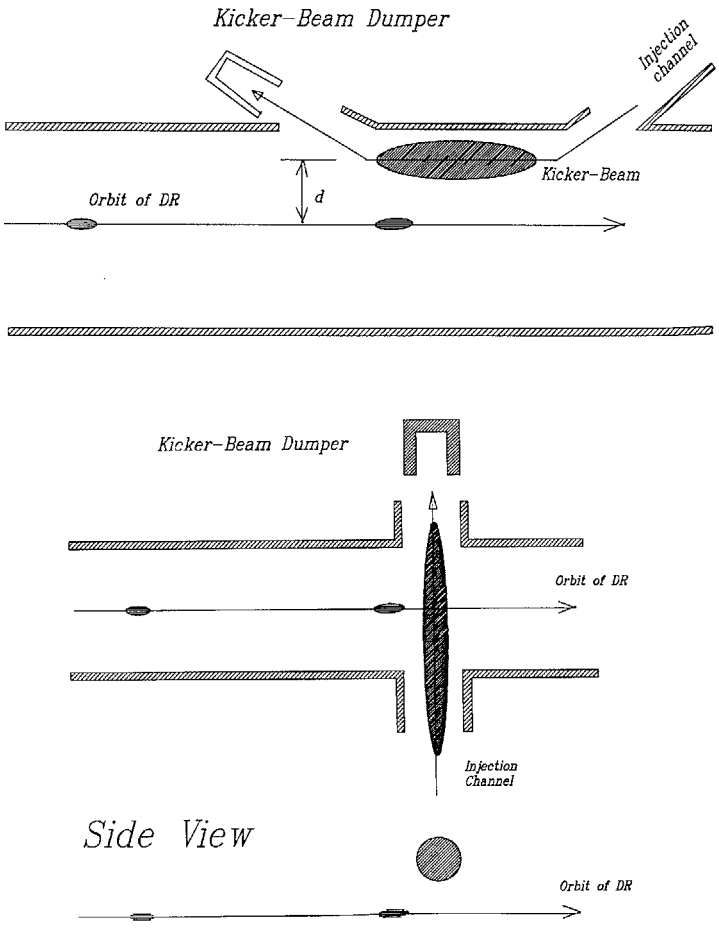

Figure 8.13: Beam-beam kicker: `Head-on' (top) and `cross' scheme (bottom)[25]. (Courtesy V. Shiltsev, 1998).

As we have seen, a small septum thickness d_{sep} reduces the requirements on the kicker and increases the extraction efficiency. For this reason, electrostatic wire septa have been employed since many years, for example, during fast extraction at the Fermilab Tevatron[27]. The Tevatron electrostatic septum consists of two 354 cm long sections with 86 cm space in between, made from 75% tungsten and 25% rhenium wires of 0.002 inch diameter and 0.1 inch spacing with an angle of 25 μrad between sections. The voltage of 93 kV results in an electric field of 83 kV/cm[27]. Very similar electrostatic deflectors have been proposed for the muon collider[28]. At high energies, the integrated strength of a wire septum often cannot provide a deflection angle large enough for clean extraction, and, in such cases, an additional thin septum magnet is positioned downstream.

In general, two types of septum magnets are widely used[26]: Lambertson iron septum dipoles and current carrying septum dipoles. The former is illustrated in Fig. 8.14. The triangular cut-out in the window frame leaves space for the circulating beam. As shown, a kicker deflects the beam horizontally into the septum, by which it is then bent vertically.

Figure 8.15 depicts a current sheet septum. A current carrying septum with thickness d and current density J generates a field $B = \mu_0 J d$. For d of the order of a millimeter, the septum is used in a pulsed mode to provide enough field strength. For larger thicknesses, dc operation is common. Septum leakage fields which affect the circulating beam are a concern. In addition to dipole and higher order fields, the septum stray field may contain a skew quadrupole component.

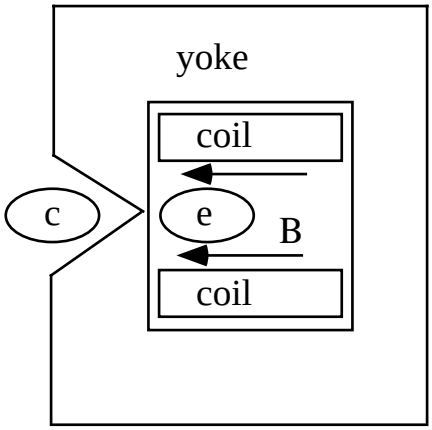

Figure 8.14: Schematic of Lambertson septum iron magnet. Picture is copied from Ref.[2].

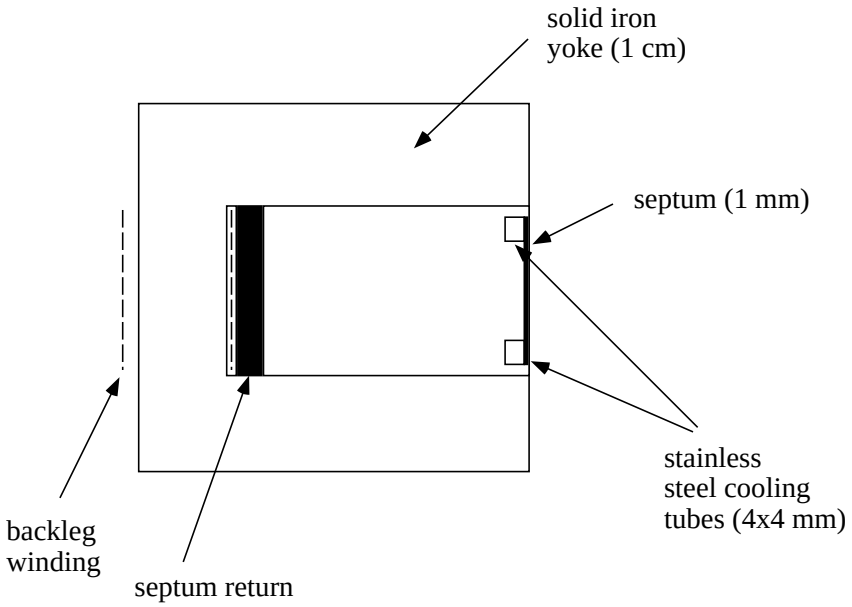

Figure 8.15: Cross section of current sheet septum [6].

8.9 Slow Extraction

Slow extraction is accomplished by exciting a third order nonlinear resonance, using sextupoles. Also a second order linear resonance can be used, in combination with octupoles. The extraction efficiency depends on the ratio of the amplitude growth per turn and the septum thickness. It can be improved with a high-beta insertion at the septum.

Figure 8.16 depicts the phase space near the 3rd order resonance, excited by sextupoles. Particles inside the inner triangle are stable, particles outside are lost rapidly, along one particular direction in phase space (in this example, towards the right). The size of the triangle depends on sextupole strengths and tune.

Near the 1/3 resonance, $3Q - q \approx 0$, with integer q, the particle motion can be described by a Hamiltonian of the form

$$H(I,\psi) = (Q - q/3)I + \frac{1}{24}(2I)^{3/2}|\tilde{K}_s|\sin(3\psi + \theta_0) \qquad (8.12)$$

where I and ψ are the action-angle variables, which are related to the transverse particle coordinates at the septum via $x_{sep} = \sqrt{2\beta_{sep}I}\cos\psi$ and $x'_{sep} = -\sqrt{2I/\beta_{sep}}\sin\psi -$

$\alpha\sqrt{2I/\beta}\cos\psi$. The term $|\tilde{K}_s|$ is the absolute value and θ_0 the complex phase of the resonant Fourier harmonic of the sextupole distribution weighted by the beta function:

$$|\tilde{K}_s|e^{-iq\theta_0} = \frac{1}{2\pi}\int_0^{2\pi} k_s(\theta)\beta^{3/2}(\theta)e^{-iq\theta}\,d\theta, \tag{8.13}$$

Here θ is the azimuthal angle around the ring, and the sextupole strength (in units of m^{-3}) is given by $k_s(\theta) = \partial^2 B_z(\theta)/\partial x^2/(B\rho)$, with $B\rho$ the magnetic rigidity.

Suppose the tune is slightly below the 3rd integer resonance, $(3Q-q) < 0$. Then a corner point of the separatrix coincides with the horizontal position coordinate x_{sep} at the septum, if $\theta_0 = 0$. Above the resonance, $(3Q - q) > 0$, the optimum choice would be $\theta_0 = \pi$. The value of θ_0 can be adjusted by changes to the sextupole configuration, or by changes to the ring optics. The particles arrive at the septum with a large amplitude on every 3rd turn. The amplitude growth over three turns, for a particle near the unstable fixed point is approximately

$$\Delta x_{sep} \approx \frac{3\pi x_{sep}^2|\tilde{K}_s|}{8\beta_{sep}^{1/2}}. \tag{8.14}$$

This shows that large sextupole strengths and a large beta function at the septum (since $x_{sep} \sim \sqrt{\beta_{sep}}$) are advantageous.

Ex.8.4. Beam offset for slow extraction
Derive Eq. (8.14).

A slow spill can be controlled by adjusting either the strength of the sextupoles or the betatron tune. More indirectly, extraction may also involve beam steering. Making use of chromaticity, particles of different momenta can progressively be brought onto the resonance. Extraction starts when the beam particles at one end of the momentum distribution fill the triangular stable area in phase space. The stable area then shrinks to zero for these particles, and subsequently particles of different momenta are being extracted.

For a slow extraction efficiency greater than 98%, the effective thickness of the septum must be of the order of 100 μm.

8.10 Crystal Extraction

Crystal extraction is quite a different extraction scheme. It was first studied at Dubna and Protvino[29], and later tested extensively at the CERN SPS[30,31] and at the Fermilab Tevatron[32]. Particles in the transverse beam halo, entering a crystal placed close to the

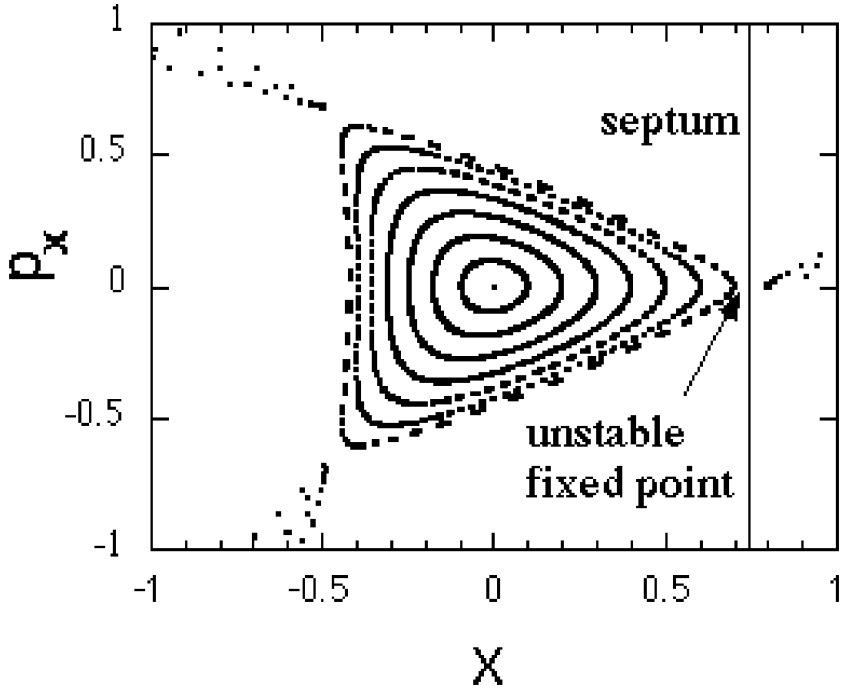

Figure 8.16: Phase space schematic for slow extraction near the 3rd integer resonance. The sextupole excitation pattern around the ring is chosen such that the maximum excursion in the horizontal coordinate x occurs at the location of the septum. The position of the septum wire is indicated as a vertical line close to the unstable fixed point.

beam, are trapped between the crystalline planes[33]. If the crystal is slightly bent, the particles can be deflected outwards, and subsequently be transported to a fixed-target experiment. Figure 8.17 shows a schematic view of crystal extraction.

Crystal extraction is foreseen as an option for the LHC. It would be parasitic to the normal collider operation, and re-utilize the halo particles which do no longer contribute to the collider luminosity.

Channeling occurs if the incident angle of the particles is smaller than the Lindhard critical angle. For the (110) planar direction in silicon the critical angle is[33]

$$\Psi_{crit} = 5\mu\mathrm{rad}\,\frac{\sqrt{Z}}{\sqrt{p[\mathrm{TeV}/c]}} \tag{8.15}$$

where p is the momentum of the incident particle and Z is its charge in units of the

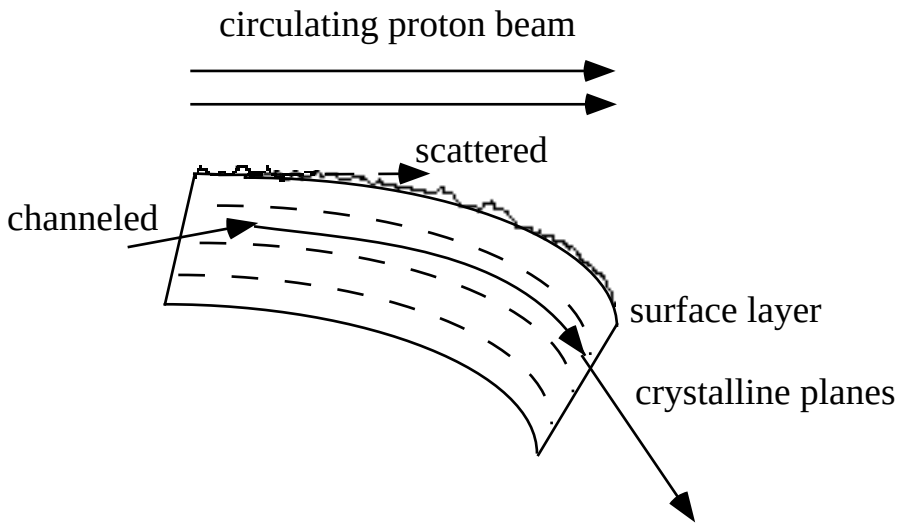

Figure 8.17: Extraction from the transverse halo of a circulating proton beam by means of a bent crystal. Particles incident with a large impact parameter are channeled and deflected outwards. Particles hitting the inefficient crystal surface layer experience multiple scattering, and may be channeled on a later turn; this is called multi-pass extraction.

electron charge.

Thermal vibrations, the discreteness of the crystal lattice, and the presence of the electrons in the target all increase the transverse energy of a channeled particle, and can ultimately lead to dechanneling. This is approximated by an exponential depletion of the number n of channeled particles with the traversed distance z:

$$n = n_0 \exp(-z/L_0) \tag{8.16}$$

The empirical parameter L_0 is called the dechanneling length, and it increases linearly with momentum. For silicon, we have[33] $L_0 \approx 0.9 \text{ m } p[\text{TeV}/c]$. Since scattering on nuclei is an important dechanneling process, the channeling can be improved by cooling of the target.

Another concern are surface imperfections. To be extracted in a single pass, particles must enter the crystal with a large impact parameter. This is necessary to avoid the inefficient surface layer, which typically is of the order a micrometers. Particle passing through the surface area, on the other hand, experience multiple scattering. These particles can re-enter the crystal on subsequent revolutions, this time at a larger impact parameter and under the right conditions to be channeled and extracted.

There is a minimum bending radius of the crystal for which channeling can occur. For the (110) plane of silicon, this critical radius is[33]

$$R_c \approx 0.4 \text{ m } p[\text{TeV}/c] \tag{8.17}$$

Ex.8.5. Channeling in a crystal
What is the maximum bending angle over a length of 3 cm, for the LHC beam energy of 7 TeV?

The efficiency of cystal extraction is defined as the number of particles extracted divided by the number of particles lost. Proton extraction efficiencies up to 18% have been obtained[31]. Using a crystal coated with a 30 μm amorphous SiO layer, pure multi-pass extraction with an efficiency of 4–7% was demonstrated[31]. The importance of multi-pass extraction implies that not only the initial impact parameter, but also global machine parameters such as the beta function at the crystal and the betatron tune play an important role for the overall efficiency.

Finally, not only protons but also heavy ions can be extracted by a bent crystal. For fully stripped Pb ions ($Z = 82$) at 22 TeV, an extraction efficiency of 10% was achieved at the SPS[31]. This was slightly lower than for protons of equivalent energy per nucleon.

8.11 References

1. G.H. Rees, "Injection", CERN Accelerator School, Gif-sur-Yvette, Paris, France, CERN 85-19, p. 331 (1985).
2. G.H. Rees, "Extraction", CERN Accelerator School, Gif-sur-Yvette, Paris, France, CERN 85-19, p. 346 (1985).
3. A. Piwinski, "Penetration of the Field of a Bunched Beam through a Ceramic Vacuum Chamber with Metallic Coating", IEEE Tr. NS-24, no. 3, p. 1364 (1977).
4. C. Gonzales, M. Morvillo, and M. D'yachkov, "Impedance Measurements on the LHC Dump Kicker Prototype", LHC Project Note 151 (1998).
5. M. Minty and R.H. Siemann, "Heavy Beam Loading in Storage Ring Radio Frequency Systems", Nucl. Instr. Methods A 376, p. 301 (1996).
6. "PEP-II An Asymmetric B Factory", Conceptual Design Report, LBL-PUB-5379 and SLAC-418 (1993).
7. Ch. Carli, S. Maury and D. Möhl, "Combined Longitudinal and Transverse Multiturn Injection in a Heavy Ion Accumulator", Proc. of 1997 IEEE PAC, Vancouver (1997).

8. P. Baudrenghien and P. Collier, “Double Batch Injection into LEP”, Proc. of EPAC96, Sitges, p. 415 (1996).
9. E. Gianfelice and H. Schönauer, “Strategies for Longitudinal Painting in the EHF Booster at Injection”, Proc. of EPAC 1988, Rome (1988).
10. G.H. Rees, “Injection and Painting”, Proc. of the Summer Study on High Energy Physics in the 1990s, Snowmass (1988).
11. G.I. Budker and G.I. Dimov, Proc. Int. Conf. on High-Energy Accelerators, Dubna 1963, Conf. 114, p. 1372 (1963).
12. E. Crosbie, A. Gorka, E. Parker, C. Potts, L. Ratner, “Injection and Acceleration of Protons in the Zero Gradient Synchrotron (ZGS) by Stripping H^- Ions”, IEEE Tr. N.S. 22, no. 3, p. 1056 (1975).
13. C.D. Moak, “Stripping in Foils and Gases”, IEEE Tr. N.S. 23, no. 2, p. 1126 (1976).
14. R.T. Free, J.S. Fraser, C.D.P. Levy, “Laser Stripping of the Triumf H^- Beam”, Proc. of 1989 PAC, Chicago, and Published in IEEE Part.Accel., p. 414-416 (1989).
15. T.K. Khoe and R.J. Lari, Proc. Conf. on High-Energy Accelerators, Geneva, 1971, p. 98 (1971).
16. J.T. Seeman, “Injection Issues of Electron-Positron Storage Rings”, Proc. of “B factories: The State of the Art in Acclerators, Detectors and Physics”, Stanford, April 6–10, 1992, and SLAC-PUB-5933 (1992).
17. M. Minty *et al.*, “Damping Time Measurements using a Fast Gated Camera”, AIP Conf. Proc., 281 J.A. Hinkson and G. Stover eds., Accelerator Instrumentation Workshop, Berkeley, p. 158 (1992).
18. M.G. Minty and W.L. Spence, “Injection Envelope Matching in Storage Rings”, Proc. of 1995 IEEE PAC, Dallas, p. 536 (1995).
19. M. Sands, “A Beta Mismatch Parameter”, SLAC internal report SLAC-AP-85 (1991).
20. T.O. Raubenheimer, L.Z. Rivkin, R.D. Ruth, “Damping Ring Designs for a TeV Linear Collider”, Proc. of the DFP Summer Study Snowmass '88, and SLAC-PUB-4808 (1988).
21. “Zeroth Order Design Report for the Next Linear Collider,” *SLAC-Report* 474 (1996).
22. F. Hinode *et al.*, “Accelerator Test Facility–Design and Study Report”, KEK Internal Report 95-4 (1995).
23. F. Bulos, “Detailed Design of PEP II Injection Kickers”, SLAC PEP-II/AP Note 5-92 (1992).
24. B.I. Grishanov, F.V. Podgorny, J. Rümmler, V.D. Shiltsev, “Very Fast Kicker for Accelerator Applications”, DESY TESLA 96–11 (1996).
25. V.D. Shiltsev, “Beam-Beam Kicker for Superfast Bunch Handling”, DESY

TESLA 95–22 (1995).
26. G.E. Fischer, “Iron Dominated Magnets”, lecture at the 1985 SLAC Summer Institute, SLAC-PUB-3726 (1985).
27. A.I. Drozhdin, N.V. Mokhov, and M. Harrison, “Study of Beam Losses during Fast Extraction of 800 GeV Protons from the Tevatron”, *FN-418* (1985).
28. A. Drozhdin, N. Mokhov, C. Johnstone, W. Wan, and A. Garren, “Scraping Beam Halo in $\mu^+\mu^-$ Colliders”, Proc. of the 4th International Conference on Physics Potential and Development of Muon Colliders, San Francisco, December 1997, and FERMILAB-Conf-98/042 (1998).
29. A.A. Asseev, *et al.*, “Peculiarities of using the bent crystal for the extraction of protons from the IHEP accelerator to the PROZA setup”, Nucl. Instr. Methods A 330, p. 39 (1993).
30. K. Elsener, *et al.*, “Proton extraction from the CERN SPS using bent silicon crystals”, Nucl. Instr. Methods B 119, p. 215 (1996).
31. K. Elsener, *et al.*, “What did we Learn from the Extraction Experiments with Bent Crystals at the CERN SPS”, Proc. of EPAC 98, Stockholm (1998).
32. C.T. Murphy, *et al.*, “First Results from Bent Crystal Extraction at the Fermilab Tevatron”, Nucl. Instr. Methods B 119, p. 231 (1996).
33. S. Pape Møller, “Crystal Channeling or How to Build a `1000 TESLA Magnet”', Ninth John Adams Memorial Lecture, CERN 94-05 (1994).

Chapter 9

Cooling

9.1 Introduction

Many applications of particle accelerators require beam cooling, by which we mean a reduction of the beam phase space volume or an increase in the beam density via dissipative forces. In electron and positron storage rings cooling naturally occurs due to synchrotron radiation, and special synchrotron-radiation damping rings for the production of low-emittance beams are an integral part of electron-positron linear colliders. For other types of particles different cooling techniques are available. Electron cooling and stochastic cooling of hadron beams are used to accumulate beams of rare particles (such as antiprotons), to combat emittance growth (*e.g.*, due to scattering on an internal target), or to produce beams of high quality for certain experiments. Laser cooling is employed to cool ion beams down to extremely small temperatures. Finally, designs of a future muon collider rely on the principle of ionization cooling. Reference[1] gives a short review of the principal ideas and the history of beam cooling in storage rings; a theoretical dicussion and a few practical examples can be found in Ref.[2].

In the presence of cooling, the evolution of the 1-dimensional beam distribution function $f(x, x', t)$ is described by the differential equation[2]

$$\frac{df(x, x', t)}{dt} = \lambda f \tag{9.1}$$

with the solution

$$f(x, x', t) = e^{\lambda t} f_0(x_0, x'_0) \tag{9.2}$$

where the subindex 0 characterizes the initial distribution or variables. The latter, x_0 and x'_0, are related to x and x' by the equation of motion including the damping. Note that the phase space density about each particle increases exponentially.

Without cooling force, the system is Hamiltonian and the local phase-space density is conserved ($df/dt = 0$), so that $\lambda = 0$.

It is common to introduce action-angle variables (I, ψ) (where I is proportional to the square of the oscillation amplitude) via the relation

$$\frac{x}{\sqrt{\beta}} = \sqrt{2I}\cos\psi(\theta) \tag{9.3}$$

$$\sqrt{\beta}\left(x' + \alpha\frac{x}{\beta}\right) = -\sqrt{2I}\ \sin\psi(\theta) \tag{9.4}$$

Cooling in the three phase-space dimensions dimensions results in an exponential damping of the 3 action invariants:

$$\left\langle \frac{\partial \dot{I}_i}{\partial I_i} \right\rangle = -\lambda_i \tag{9.5}$$

where $i = (x, z, s)$. The angular brackets denote an average over both angle variables and time,

$$< ... >= \int_0^{2\pi} \frac{d\psi}{2\pi}\,\frac{d\theta}{2\pi}\,(...) \tag{9.6}$$

and the λ_i are the damping rates in the three planes. Some algebra yields

$$\begin{aligned}
\sum_i \left\langle \frac{\partial \dot{I}_i}{\partial I_i} \right\rangle &= \sum_i \left\langle \sum_k \frac{\partial}{\partial I_i}\frac{\partial I_i}{\partial p_k} F_k \right\rangle \\
&= \sum_i \left\langle \sum_k \frac{\partial}{\partial I_i}\frac{\partial I_i}{\partial p_k} F_k + \frac{\partial}{\partial \psi_i}\frac{\partial \psi_i}{\partial p_k} F_k \right\rangle \\
&= \left\langle \sum_k \frac{\partial F_k}{\partial p_k} \right\rangle
\end{aligned} \tag{9.7}$$

where we have made use of the fact that the average over ψ of any derivative with respect to ψ is zero. The sum of the action damping coefficients is

$$\lambda_x + \lambda_z + \lambda_s = -\left\langle \frac{\partial F_x}{\partial p_x} + \frac{\partial F_z}{\partial p_z} + \frac{\partial F_s}{\partial p_s} \right\rangle =< -\vec{\mathrm{div}}_{\vec{p}}\vec{F} >, \tag{9.8}$$

independent of any coupling between the three planes of motion.

Cooling due to synchrotron radiation and due to ionization cooling is approximately described by a cooling force that is anti-parallel to the particle velocity[2]:

$$\vec{F} = -a\vec{v} \tag{9.9}$$

where the coefficient a may depend on the particle energy. The cooling is accompanied by an energy loss

$$\frac{dE}{dt} = -W = \vec{F} \cdot \vec{v} = -av^2, \tag{9.10}$$

which can be compensated by an rf system. Assuming ultrarelativistic particles, the cooling force of Eq. (9.9) may be rewritten in terms of the energy loss as $\vec{F} = -\vec{v}W/c^2$, and direct evaluation yields:

$$-\vec{\mathrm{div}}_{\vec{p}} \cdot \vec{F} = \left(\frac{W}{pc}\right)\left[2 + \frac{\partial \ln W}{\partial \ln p}\right] \tag{9.11}$$

Upon insertion into Eq. (9.8) the total decrease rate in phase space volume can be calculated. Equations (9.8) and (9.11) state that the sum of the three damping rates is a constant, only depending on the total rate of energy loss. In the special case of synchrotron radiation, this is known as the Robinson theorem.

One might think it would be possible to produce a beam of nearly zero temperature by cooling for a very long time. However, there is always noise inherent to all cooling forces, which prevents reaching this limit and gives rise to an equilibrium emittance. In the case of synchrotron radiation this noise is due to quantum fluctuations, in ionization cooling it is due to multiple scattering, and in the case of stochastic cooling there is electronic noise in the detector-amplifier chain and Schottky noise from the finite number of particles in the beam.

With such noises present, the evolution of the distribution function $f(I,t)$ is described by a Fokker-Planck equation of the form

$$\frac{\partial f(I,t)}{\partial t} = \frac{\partial}{\partial I}\left(-\left\langle \frac{\Delta I}{\Delta t}\right\rangle f(I,t)\right) + \frac{1}{2}\frac{\partial^2}{\partial I^2}\left(\left(\left\langle \frac{(\Delta I)^2}{\Delta t}\right\rangle f(I,t)\right)\right) \tag{9.12}$$

where the angular brackets denote an average over the beam distribution. Sometimes, for example, the Fokker-Planck terms $< \Delta I >$ and $< (\Delta I)^2 >$ are linear in I and constant, respectively, and the equation reduces to

$$\frac{\partial f}{\partial t} = \frac{\partial}{\partial I}\left(\lambda I f + \frac{D}{2}\frac{\partial f}{\partial I}\right) \tag{9.13}$$

The beam then asymptotically approaches the distribution, $f_\infty \propto \exp(-I/I_0)$, with the equilibrium emittance

$$I_0 = \frac{D}{2\lambda} \tag{9.14}$$

Using Eq.(9.13), it is easily verified that this distribution is stationary: $\partial f_\infty/\partial t = 0$.

If a radiation length contains more than one particle, the cooling of various particles is coupled. Under these circumstances, the beam is cooled only when particles enter or leave the common interaction region (`mixing').

Ex.9.1. Longitudinal damping rate with beam cooling
Consider two particles which interact simultaneously with the cooling system[2]*. Let the cooling act on the momentum variable only. The equations of motion then read*

$$\frac{dp_1}{dt} = -\lambda(p_1 + p_2) \tag{9.15}$$

and

$$\frac{dp_2}{dt} = -\lambda(p_1 + p_2) \tag{9.16}$$

Calculate the damping rate of the centroid motion and the momentum spread.

9.2 Electron Cooling

Electron cooling was proposed in 1966 by G.I. Budker[4]. The basic idea of electron cooling is the heat exchange between a stored hadron beam and an accompanying electron beam via Coulomb collisions. The temperature of the electron beam is held constant. It should be lower than the temperature of the hadron beam to be cooled. This is easily fulfilled since for equal ion and electron velocities, $v_e \approx v_i$, the temperature of the ion beam is

$$T_e \approx \frac{m_e}{M} T_{ion}, \tag{9.17}$$

where M and m_e denote the ion and electron masses, respectively. Because of their mass ratio, the temperature of the ion beam is much larger than that of the electron beam. The average velocities of the hadron and electron beams should coincide in the cooling interaction region, in order to maximize the Coulomb cross section. Viewed in the electron rest frame, moving with the electron beam, the ions are 'stopped' similarly to the slowing down of charged particles traversing matter, because in the Coulomb collisions energy is transferred from the ions to the electrons. The typical layout of an electron cooler and a photo of the electron cooling system at LEAR are depicted in Figs. 9.1 and 9.2, respectively.

Transverse and longitudinal temperatures of the ion beam can be defined by analogy with kinetic gas theory:

$$T_\perp = \frac{M\overline{u_\perp^2}}{k_B} \tag{9.18}$$

and

$$T_{||} = \frac{M\overline{\Delta u_{||}^2}}{k_B} \tag{9.19}$$

where M is the ion mass and u the ion velocity. The two temperatures are usually not the same. The electron-beam temperature is defined in the same way.

The cooling force may be estimated by considering the collision of a single ion with a single electron in a reference frame where the electron is at rest before the collision[2].

We split the collision into two steps. During the first step, electron and ion approach each other, in the second step they are separating again. We assume that during the first part the electron is accelerated by the field of the ion and that it moves in the direction of the impact parameter. The situation is sketched in Fig. 9.3.

At the end of the first time step, the electron velocity is

$$\Delta v_e = \frac{Z r_e c^2}{\rho u} \tag{9.20}$$

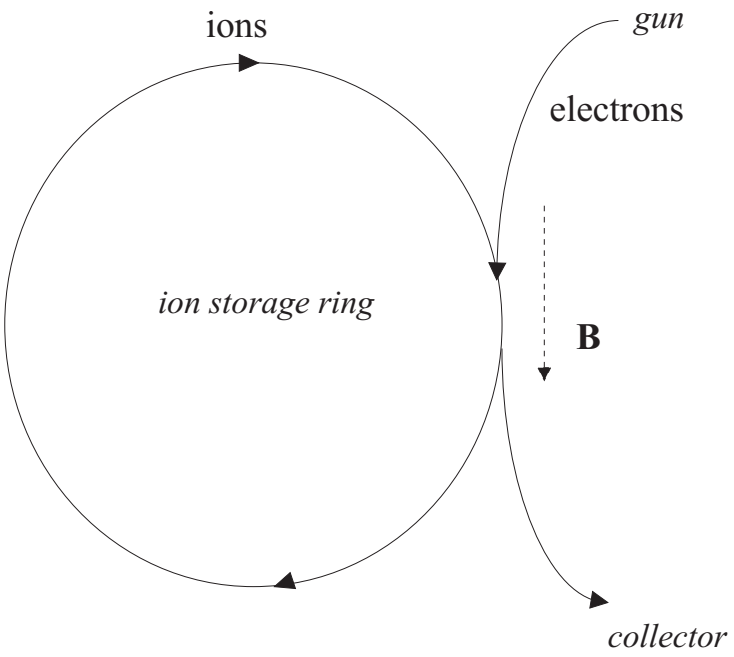

Figure 9.1: Schematic of electron cooling for an ion storage ring.

where u is the velocity of the ion and ρ the (initial) impact parameter. At this time the electron has moved about a distance

$$\Delta\rho \approx \frac{Zr_e c^2}{u^2} \tag{9.21}$$

The average variation of the ion momentum projection on the direction u is

$$\left\langle \frac{dp_u}{dt} \right\rangle = u n_e m_e c^2 \int_{\rho_{min}}^{\rho_{max}} \left(\frac{Zr_e c}{\rho u} - \frac{Zr_e c}{(\rho - \Delta\rho)u} \right) 2\pi\rho \, d\rho \tag{9.22}$$

where n_e denotes the local density of the electron beam, and m_e the electron mass. Expanding in powers of $\Delta\rho$ and keeping only the leading contribution, one finds

$$\left\langle \frac{dp_u}{dt} \right\rangle = \frac{2\pi n_e r_e^2 Z^2 m_e c^4}{u^2} \, L_C \tag{9.23}$$

where we have introduced the Coulomb logarithm $L_C \equiv \ln\left(\frac{\rho_{max}}{\rho_{min}}\right)$. As an upper

Figure 9.2: Electron cooling system at LEAR. (Courtesy M. Chanel, 1999).

integration limit ρ_{max} we may take the Debye shielding length of the electron beam:

$$r_D \approx \left[\frac{k_B T}{4\pi m_e c^2 n_e r_e}\right]^{1/2} \tag{9.24}$$

A lower limit can be determined from the validity of the approximations made above, or from the maximum momentum transfer to the electron (classical head-on collision):

$$\rho_{min} = \frac{Z r_e c^2}{u^2} \tag{9.25}$$

In numerical estimates, L_C is usually taken to be constant, of the order of 10.

The averaging of Eq. (9.23) over the electron distribution function f_e results in the cooling force

$$F_{el} = \left\langle \frac{d\vec{p}}{dt} \right\rangle = 2\pi Z^2 r_e^2 m_e c^4 L_C \int d^3 v_e f_e(\vec{v}_e) \frac{\vec{v} - \vec{v}_e}{(\vec{v} - \vec{v}_e)^3} \tag{9.26}$$

The result of a more precise evaluation of the cooling force starting from the Rutherford cross section agrees within a factor of 2 with Eq. (9.26). The cooling can also be thought of as an excitation of plasma oscillations in the electron beam.

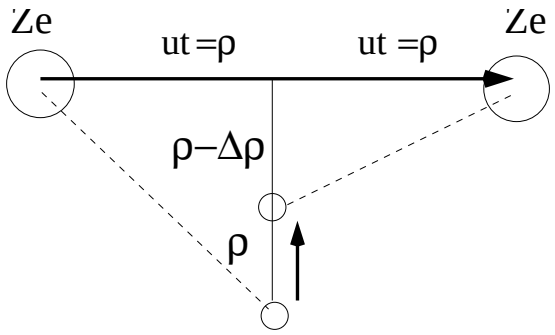

Figure 9.3: Collision of one ion and one electron during electron cooling[2].

The cooling time τ_{el} follows from[7]

$$\frac{1}{\tau_{el}} = \left|\frac{1}{u}\frac{du}{dt}\right| = \left|\frac{F_{el}}{Mu}\right| \tag{9.27}$$

In the laboratory frame the cooling time is larger by a factor γ due to time dilation (there is a further factor of γ due to Lorentz contraction if the distribution function f_e is taken to be that in the laboratory frame). In the limit of large ion velocities, the electron velocity may be replaced by a delta function; in the opposite limit an isotropic Gaussian distribution is assumed. The cooling time in the two limits reads[7]:

$$\tau = \frac{\gamma^2}{\eta}\frac{M}{m_e}\frac{1}{Z^2 r_e^2 c^4}\frac{1}{n_L L_C}\begin{cases} \frac{1}{4\pi}u^3 & u \gg v_{e,rms} \\ \frac{3}{2\sqrt{2\pi}}\left(\frac{\frac{3}{2}k_B T_e}{m_e}\right)^{3/2} & u < v_{e,rms} \end{cases} \tag{9.28}$$

where η is the ratio of the cooling section length to the ring circumference, and n_L the electron beam density in the laboratory frame. The equation shows that electron cooling becomes inefficient for high energies, $\gamma \gg 1$, and that the cooling time is short for light ions of high charge. The cooling time of hot beams scales as u^3, while the cooling time of cold beams is independent of the ion velocities and only depends on the electron temperature.

Figure 9.4 shows a schematic of the transverse and longitudinal cooling forces, illustrating the two different cooling regimes incurred for high and low ion velocities.

Typical example parameters for electron cooling are $k_B T_e \approx 0.2$ eV, $n_L = 3 \times 10^8$ cm^{-3}, $L_C = 10$, $\eta = 0.05$, $\gamma = 1$, and $Z = 1$, which results in a cooling time of 40 s.

In reality, there are two additional effects which considerably reduce the cooling times: First, the electron velocity distribution is not Gaussian, but Maxwellian, and

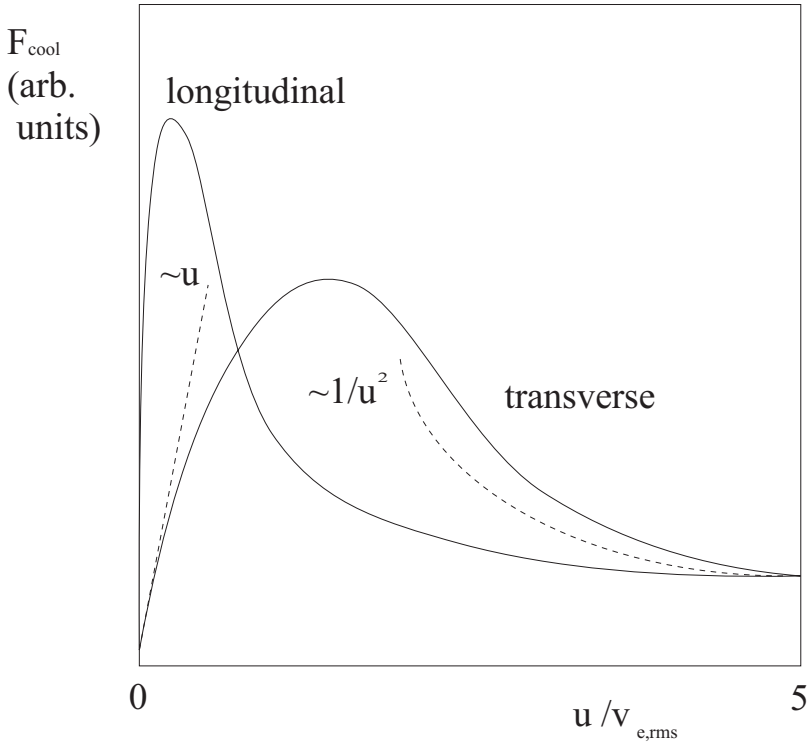

Figure 9.4: Cooling force in a flattened electron beam as a function of ion velocity. The dashed curve corresponds to the asymptotic formulae derived in the text; picture redrawn from Ref.[7].

due to acceleration in the electron gun, the distribution is flattened in the longitudinal direction. This flattening leads to much shorter longitudinal cooling times. Second, a longitudinal magnetic field is employed to guide and confine the electron beam. This results in cyclotron motion of the electrons. If the cyclotron period is small compared with a typical ion-electron collision time, the cyclotron motion decreases the effective transverse temperature of the electron beam, and could reduce the cooling times, to values below one tenth of a second[2,5,7].

The first experiments of electron cooling were performed at the NAP-M storage ring of the Budker INP in Novosibirsk, where a 65-MeV antiproton beam was cooled down to a final momentum spread of 1.4×10^{-6} and to an angular divergence of 12.5 μrad, much smaller than the 3 mrad angular divergence of the 0.3-A 50-keV electron beam. Cooling times of the order of 25 ms were achieved[2].

The cooling stops when the temperatures of the electron and ion beam are equal.

The velocity of a cooled coasting ion beam is equal to that of the electron beam, $v_{ion} = v_e$. This is useful for tuning the ion beam energy.

To relate electron cooling times for different types of particle beams, we note that the cooling rate scales like[1]

$$\frac{1}{\tau} \propto \frac{Z^2}{A} \tag{9.29}$$

where A is the atomic mass number of the ion, and Z its charge number (in units of the electron charge). We thus expect that cooling is faster for highly charged ions. However, these ions can also more easily pick up cooling electrons and get lost. The rate of recombination due to radiative electron capture scales approximately as[1]

$$\frac{1}{\tau_r} \propto Z^2 \tag{9.30}$$

If the electron beam temperature is low compared with that of the ion beam, the electron cooling rate scales as

$$\frac{1}{\tau} \propto \frac{1}{u^3} \sim \frac{1}{\theta_{x,y}^3} \tag{9.31}$$

where $\theta = \sqrt{\epsilon/\beta_{x,y}}$ is the transverse rms divergence (and β here the lattice beta function). One might thus imagine that a large value of $\beta_{x,y}$ would give the best cooling results. However, for a large value of β also the beam size is large, and the ions sample the nonlinear space-charge field of the electron beam. This space-charge effect complicates the electron-ion velocity matching. In addition, a large ion beam may only incompletely overlap with the electron beam. For this reason, an intermediate beta function turns out to be optimal, where the ion beam is slightly smaller than the electron beam.

One would also expect that the cooling rate increases in proportion to the electron beam current. In reality, for larger current one observes a tendency of saturation. Again, the limit arises from the space-charge force in the electron beam.

Let us have a closer look at the electron space-charge effects. Consider a cylindrically symmetric beam with longitudinal density $\lambda = I/(\beta c)$, where I is the current and c the speed of light, and of radius a. For a uniform charge distribution the space charge force is linear inside the radius a:

$$E_r = \frac{2\lambda e}{4\pi\epsilon_0 a^2} r \tag{9.32}$$

Sufficiently far away from the gun, the beam reaches an equilibrium state where the sum of kinetic and potential energy is a constant for all particles and[8]:

$$m_e c^2 \gamma(r) = mc^2\gamma(0) + e\int_0^r dr'\ E_r(r') \tag{9.33}$$

or

$$\gamma(r) = \gamma(0) + \lambda r_0 \frac{r^2}{a^2} \tag{9.34}$$

Since

$$\frac{\Delta v(r)}{v} = \frac{1}{\gamma^2 - 1} \frac{\Delta\gamma(r)}{\gamma} \tag{9.35}$$

the velocity distribution in the electron beam is parabolic as a function of radial position. For high currents, the increase in the velocity spread of the electron beam degrades the cooling force. The situation is illustrated in Fig. 9.5, which shows the velocity of electron and ion beams as a function of radial position. It is evident that a nonzero dispersion at the electron cooler can reduce the average velocity difference between electrons and (off-momentum) injected beam, thereby improving the performance. The optimum value of the dispersion function scales as[9,10]

$$D \propto \sqrt{\frac{U a^2}{I(\Delta p/p)_{rms}}} \tag{9.36}$$

where U is the accelerating voltage of the electron beam, I the electron current, $(\Delta p/p)_{rms}$ the energy spread of the ion beam, and a the electron beam size. The positive effect of a nonzero dispersion was confirmed by observations[9,10].

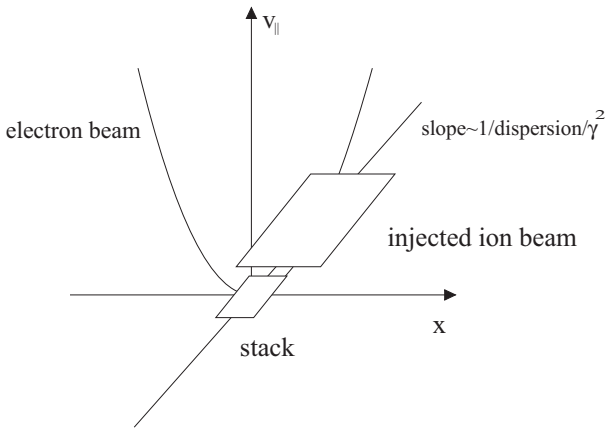

Figure 9.5: Velocity vs. horizontal position of the electron and ion beams. Due to space charge the electron velocities lie on a parabola; the ion velocity varies linearly, with a slope inversely proportional to the dispersion. Because of betatron oscillations, ions occupy a large area in phase space, as indicated[9,10].

Finally, it is worth mentioning that for relativistic energies electron cooling becomes less efficient; see *e.g.*, Eq. (9.28). In addition, higher electron-beam energies would be required in the cooling system.

For the cooling of high-energy beams, it has been proposed to store the electron beam in a storage ring, sharing a common straight section with the ion or proton storage ring, where the cooling takes place[11,12].

The emittance of the electron beam is then maintained by radiation damping. In such scheme, the bucket spacing of the electron storage ring should be an integral multiple of the bucket spacing of the ion storage ring[12]:

$$\frac{C_e}{h_e} = n\frac{C_i}{h_i} \qquad (n \text{ integer }) \tag{9.37}$$

where h_e and h_i denote the harmonic numbers of the electron and ion rings, and C_e and C_i their circumferences.

Ex.9.2. Temperature of a cooled beam

For each plane of motion a beam temperature can be defined by analogy with kinetic gas theory:

$$\frac{< p_x^2 >}{2m} = \frac{1}{2}k_B T_x \qquad \frac{< p_y^2 >}{2m} = \frac{1}{2}k_B T_y \qquad \frac{< p_{||}^2 >}{2m} = \frac{1}{2}k_B T_{||} \tag{9.38}$$

where all quantities refer to the beam rest frame.

a) Show that $T_x = \frac{mc^2}{k_B}\beta\,\gamma\frac{\epsilon_N}{\beta_x}$ *and* $T_{||} = \frac{mc^2}{k_B}\beta^2\sigma_p^2$ *where* ϵ_N *is the normalized emittance,* $\sigma_p = (\Delta p/p)_{rms}$ *the rms momentum spread in the laboratory frame, and* β_x *the horizontal beta function (so the temperature is position dependent).*
b) Calculate the horizontal and longitudinal temperature for the beam from a proton linac at injection into a cyclotron, with $\epsilon_N = 0.5$ *mm mrad,* $\beta\gamma \approx 0.7$, $\beta_x = 10$ *m, and* $\Delta p/p \approx 10^{-3}$. *Compare this with the transverse and longitudinal temperatures of an electron, which is generated at the cathode with* $k_B T^c = 0.1$ *eV in all directions and then accelerated by a voltage* $U_0 = 100$ *kV.*
c) What is the transverse Debye radius of the electron beam at this temperature? Assume a typical electron-beam density of 3×10^8 cm^{-3} *in the laboratory frame.*
d) For a longitudinal solenoidal guide field of strength 500 Gauss, calculate the electron cyclotron period and compare it with a typical impact time of $\sim r_D/u_\perp$, *where* $u_\perp$ *is the relative transverse velocity (since the electron beam temperature is much smaller, this is determined by the temperature of the proton beam).*

Ex.9.3. Recombination of ion beams with electron cooling

Assume an electron cooler for protons provides a cooling time of 10 ms, with a recombination time of 10^5 *s. Suppose the same cooling system is used for a beam of fully stripped lead ions (*$A = 207$, $Z = 82$*). What is the fraction of lead ions that would be lost by recombination during one cooling time?*

Ex.9.4. Required energy of electron beam for electron cooling
What would be the electron-beam energy required to cool the 7-TeV LHC proton beam?

Ex.9.5. Derivation of the Debye length
Derive the formula for the Debye length, Eq. (9.24), by calculating the electron density distribution in the potential of the ion charge and assuming the electrons are in thermal equilibrium. Make appropriate approximations.

Ex.9.6. Interaction probabilities with electron cooling
Compare the minimum ion-electron interaction time $\Delta t = b_{min}/u$ (in the beam frame), with the time of traversal through a 10 m cooling section. Estimate the ion velocity u assuming a normalized emittance 10 μm and a 5 m beta function. At which value of γ are the two times equal?

9.3 Laser Cooling

9.3.1 Ion Beams

Laser cooling of atoms trapped in electromagnetic traps is well known and widely used. In 1981 P. Channel suggested to apply laser cooling also to ions in a storage ring[13].

The idea of laser cooling exploits the Doppler shift in frequency to interact selectively with ions of a certain energy. The Doppler shifted frequency in the ion rest frame is

$$\omega' = \gamma\omega(1 - \beta\cos\theta) \tag{9.39}$$

where θ is the angle between the ion velocity and the incident laser. Ions with a velocity β so that $\omega = \omega_{AB}$, corresponding to a transition $A \rightarrow B$ of the ion electronic state, abosrb photons, which are subsequently re-emitted. The emission is isotropic, while the momentum received during absorption is in the direction of the laser. In one absorption, the ion acquires the recoil velocity:

$$v_r = \frac{\hbar\omega_{AB}}{m_{ion}c} \tag{9.40}$$

where m_{ion} is the ion mass. To avoid isotropic stimulated emission, while yet maintaining a short cooling time, the upper level B of the ion should have a short decay time. The ultimate temperature that can be reached is determined either by the energy of a single absorbed photon, or by a balance of cooling and heating due to the randomness in the spontaneous emission recoils,

$$T_{min} = \frac{7}{20}\frac{\hbar\Gamma}{k_B}, \tag{9.41}$$

where Γ is the spontaneous decay rate (inverse lifetime) of the excited ion state. Laser cooling is illustrated schematically in Figs. 9.6 and 9.7.

As an example[7], consider a 100-keV $^7Li^+$ beam. The ion has a closed transition at 548.5 nm, which can be reached by CW dye lasers. The lifetime of the upper state is 43 ns. The change in energy due to a single absorption is 12 meV. A few mW laser power on a 5-mm spot result in a spontaneous emission of 1.2×10^7 s^{-1}, or about 15 absorptions in an interaction region of 2 m length. This corresponds to a change in energy of 0.2 eV. To cool an ion beam with an energy spread of 1 eV would only require a few revolutions, or a few tenths of microseconds. The ultimate temperature corresponds to the energy of a single kick, *i.e.*, 12 meV.

Laser cooling requires adequate energy levels and transitions that can be reached by tunable lasers. So far, only 4 ion species fulfill this condition ($^7Li^+$, $^9Be^+$, $^{24}Mg^+$,

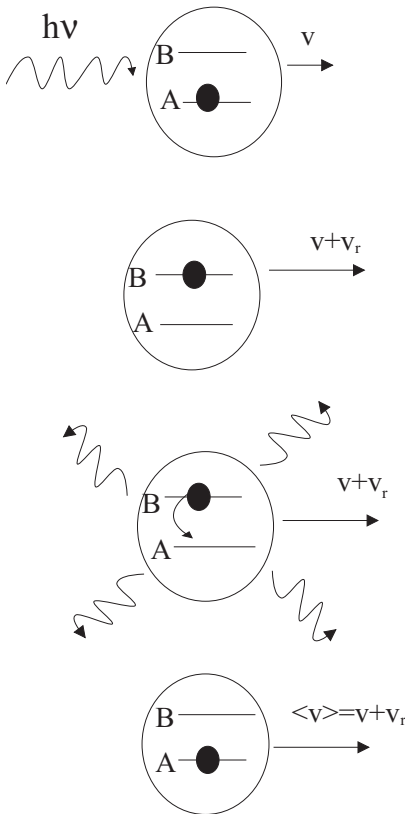

Figure 9.6: Photon absorption and emission during laser cooling[7].

and $^{166}Er^{+}$). Laser cooling was demonstrated experimentally in TSR and ASTRID, where energy spreads less than 10^{-6} were obtained for Li beams.

So far laser cooling affects mainly the longitudinal temperature of a beam. However, it is believed that by resonantly coupling the synchrotron and betatron motion, the very fast laser cooling can be extended to the transverse phase space[15]. The coupling between synchrotron motion and horizontal betatron motion may be provided either by a special coupling cavity[16], or, more simply, by momentum dispersion in a regular rf cavity[17]. With such coupling present, the transverse cooling is considerably improved if the tunes are close to a linear resonance:

$$\nu_x - \nu_s \approx k \tag{9.42}$$

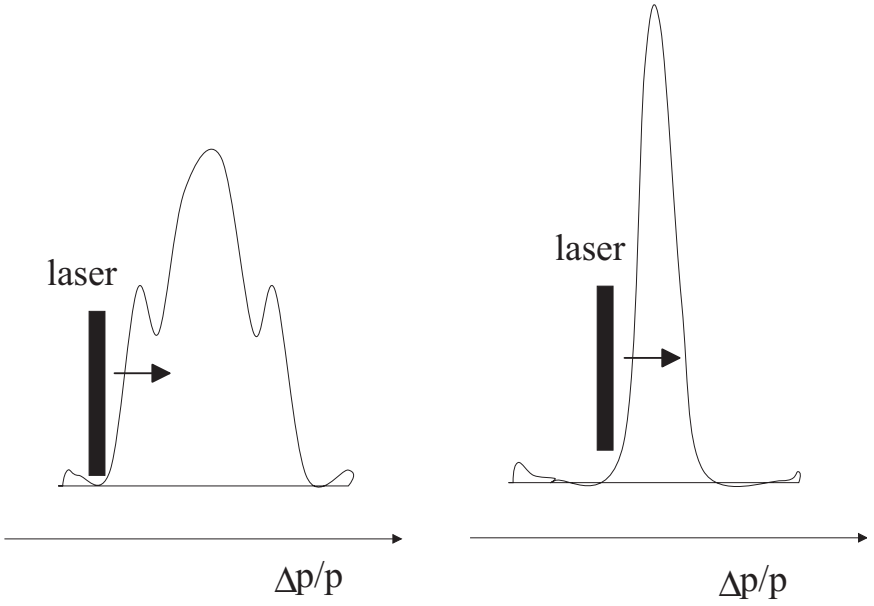

Figure 9.7: Evolution of ion velocity distribution during laser cooling of a bunched ion beam.

$$\nu_x - \nu_y \quad \approx \quad l \tag{9.43}$$

where k and l are integers.

Ex.9.7. Beam temperature with laser cooling
Consider laser cooling for 100 keV Mg^+ ions ($A = 24$). Suppose the laser operates at a wavelength of 280 nm, equal to a short-lived transition with a natural linewidth of 46 MHz. (a) Which relative ion velocity corresponds to the laser tuning range of 20 GHz? (b) What is the ultimate temperature one might hope to achieve?

9.3.2 Electron Beams

A different type of laser cooling was proposed by Telnov[18] for e^+e^- linear colliders, as a scheme to reduce the transverse emittances and to reach ultimate luminosities. Collision of an electron beam with a high-power laser beam does not change the beam spot size, nor much the angular divergence. Only the beam energy is decreased, for example, from an inital value E_0 to E. This means that in a laser-cooling stage the two transverse normalized emittances decrease by a factor E/E_0. Telnov estimated

that ultimate emittances of $\gamma\epsilon_{x,y} = 2 \times 10^{-7}$ m could be achieved, far better than what can be delivered by conventional damping rings.

More recently, Huang and Ruth studied a laser-electron storage ring (LESR) where radiative laser cooling overcomes the intrabeam scattering effect[19]. The LESR is sketched in Fig. 9.8. It consists of bending magnets, an rf cavity, an injector, and a laser-beam interaction region. A circulating bunch in the ring counterpropagates on each turn through the intense laser pulse. The laser pulse is stored in a high-Q optical resonator, whose path length is adjusted such that the laser-pulse repetition frequency equals the beam revolution frequency. Thus, the a single laser pulse can interact several 10^4 times with the same electron bunch. The LESR can be configured either as a damping ring producing beams with very small transverse emittances, or as a high-intensity X-ray source.

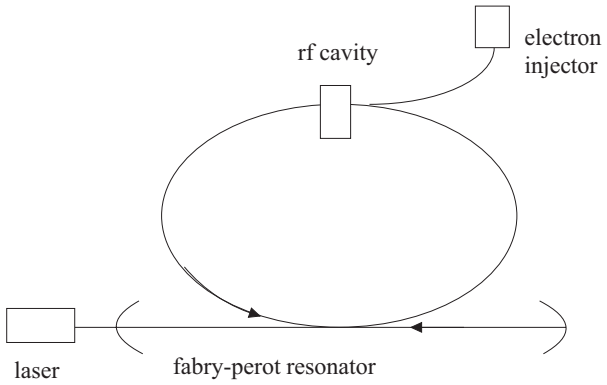

Figure 9.8: Schematic of a laser-electron storage ring[19].

The effect of the laser field is the same as that of a wiggler static with peak field strength[20]

$$B_w = \frac{2}{c}\sqrt{2Z_0 I} \tag{9.44}$$

where I is the laser intensity and Z_R the vacuum impedance (377 Ω). The power radiated in the laser field is then

$$P_\gamma = \frac{32\pi}{3} r_e^2 \gamma^2 I \tag{9.45}$$

and the energy loss of an electron per turn

$$(\Delta E)_\gamma = \int P_\gamma \frac{dz}{2c} = \frac{32\pi}{3} r_E^2 \gamma^2 \frac{E_L}{Z_R \lambda_L}, \tag{9.46}$$

where Z_R is the laser Rayleigh length. The latter characterizes the depth of focus of the laser beam and is equivalent to a laser-beam beta function. In Eq. (9.46), we have assumed that the laser beam is diffraction limited (so that the effective laser emittances are $\epsilon_{L,\,x,y} \approx \lambda_L/(4\pi)$), in which case its transverse spot area Σ_L at the focal point is given by: $\Sigma_L \equiv 2\pi\sigma_{L,x}\sigma_{L,y} = Z_R\lambda_L/2$.

From the energy loss per turn we can compute the longitudinal damping time. It corresponds to a number of turns equal to

$$n_d = \frac{E}{(\Delta E)_\gamma} = \frac{1.6\times 10^5 \lambda_L[\mu\mathrm{m}]]Z_R[\mathrm{mm}]}{E_L[\mathrm{J}]\;E[\mathrm{MeV}]}, \tag{9.47}$$

with E the beam energy.

Ex.9.8. Damping times with laser cooling
Calculate n_d for the parameters $E_L \approx 1$ J, $\lambda_L \approx 1$ μm, $Z_R \approx 1$ mm, and $E \approx 100$ MeV. What is the equivalent damping time for an average ring radius of 1 m?

The transverse emittances are damped at the same rate as the energy spread,

$$\Gamma^{RLC}_{x,y} \equiv -\frac{1}{\epsilon_{x,y}}\left\langle \frac{d\epsilon_{x,y}}{dt}\right\rangle = \frac{1}{n_d T_{rev}} = \frac{\Delta E_\gamma/E}{T_{rev}}, \tag{9.48}$$

where T_{rev} is the revolution time.

The laser field does not only provide damping, but in the same way as regular synchrotron radiation, it also introduces a quantum excitation. The quantum excitation consists of two parts: a dispersive component, which is dominant in conventional storage rings, and a component due to the finite opening angle of photon emission ($\theta \sim 1/\gamma$). The LESR is designed with zero optical dispersion in the laser-beam interaction region. A small amount of dispersion generated by the wiggler field is negligible compared with the effect of the opening angle, since the wiggle angle is much smaller than $1/\gamma$. This is quite different from the situation in a conventional ring, where the dispersive part is always much larger than the opening-angle contribution. Thus, in a conventional ring the emittance is determined by the dispersion (via the 'curly $\mathcal{H}$'), while in the LESR it is defined only by the opening angle.

The number of photons scattered into a frequency interval $d\omega$ is[21]

$$\frac{dN_\gamma}{d\omega} = \frac{1}{\hbar\omega}\frac{dE_\gamma}{d\omega} = \frac{3(\Delta E)_\gamma}{\hbar\omega_m^2}\left[1 - 2\left(\frac{\omega}{\omega_m}\right) + 2\left(\frac{\omega}{\omega_m}\right)^2\right] \tag{9.49}$$

where the energy loss per turn $(\Delta E)_\gamma$ was given above, and $\omega_m = 4\gamma^2\omega_L = 8\pi\gamma^2 c/\lambda_L$ is the maximum photon frequency. The photon frequency ω and the scattering angle

θ are related by

$$\omega = \frac{\omega_m}{1+\gamma^2\theta^2} \tag{9.50}$$

The transverse recoil of the electron is $\delta\psi = \hbar\omega\theta/E$, causing an average change in the transverse emittances of $\Delta\epsilon^n_{x,y} \approx \beta^*_{x,y}\,\delta\psi^2/4$. Here, one factor of 2 is due to the projection onto a transverse plane, the other is due to averaging over the betatron phase.

Integrating over the photon spectrum yields the average emittance excitation per turn

$$\Delta(\epsilon^n_{x,y}) = \frac{\gamma\beta^*}{2}\int_0^{\omega_m} d\omega \frac{\delta\psi^2}{2}\frac{dN_\gamma}{d\omega} = \frac{3}{10}\frac{\lambda_c}{\lambda_L}\frac{(\Delta E)_\gamma}{E}\beta^*_{x,y} \tag{9.51}$$

where $\beta^*_{x,y}$ is the beta function at the laser-electron interaction point, and $\lambda_c = h/(mc) \approx 2.43\times10^{-12}$ m the electron Compton wavelength. The average emittance excitation per unit time reads

$$\left\langle \frac{d\epsilon^n_{x,y}}{dt} \right\rangle = \frac{(\Delta E)_\gamma}{T_{rev}} \tag{9.52}$$

As usual, the balance of damping, Eq. (9.48), and excitation, Eq. (9.52), determines the equilibrium emittance:

$$\epsilon^n_{x,y} = \frac{3}{10}\frac{\lambda_c}{\lambda_L}\beta^*_{x,y} \tag{9.53}$$

According to Eq. (9.53), small emittances require a small beta function $\beta^*_{x,y}$. In addition, reducing the value of β^* also helps for matching the electron beam to the laser spot size for confining the energy of the laser pulse.

Longitudinally, the energy spread is increased by the energy fluctuation of the emitted photons:

$$\left\langle \frac{d(\sigma_E)^2}{dt} \right\rangle = \frac{1}{T_{rev}}\int_0^{\omega_m} d\omega\ (\hbar\omega)^2\ \frac{dN_\gamma}{d\omega} = \frac{7}{10}\ \frac{\hbar\omega_m\ (\Delta E)_\gamma}{T_{rev}} \tag{9.54}$$

As in a normal storage ring, the longitudinal damping occurs at a rate

$$\frac{1}{\sigma_E^2}\left\langle \frac{d(\sigma_E)^2}{dt} \right\rangle = -2\frac{\Delta E_\gamma/E}{T_{rev}} \equiv -\Gamma_s^{RLC} \tag{9.55}$$

Equating the excitation and damping terms yields the equilibrium energy spread[19]

$$\sigma_\delta \equiv \frac{\sigma_E}{E} = \sqrt{\frac{7}{5}\frac{\lambda_c}{\lambda_L}\gamma} \tag{9.56}$$

which tends to be larger than in a conventional storage ring.

Ex.9.9. Equilibrium emittances with laser cooling
As an example, consider a ring with $E = 100$ MeV and $\beta^*_{x,y} = 1$ cm, and a laser with wavelength $\lambda_L = 1$ μm. Calculate the equilibrium emittance and relative energy spread.

The increased energy spread widens the beam size in the arcs, where the dispersion function is large. Thereby it both reduces the emittance growth rate due to intrabeam scattering and it keeps the incoherent space-charge tune shift at an acceptable value (for the above parameters, a bunch population of 10^{10} and 6 mm rms bunch length, the tune shift is about 0.01) [19]. However, the large energy spread demands a good chromatic correction, and a high-frequency rf system in order to maintain a short bunch length.

The depletion of the laser pulse due to its interaction with the electron beam is negligible. Nor does the laser-pulse energy significantly decrease over several damping times, if the two mirrors of the optical resonator have a reflectivity of 99.99% or better.

9.4 Thermal Noise and Crystalline Beams

Laser or electron cooling produce extremely cold beams. These beams have unusual noise spectra [22]. Suppose the azimuthal density of a stored proton beam is described by a Fourier expansion as

$$\rho(\theta, t) = \sum_{n=-\infty}^{\infty} \frac{A_n(t)}{2\pi} \exp(in\theta) \tag{9.57}$$

and

$$A_n(t) = \sum_{a=1}^{N} e^{-in\theta_a(t)} \tag{9.58}$$

where a counts the particles and N is the total number of particles in the beam. In an ordinary beam, where the fluctuations arise from so-called Schottky or 'shot' noise, we have $< |A_n|^2 >= N$.

Interaction of the particles via the external environment (characterized by the longitudinal impedance) suppresses the density fluctuation at the nth revolution harmonic as [22]

$$< |A_n|^2 >= \frac{N}{1 + N/N_{th}} \tag{9.59}$$

where the threshold number N_{th} follows from equating the longitudinal coherent frequency shift

$$\Omega_n^2 = n^2 \frac{N r_p mc 4\pi\omega_0\omega_0'}{Z_0 C} \left(\frac{Z_n}{n}\right) \tag{9.60}$$

with $\omega_0' = d\omega_0/dp$, Z_0 the vacuum impedance, C the circumference and r_p the classical particle radius, to the spread in revolution frequency $n\ \delta\omega$ near $n\omega_0$. This yields[22]:

$$N_{th} = \frac{CZ_0\ \delta\omega^2}{4\pi r_p mc\omega_0\omega_0'}\ \left(\frac{n}{Z_n}\right) \tag{9.61}$$

When the beam is cooled, N_{th} becomes smaller than N. Under these conditions the noise power of the beam does no longer depend on the number of particles. Instead it is a direct measure of the beam temperature:

$$< |A_n|^2 > \approx N_{th} \propto \delta\omega^2\ \left(\frac{n}{Z_n}\right) \tag{9.62}$$

The impedance Z_n/n can be determined from the observed shift in coherent frequency as a function of beam current. The remarkable suppression of the noise spectrum for a cold beam was first observed with an electron-cooled proton beam at the NAP-M storage ring in Novosibirsk[22].

The fast cooling techniques open up the exciting possibility to generate a new state of matter: a crystalline beam. Crystalline beams were proposed by Dikanski and Pestrikov[23], motivated by the observation at NAP-M[22]. Theoretical studies of crystal beams were first performed by Schiffer and Rahman[24,25], and later by Wei, Li, Sessler, Okamoto, and others[26,27,28].

A crystalline beam is an ordered state, where the particles forming the beam `lock' into fixed positions so that the repelling intra-particle Coulomb forces just balance the external focusing force. Crystalline beams might provide a venue for obtaining ultra-high luminosity in colliders.

The generation and possible maintenance of the ordered state was investigated with molecular dynamics (MD) methods starting from a Hamiltonian describing the external focusing and the inter-particle forces in the beam-frame. For example, in a combined-function cyclotron magnet, this Hamiltonin reads

$$H = \frac{1}{2}(P_x^2 + P_y^2 + P_z^2) - \gamma x P_z + \frac{1}{2}(1-n)x^2 + \frac{1}{2}ny^2 + V_c(x,y,z) \tag{9.63}$$

with $n \equiv -\partial B_y/\partial x\ \rho/B_0$ measuring the strength of the quadrupole field, ρ the bending radius associated with the dipole field B_0, and the potential

$$V_c = \sum_j [(x_j - x)^2 + (y_j - y)^2 + (z_j - z)^2]^{-1/2} \tag{9.64}$$

where the summation is over all other particles. In the above Hamiltonian all dimensions were scaled by the characteristic distance $\xi = r_0\rho^2/\beta^2\gamma^2$, time is measured in units of $\rho/(\beta\gamma c)$, and energy in units of $\beta^2\gamma^2 Z^2 e^2/\xi$.

The beam-frame is an accelerated frame of reference, and the above Hamiltonian includes, so to speak, the relativistic generalization of centrifugal and Coriolis forces[26]. The effect of shear, given by the term $\gamma x P_z$, can render the Hamiltonian unbounded. This and the time dependent focusing in an alternating gradient focusing lattice may heat and melt the crystal.

Studying the circumstances under which the crystal is stable, one finds that two conditions have to be fulfilled in order to maintain the crystalline state[27]:

1. the storage-ring must be alternating focusing and the beam energy must be below the transition energy

2. the ring lattice periodicity should be larger than 2 times the maximum betatron tune.

. The first condition arises from the requirement of stable kinematic motion. The second condition ensures that these is no linear resonance between crystal phonon modes and the machine lattice periodicity[28].

Although the crystalline ground state will show a periodic variation of its shape as the beam travels around the storage ring, at low temperatures very little heat is absorbed by the crystal and the crystal can remain stable for a very long time.

When the ion density is very low, the crystalline ground state is a 1-dimensional chain stretching around the ring. The 1D crystal changes into a 2D structure at a density where the nearest-neigbor distance Δ_z (in the scaled units) obeys the equality [26]

$$\min(\nu_y^2, \nu_x^2 - \gamma^2) = \frac{4.2}{\Delta_z^3} \tag{9.65}$$

The 2D structure extends into the transverse plane of weaker focusing. At still larger densities, a 3D crystal is formed.

9.5 Beam Echoes

An echo is a coherent oscillation which grows out of a quiet beam with some delay after the application of two independent pulse excitations. Echoes can occur in unbunched and in bunched beams, both transversely and longitudinally. The shape and magnitude of the echo signal contains information on diffusion processes in the beam and on the beam temperature (*e.g.* energy spread). Echoes may thus become a useful diagnostics tool for beam cooling.

We first give a simple illustration how an echo signal can arise. We next calculate the echo signal in the transverse plane, following closely the pioneering work by Stupakov[29]. Then we discuss experimental results obtained with longitudinal echoes in unbunched beams.

9.5.1 *Illustration*

The successive application of a dipole kick (at time $t = 0$) and a quadrupole kick (at time $t = \tau$) can generate an echo signal (at time $t \approx 2\tau$), as illustrated schematically in Fig. 9.9.

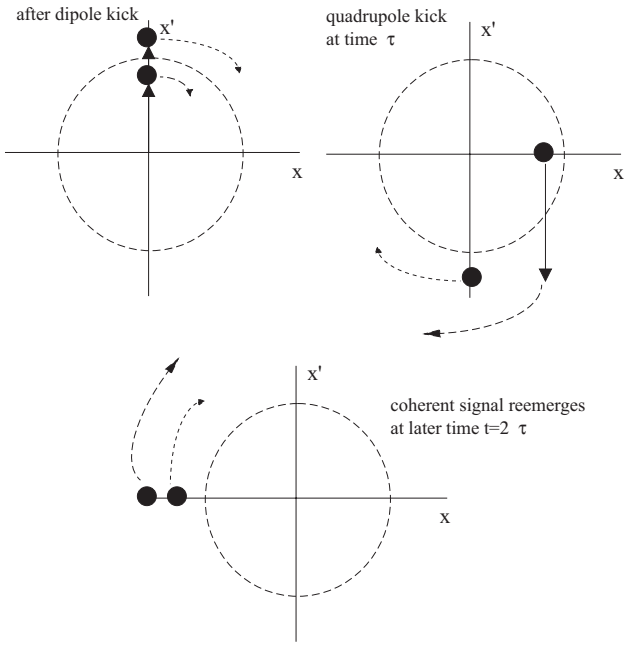

Figure 9.9: Two-particle model of signal recoherence after applying first a dipole kick and then a quadrupole kick[30]. For the echo generation it is essential that the betatron tune depends on the oscillation amplitude.

9.5.2 *Calculation of Transverse Echo*

We now want to calculate the response of the beam centroid to the dipole and quadrupole kick and derive an analytical expression for the echo response. To describe the transverse motion of particles in a storage ring, we here employ the normalized coordinates

$$\hat{y} = \frac{y}{\sqrt{\beta}} \qquad \text{and} \qquad \hat{p} = \frac{1}{\nu\Omega}\frac{dy}{dt} \tag{9.66}$$

where β is the beta function, Ω the revolution frequency, and ν the tune. The beam dynamics can be studied using the distribution function $\rho(\hat{p}, \hat{y}, t)$ with $\int \rho(\hat{p}, \hat{y}, t)\, d\hat{p}d\hat{y} =$

1. The initial distribution is assumed to be Gaussian:

$$\rho(\hat{p},\hat{y},0) = \frac{1}{2\pi J_0}\exp\left(-\frac{\hat{p}^2+\hat{y}^2}{2J_0}\right) \tag{9.67}$$

with J_0 a constant equal to the rms beam emittance. It is customary to introduce so-called action-angle coordinates (J,ϕ) via:

$$\hat{y} = \sqrt{2J}\cos\phi \tag{9.68}$$
$$\hat{p} = -\sqrt{2J}\sin\phi \tag{9.69}$$

The initial distribution function then assumes the form

$$\rho_0(J,\phi) = \rho(J,\phi,0) = \frac{1}{2\pi J_0}\exp\left(-\frac{J}{J_0}\right) \tag{9.70}$$

and the transformation corresponding to free betatron oscillations conserves the action J:

$$J(t) = J(0) \tag{9.71}$$
$$\phi(t) = \phi(0)+\nu\Omega t \tag{9.72}$$

In the original coordinates this oscillation reads

$$\hat{p}(t) = \hat{y}(0)\ \cos\nu\Omega t + \hat{p}(0)\ \sin\nu\Omega \tag{9.73}$$
$$\hat{y}(t) = -\hat{y}(0)\ \sin\nu\Omega t + \hat{p}(0)\ \cos\nu\Omega \tag{9.74}$$

We assume that the tune ν depends on the amplitude of the oscillation as

$$\nu = \nu(J) = \nu_0 + \Delta\nu\frac{J}{J_0} \tag{9.75}$$

where $\Delta\nu$ has the meaning of a tune spread. This tune shift with amplitude is crucial for the echo effect.

From the distribution function $\rho(J,\phi,t)$ we can calculate the evolution of the averaged (centroid) displacement, by means of a simple integration:

$$<\hat{y}>=\int_{-\infty}^{\infty}d\hat{p}\int_{-\infty}^{\infty}\hat{y}\rho(\hat{p},\hat{y},t)d\hat{y} = \sqrt{2}\int_0^{\infty}\sqrt{J}\,dJ\ \int_0^{2\pi}\cos\phi\,\rho(J,\phi,t)\,d\phi \tag{9.76}$$

The evolution of the distribution function is governed by the Vlasov equation:

$$\frac{\partial\rho}{\partial t}+\frac{d\rho}{\partial\hat{y}}\frac{d\hat{y}}{dt}+\frac{\partial\rho}{\partial\hat{p}}\frac{d\hat{p}}{dt}=0 \tag{9.77}$$

Alternatively and equivalently, the distribution function at time t can be obtained by expressing the coordinates $\hat{p}(t)$ and $\hat{y}(t)$, or the corresponding action-angle variables, in terms of those at time 0. In other words, the Hamiltonian mapping induces the following transformation of the distribution function:

$$\rho(\hat{p}(0), \hat{y}(0), 0) \rightarrow \rho(\hat{p}(t), \hat{y}(t), t) = \rho(\hat{p}(\hat{p}(t), \hat{y}(t), 0), \hat{y}(\hat{p}(t), \hat{y}(t), 0), 0) \quad (9.78)$$

which links the distributions at times 0 and t. We will use the second method for computing $\rho(\hat{p}, \hat{y}, t)$.

Suppose that at time $t = 0$, the beam is displaced from the closed orbit by a transverse dipole kick of size $\Delta\hat{p} = \epsilon$. This dipole kick gives rise to the new distribution function:

$$\rho_1(\hat{p}, \hat{y}) = \rho_0(\hat{p}(0) - \epsilon, \hat{y}(0)) \quad (9.79)$$

where the ρ_0 is our initial Gaussian function at time $t = 0$. Assuming that the kick ϵ is small, we can expand the above equation to first order:

$$\rho_1(\hat{p}, \hat{y}) \approx \rho_0(\hat{p}, \hat{y}) - \epsilon\frac{\partial\rho_0}{\partial\hat{p}} = \rho_0(J) + \epsilon\sqrt{2J}\sin\phi\,\frac{d\rho(J)}{dJ} \quad (9.80)$$

The kick is followed by a free betatron oscillation over a time τ. This changes the distribution function as

$$\rho_2(J, \phi, \tau) = \rho_1(J, \phi - \nu\Omega\tau) \quad (9.81)$$

Inserting the previous expression for ρ_1 we find

$$\rho_2 = \rho_0(J) + \epsilon\sqrt{2J}\sin(\phi - \nu(J)\Omega\tau)\frac{d\rho_0(J)}{dJ} \quad (9.82)$$

Using Eqs. (9.75), (9.76), and (9.82), and performing the integration, we find the centroid motion after the dipole kick:

$$< \hat{y} >= \epsilon\left[\frac{1 - \Delta\nu^2\Omega^2\tau^2}{(1 + \Delta\nu^2\Omega^2\tau^2)^2}\sin\nu_0\Omega\tau + \frac{2\Delta\nu\,\Omega\tau}{(1 + \Delta\nu^2\Omega^2\tau^2)^2}\,\cos\nu_0\Omega\tau\right] \quad (9.83)$$

It is illustrated in Fig. 9.10 and clearly shows the decoherence of the signal. For large τ, the average displacement $< \hat{y} >$ decreases as τ^{-2}.

Now at time, $t = \tau$ we apply a quadrupole kick of strength q:

$$\hat{p}_{new} = \hat{p}_{old} + \Delta\hat{p}_{quad} = \hat{p}_{old} - q\hat{y} \quad (9.84)$$

The new distribution function is

$$\rho_3(\hat{p}, \hat{y}) = \rho_2(\hat{p} - \Delta\hat{p}_{quad}, \hat{y}) \quad (9.85)$$

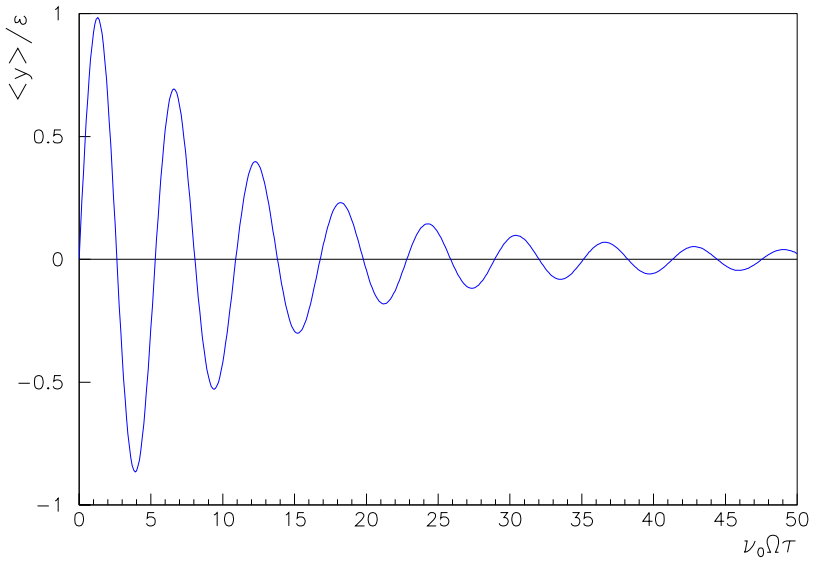

Figure 9.10: Average displacement of the beam as a function of time following a dipole kick, for a tune spread $\Delta\nu \approx 10\ \%$[29].

To perform again a Taylor expansion, we assume that also the quadrupole kick is small, or, more precisely, that

$$q\nu\Omega\tau \ll 1 \tag{9.86}$$

Inserting all the terms from above we have

$$\begin{aligned}\rho_3(\hat{p},\hat{y}) \quad &\approx \quad \rho_0(J) + \epsilon\sqrt{2J}\sin(\phi-\nu(J)\Omega\tau)\ \frac{d\rho_0(J)}{dJ} \\ &\quad +q\hat{y}\frac{\partial}{\partial\hat{p}}\left[\rho_0(J) + \epsilon\sqrt{2J}\sin(\phi-\nu(J)\Omega\tau)\frac{d\rho_0(J)}{dJ}\right]\end{aligned} \tag{9.87}$$

The echo effect is contained in the last term on the right-hand side of this equation. Using the relation

$$\frac{\partial}{\partial\hat{p}} = -\sqrt{2J}\sin\phi\frac{\partial}{\partial J} - \frac{1}{\sqrt{2J}}\cos\phi\frac{\partial}{\partial\phi} \tag{9.88}$$

the largest term that contributes to the echo comes from the derivative of $\sin(\phi -$

$\nu(J)\Omega\tau)$ with respect to J. Denoting this term by ρ_3^{echo} one has

$$\rho_3^{echo} \approx 2\epsilon q \Delta\nu\, \Omega\tau \sin(\phi)\cos(\phi - \nu(J)\Omega\tau)\frac{J}{J_0}\frac{d\rho_0(J)}{dJ} \tag{9.89}$$

Following the quadrupole wake, there is another free betatron oscillation of duration s, with

$$\rho_4(J,\phi) = \rho_3^{echo}(J, \phi - \nu\Omega s) \tag{9.90}$$

Putting this into Eq. (9.76) and integrating, we finally obtain the equation for the echo response:

$$< \hat{y}^{echo} > \approx q\epsilon\Delta\nu\Omega\tau \left[\frac{A(A^2-3)}{(1+A^2)^3}\cos\nu_0\Omega(\tau - s) + \frac{3A^2-1}{(1+A^2)^3}\sin\nu_0\Omega(\tau - s)\right] \tag{9.91}$$

where $A \equiv \Delta\nu\ \Omega(\tau - s)$. The echo is illustrated in Fig. 9.11 as a function of the time difference $(\tau - s)$, for a tune spread of 10% ($\Delta\nu/\nu_0 = 0.1$). The peak of the echo signal is proportional to the strengths of the two kicks and does not depend on the time interval between them; though the time of occurrence around $s = \tau$ does.

9.5.3 Measurements of Longitudinal Echoes

Let us now turn to experimental results for longitudinal echoes in unbunched beams. Such experiments were performed at the Fermilab Accumulator[31] and at the CERN SPS[32]. In these studies, two rf kicks were applied at frequencies f_{kick1} and f_{kick2}. The response was observed at the difference frequency[31]

$$f_{echo} = f_{kick2} - f_{kick1} \tag{9.92}$$

For example if $h_{kick1} = 10$ and $h_{kick2} = 9$ (h is the harmonic number), the response occurred near the fundamental frequency $h_{echo} = 1$. The time of the echo is

$$t_{echo} = \frac{f_{kick1}}{f_{kick2} - f_{kick1}}\Delta t \tag{9.93}$$

where Δt is the time separation between the two kicks.

The presence of diffusion destroys the reversibility of the decoherence. Diffusion thus reduces the response of the echo signal, especially for echoes at large times t_{echo}. The amplitude of the echo is of the form[31]

$$I_{echo} \propto J_1(k_1\delta\Delta t)\exp(-k_2\nu t_{echo}^3) \tag{9.94}$$

where δ is proportional to the kick strength, Δt denotes the time between the kicks, k_2 is a constant which depends on the two kick harmonics (and on the echo harmonic),

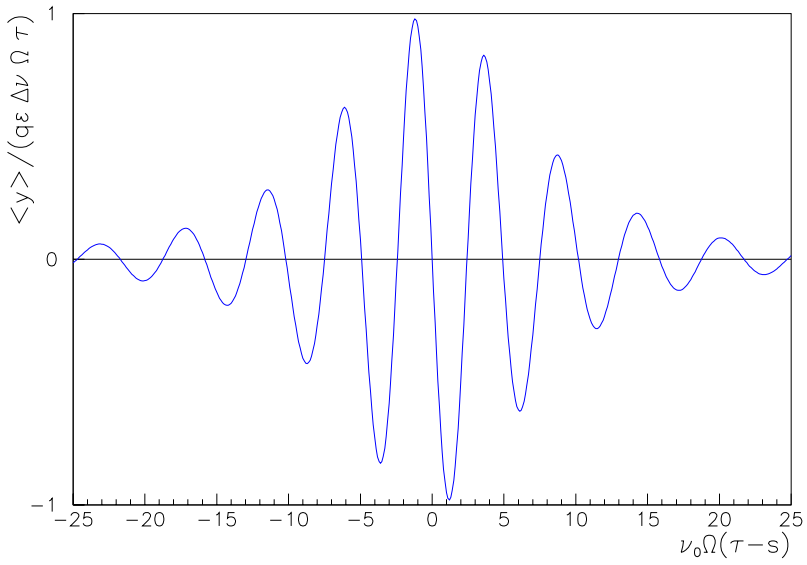

Figure 9.11: Echo signal of the beam after a second (quadrupole) kick was applied[29].

ν is the diffusion rate (or collision rate), and t_{echo} the time from the first kick to the center of the echo. This decorrelation due to diffusion results in an exponential decay of the echo signal as t^3. By comparing the echo responses for different sets of harmonics, the contributions from the Bessel function and from the diffusion can be distinguished. In the Tevatron Accumulator, a diffusion of $\nu \approx 3 \times 10^{-4}$ Hz was measured, which suppressed the response signal already within the first lobe of the Bessel function[31].

Further points should be mentioned. At the center of the echo signal the response is zero. We have seen the same behavior in our above analysis for the transverse echo (compare Fig. 9.11). It is related to the fact that the echo signal is proportional to the slope of the distribution function, which is zero at the center of a symmetric bunch. The separation of the two peaks, on either side of this zero, is inversely proportional to the energy spread within the bunch as[31]

$$\Delta t_{peak} = \frac{\beta^2}{h_{echo}\pi f_{rev}|\eta|\frac{\sigma_E}{E}} \tag{9.95}$$

where η is the slippage factor, f_{rev} the revolution frequency, and β the velocity divided by the speed of light ($\beta = v/c$). This equation was confirmed experimentally.

If the distribution function is not Gaussian, the shape of the echo response changes. The echo signal thus could permit a reconstruction of the actual beam distribution. Care has to be taken, as the echo shape may also be modified by longitudinal wake fields.

Another interesting observation was that for sufficiently large energy spread the notch at the center of the echo signal disappeared. A possible explanation is the contribution from higher-order momentum compaction (or slippage) to the spread in revolution frequencies:

$$\frac{\Delta f}{f_{rev}} = -\frac{\eta}{\beta^2}\frac{\Delta E}{E_0} = -\frac{1}{\beta^2}\frac{\Delta E}{E_0}\left(\eta_0 + \eta_1 \frac{1}{\beta^2}\frac{\Delta E}{E_0} + \ldots\right) \tag{9.96}$$

For larger energy spread, the nonlinear contributions destroy the linear correlation between energy and particle phase.

9.6 Ionization Cooling

The successful operation of a future muon collider requires a reduction of the 6-dimensional beam phase space by about a factor of 10^{-6}. The proposed approach to achieving this reduction is ionization cooling. Ionization cooling is similar to electron cooling, but the electron beam is replaced by a solid or liquid.

In ionization cooling the muon beam is passed through some material where the muons lose energy, experiencing an average force opposite to their momentum, as in Eq. (9.9). The average energy loss is described by the so-called Bethe-Bloch formula:

$$-\frac{dE_\mu}{ds} = 4\pi N_A r_e^2 m_e c^2 \rho \frac{Z}{A}\frac{1}{\beta^2}\left[\ln\left(\frac{2m_e c^2 \beta^2 \gamma^2}{I}\right) - \beta^2 - \frac{\delta}{2}\right] \tag{9.97}$$

where N_A is Avogadro's number, the product $4\pi N_A r_e^2 m_e c^2$ equals 0.3071 MeV cm^2 g^{-1}, ρ is the material density, A and Z are mass number and atomic number, respectively, and δ represents a *density effect* (shielding by the atomic electrons) and at high energies approaches $2\ln\gamma$. The energy loss per length for Beryllium is shown in Fig. 9.12 as a function of the incident muon momentum. Only the longitudinal energy is restored by rf sections, resulting in a transverse cooling. The process must be repeated many times to achieve a large cooling factor. Figure 9.13 illustrates the concept of transverse ionization cooling.

The equation describing transverse cooling is[35]

$$\frac{d\epsilon_n}{ds} = -\frac{1}{\beta^2}\frac{dE_\mu}{ds} + \frac{1}{\beta^3}\frac{\beta_\perp}{2}\frac{(14\text{MeV})^2}{E_\mu m_\mu c^2 L_R} \tag{9.98}$$

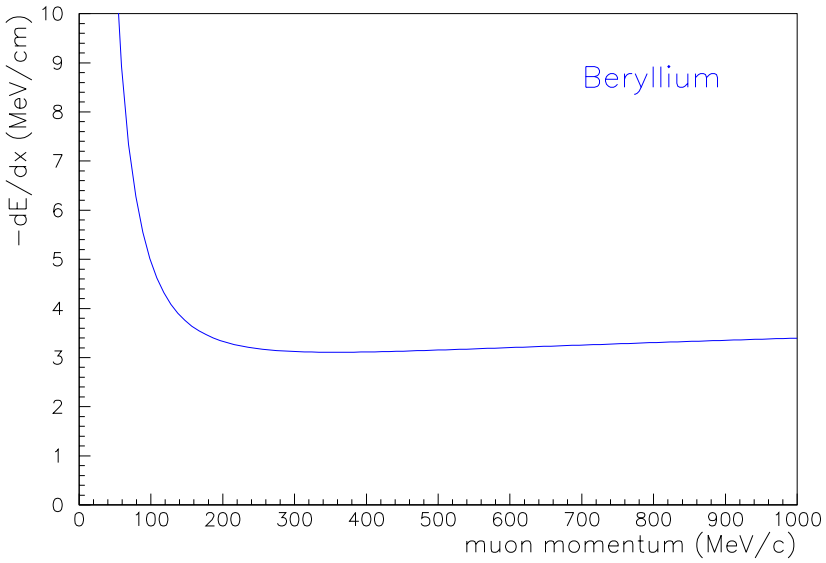

Figure 9.12: Average muon energy loss per length in Beryllium[33].

where ϵ_n is the normalized emittance, E_μ the total muon energy, $\beta_\perp$ the beta function at the absorbing material, dE_μ/ds the energy loss per unit length, and L_R the radiation length. The first term in this equation describes the cooling, and the second the heating term due to multiple scattering. The heating is minimized if $\beta_\perp$ is small, and L_R large (low Z material).

If no further action is taken, the energy spread evolves according to

$$\frac{d(\Delta E)^2}{ds} = -2\frac{d\left(\frac{dE_\mu}{ds}\right)}{dE_\mu} < (\Delta E_\mu)^2 > + \frac{d(\Delta E_\mu)^2_{\text{straggling}}}{ds} \tag{9.99}$$

where the first term is the cooling (or heating) due to the average energy loss and the second is the "energy-straggling" term given by[36]

$$\frac{d(\Delta E_\mu)^2_{\text{straggling}}}{ds} \approx 2\pi(r_e m_e c^2)^2 N_0 \frac{Z}{A}\rho\gamma^2 \tag{9.100}$$

where N_0 is Avogadro's number and ρ the density.

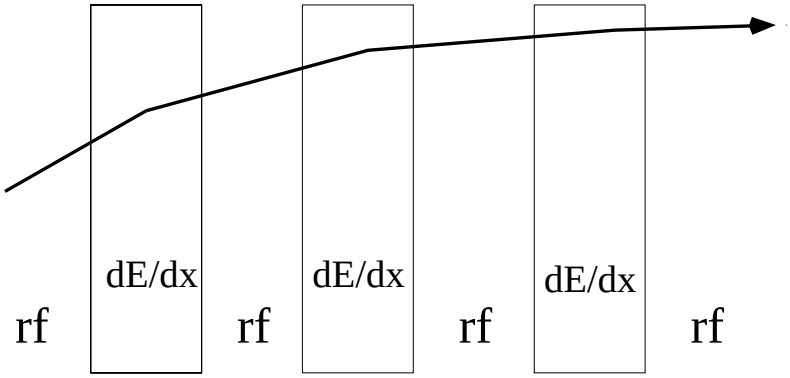

Figure 9.13: Schematic of ionization cooling in the transverse phase space using a series of low-Z energy absobers and reacceleration[34].

The energy spread is reduced by a transverse variation in absorber thickness at a location with dispersion, as shown in Fig. 9.14. The use of such wedges reduces the longitudinal emittance, and it increases the transverse emittance. Thus, the longitudinal cooling is based on emittance exchange with the transverse plane.

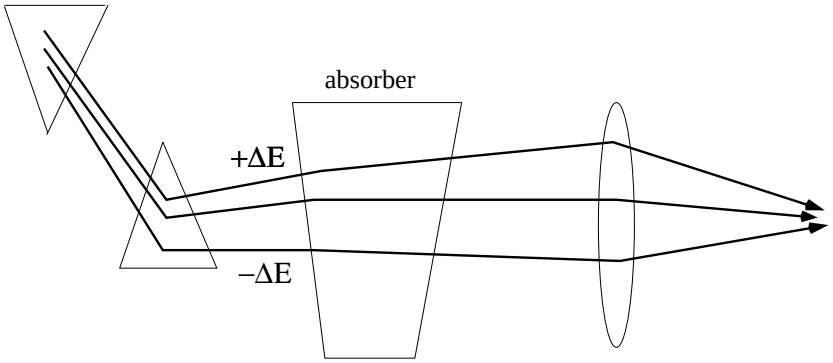

Figure 9.14: Schematic of ionization cooling in the longitudinal phase space using a wedge[34].

Ex.9.10. Damping rates and equilibrium emittances with ionization cooling
The emittance evolution in an ionization cooling system is described by the equation

$$\frac{d\epsilon_n}{ds} = -\frac{1}{\beta^2}\frac{dE_\mu}{ds}\frac{\epsilon_n}{E_\mu} + \frac{1}{\beta^3}\frac{\beta_\perp}{2}\frac{(14\mathrm{MeV})^2}{E_\mu m_\mu c^2 L_R} \tag{9.101}$$

where ϵ_n is the normalized emittance, $\beta_\perp$ the beta function at the absorbing material, dE_μ/ds the energy loss per unit length, and L_R the radiation length. Consider a muon beam with an initial normalized emittance of 0.01 m-rad and a kinetic energy E_k of 150 MeV. The muon mass is about 105.7 MeV.
(a) Calculate the average cooling rate λ (in units of m^{-1}) and the emittance reduction in a 10-m long cooling section containing 320 cm of liquid H_2 (radiation length L_R equal to 890 cm). Assume that the beta function at the absorber is 10 cm, and that the minimum energy loss per length, dE_μ/ds is 0.29 MeV/cm.
(b) Ignoring the second (heating) term, how many such stages and which total length would be required to damp the transverse emittance by a factor 10? In reality the complete cooling system might have a length of 500 m. Which fraction of muons is left after traversing this distance at 150 MeV? Note that the muon lifetime at rest is $2.2\ \mu$s.
(c) What is the minimum normalized emittance that can be achieved in such a cooling system of arbitrary length?
(d) Can you derive the above equation? Note that the projected angular distribution due to multiple scattering is approximately Gaussian with an rms width after distance s equal to

$$\theta \approx \frac{14\ \mathrm{MeV}}{\beta cp}\sqrt{\frac{s}{L_R}} \tag{9.102}$$

9.7 Comparison of Cooling Techniques

Table 9.1 compares the different cooling methods. Synchrotron radiation works mainly for electrons and positrons, ionization cooling can be used for muons, laser cooling for ions. Stochastic cooling and electron cooling are rather universal, and complementary: Stochastic cooling functions best for a hot beam, while the electron cooling time decreases with decreasing beam temperature. The stochastic cooling takes care of the beam tails, whereas the electron cooling freezes the core. Stochastic cooling favors high beam velocities; for electron cooling it is the opposite. Both electron and stochastic cooling are by now well established and used at various storage and accumulation rings. Laser cooling in a synchrotron was demonstrated only recently. This scheme is applicable for 4 types of ions only: Mg^+, Li^+, Be^+ and Er^+. Momentum spreads of less than 10^{-6} have been achieved. Perhaps laser cooling will even allow to enter a new regime of low temperatures and to generate *crystalline beams*. The cooling times for laser cooling are of the order of 10 or 100s of microseconds, only surpassed by the time scale projected for ionization cooling.

Table 9.1: Comparison of cooling techniques, modified from Ref. [7]; N is the number of particles in the beam.

technique	stoch.	electron	synchr. rad.	laser	ioniz.
species	all	ions	e^+e^-	some ions	muons
favored beam velocity	high	medium $0.01 < \beta < 0.1$	very high $\gamma > 100$	any $\gamma < 5$	medium
beam intensity	low	any	any	any	any
cooling time	$N \cdot 10^{-8}$ s	1–10^{-2} s	$\sim 10^{-3}$ s	$\sim 10^{-4}$–10^{-5} s	$< 10^{-7}$ s
favored temp.	high	low	any	low	any

9.8 References

1. D. Möhl, “Phase Space Cooling in Storage Rings”, Physica Scripta, Vol. T22, p. 21 (1988).

2. D.V. Pestrikov, “Beam Cooling”, lecture at the joint US-CERN-Russia-Japan Accelerator School, Montreux, Switzerland 1998.
3. Ya.S. Derbenev, N.S. Dikansky, D.V. Pestrikov, Proc. of the 2-nd All Union Part. Acc. Conf. v.2, p. 62, Moscow, Nauka 1970.
4. G.I. Budker, Atomnaja Energia 22, p. 346 (1967).
5. Ya.S. Derbenev, A.N. Skrinsky, Proc. of the 10th Internat. Conf. on High Energy Accel. v.1, p. 516, Serpukhov (1977).
6. J. Bosser, “Electron Cooling”, in 4th Advanced Accelerator Physics Course, CERN Accelerator School, CERN 92-01 (1992).
7. S.P. Møller, “Cooling Techniques”, CERN Acc. School, Jyvaeskylae 1992, CERN-94-01 (1994).
8. A.W. Chao, “Physics of Collective Beam Instabilities in High Energy Accelerators”, Wiley (1993).
9. J. Bosser, C. Carli, M. Chanel, L. Marie, D. Möhl, “On the Optimum Dispersion Function of a Storage Ring for Electron Cooling with High Space-Charge”, contributed to ECOOL99, to be published in NIM A (1999).
10. J. Bosser, C. Carli, M. Chanel, C. Hill, A. Lombardi, R. MAccaferri, S. Maury, D. Möhl, G. Molinari, S. Rossi, E. Tanke, G. Tranquille, M. Vretenar, “Experimental Investigation of Electron Cooling and Stacking of Lead Ions in a Low Energy Accumulation Ring” (1999).
11. C. Rubbia, Proc. of the Workshop on Producing High Luminosity High Energy Proton-Antiproton Collisions, Berkeley, LBL-7574, p. 98 (1978).
12. S.Y. Lee, P. Colestock, and K.Y. Ng, “Electron Cooling in High Energy Colliders”, FERMILAB-FN-657 (1997).
13. P.J. Channel, J. Appl. Phys. 52, p. 3791 (1981).
14. J.S. Hangst, J.S. Nielsen, O. Poulsen, P. Shi, and J.P. Schiffer, “Laser Cooling of a Bunched Beam in a Synchrotron Storage Ring”, Phys. Rev. Let. 74, p. 4432 (1995).
15. T. Kihara, H. Okamoto, Y. Iwashita, K. Oide, G. Lamanna and J. Wei, “Study of Three-Dimensional Laser Cooling Method Based on Resonant Linear Coupling”, KEK Preprint 98-158 (1998).
16. H. Okamoto, A.M. Sessler, D. Möhl, Phys. Rev. Lett. 72, 3977 (1994).
17. H.Okamoto, Phys. Rev. E50, 4982 (1994).
18. V. Telnov, “Laser Cooling of Electron Beams for Linear Colliders”, SLAC-PUB-7337 (1996).
19. Z. Huang and R.D. Ruth, “Laser Electron Storage Ring”, Phys.Rev.Lett. 80, p. 976 (1998).
20. K.-J. Kim, S. Chattopadhyay, C.V. Shank, Nucl. Instr. Meth. in Phys. Res. A 341, p. 351 (1994).
21. A. Hofmann, SSRL ACD-Note 38 (1986).

22. E.N. Dementev, N.S. Dikanski, A.S. Medvedko, V.V. Parkhomchuk, D.V. Pestrikov, "Measurement of the Thermal Noise of a Proton Beam in the NAP-M Storage Ring", Sov. Phys. Tech. Phys. 25, p. 1001 (1980).
23. N.S. Dikanski and D.V. Pestrikov, in Proc. of Workshop on Electron Cooling and Related Applications, Karlsruhe 1984, ed. by H. Poth, KfK 3846 (1984).
24. A. Rahman and J.P. Schiffer, "Structure of One-Component Plasma in an Extrenal Field: A Molecular Dynamics Study of Particle Arrangement in a Heavy-Ion Storage Ring", Phys. Rev. Letters 57, no. 9, p. 1133 (1986).
25. A. Rahman and J.P. Schiffer, "Feasibility of a Crystalline Condensed State in Cooled Ion Beams of a Storage Ring", Z. Phys. A 331, p. 71 (1988).
26. J. Wei, X.-P. Li, A.M. Sessler, "Low-Energy States of Circulating Stored Ion Beams: Crystalline Beams", Phys. Rev. Lett. 73, p. 3089 (1994).
27. J. Wei, H. Okamoto, A.M. Sessler, "Necessary Conditions for Attaining a Crystalline Beam", Phys. Rev. Lett. 80, p. 2606 (1998).
28. X.-P. Li, A.M. Sessler, J. Wei, "Crystalline Beam in a Storage Ring: How Long Can it Last?" Proc. EPAC94, London, p. 1379 (1994).
29. G. Stupakov, "Echo Effect in Hadron Colliders", SSCL-579 (1992)
30. This picture arose in a discussion with K.-J. Kim during this accelerator school.
31. L.K. Spentzouris and P. Colestock, "Coherent Nonlinear Longitudinal Phenomena in Unbunched Sycnhrotron Beams", invited talk at IEEE PAC97, Vancouver (1997).
32. O.S. Brüning, "On the Possibility of Measuring Longitudinal Echos in the SPS", CERN SL/95-83 (1995).
33. "$\mu^{=}\mu^{-}$ Collider. A Feasibility Study." Submitted to the APS Summer Study, Snowmass 1996, on "New Directions for High-Energy Physics", BNL-52503 (1996).
34. The MUCOOL Collaboration, "Ionization Cooling Research and Development Program for a High Luminosity Muon Collider" (1998).
35. D. Neuffer, Part. Acc. 14, 75 (1983).
36. R.C. Fernow and J.C. Gallardo, "Muon Transverse Ionization Cooling: Stochastic Approach", Phys. Rev. E52, 1039 (1995).

Chapter 10

Acknowledgements

We would like to thank A. Chao, R. Assmann, K. Bane, R. Bartolini, C. Bovet, H. Burkhardt, J. Byrd, Y. Cai, M. Chanel, J. Corbett, M. Donald, P. Emma, R. Garoby, M. Giovannozzi, T. Himel, K. Hirata, A. Hofmann, B. Holzer, J. Irwin, H. Koiso, A.D. Krisch, P. Martin, O. Meincke, D. Möhl, K. Oide, N. Phinney, T. Raubenheimer, I. Reichel, J. Safranek, J. Seeman, M. Seidel, P. Tenenbaum, D. Whittum, U. Wienands, and Y. Yan for valuable information, stimulating discussions, and for providing most of the material presented for use in this lecture. We are grateful to numerous further colleagues at SLAC, CERN, and KEK in particular those working on SLC, PEP-II, LEP, the ATF, and SPEAR for their untiring support, cooperation and inspiration.